NATIONAL SCIENCE FOUNDATION

Print ISSN 1391-4588
E - ISSN 2362-0161
Volume 53 No. 3
September 2025

Journal of the National Science Foundation of Sri Lanka

www.nsf.gov.lk

NATIONAL SCIENCE FOUNDATION

JOURNAL OF THE NATIONAL SCIENCE FOUNDATION OF SRI LANKA

Contact details
Editorial Office, National Science Foundation,
47/5, Maitland Place, Colombo 07, Sri Lanka.

E-mail : jnsf@nsf.gov.lk
Phone : +94-11- 2696771
JNSF online submission portal :
https://jnsfsl.sljol.info/about/submissions
JNSF home page :
http://www.nsf.gov.lk/ index.php/nsfscience magazine

Publication : Published quarterly (March, June, September and December) by the National Science Foundation of Sri Lanka.

Manuscripts: Research Articles, Research Communications, Reviews and Correspondences in all fields of Science and Technology can be submitted for consideration for publication. A guide to the preparation of manuscripts is provided in each issue. The guidelines may also be obtained by visiting the NSF website or JNSF online submission portal.

Disclaimer: No responsibility is assumed by the National Science Foundation of Sri Lanka for statements and opinions expressed by contributors to this Journal.

Publication : free A publication fee of US$ 250 will be levied for each manuscript in two stages except, when the corresponding author is affiliated with a Sri Lankan institution.

- A processing fee of US$ 20 will belevied for each manuscript at peer-review stage.
- Remaining US$ 230 will be charged for accepted articles at the time of publication.

Indexing : **The JNSF is indexed in Science Citation Index Expanded, Journal Citation Reports/Science Edition, BIOSIS Previews, Zoological Record, Biological Abstracts, Chemical Abstracts, Scopus, DOAJ, TEEAL, Ulrich's, AGRICOLA and EBSCOhost, CAB Abstracts, SafetyLit, Journal TOCs, EBSCO Applied Science & Technology Source Ultimate**

JOURNAL OF THE
NATIONAL SCIENCE FOUNDATION
OF SRI LANKA

Volume 53 Number 3 September 2025

C O N T E N T S

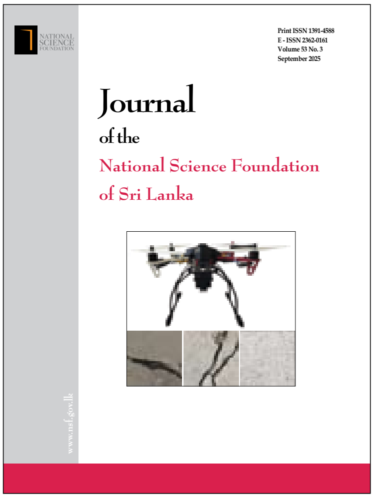

Cover: A drone modified to detect cracks in concrete structures (top) and several pictures taken from the drone (bottom)
See J.Natn.Sci.Foundation Sri Lanka 2025 53(3): 273 - 282

J.Natn.Sci.Foundation Sri Lanka 2025 53 (3): 205
DOI: http://dx.doi.org/10.4038/jnsfsr.v53i3.12761

EDITORIAL

Public trust in science and scientists

Evidence based decision making on most matters of public interest concerned with the welfare of the public require the application of scientific knowledge. It is reasonable to suppose that the extent to which policy makers base their decisions on scientific evidence, will be influenced by the apparent extent of public trust in science. In the absence of such trust, policy makers are more likely to be influenced by personal bias and by other factors of a socio-political nature.

Research carried out suggests that in most countries there is considerable public trust in science. However, this is often not explicitly expressed nor are there easy pathways to make policy makers aware of this. It should be noted that trust in science is the not the same as trust in scientists. Scientists, particularly those who take up advocacy positions on contentious local issues will be trusted on whether they are perceived to be acting in the interest of the public or in their own interest. In the current context of ease of disinformation through the internet and social media, individual scientists are vulnerable to unfair judgement. Thus, collective advocacy by professional and academic associations are much more likely to be trusted by the public.

In this connection, it is noteworthy that the National Academy of Sciences Sri Lanka has recently launched an ambitious, multifaceted programme in collaboration with the Sri Lanka Association for the Advancement of Science on "Rebuilding Trust in Science". The fact that the programme is supported by the private sector is a particularly encouraging development for Sri Lanka.

Ajit Abeysekera

J.Natn.Sci.Foundation Sri Lanka 2025 53 (3): 207 - 217
DOI: http://dx.doi.org/10.4038/jnsfsr.v53i3.12582

REVIEW ARTICLE

Mycology

Lichens of Sri Lanka: Past discoveries, present knowledge, and future directions

B Weerakoon[1], P Wolseley[2], S Wijesundara[3], S Nissanka[4] and G Weerakoon[2*]
[1] *Postgraduate Institute of Agriculture, University of Peradeniya, Peradeniya, Sri Lanka.*
[2] *Algae, Fungi and Plant Division, Department of Sciences, Natural History Museum, London, UK.*
[3] *National Institute of Fundamental Studies, Hantana Road, Kandy, Sri Lanka.*
[4] *Department of Crop Science, Faculty of Agriculture, University of Peradeniya, Peradeniya, Sri Lanka.*

Submitted: 03 March 2025; Revised: 21 July 2025; Accepted: 25 July 2025

Abstract: Lichens are an important component of Sri Lankan biodiversity and have contributed greatly to the tropical diversity as well as to their application as bioindicators of changing environmental conditions. This review summarises 49 selected research publications on the taxonomic and chemical diversity of lichens, their application as bioindicators, and as a source of bioactive compounds that have medicinal properties against microorganisms with the potential of curing some diseases. The chemical properties of lichens and associated fungi and mycobionts have been a major focus in recent years, and several useful compounds have been identified that have benefits for human health. Several areas of the country are well surveyed and further surveys in new areas will aim to discover new species and document lichen diversity, and responses to environmental pollution. These results highlighted the importance of ongoing research in Sri Lanka in a tropical and global lichen context.

Keywords: Bio-indicators, lichen diversity, pollution, taxonomy, tropical forests

INTRODUCTION

Different ecosystems and forest types in Sri Lanka

Sri Lanka is a continental island (7.8731° N, 80.7718° E) with an area of 65,610 km^2 located in the Indian Ocean, southeast of mainland India, in the tropical belt, and has a hot and humid climate (Chandrajith, 2020; Punyawardena, 2020). The mean annual temperature is 27.5 ^{0}C in the lowlands, and 15.9 ^{0}C in the highlands. Sri Lanka has two monsoon seasons and two inter monsoon seasons receiving 900 mm - 5500 mm rain p.a. The Southwest monsoon (SWM) (May- September) brings a high rainfall to the Southwest part of the country while Northeast monsoon (NEM) (December- February) causes heavy rains throughout the country. During SWM, the highest rainfall is received by the mid-elevations of the western slopes of the highlands. During NEM period, the highest rainfall is received by north-eastern parts of the central highlands (Punyawardena, 2020). According to the topography, Sri Lanka is divided into three topographical zones; low-country (< 300 m amsl), mid-country (300-900 m amsl), and upcountry (> 900 m amsl) (Chandrajith, 2020). Following the amount of rainfall received and its distribution, Sri Lanka is divided into three climatic zones; wet zone, intermediate zone and dry zone (Punyawardena, 2020).

Within the tropical climatic belt, several forest types can be seen in Sri Lanka relating to their geographical distribution (MOE, 2012). Dry forests, lowland rainforests, sub montane forests, and montane forests are the main forest vegetation types recorded (Kathriachchi,

* Corresponding author (gothamie.weerakoon2@nhm.ac.uk; https://orcid.org/0000-0001-8290-2910)

2012; Perera, 2012; Wijesundara, 2012). Grasslands and mangroves are the main components of the non-forest vegetation type of the country (Jayatissa, 2012; Perera, 2012).

Present understanding about lichens

A lichen is a self-sustaining ecosystem formed by the interaction of an exhabitant fungus (mycobiont) and an extracellular arrangement of one or more photosynthetic partners (photobionts) and an intermediate number of other microscopic organisms (Hawksworth & Grube, 2020). The photosynthetic partner of a lichen is an alga and/or a cyanobacterium. In addition, bacteria, secondary fungi, and endolichenic fungi can be involved in the lichen symbiosis association (Weerakoon, 2015; Lücking & Spribille, 2024). The photobionts produce carbohydrates, and the mycobiont produces the lichen structure, including protective mechanisms to maintain photobiont viability. There is a growing suggestion that the association is an obligate parasitism maintained by the mycobiont (Morillas *et al.*, 2022).

Lichens can have both sexual and asexual reproduction. Both photobiont and mycobiont may reproduce asexually within the lichen. However, sexual reproduction only occurs in the mycobiont partner. Spores and asexual thallus propagules with both symbionts can be dispersed by wind, water, or mechanical forces. After being dispersed, a new lichen thallus may establish in the new habitat, if it is environmentally suitable (Purvis, 2000; Weerakoon, 2015). According to Brunialti *et al.* (2021), species which show sexual reproduction are more widely distributed than the species with asexual vegetative reproduction. Also, they reported a nested assemblage of vegetatively reproducing lichens mainly in old growth forests, while sexually reproducing lichen species showed a high turnover.

There are about 20,000 lichen species identified throughout the world (Lücking *et al.*, 2017; Finger Lakes Land Trust, 2024), and lichenologists believe there are more species yet to be discovered (Lücking & Spribille, 2024). In Sri Lanka, the lichen flora is poorly studied. Most Sri Lankan surveys have been conducted in the central highlands and wet zone lowlands, however, the intermediate zone and the dry zone lichens are less explored (Weerakoon, 2015; Jayalal *et al.*, 2020).

Lichens are found on a wide variety of substrates including soil (terricolous), rock (saxicolous), decaying wood (lignicolous), trees (corticolous), and leaves (foliicolous). Lichens are grouped according to the shape and morphology of the thallus (Purvis, 2000). The main types being crustose (a crust-like thallus), foliose (a leaf-like thallus), fruticose (a bush-like thallus), filamentous (a bushy thread-like thallus), and squamulose (a micro leafy thallus). Foliose, filamentous and fruticose lichens are known as macro-lichens and the remainder are referred to as micro-lichens (Purvis, 2000; Weerakoon, 2015).

In the Eastern Himalaya and Western Ghats, the majority of lichens are recorded on tree trunks and the dominant group on tree trunks is crustose (Pinokiyo et al., 2008, Vinayaka et al., 2016). Also crustose lichens are recorded as the most abundant group across all habitats in temperate and tropical regions (Nayaka & Upreti, 2005; Rout *et al.*, 2010; Dudani *et al.*, 2015). Foliose and fruticose lichens are common in well-lit canopy gaps and openings and become more common at higher elevations in tropical forests (Joshi *et al.*, 2011; Kumar *et al.*, 2011; Abas & Din, 2021; Orock & Fonge, 2022).

Research conducted in tropical regions has shown that Graphidaceae is the largest and most diverse family of crustose lichens in the tropics, and that the global hotspot for this family is South India and Sri Lanka (Lücking *et al.*, 2014). Lichens in tropical regions become more abundant, dense, and widely scattered with increasing elevation above 1000 m (Baniya *et al.*, 2010; Kumar *et al.*, 2011; Costas *et al.*, 2021; Bhagarathi *et al.*, 2022; Orock & Fonge, 2022). Further, Pinokiyo *et al.* (2008) also recorded a unimodal pattern in lichen diversity in relation to altitude from a study conducted in Arunachal Pradesh in India.

Lichens produce both primary and secondary metabolites (Ren *et al.*, 2023). Primary metabolites are used in structural growth and development of the lichen thallus by both symbionts, while secondary compounds are only produced by the fungus and have a range of protective functions in the lichen. Secondary metabolites are small, complex, water insoluble, crystalline compounds deposited on the hyphae of the fungus. There are three main pathways for synthesizing these compounds; acetyl-malonate, mevalonate, and shikimate pathways (Ren *et al.*, 2023). There are over 1000 lichen secondary compounds identified so far (Ren *et al.*, 2023). These compounds have been known to protect the thallus from herbivory and UV radiation (Schweiger *et al.*, 2021), and to contribute to ecological services such as nutrient cycling, habitat formation, and soil formation (Prokopiev *et al.*, 2025). Lichen secondary compounds also have an active pharmaceutical role in human health as anti-bacterial, anti-cancer, anti-fungal, anti-inflammatory, anti-microbial, antioxidant, and wound healing agents (Moreira *et al.*, 2015; Bhattacharyya *et al.*, 2016; Ren *et al.*, 2023).

Lichens are one of the commonly used bioindicators for assessing atmospheric air quality since their growth and development depend on air borne resources, thus any atmospheric changes may have an impact on them (Nimis *et al.*, 2002 Conti, 2008; Delves *et al.*, 2023). A significant change in lichen communities can be observed due to air pollutants such as sulphur dioxide (SO_2) from burning coal and fossil fuels, and ammonia (NH_3) from agricultural activity (Sutton *et al.*, 2009). In temperate countries and conditions, lichen communities have been widely used to recognise the impact of atmospheric pollution. An Index of Atmospheric Purity (IAP) was developed by Leblanc and DeSloover in 1970 as a method to assess air quality using lichens as bioindicators, and has since been widely used in temperate regions (Gombert *et al*., 2004). Biomonitoring studies using lichens have contributed to creating regional policies such as introducing critical levels and loads of pollutants affecting the lichens, such as NH_3 (Sutton *et al.*, 2009). NH_3 is a pollutant alkaline gas that causes an increase in the bark pH of the surrounding vegetation. Lichens that prefer a lower bark acidity (acidophytes) are eliminated from the habitat and replaced by lichens that are tolerant of the increased bark pH (Wolseley *et al.*, 2006). Modelling studies have shown that natural habitats in South Asia, such as Himalayan forests, are threatened by increasing atmospheric nitrogen deposition (Ellis *et al.*, 2022). Further, deposited particulate matter has been shown to affect lichen thalli close to highways (Marmor & Randlane, 2007), and lichens have been used to monitor heavy metal pollution due to Pb in urban areas (Hasairin *et al.*, 2020).

Globally, lichens are well studied in many research fields such as ecology, environmental monitoring, air quality, and medical studies as well as having commercial and cultural values in some countries (Lücking & Spribille, 2024). However, the lichen flora in Sri Lanka is less studied compared to other countries in tropical Asia (Weerakoon *et al*., 2019). This review summarizes the findings of selected lichenological research in Sri Lanka, the status, and the potential for lichenology in Sri Lanka.

Lichen diversity and distribution in Sri Lanka

History of lichen surveys in Sri Lanka

G.H.K. Thwaites was the director of the Botanic Gardens in Sri Lanka from 1857-1880 and made the first lichen collection in Sri Lanka, duplicates of which are deposited in the Natural History Museum in London and other herbaria in Europe (Weerakoon, 2013). Using this collection, Leighton in 1869, published 196 lichen species for Sri Lanka, including 43 species new to science. Many foreign lichenologists conducted field explorations in the country and results were published in late 19th and 20th centuries (Nylander 1866:1900; Alston, 1938; Kurokawa, 1973; Kurokawa & Mineta 1973). Under the 'Flora of Ceylon' project by the Smithsonian Institute, R. Santesson, A. Tehler and L. Wheeler (1970 - 1976) studied the lichen diversity in different parts of the country. Mason Hale made a significant contribution to the lichen flora in Sri Lanka from 1976 to 1981 including 'A revision of the lichen family Thelotremataceae in Sri Lanka' in 1981 (Hale, 1981). Brunnbauer (1984 - 1987) updated the Sri Lankan lichen flora to 546 species. Lichen discoveries by Jayasuriya (1984), Moberg (1986 and 1987), Awasthi (1991), Makhija and Patwardhan (1992) and Vezda *et al.* (1997) brought the lichen checklist to 659 species (Weerakoon, 2015). A group of local and foreign lichenologists initiated a series of lichen workshops from 1999 onwards and continued to increase the lichen knowledge and interest of Sri Lankan researchers (Wijesundara & Karunaratne, 2015). After 2010, local experts contributed more to reporting and describing new lichen species.

Lichen species delimitation in Sri Lanka was supported by morphology and gene-based analyses conducted on specimens collected from the Central Mountain range. Studies in Knuckles showed that lichen specimens in the genus *Pyrenula* of family Pyrenulaceae are not derived from the same ancestor and can be divided into two groups (Weerakoon *et al.*, 2012 a). In the Horton Plains, Jayalal *et al.* (2012) described two new foliose lichen species in genus *Anzia*. Also, morphological descriptions continued, particularly in crustose species, following Weerakoon's research in the Knuckles Mountain range (Weerakoon *et al.*, 2012a; 2012b; 2012c; Wijeyaratne *et al.*, 2012). Further, three new lichen species in genera *Heterodermia*, *Malmidea*, and *Protoparmelia* and an identification key for the genus *Heterodermia* were published for Sri Lanka (Weerakoon & Aptroot, 2013). Research on the family Graphidaceae added 13 new species (Weerakoon *et al.*, 2014) and 6 new species from the montane forests of Horton Plains by Weerakoon *et al.* (2015). From an examination of a collection made in the early 1990's, Weerakoon & Aptroot (2014) recorded 207 lichens new to Sri Lanka including three species new to science, 91 new records for the Indian subcontinent, and four new records for Asia.

Further research by Weerakoon *et al.* (2016) and Weerakoon and Aptroot (2016) increased the number of new records for Sri Lanka to 152 species of which 17 were described as new to science, 86 records as new to the Indian subcontinent and eight as new to Asia. In the same year the first record of genus *Cora* in the eastern palaeotropics was described from the Sinharaja rain forest reserve, Sri Lanka (Lucking *et al.*, 2016). Furthermore, three new *Ocellularia* species (Family Graphidaceae) were identified from Sri Lanka (Li *et al.*, 2016). In 2018, further ten species were recorded with three species new to science by Aptroot & Weerakoon (2018). *Leightoniella zeylanensis,* an endemic species, was rediscovered and classified under family Pannariaceae using molecular analysis (Weerakoon *et al.*, 2018).

In 2019, the first record of palaeotropical *Allographa* with pigmented lirellae (Family Graphidaceae) was recorded from Sri Lanka together with a global key for all *Allographa* species with colourful lirellae. These *Allographa* species were previously recorded only from the Neotropics and from Africa (Jatnika *et al.*, 2019).

Six new species of *Allographa* and *Graphis* of Graphidaceae with 106 new records were reported with a key to genera for Sri Lanka by Weerakoon *et al.* in 2019. The total number of species of *Allographa* and *Graphis* in Sri Lanka amounted to 124 species, making Sri Lanka the hotspot for *Allographa* and *Graphis* diversity in the world. Research on genus *Phyllopsora* in Asia documented 18 species for Sri Lanka and a taxonomic key for Asian species (Kistenich *et al.*, 2019). In 2020, Kistenich *et al.* also recorded *Aciculopsora* in Sri Lanka*,* the first record in the paleotropics of a genus previously known only in neotropics.

With the contribution of local and foreign lichenologists, the documented lichen flora in Sri Lanka (as of 2020) stands at 876 species across 233 genera in 60 families (Jayalal *et al.*, 2020). Since then following further research on historic lichen collections from Sri Lanka, Elvebakk (2021) has described a new species of cyanolichen, *Gibbosporina cyanea*, based on the holotype collected by Thwaites in the 1860s.

Factors affecting the lichen distribution in Sri Lanka

Lichens are distributed across all climatic regions of Sri Lanka and the distribution pattern differs in each region. Environmental variables such as rainfall, humidity, and temperature affect this variation (Weerakoon, 2015). Altitude strongly affects lichen distribution and community composition (Weerakoon *et al.*, 2020) so that lichen diversity increased with altitude. As observed in mountain forests in the wet-zone (Weerakoon *et al.*, 2020), Gunawardena and Wijeyaratne, (2020) also described high lichen diversity in the Ritigala forest, an isolated mountain in the dry-zone of the country. The study also reported the influence of light exposure on lichen communities, the preference for sunny areas by lichens with a green algal photobiont and for shaded habitats by cyanobacterial lichens.

Factors that affect lichen diversity and distribution include forest disturbance (Weerakoon *et al.*, 2010; Weerakoon *et al.*, 2020). In the Knuckles Mountain range, Sri Lanka (in the central highlands) the highest lichen diversity was recorded in pristine forest while monoculture plantations such as tea, pine and acacia had the lowest lichen diversity (Weerakoon *et al*., 2010; Weerakoon *et al*., 2020). These studies also demonstrated that corticolous lichen diversity increased where tree diversity was high in undisturbed forests. De Silva and Senanayake (2015) recorded low lichen diversity in a monoculture pine plantation compared with adjoining secondary forest in Pussellawa in the central highlands. The lichen diversity was higher in the montane forest islands than in continuous forests in the Horton Plains National Park – the southern part of the central highlands where fire caused frequent disturbance (Jayalal *et al.*, 2017).

Other research in Sri Lankan lichenology

Although the chemical composition of lichens has been used to define lichen species, many studies have been conducted on lichens to assess the application of lichen compounds to human health and environmental problems.

Chemical compounds of lichens and their potential applicability

The chemical properties of lichens and their uses were studied in Sri Lanka from the early 2000s (Karunaratne *et al.*, 2005) including an investigation of larvicidal assays in relation to mosquito larvae (Nanayakkara *et al.*, 2005). An investigation of secondary metabolites in butterfly larvae highlighted the role of secondary metabolites in protecting lichens from herbivores (Karunaratne *et al.*, 2008). Secondary metabolites were used to define new species (Kathirgamanathar *et al.*, 2006; Bombuwela *et al.*, 2008) and then further developed to assess their application to human health. Several recent studies have highlighted the potential of secondary chemical compounds generated from lichen fungi in medical research. Studies have shown that lichens in the *Parmotrema* genus have antioxidant properties (Samanthi *et al.*, 2015). Two lichen species in genus *Parmotrema*, *P. rampoddense* and *P. tinctorum*, showed potential importance as a source for future antimicrobial drugs (Shiromi *et al.*, 2021). Additionally, the anti-diabetic properties of the secondary metabolites of *Cladonia* sp. were documented by Karunaratne *et al.* (2014).

Antibacterial compounds of lichen-associated fungi in mangrove habitats were identified by Happitiya *et al.* (2023a; 2023b). Weerasinghe *et al.* (2021) also tested the antioxidant, anti-inflammatory and antibacterial properties of the secondary metabolites extracted from endolichenic fungi from lichens which occurred in mangrove habitats in Negombo, Sri Lanka. The antioxidant, anti-lipase, and anti-amylase properties of the secondary metabolites in endolichenic fungi are documented together with their anti-inflammatory properties (Maduranga *et al.*, 2018, 2021). A novel chemical compound extracted from an endolichenic fungus *Amandinea medusulina* found in mangrove ecosystems showed a moderate activity against human lung cancer (Santhirasegaram *et al.*, 2020). In 2022, a chemical compound with high antibiotic properties was extracted from a mangrove associated lichen. The compound has high anti-oxidant properties, moderate anti-inflammatory properties, some antibacterial activities, and moderate cytotoxicity against oral cancer. This chemical was extracted from an endolichenic fungus recorded from the host lichen *Bactrospora myriadea* from the Negombo lagoon mangrove community (Weerasinghe *et al.*, 2022). Further, secondary metabolites extracted from endolichenic fungi of mangrove associated lichens *Arthonia antillarum* and *Bactrospora myriadea* have shown cytotoxicity against human breast, oral and lung cancers (Shevkar *et al.*, 2024).

Using lichens as bio-indicators for assessing forest ecosystem health

Lichens have been used to detect changes in communities in response to changes in environmental conditions as well as air quality, and more recently to global warming. Changes in lichen communities of forests in relation to disturbance was quantified in plots in habitats in the Knuckles Mountain range, Sri Lanka (Weerakoon, 2013). Weerakoon *et al.* (2020) showed that 57 out of 60 indicator lichens were serving as strong and unique indicator species for an individual vegetation type in Knuckles mountain range. Of these, the prevalence of crustose species in the genera *Myriotrema*, *Ocellaria*, and *Porina* was associated with the undisturbed montane and sub-montane forests in Sri Lanka (Weerakoon *et al.*, 2010). In 2010, Jayalal also found several foliose lichen genera that were good indicators of ecological continuity in the Horton Plains National Park. These results support the use of corticolous lichens to evaluate the habitat conditions in tropical forests of Sri Lanka (Jayalal, 2010; Weerakoon, 2010; Weerakoon *et al.*, 2010; Weerakoon *et al.*, 2020).

Air pollution monitoring in Sri Lanka using lichens

Lichens have been used as air pollution indicators in several locations in Sri Lanka. The IAP in the Horton Plain National Park, Sri Lanka was calculated from the lichen diversity. The low concentrations of NO_2 and SO_2 facilitated a high lichen diversity in the area (Jayalal *et al.*, 2017). Similarly, the IAP was negatively correlated with the NO_2 and SO_2 levels at different locations in Kegalle in the Sabaragamuwa province (Yatawara & Dayananda, 2019). These studies have helped to identify air pollution tolerant indicator species, such as *Pyxine* sp. A recent study was conducted as a collaborative work in Sri Lanka and India, to assess the use of lichens as air pollution indicators. A comparison of lichen diversity and air pollution status in selected locations in and around Kandy city (Sri Lanka) showed a higher lichen diversity in less air-polluted locations. The highest species richness was recorded from the Hantana forest, which was located away from the city centre, compared to the Udawatta Kele and Gannoruwa forests, which were located in and around Kandy city (Preeti *et al.*, 2023). Further work recorded higher lichen species richness in the University of Peradeniya, a semi- disturbed area, than in the polluted area around the lake in Kandy city (Edirisinghe & Athukorala, 2024). Similarly, Gunawardena *et al.* (2021) recorded higher lichen species richness in the University of Peradeniya than in the Kandy city centre, where they also detected increased secondary metabolites produced as a response to pollution stress.

Atmospheric pollution from NH_3 is an emerging threat to both environmental and human health, and South Asia is considered a hotspot of NH_3 pollution. An experimental study is ongoing in a sub-montane forest reserve as a part of the South Asian Nitrogen Hub project to assess lichen responses to the elevated NH_3 levels in order to understand real world NH_3 pollution conditions (Sutton *et al.*, 2022). The multi-layer model used in this study is applicable for identifying the fate of NH_3 in tropical forest ecosystems with special focus on lichen bio-indicators, that will provide vital evidence to inform the establishment of NH_3 critical levels and associated nitrogen policy development in Sri Lanka and the South Asian region (Deshpande *et al.*, 2024).

Lichen biomonitoring on particle deposition in Sri Lanka

Airborne particles directly impact human health. They are one of the major factors causing respiratory tract inflammations and diseases. Very few studies were conducted using lichens as bio-monitors for pollutant deposition. Assessing metal deposition on lichens is a proxy for the status of the air quality. Samples of *Heterodermia speciosa* were collected from Colombo (Western Province) and Kurunegala (North-western Province) in Sri Lanka and analysed for metal deposition. They recorded K, Ca, Ti, Fe, Mn, Zn, and Pb from analysed lichen thalli. X-ray fluorescence spectrometry shows that metal deposition is higher in Colombo than in Kurunegala, indicating the air pollution in Colombo is more than in Kurunegala (Gunathilaka *et al.*, 2011).

CONCLUSION

The rich lichen diversity in Sri Lanka has been demonstrated from previous lichenological surveys conducted in limited geographical areas in the country. Further surveys of undocumented areas of Sri Lanka will reveal new records and species to confirm Sri Lanka as a hotspot for tropical lichens, highlighting the contribution to global lichen diversity. Also, medicinal properties of lichens and their use as bioindicators have been explored in recent years. Several chemical compounds extracted from lichens have shown antibiotic, antibacterial, anti-microbial, antioxidant, anti-diabetic, anti-inflammatory, and anti-cancer properties. These chemicals compounds could be used in the pharmaceutical industry to generate income and provide benefits for human health. Further, lichens have been used as bioindicators to monitor air quality in Sri Lanka responding to atmospheric NO_2, SO_2, and metal levels in different parts of the country, especially in urban areas. Ongoing studies can be used as baseline information for proposing critical levels of air pollutants, such as NH_3, for tropical regions. Also, sensitive and tolerant lichen species to changes in air quality can be proposed based on current studies. Critical levels of NH_3 are already established in countries in temperate regions, where citizen monitoring programs have been conducted to increase community engagement on monitoring air quality using bioindicators. Public awareness and engagement on lichen biomonitoring and lichen conservation should be another future direction in lichen studies in Sri Lanka.

REFERENCES

Abas, A., & Din, L. (2021). The Diversity of Lichens along Elevational Gradients in the Tropical Montane Forest of Selangor, Malaysia. *Sains Malaysiana*, *50*(4), 1199-1209. http://doi.org/10.17576/jsm-2021-5005-01

Alston, A. H. G. (1938). *Kandy Flora*, Colombo, Sri Lanka.

Aptroot, A., & Weerakoon, G. (2018). Three new species and Ten new records of Trypetheliaceae (Ascomycota) from Sri Lanka. *Cryptogramie, Mycologie*, *39*(3), 373-378. http://doi.org/10.7872/crym/v39.iss3.2018.373

Awasthi, D. D. (1991). A key to the microlichens of India, Nepal and Sri Lanka. *Bibliotheca Lichenologica*, *40*, 1-337.

Baniya, C. B., Solhoy, T., Gauslaa, Y., & Palmer, W. (2010). The elevation gradient of lichen species richness in Nepal. *The Lichenologist*, *42*(1), 83-96. http://doi.org/10.1017/S0024282909008627

Bhagarathi, L. K., Maharaj, G., Da Silva, P. N. B., & Subramanian, G. (2022). A review of the diversity of lichens and what factors affect their distribution in the neotropics. *GSC Biological and Pharmaceutical Sciences*, *20*(3), 27-63. https://doi.org/10.30574/gscbps.2022.20.3.0348

Bhattacharyya, S., Deep, P. R., Singh, S., & Nayak, B. (2016). Lichen secondary metabolites and its biological activity. *American journal of Pharmtech research*, *6*(6), 28-44

Bombuwela, K., Kathirgamanathar, S., Thadani, V., Jayalal, R. G. U., Adikaram, N. K. B., Wijesundara, D. S. A., Andersen, R., Wolseley, P., & Karunaratne, V. (2008). Chemistry of *Heterodermia microphylla*, a lichen new to Sri Lanka. *Journal of the National Science Foundation Sri Lanka*, *36*(3), 251-252.

Brunialti, G., Giordani, P., Ravera, S., & Frati, L. (2021). The reproductive strategy as an important trait for the distribution of lower-trunk epiphytic lichens in Old-growth vs. non-old growth forests. *Forests*, *12*, 27. https://doi.org/10.3390/f12010027

Brunnbauer, W. (1984 - 1986). Die Flechten von Sri Lanka in der Literatur. *Botanische Abteilung*, Naturehistorisches Museums Wien, (in 14 teilen, als Kopien verteilt).

Chandrajith, R. (2020). Geology and geomorphology. In: *The soils of Sri Lanka. World soils book series*. Mapa R. Eds. Springer, Cham. 13-22. https://doi.org/10.1007/978-3-030-44144-9_3

Conti, M. E. (2008). Lichens as bioindicators of air pollution. *WIT Transactions on State of The Art in Science and Engineering*, *30*, 111-162. http://doi.org/10.2495/978-1-84564-002-6/05

Costas, S. M., Canton, N., & Rodriguez, J. M. (2021). The relative effect of altitude and aspect on saxicolous lichen communities at mountain summits from central-west of Argentina. *Rodriguésia*, *72*: e00282020. 2021. http://dx.doi.org/10.1590/2175-7860202172064

De Silva, C. M. S. M., & Senananyake, S. P. (2015). Assessment of epiphytic lichen diversity in pine plantations and adjacent secondary forest in Peacock Hill, Pussellawa, Sri Lanka. *International Journal of Modern Botany*, *5*(2), 29-37

Delves, J., Lewis, J. E. J., Ali, N., Asad, S. A., Chatterjee, S., Crittenden, D., Jones, M., Kiran, A., Pandey, B. P., Reay, D., Sharma, S., Tshering, D., Weerakoon, G., van Dijk, N., Sutton, M. A., Wolseley, P. A., & Ellis, C. J. (2023). Lichens as spatially transferable bioindicators for monitoring nitrogen pollution. *Environmental Pollution*, *328*, 121575. https://doi.org/10.1016/j.envpol.2023.121575

Deshpande, A. G., Jones, M. R., van Dijk, N., Mullinger, N. J., Harvey, D., Nicoll, R., Toteva, G., Weerakoon, G., Nissanka, S., Weerakoon, B., Grenier, M., Iwanica, A., Duarte, F., Stephens, A., Ellis, C. J., Vieno, M., Drewer, J., Wolseley, P. A., Nanayakkara, S., Prabashwara, T., Bealet, W. J., & Sutton, M. A. (2024). Estimation on ammonia deposition to forest ecosystems in Scotland and Sri Lanka using wind-controlled NH_3 enhancement experiments. *Atmospheric Environment*, *320*, 120325. https://doi.org/10.1016/j.atmosenv.2023.120325

Dudani, S. N., Nayaka, S., Mahesh, M. K., Chandran, M. D. S., & Ramachandra, T. V. (2015). Lichen diversity in the Sacred forest fragments of Central Western Ghats. *Journal of Biodiversity Management and Forestry*, *4*(2). http://dx.doi.org/10.4172/2327-4417.1000139

Edirisinghe, E. S. M., & Athukorala, A. D. S. N. P. (2024). Can lichens be indicators for air pollution monitoring in Kandy city, Sri Lanka? *Brazilian Journal of Science*, *3*(8), 117-134.

Ellis, C. J., Steadman, C. E., Vieno, M., Chatterjee, S., Jones, M. R., Negi, S., Pandey, B. P., Rai, H., Tshering, D., Weerakoon, G., Wolseley, P., Reay, D., Sharma, S., and Sutton, M. (2022). Estimating nitrogen risk to Himalayan forests using thresholds for lichen bioindicators. *Biological Conservation*, *265*, 109401. http://doi.org/10.1016/j.biocon.2021.109401

Elvebakk, A. (2021). *Gibbosporina cyanea* (Pannariaceae), a new bipartite cyanolichen from Sri Lanka with comparisons to related paleotropical cyanogenera. *The Lichenologist*, *53*, 291- 298. http://doi.org/10.1017/S002428292100027X

Finger Lakes Land Trust. https://www.fllt.org/a-closer-look-earth-clothing-discovering-the-diversity-and-life-history-of-lichens/

Gombert, S., Asta, J., & Seaward, M. R. D. (2004). Assessment of lichen diversity by index of atmospheric purity (IAP), index of human impact (IHI) and other environmental factors in an urban area Grenoble, southeast France. *Science of the total environment*, *324*, 183-199. http://doi.org/10.1016/j.scitotenv.2003.10.036

Gunathilaka, P. A. D. H. N., Ranundeniya, R. M. N. S., Najim, M. M. M., & Seneviratne, S. (2011). A determination of air pollution in Colombo and Kurunegala, Sri Lanka, using energy dispersive X-ray fluorescence spectrometry on *Heterodermia speciosa*. *Turkish Journal of Botany*, *35*, 439-446. http://doi.org/10.3906/bot-1006-15

Gunawardena, K. W., & Wijeyaratne, S. C. (2020). Species diversity and altitudinal preferences of lichens on selected substrata in Ritigala Strict Natural Reserve. *Journal of the National Science Foundation Sri Lanka*, *48*(1), 49-56. http://dx.doi.org/10.4038/jnsfsr.v48i1.9933

Gunawardena, W. G. D. I., Edirisinghe, E. S. M., Abayasekara, C. L., & Athukorala, A. D. S. N. P. (2021). Air pollution affects lichen species richness, species density, relative growth form abundance and their secondary metabolite production: a case study in Kandy district, Sri Lanka. *Ruhuna Journal of Science*, *12*(2), 115-127. http://doi.org/10.4038/rjs.v12i2.106

Hale, M. E. (1981). A revision of the lichen family Thelotremataceae in Sri Lanka. *Bulletin of the British Museum (Natural History)*, *8*, 227-332.

Happitiya, H. A. D. N. N., Nanayakkara, C. M., Ariyawansa, K. G. S. U., Ediriweera, S. S., Wijayawardene, N. N., Jayasinghe, R. P. P. K., Don-Qin, D., & Karunarathna. S. C. (2023 a). Antibacterial activities of lichen-associated fungi in mangrove ecosystems in Sri Lanka as potent candidates for novel antibiotic agents. In: *Proceedings of SLIIT International Conference on Advancements in Sciences and Humanities*, 1-2 December, Colombo, 397-403.

Happitiya, H. A. D. N. N., Nanayakkara, C. M., Ariyawansa, K. G. S. U., Ediriweera, S. S., Wijayawardene, N. N., Jayasinghe, R. P. P. K., Don-Qin, D., & Karunarathna. S. C. (2023 b). Lichen- associated fungi inhabiting from a mangrove ecosystem in Sri Lanka: A novel source of antibacterial agents. *SLIIT Journal of Humanities and Sciences*. *4*(2), 40-49. http://doi.org/10.4038/ajhs.v4i2.58

Hasairin, A., Pasaribu, N., & Siregar, R., (2020). Accumulation of Lead (Pb) in the lichen thallus of mahogany trees in Medan city road. *Water Air Soil Pollut*, *231*, 256. https://doi.org/10.1007/s11270-020-04625-8

Hawksworth, D. L., & Grube, M. (2020). Lichens redefined as complex ecosystems. *New Phytologist, 227*, 1281-1283.

Jatnika, M. F., Weerakoon, G., Arachchige, O., Noer, I. S., Voytsekhovich, A., & Lücking, R. (2019). Discoveries through social media and in your own backyard: two new species of *Allographa* (Graphidaceae) with pigmented lirellae from the paleotropics, with a world key to species of this group. *The Lichenologist*, *51*(3), 227-233. http://doi.org/10.1017/S0024282919000094

Jayalal, R. G. U. (2010). Study of Diversity and Taxonomy of lichens in the Horton Plains National Park with a view to biomonitor the ecosystem health. *Doctor of Philosophy thesis*, University of Peradeniya

Jayalal, U., Wolseley, P., Gueidan, C., Aptroot, A., Wijesundara, S., & Karunarathne, V. (2012). *Anzia mahaeliyensis* and *Anzia flavotenuis*, two new lichen species from Sri Lanka. *The Lichenologist*, *44*(3), 381-389. http://doi.org/10.1017/S0024282911000946

Jayalal, R. G. U., Ileperuma, O. A., Wolseley, P., Wijesundara, D. S. A., & Karunaratne, V. (2017). Correlation of atmospheric purity index to the diversity of lichens in the Horton plains national park, Sri Lanka. *Ceylon Journal of Science*, *46*(2), 13-29. http://doi.org/10.4038/cjs.v46i2.7426

Jayalal, U., Weerakoon, G., Wolseley, P., Wijesundara, S., & Karunaratne, V. (2020). A provisional list of lichens in Sri Lanka. In: *The National Red List 2020- Conservation status of the flora of Sri Lanka.* Biodiversity Secretariat of the Ministry of Environment and the National Herbarium, Department of National Botanic Gardens, Peradeniya, 214-225.

Jayasuriya, A. H. M. (1984). Flora of Ritigala Nature Reserve, Sri Lanka. *Forester*, *XVI*(3 &4).

Jayatissa, L. P. (2012). Present Status of Mangroves in Sri Lanka In: *The National Red List 2012 of Sri Lanka; Conservation Status of the Fauna and Flora.* Weerakoon, D.K. & S. Wijesundara Eds., Ministry of Environment, Colombo, Sri Lanka. 197-199.

Joshi, S., Upreti, D. K., & Das, P. (2011). Lichen diversity assessment in Pindari Glacier Valley of Uttarakhand, India. *Geophytology*, *41*(1-2), 25-41

Karunaratne, V., Bombuwela, K., Kathirgamanathar, S., & Thadhani, V. M. (2005). Lichens: a chemically important biota. *Journal of the National Science Foundation Sri Lanka*, *33*(3), 169-186

Karunaratne, V., Kathirgamanathar, S., Wijesekera, A., Wijesundara, D. S. A., & Wolseley, P. (2008). Insight into the unique butterfly - lichen association between *Talicada nyseus nyseus* and *Leproloma sipmanianum*. *Journal of Plant interactions*, *3*(1), 25-30. http://doi.org/10.1080/17429140701740061

Karunaratne, V., Thadhani, V. M., Khan, S. N., & Choudhary, M. I. (2014). Potent α-glucosidase inhibitors from the lichen *Cladonia* species from Sri Lanka. *Journal of the National Science Foundation Sri Lanka*, *42*(1), 95-98. http://dx.doi.org/10.4038/jnsfsr.v42i1.6684

Kathirgamanathar, S., Wickramasinghe, A., Bombuwela, K., Wolseley, P., & Karunaratne, V. (2006). Chemistry of two new Leprarioid lichens from Sri Lanka. *Journal of the National Science Foundation Sri Lanka*, *34*(2), 85-90.

Kathriarachchi, H. S. (2012). Present status of Lowland Wet Zone Flora of Sri Lanka. In: *The National Red List 2012 of Sri Lanka; Conservation Status of the Fauna and Flora.* Weerakoon, D.K. & S. Wijesundara Eds., Ministry of Environment, Colombo, Sri Lanka. 175-180.

Kistenich, S., Bendiksby, M., Vairappan, C. S., Weerakoon, G., Wijesundara, S., Wolseley, P. A., & Timdal, E. (2019). A regional study of the genus Phyllopsora (Ramalinaceae) in Asia and Melanesia. *MycoKeys*, *53*, 23-72. http://doi.org/10.3897/mycokeys.53.33425

Kistenich, S., Bendiksby, M., Weerakoon, G., & Timdal, E. (2020). A revision of the genus *Aciculopsora* (Ramalinaceae), with the description of one new species and one new combination. *Plant and Fungal Systematics*, *65*(1), 200-209. https://doi.org/10.35535/pfsyst-2020-0015

Kumar, R. S., Thajuddin, N., & Upreti, D. K. (2011). Diversity of Lichens in Kollihills of Tamil Nadu, India. *International Journal of Biodiversity and Conservation, 3*(2), 36-39

Kurokawa, S., (1973). Supplementary notes on the genus *Anaptychia. Journal of the Hattori Botanical Laboratory*. *37*, 563-607.

Kurokawa, S., & Mineta, M. (1973). Enumeration of Parmeliae of Ceylon. Ann. Rept. Noto Marine Lab., Univ. Kanazawa, *13*, 71-76.

Leighton, W. A. (1869). The Lichens of Ceylon, collected by G. H. K. Thwaites. - *Trans. Linn. Soc. London*, *27*, 161-185.

Li, G. J., Hyde, K. D., Zhao, R. L., Hongsanan, Abdel-Aziz, F. A., Abbel-Wahab, M. A., Alvarado, P., Alves-Silva, G., Ammirati, J. F., Ariyawansa, H. A., Baghela, A., Bahkali, A. H., Beug, M., Bhat, D. J., Bojantchev, D., Boonpratuang, T., Bulgakov, T. S., Camporesi, E., Boro, M. C., Ceska, O., Chakraborty, D., Chen, J. J., Chethana, K. I. *et al*., (2016). Fungal Diversity Notes 253-366: taxonomic and phylogenetic contribution to fungal taxa. *Fungal diversity*. http://doi.org/10.1007/s13225-016-0366-9

Lücking, R., Forno, M. D., Moncada, B., Coca, L. F., Vargas-Mendoza, L. Y., Aptroot, A., Arias, L. J., Besal, B., Bungartz, F., Cabrera-Amaya, D. M., Cáceres, M. E. S., Chaves., J. L., Eliasaro, S., Gutiérrez, M. C., Marin, J. E. H., Herrera-Campos, M. d. A., Holgado-Rojas, M. E., Jonitz, H., Kukwa, M., Lucheta, F., Madriñán, S., Marcelli, (2016). Turbo-taxonomy to assemble a megadiverse lichen genus: seventy new species of *Cora* (Basidiomycota: Agaricales: Hygrophoraceae), honouring David Leslie Hawksworth's seventieth birthday. *Fungal Diversity*. 84, 139-207. http://doi.org/10.1007/s13225-016-0374-9

Lücking, R., Hodkinson, B. P., & Leavitt, S. D. (2017). The 2016 classification of lichenized fungi in the Ascomycota and Basidiomycota- Approaching one thousand genera. *The Bryologist*, *119*(4), 361-416. https://doi.org/10.1639/0007-2745-119.4.361

Lücking, R., & Spribille, T. (2024). *The lives of Lichens: A natural history*. Princeton and Oxford: Princeton University Press.

Lücking, R., Johnston, M. K., Aptroot, A., Kraichak, E., Lendemer, J. C., Boonpragob, K., Cáceres, M. E. S., Ertz, D., Ferraro, L. I., Jia, Z., Kalb, K., Mangold, A., Manoch, L., Mercado-Díaz, J. A., Moncada, B., Mongkolsuk, P., Papong, K. B., Parnmen, S., Peláez, R. N., Poengsungnoen, V., Plata, E. R., Saipunkaew, W., Sipman, H. J. M., Sutjaritturakan, J., Broeck, D. V., Konrat, M. V., Weerakoon, G., & Lumbsch, H. T. (2014). One hundred and seventy-five new species of Graphidaceae: closing the gap or a drop in the bucket? *Phytotaxa*, *189*(1), 7-38. http://dx.doi.org/10.11646/phytotaxa.189.1.4

Maduranga, K., Attanayake, R. N., Santhirasegaram, S., Weerakoon, G., & Paranagama P. A. (2018). Molecular phylogeny and bioprospecting of Endolichenic Fungi (ELF) inhabiting in the lichens collected from a mangrove ecosystem in Sri Lanka. *PLoS ONE*, *13*(8): e0200711. https://doi.org/10.1371/journal.pone.0200711

Maduranga, H. A. K., Weerasinghe, W. R. H., Attanayake, R. N., Santhirasegaram, S., Shevkar, C. D., Kate, A. S., Weerakoon, G., Samanthi, K. A. U., Kalia, K., & Paranagama, P. A. (2021). Identification of novel bioactive compounds, Neurosporalol 1 and 2 from an endolichenic fungus, Neurospora ugadawe inhibited in the lichen host, Graphis tsunodae Zahlbr, from mangrove ecosystem in Puttalam lagoon, Sri Lanka. *Asian Journal of Chemistry*, *33*(6), 1425-1432. https://doi.org/10.14233/ajchem.2021.23229

Makhija, U., & Patwardhan, P. G. (1992). Nomenclatural notes on some species of Trypethelium. *International Journal of Mycology and Lichenology*, *5*(3), 237-251.

Marmor, L., & Randlane, T. (2007). Effects of road traffic on bark pH and epiphytic lichens in Tallinn. *Folia Cryptog. Estonica, Fasc*. *43*, 23-37

Moberg, R. (1986). Rolfidium, a new lichen genus from Sri Lanka. *Lichenologist*, *18*(4), 305-307

Moberg, R. (1987). Lichens selecti exsiccate Upsalensis- Fasc. 2(Nos 26-50), *Thunbergia*, 5. 1-9.

MOE (2012). *The National Red List 2012 of Sri Lanka; Conservation Status of the Fauna and Flora*. Ministry of Environment, Colombo, Sri Lanka.

Moreira, A. S. N., Braz-Filho, R., Mussi-Dias, V., & Vieira, I. J. C. (2015). Chemistry and biological activity of *Ramalina* lichenized fungi. *Molecules*, *20*, 8952-8987. http://doi.org/10.3390/molecules20058952

Morillas, L., Roales, J., Cruz, C., & Munzi, S. (2022). Lichen as multi partner symbiotic relationships. *Encyclopedia*, *2*, 1421-1431. https://doi.org/10.3390/encyclopedia2030096

Nanayakkara, C., Bombuwela, K., Kathirgamanathar, S., Adikaram, N. K. B., Wijesundara, D. S. A., Hariharan, G. N., Wolseley, P., & Karunaratne, V. (2005). Effect of some lichen extracts from Sri Lanka on larvae of *Aedes aegypti* and the fungus *Cladosporium cladosporioides*. *Journal of the National Science Foundation Sri Lanka*, *33*(2), 147-149

Nayaka, S., & Upreti, D. K. (2005). Status of Lichen diversity in Western Ghats, India. *Sahyadri E-News, Western Ghats Biodiversity Information System* - Issue XVI

Nimis, P. L., & Purvis, O. W. (2002). Monitoring lichens as indicators of pollution. P. L. Nimis, C. Scheidegger and P. A. Wolseley (eds.), *Monitoring With Lichens*, Kluwer Academic Publishers, Netherlands. 7-10.

Nylander, W. (1866). Prodromi lichenographiae Scandinaviae Sulementia. Lichens Laoniae Orientalis. *Not. Sallsk. F. FI. Fenn. Forhadl*. (nova ser) *5*, 99-152.

Nylander, W. (1900). Lichens Ceylonenses et Additamentum ad Lichens Japoniae. *Acta Soc. Sci. Fennicae*, *26*, 1-33.

Orock, A. E., & Fonge, B. A. (2022). Diversity of lichens at Mount Cameroon, south west region, Cameroon. *International Journal of Biodiversity and Conservation*, *14*(2), 72- 93. http://doi.org/10.5897/LIBC2021.1517

Perera, A. (2012). Present Status of Dry-zone Flora in Sri Lanka. In: *The National Red List 2012 of Sri Lanka; Conservation Status of the Fauna and Flora.* Weerakoon, D.K. & S. Wijesundara Eds., Ministry of Environment, Colombo, Sri Lanka. 165-174.

Pinokiyo, A., Singh, K. P., & Singh, J. S. (2008). Diversity and distribution of lichens in relation to altitude within a protected biodiversity hot spot, north-east India. *The Lichenologist*, *40*(1), 47-62. http://doi.org/10.1017/S0024282908007214

Preeti, K., Tejhani, M., Pandey, V., Dutta, V, Das, P., Weerakoon, B., Chatterjee, S., Ranasinghe, H., & Nissanka, S. (2023). Impacts of Pollution on Tropical Montane and Temperate Forests of South Asia: Preliminary Studies by Postgraduate Students in India and Sri Lanka. In: *Ecosystem and Species Habitat Modeling for Conservation and Restoration* (eds. Dhyani, S., Adhikari, D., Dasgupta, R., Kadaverugu, R), 355-372, Springer, Singapore. https://doi.org/10.1007/978-981-99-0131-9_19

Prokopiev, I. A., Sazanova, K. V., Sleptsov, I. V., Filippova, G. V., Kuzmina, N. P., Frolova, D. A., & Zholobova, Z. O. (2025). Effect of Secondary metabolites of lichens on microbial communities in permafrost forest soils. *Contemporary Problems of Ecology*, *18*(1), 82-100.

Punyawardena. B. V. R. (2020). Climate. In: *The soils of Sri Lanka. World soils book series*. Mapa R. Eds. Springer, Cham. 13-22. https://doi.org/10.1007/978-3-030-44144-9_2

Purvis, W. (2000). *Lichens*. Natural History Museum, London

Ren, M., Jiang, S., Wang, Y., Pan, X., Pan, F., & Wei, X. (2023). Discovery and excavation of lichen bio active natural products. *Frontiers in Microbiology*, *14*, 1177123. http://doi.org/10.3389/fmicb.2023.1177123

Rout, J., Das, P., & Upreti, D. K. (2010). Epiphytic lichen diversity in a reserve forest in southern Assam, northern India. *Tropical Ecology*, *51*(2), 281- 288

Samanthi, K. A. U., Wickramaarachchi, S., Wijerathne, E. M. K., & Paranagama, P. A. (2015). Two new antioxidant active polyketides from *Penicillium citrinum*, an endolichenic fungus isolated from Parmotrema species in Sri Lanka. *Journal of the National Science Foundation Sri Lanka*, *43*(2), 119-126

Santhirasegaram, S., Wickramarachchi, S. R., Attanayake, R. N., Weerakoon, G., Samarakoon, S., Wijeratne, K., & Paranagama, P. A. (2020). A novel cytotoxic compound from the endolichenic fungus, *Xylaria psidii* inhibiting the lichen, *Amandinea medusulina*. *Natural Product Communications*, *15*(7), 1-8. http://doi.org/10. 1177/ 1934 578X 20933017

Schweiger, A. H., Ullmann, G. M., Nurk, N. M., Triebel., D., Schobert, R., & Rambold, G. (2021). Chemical properties of key metabolites determine the global distribution of lichens. *Ecological Letters*, *25*, 416- 426. http://doi.org/10.1111/ele.13930

Shevkar, C., Weerasinghe, R., Dubey, G., Attanayake, R. N., Weerakoon, G., Kalia, K., Paranagama, P., & Kate, A. S. (2024). Bioprospecting of endolichenic fungus *Phanerochaeta chrysosporium* from mangrove associated lichen *Bactrospora myriadea* for anticancer leads. *Indian Journal of Microbiology*. http://doi.org/10.1007/s12088-024-02424-1.

Shiromi, P. S. A. I., Hewawasam, R. P., Jayalal, R. G. U., Rathnayake, H., Wijayaratne, W. M. D. G. B., & Wanniarachchi, D. (2021). Chemical composition and antimicrobial activity of two Sri Lankan lichens, *Parmotrema rampoddense*, and *Parmotrema tinctorum* against methicillin-sensitive and methicillin-resistant *Staphylococcus aureus*. *Evidence- Based Complementary and Alternative Medicine*, 9985325. https://doi.org/10.1155/2021/9985325

Sutton, M. A., Wolseley, P. A., Leith, I. D., van Dijk, N., Tang, Y. S., James, P. W., Theobald, M. R., & Whitfleld, C. (2009). Estimation of ammonia critical level for epiphytic lichens based on observations at farm, landscape and national scales, *Atmospheric Ammonia* (Sutton, M.A., Reis, S and Baker, S. M. H. eds), Springer, 71-86.

Sutton, M. A., Wolseley, P. A., van Dijk, N., Deshpande, A. G., Dragosits, U., Twigg, M., Tang, Y. S., Braban, C., Levy, P., Bealey, W. J., Weerakoon, G., Jiang, J., Stevenson, D. S., Weerakoon, B., Nissanka, S. P., & Jones, M. R. (2022). 15 years on: Rationale and reflection on the 2006 Edinburgh Ammonia workshop in the light of emerging evidence. In: *TEXTE Review of internationally proposed critical levels for ammonia- conference proceedings*. German Environment Agency, 50-60.

Vezda, A., Brunnbauer, W., & Breuss, O. (1997). *Foliicole Flechten aus Sri Lanka*. Annalen des Naturhisrorischen Museums in Wien, 99B, 737-742.

Vinayaka, K. S., Chetan, H. C., & Mesta, A. R. (2016). Diversity and distribution patterns of Lichens in the mid-elevation wet evergreen forest, South Western Ghats, India. *International Journal of Research Studies in Biosciences*, *4*(1), 15-20

Weerakoon, G. S. K., Somaratne, S., Wolseley, P. A., & Wijeyaratne, S. C. (2010). Corticolous lichens as indicators of different forest management practices in the Dotalugala-Knuckles mountain range, In: *Proceedings of the 15th International Forestry and Environment Symposium*, 26-27 November 2010, University of Sri Jayawardenapura, Sri Lanka. 182-189

Weerakoon, G., Aptroot, A., Lumbsch, H. T., Wolseley, P. A., Wijeyaratne, C., & Gueidan, C. (2012 a). New molecular data on Pyrenulaceae from Sri Lanka reveal two well-supported groups within this family. *The Lichenologist*, *44*(5), 639-647. http://doi.org/10.1017/S0024282912000333

Weerakoon, G., Wijeyaratne, S. C., Wolseley, P. A., Plata, E. R., Lücking, R., & Lumbsch, H. T. (2012 b). Six new species of Graphidaceae from Sri Lanka, *The Bryologist, 115*(1), 74-83. http://doi.org/10.1639/0007-2745-115.1.74

Weerakoon, G., Rivasplata, E., Lumbsch, T., & Lücking, R. (2012 c). Three new species of *Chapsa* (lichenized Ascomycota: Ostropales: Graphidaceae) from tropical Asia. *The Lichenologist*, *44*(3): 373-379. http://doi.org/10.1017/S0024282911000892

Weerakoon, W. M. G. S. K. (2013). Some environmental factors influencing diversity of corticolous lichens in selected disturbed and undisturbed vegetation types in Knuckles Mountain range in Sri Lanka. *Doctor of Philosophy thesis*, University of Sri Jayawardenapura

Weerakoon, G., & Aptroot, A. (2013). Some new lichen species from Sri Lanka, with a key to the genus *Heterodermia* in Sri Lanka. *Cryptogamie, Mycologie*, *34*(4). 321-328. http://doi.org/10.7872/crym.v34.iss4.2013.321

Weerakoon, G., & Aptroot, A. (2014). Over 200 new lichen records from Sri Lanka, with three new species to the science, *Cryptogamie, Mycologie*, *35*(1): 51-62

Weerakoon, G., Lücking, R., & Lumbsch, H. T. (2014). Thirteen new species of Graphidaceae (lichenized Ascomata: Ostropales) from Sri Lanka, *Phytotaxa 189*(1): 331-347. http://dx.doi.org/10.11646/phytotaxa.189.1.24

Weerakoon, G. (2015). Fascinating lichens in Sri Lanka. Dilmah tea, Colombo, Sri Lanka

Weerakoon, G., Jayalal, U., Wijesundara, S., Karunaratne, V., & Lücking, R. (2015). Six new Graphidaceae (lichenized Ascomata: Ostropales) from Horton plains National Park, Sri Lanka. *Nova Hedwigia*, http://doi.org/10.1127/nova_hedwigia/2015/0241

Weerakoon, G., Wolseley, P. A., Arachchige, O., Caceres, M. E. S., Jayalal, U., & Aptroot, A. (2016). Eight new lichen species and 88 new records from Sri Lanka. *The Bryologist*, *119*(2), 131-142. http://doi.org/10.1639/0007-2745-119.2.131

Weerakoon, G., & Aptroot, A. (2016). Nine new lichen species and 64 new records from Sri Lanka. *Phytotaxa*, *280*(2), 152-162. http://dx.doi.org/10.11646/phytotaxa.280.2.5

Weerakoon, G., Aptroot, A., Wedin, M., & Ekman, S. (2018). *Leightoniella zeylanensis* belongs to the Pannariaceae. *Nordic Journal of Botany*. e01880. http://doi.org/10.1111/njb.01880

Weerakoon, G., Aptroot, A., Lücking, R., Arachchige, O., & Wijesundara, S. (2019). *Graphis* and *Allographa* (lichenized Ascomata: Graphidaceae) in Sri Lanka, with six new species and a biogeographical comparison investigating a potential signature of the 'biotic ferry' species interchange. *The Lichenologist*, *51*(6), 515-559. http://doi.org/10.1017/S0024282919000392

Weerakoon, G., Wolseley, P., Will-Wolf, S., & Wijeyaratne, C. (2020). Corticolous lichen species as indicators of disturbed/undisturbed vegetation types in the central mountains of Sri Lanka. *The Lichenologist*, *52*, 233-245. http://doi.org/10.1017/S0024282920000109

Weerasinghe, R. H., Maduranga, K., Attanayake, R. N., Shevkar, C., Kate, A. S., Weerakoon, G., Kalia, K., & Paranagama, P. A. (2021). Bioactive properties and metabolite profiles of endolichenic fungi in mangrove ecosystem of Negombo lagoon, Sri Lanka. *Natural Product Communications*, *16*(10), 1-14. http://doi.org/10.1177.1934578X211048652.

Weerasinghe, R. H., Shevkar, C. D., Maduranga, K., Pandey, K. H., Attanayake, R. N., Kate, A. S., Weerakoon, G., Behera, S. K., Kalia, K. S., & Paranagama, P. A. (2022). Bioprospecting of an endolichenic fungus *Phanerochaete sordida* isolated from mangrove associated lichen *Bactrospora myriadea*. *Hindawi Journal of Chemistry*, *22*. https://doi.org/10.1155/2022/3193689

Wijesundara, S. (2012). Present Status of Montane Forests in Sri Lanka. In: *The National Red List 2012 of Sri Lanka; Conservation Status of the Fauna and Flora.* Weerakoon, D.K. & S. Wijesundara Eds., Ministry of Environment, Colombo, Sri Lanka. 181-185.

Wijesundara, S., & Karunaratne, V. (2015). Third National Workshop on Lichens: over fifteen years of progress in lichen research in Sri Lanka. *Journal of the National Science Foundation Sri Lanka*, *43*(2), 195-196.

Wijeyaratne, S. C., Lücking, R., & Lumbsch, T. (2012). Three new crustose lichen species from Sri Lanka. *Nova Hedwigia*, *94*(1-2), 367-372. http://doi.org/10.1127/0029-

5035/2012/0008

Wolseley, P. A., Theobald, M. R., & Sutton, M. A. (2006). Detecting changes in epiphytic lichen communities at sites affected by atmospheric ammonia from agricultural sources. *The Lichenologist*, *38*(2), 161-176. http://doi.org/10.1017/S0024282905005487

Yatawara, M., & Dayananda, N. (2019). Use of corticolous lichens for the assessment of ambient air quality along rural-urban ecosystems of tropics: a study in Sri Lanka. *Environmental Monitoring and Assessment*, *191*: 179. https://doi.org/10.1007/s10661-019-7334-2

J.Natn.Sci.Foundation Sri Lanka 2025 53 (3): 219 - 232
DOI: http://dx.doi.org/10.4038/jnsfsr.v53i3.12375

RESEARCH ARTICLE

Mathematical Modelling

Optimal control strategies for diabetes population management using mathematical models

TDT Madhushika[1*], LW Somathilake[2] and MCS Fernando[3]
[1] *Department of Mathematics and Philosophy of Engineering, Faculty of Engineering Technology, The Open University of Sri Lanka, Nawala, Sri Lanka.*
[2] *Department of Mathematics, Faculty of Science, University of Ruhuna, Matara, Sri Lanka.*
[3] *Department of Mathematics, Faculty of Science, University of Kelaniya, Kelaniya, Sri Lanka.*

Submitted: 26 September 2024; Revised: 22 July 2025; Accepted: 29 July 2025

Abstract: Diabetes is a long-lasting medical condition that affects the entire world. In the present paper, we modify and analyze an existing mathematical model for diabetes population dynamics, considering control strategies. We presented two models, and the first model was developed with the assumption that the total population grows logistically. The second model was constructed by employing strategies in pursuit of controlling the growth of the diabetic population. Using Pontryagin's maximum principle, we characterized the optimal controls. The optimality systems were solved using the forward-backward sweep iteration with the fourth-order Runge-Kutta method. This shows that the incidence rate of pre-diabetes is a crucial factor in estimating the burden of diabetes. It can also be concluded that by applying control strategies such as awareness of diet plans and regular testing, the number of incidences of pre-diabetes decreases by nearly 45% and the number of diabetes incidences, with and without complications, declined by approximately 75% over the period of 50 years.

Keywords: Diabetes population dynamics, optimal control, Pontryagin's maximum principle.

INTRODUCTION

Diabetes is a chronic disease that substantially affects people's health, and the global pandemic affects all nations. The International Diabetes Federation estimates that 537 million adults worldwide had diabetes in 2021, and one person dies from it every five seconds. Therefore, approximately 17,280 adults die due to diabetes per day worldwide (International Federation of Diabetes, 2025). Diabetes is characterized by issues with the insulin hormone. The World Health Organization claims that diabetes develops when the pancreas does not produce enough insulin or when the body cannot effectively use the insulin that is produced in the pancreas. As a result of this fact, the level of glucose in the blood rises in general (WHO, 2025).

According to the World Health Organization (WHO), there are three main types of diabetes called Type 1, Type 2, and Gestational Diabetes. Type 1 diabetes arises when the pancreas does not produce insulin or does not produce a sufficient amount of insulin. Approximately 5-10% of all diabetes cases are Type 1. Type 2 diabetes occurs when the patient's body does not respond properly to insulin. The majority of diabetics (90–95%) have Type 2. Some people have "prediabetes," which means their blood sugar is high, but not high enough to be diagnosed with type 2 diabetes. Pre-diabetes increases the chances of developing type 2 diabetes. Gestational diabetes occurs when women are pregnant. Although gestational diabetes typically goes away after delivery, it increases the risk of type 2 diabetes in the future.

* Corresponding author (thilinim832@gmail.com; https://orcid.org/0009-0005-9647-1847)

Diabetes requires expensive, time-consuming treatment and care due to its chronic nature and serious complications, which have an impact on the whole of society. Therefore, a large number of research studies have been conducted using optimal control strategies to decrease the diabetes burden over the past years. In a related study, in 2020, Abdelfatah Kouidere and co-authors proposed a mathematical model in an effort to reduce the impact of behavioral influences and reduce the number of diabetics with treatable complications (Kouidere *et al.*, 2020). They employed control theory to characterize the optimal control strategies to manage these complications. The effectiveness of the suggested control strategy was demonstrated by the numerical simulation of the results. In 2014, M. Derouich and co-authors presented an optimal control approach to the dynamics of the diabetes population (Derouich *et al.*, 2014). They demonstrated the existence of an optimal control and then monitored the population density in each compartment using an implicit finite-difference method. According to their model, by using optimal control strategies, the number of diabetics with and without complications can be significantly decreased over the course of ten years. In the paper by Kouidere *et al.*, (2021), the authors have considered the negative impact of lifestyle on diabetic patients and presented a model for diabetic population dynamics. On the basis of age, they emphasized how socio-environmental factors affect diabetic patients negatively. Also, they presented an optimal strategy for implementing the best awareness campaigns aimed at protecting diabetes patients from the negative impact of a lifestyle that leads to complications. They used Pontryagin's maximum principle to classify the optimal controls, and an iterative approach was used to solve the optimality problem. MATLAB was utilized to complete the numerical simulation. The effectiveness of the suggested control strategies was demonstrated by the numerical simulation of the results.

T. T. Yusuf proposed a deterministic model for effective health management of diabetic patients using two different control strategies: careful management of patients with complications to keep them from developing further complications, and management of patients before complications arise (Yusuf, 2015). In order to determine the best combination of control strategies that will reduce the cost of putting the suggested strategies into practice, as well as the incidence of complications within the population, they formulated a fixed-time optimal control problem subject to the dynamics of the model. To prove the existence and uniqueness of the optimal control, they have used Pontryagin's maximum principle. Their findings demonstrated that those without complications should be given preference in cases where there are insufficient resources to treat all patients medically in order to keep them free from complications. The growing issue of the diabetes epidemic in Sri Lanka was investigated by P. Katulanda, M. H. R. Sheriff, and D. R. Matthews (Katulanda *et al.*, 2009). They claim that the largest study ever conducted on the prevalence of diabetes in Sri Lanka was released in 2005. It revealed a 14.2% prevalence in men and a 13.5% prevalence in women. They came to the conclusion that Sri Lanka is one of the nations with the highest diabetes prevalence rates in the world and that the data on the prevalence of diabetes in the country clearly shows an upward trend. At the time, an estimated 2.8 million adults in Sri Lanka had diabetes mellitus, with a considerable proportion remaining undiagnosed. A cross-sectional study was conducted on diabetes complications in Sri Lankan adults admitted to two government hospitals by U. Navaseelan and K. Judenimal (Navaseelan & Judenimal, 2017). This study found a significant number of diabetic patients with diabetes mellitus visiting diabetic clinics, in particular hospitals in the Eastern Province of Sri Lanka, as well as co-morbidities and complications related to their diabetes mellitus. Additionally, this study confirms that there is a paucity of patient information regarding diabetes prevention, complications, and treatment. It is unquestionably important to arm patients with the data they need to get the most out of their diabetes treatment.

METHODOLOGY

A Mathematical model for pre-diabetes (E), Diabetes without complications (D) and diabetes with complications (C).

We take into account the model formulated by A. Boutayeb *et al.* (Derouich *et al.*, 2014) by considering three compartments, Pre-diabetes (E), Diabetes free from complications (D) and Diabetes with complications (C).

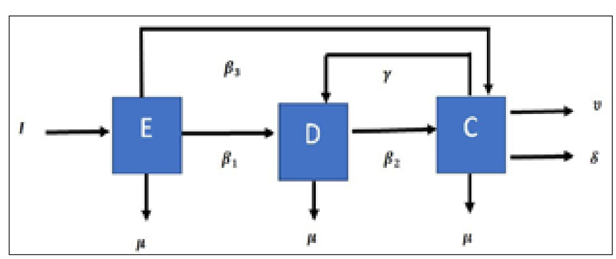

Figure 1: Flow diagram of *EDC* Model.

The flow diagram of the model (*EDC* model) is shown in Figure 1.

The *EDC* model is presented in systems of equations 1.

$$\frac{dE}{dt} = I - (\mu + \beta_3 + \beta_1)E,$$

$$\frac{dD}{dt} = \beta_1 E - (\mu + \beta_2)D + \gamma C, \quad \text{...(1)}$$

$$\frac{dC}{dt} = \beta_3 E + \beta_2 D - (\mu + \gamma + \upsilon + \delta)C.$$

Description of the model variables and parameters is given in Table 1. Unit of each of the model parameter is per year.

The parameter v represents the rate at which individuals with diabetes develop severe disabilities due to complications such as diabetic retinopathy (leading to blindness), diabetic neuropathy (resulting in pain and amputations), diabetic nephropathy (causing kidney failure), cardiovascular diseases (like heart attacks and strokes), diabetic foot diseases (leading to severe infections and amputations), and cognitive impairments (increasing the risk of dementia), critically impacting the population's health burden and the effectiveness of the optimal control strategy aimed at minimizing this burden through the objective functional $J(u)$.

The flow diagram of the model with control strategies is given in Figure 2. Here u is a control variable, in diabetes population models, such as lifestyle modification efforts, health education, early detection programmes, etc.

Table 1: Description of the model variables and parameters

Parameter / variable	Description
E	Cases of pre-diabetes
D	Cases of diabetes free from complications
C	Cases of diabetes with complications
$n = E + D + C$	The population size of diabetes and pre- diabetes
N	The total population size
I	Incidence of pre-diabetes
μ	Natural death rate
β_1	The rate of developing diabetes
β_2	The complication development rate in a diabetic person
β_3	The rate at which people with pre-diabetes develop complications
γ	Curing rate of complications
v	Severely disabling rate of diabetes with complications
δ	The death rate of people with diabetes complications

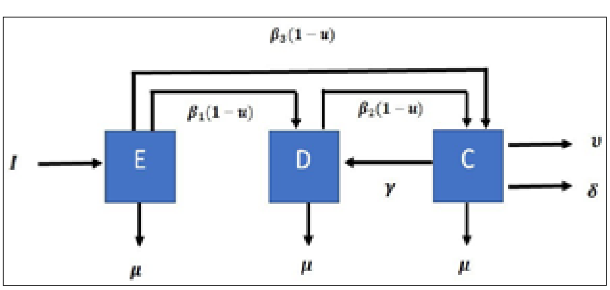

Figure 2: *EDC* model with control u.

$$\frac{dE}{dt} = I - \left(\mu + (\beta_3 + \beta_1)(1-u)\right)E,$$

$$\frac{dD}{dt} = \beta_1(1-u)E - \left(\mu + \beta_2(1-u)\right)D + \gamma C, \quad \text{...(2)}$$

$$\frac{dC}{dt} = \beta_3(1-u)E + \beta_2(1-u)D - (\mu + \gamma + \upsilon + \delta)C,$$

For this optimization process, the objective functional has been constructed by considering the competitive nature of *D, C* with *u*. Managing diabetes at the population level presents a trade-off between intervention costs and health outcomes. Increasing control efforts, such as treatment, screening, or education, can reduce the number of people with diabetes and further with complications, but incur higher immediate costs. In contrast, minimal control reduces short-term costs but increases long-term health and economic burdens. Therefore, an optimal balance between these two concepts is needed to minimize the overall cost of maintaining diabetes within the population. Thus, in this study, the objective functional $J(u)$ is defined in the following manner:

$$J(u) = \int_0^T (D + C + Au^2)dt. \quad ...(3)$$

Where;

A - Positive weight that balances the size of terms,
T - Terminal time of the optimal control process.

Define the set of control by
$U = \{u(t)|u, \quad is\ measurable, \quad 0 \leq u(t) \leq 1, t \in [0, T]\}$
The aim is to characterize an optimal control $u^* \epsilon U$ satisfying:

$$J(u^*) = \min_{u \epsilon U} J(u).$$

We use a modified version of this mathematical model (Derouich *et al.*, 2014) to explain the dynamics of diabetes. We aim to forecast the impact of control strategies on the population over a long period. However, the model presented by Derouich *et al*. (2014) is not applicable for long-term forecasting because it does not take into account the growth of the total population over time. Additionally, our control strategies differ from those considered by them, to check whether we could get better results compared to the existing study.

Modification of the *EDC* model considering time-dependent incidence of Pre-diabetes *(I)*.

In the model (equations 2), the incidence of pre-diabetes is constant throughout the considered time period. But if the considered time period is long, the incidence rate of pre-diabetes could not be constant as the total population grows as time increases. The study indicated about rising diabetes prevalence, with estimates of 2%–6% during the 1990s and 8%–15% in the 2000s–2010s (Prasan Rannan-Eliya *et al*., 2023). Based on the preliminary report of the *Census of Population and Housing 2024 Enumeration Stage*, (2025) , Sri Lanka's total population rose from 14.8 million in 1981 to 21.7 million in 2024, indicating a significant population increase over the period. Furthermore, there is compelling evidence from several studies indicating that the prevalence of prediabetes has significantly grown in Sri Lanka throughout the last two to three decades (Akhtar *et al.*, 2023). Hence, assuming that the incidence of pre- diabetes $I(t)$, at time t, is proportional to the total population size $N(t)$, at time t, is justifiable and can be used to modify the underlined mathematical model.

Therefore, the *EDC* model can be modified by replacing I by αN, where α is the proportional constant. That is,

$$I \propto N \Rightarrow I = \alpha N. \quad ...(4)$$

Moreover, the census data and demographic trends in Sri Lanka over the past few decades reflect the logistic growth model. The population growth rate averaged approximately 2.6% annually before the early 1970s, then declined steadily to below 1% by the early 2000s. This trajectory reflects the characteristic pattern of logistic growth, with an initial phase of rapid acceleration, followed by a peak growth period, and a subsequent deceleration as the population approaches a stable level (*Sri Lanka - Population, Migration, Density | Britannica*, 2025). The logistic growth model takes the following form (Stewart, 2012)

$$\frac{dN}{dt} = rN\left(1 - \frac{N}{K}\right). \quad ...(5)$$

Here, r is the growth rate, and K is the carrying capacity of the population. The solution of this model takes the form;

$$N(t) = \frac{K}{1 + e^{-r(t-t_0)}} \quad ...(6)$$

The future total population size in Sri Lanka can be forecasted by estimating the parameters of equation 6 using the available census data. The estimated parameters are $r = 0.0228$, $K = 3.9474 \times 10^7$, and $t_0 = 2007$.

The *EDC* model is modified by replacing I by αN is given in the system of equations 7.

$$\frac{dE}{dt} = \alpha N - (\mu + (\beta_3 + \beta_1)(1-u))E,$$

$$\frac{dD}{dt} = \beta_1(1-u)E - (\mu + \beta_2(1-u))D + \gamma C, \quad ...(7)$$

$$\frac{dC}{dt} = \beta_3(1-u)E + \beta_2(1-u)D - (\mu + \gamma + \upsilon + \delta)C.$$

Theorem 1.

The set,

$$\Omega = \left\{ (E, D, C) \epsilon \mathbb{R}^3 / \, 0 \le E, D, C \le \frac{\alpha N}{\mu} \right\}$$

is positively invariant under system 7, thereby guaranteeing the existence and positivity of solutions within this region.

Proof: This has been proven by Derouich *et al.*, (2014) for the case when N is constant. However, the same process can further be used to obtain the result for the case when N is a variable quantity since it is a bounded quantity, as it will not exceed the carrying capacity.

Characterization of the optimal control

In order to derive the necessary conditions for optimal control, we can apply Pontryagin's maximum principle (Chambers *et al.*, 1965).

Theorem 2. *Given an optimal control u^* and solutions E^*, D^* and C^* of the associated state system 7, there exist adjoint variables λ_1, λ_2 and λ_3 satisfying;*

$$\begin{aligned} \lambda_1{}' &= (\lambda_1 - \lambda_2)(1 - u^*)\beta_1 + (\lambda_1 - \lambda_3)(1 - u^*)\beta_3 + \mu\lambda_1, \\ \lambda_2{}' &= -1 + \beta_2(1 - u^*)(\lambda_2 - \lambda_3) + \mu\lambda_2, \\ \lambda_3{}' &= -1 + (\lambda_3 - \lambda_2)\gamma + \lambda_3(\mu + \nu + \delta). \end{aligned} \quad \text{...(8)}$$

With transversality conditions: $\lambda_1(T) = \lambda_2(T) = \lambda_3(T) = 0$ *and the optimal control:*

$$u^* = min\left(1, max\left(0, \frac{1}{2A}[E^*\beta_1(\lambda_2 - \lambda_1) + E^*\beta_3(\lambda_3 - \lambda_1) + D^*\beta_2(\lambda_3 - \lambda_2)]\right)\right). \quad \text{...(9)}$$

Proof: Hamiltonian H, at time t, is defined by,

$$H = D + C + Au^2 + \lambda_1 f_1(E^*, D^*, C^*) + \lambda_2 f_2(E^*, D^*, C^*) + \lambda_3 f_3(E^*, D^*, C^*).$$

Here;

$$f_1(E, D, C) = \alpha N - \big(\mu + (\beta_3 + \beta_1)(1 - u)\big)E,$$

$$f_2(E, D, C) = \beta_1(1 - u)E - \big(\mu + \beta_2(1 - u)\big)D + \gamma C,$$

$$f_3(E, D, C) = \beta_3(1 - u)E + \beta_2(1 - u)D - (\mu + \gamma + \upsilon + \delta)C.$$

Optimality condition u^* is found such that H is optimized. The critical value u^* is given by the solution of the equation $\frac{dH}{du} = 0$. That is;

$$2Au + \lambda_1(\beta_1 + \beta_3)E + \lambda_2(-\beta_1 E + \beta_2 D) - \lambda_3(\beta_3 E + \beta_2 D) = 0,$$

$$u^* = \frac{1}{2A}[\beta_1 E^*(\lambda_2 - \lambda_1) + \beta_3 E^*(\lambda_3 - \lambda_1) + \beta_2 D^*(\lambda_3 - \lambda_2)]$$

The adjoint variables λ_1, λ_2 and λ_3 are obtained by solving the following system:

$$\begin{aligned} \lambda_1{}' &= -\frac{dH}{dE} = (\lambda_1 - \lambda_2)(1 - u^*)\beta_1 + (\lambda_1 - \lambda_3)(1 - u^*)\beta_3 + \mu\lambda_1, \\ \lambda_2{}' &= -\frac{dH}{dD} = -1 + \beta_2(1 - u^*)(\lambda_2 - \lambda_3) + \mu\lambda_2, \\ \lambda_3{}' &= -\frac{dH}{dC} = -1 + (\lambda_3 - \lambda_2)\gamma + \lambda_3(\mu + \nu + \delta). \end{aligned} \quad \text{...(10)}$$

provided with respect to conditions,

$$\rightarrow \lambda_1(T) = \lambda_2(T) = \lambda_3(T) = 0.$$

Modification of the *EDC* model considering two control strategies

Furthermore, we can modify system 1 by introducing new controls:

- u_1 - Awareness of diet plans.
- u_2 - Awareness of Regular testing for diabetes without complications.

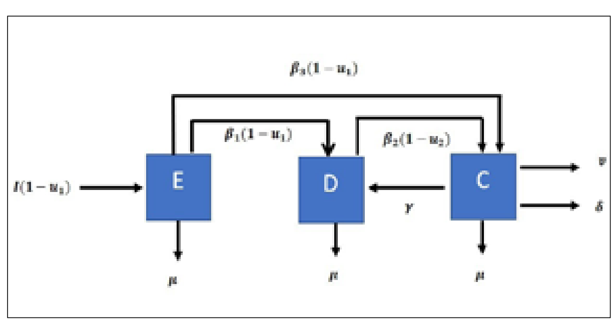

Figure 3: EDC model with two controls, u_1, u_2.

Based on the above controls, the proposed model is depicted in Figure 3.

$$\frac{dE}{dt} = I(1-u_1) - \big(\mu + (\beta_3+\beta_1)(1-u_1)\big)E,$$
$$\frac{dD}{dt} = \beta_1(1-u_1)E - \big(\mu + \beta_2(1-u_2)\big)D + \gamma C, \qquad ...(11)$$
$$\frac{dC}{dt} = \beta_3(1-u_1)E + \beta_2(1-u_2)D - (\mu + \gamma + \upsilon + \delta)C.$$

The aim of this process is to minimize the following objective functional,

$$J(u_1,u_2) = \int_0^T (D + C + Au_1{}^2 + Bu_2{}^2)dt, \qquad ...(12)$$

where;

A, B - Positive weights that balance the size of terms. The objective is to characterize an optimal control $u_1{}^*, u_2{}^* \in U$ satisfying;

$$J(u_1{}^*, u_2{}^*) = \min_{u_1,u_2 \in U} J(u_1,u_2).$$

Existence and positivity of solutions

Theorem 3

The set $\Omega = \left\{(E,D,C)\epsilon\mathbb{R}^3 / \, 0 \le C, D, E \le \frac{I}{\mu}\right\}$ *is positively invariant under the system 11.*

Proof:

$$\frac{dE}{dt} = I(1-u_1) - \big(\mu + (\beta_3+\beta_1)(1-u_1)\big)E,$$
$$\frac{dE}{dt} \ge -\big(\mu + (\beta_3+\beta_1)(1-u_1)\big)E.$$

By the differential form of Gronwall's inequality:

This implies $E(t) > 0$.

Assuming that ∃, some time $t_* > 0$ such that $D(t_*) = 0$, other variables are positive and $D(t) > 0$ for $t \in [0, t_*]$. By the second equation of the system 11:

$$\frac{dD}{dt} = \beta_1(1-u_1)E - \big(\mu + \beta_2(1-u_2)\big)D + \gamma C,$$
$$\frac{dD}{dt} + (\mu + \beta_2)D = \beta_1(1-u_1)E + \beta_2 u_2 D + \gamma C.$$

Multiplying both sides by $e^{(\mu+\beta_2)t}$,

$$\frac{d}{dt}\left(De^{(\mu+\beta_2)t}\right) = e^{(\mu+\beta_2)t}[\beta_1(1-u_1)E + \beta_2 u_2 D + \gamma C].$$

Integrating this from 0 to t_*,

$$\int_0^{t_*} \frac{d}{dt}\left(De^{(\mu+\beta_2)t}\right) = \int_0^{t_*} e^{(\mu+\beta_2)t}[\beta_1(1-u_1)E + \beta_2 u_2 D + \gamma C]dt,$$

We obtain the result

$$D(t_*) = e^{-(\mu+\beta_2)t_*}\left[D(0) + \int_0^{t_*} e^{(\mu+\beta_2)t}[\beta_1(1-u_1)E + \beta_2 u_2 D + \gamma C]dt\right].$$

$D(t_*) > 0$, which contradicts $D(t_*) = 0$. Consequently, $D(t) > 0 \ \forall t \in [0, T\,]$.

By the third equation of the system 11:

$$\frac{dC}{dt} = \beta_3(1-u_1)E + \beta_2(1-u_2)D - (\mu + \gamma + \upsilon + \delta)C,$$

$$\frac{dC}{dt} \ge -(\mu + \gamma + \upsilon + \delta)C \quad (\because \ E(t) > 0 \ and \ D(t) > 0).$$

By the differential form of Gronwall's inequality,

$$C(t) = C(0).\,exp(-(\mu + \gamma + \nu + \delta)t) > 0,$$

This implies; $C(t) > 0$.

By adding equations of the system 11, we obtain:

$$\frac{dn}{dt} = I - \mu n - (\upsilon + \delta)C \le I - \mu n,$$

where $n = E + D + C$.

By integrating, we obtain:

$$n \le \frac{I}{\mu} - \left(\frac{I}{\mu} - n(0)\right)e^{-\mu t},$$

This implies $n(t) \le \frac{I}{\mu}$.

Theorem 4

The system 11 that satisfies a given initial condition $(E(0), D(0), C(0)) \in \Omega$ *has a unique solution.*

Proof: Let;

$$X = \begin{pmatrix} E \\ D \\ C \end{pmatrix}, \text{ and } \psi(X) = X_t = \begin{pmatrix} \frac{dE}{dt} \\ \frac{dD}{dt} \\ \frac{dC}{dt} \end{pmatrix}.$$

Therefore, the system 11 can be rewritten as follows:

$$\psi(X) = X_t = AX + B,$$

where,

$$A = \begin{pmatrix} -[\mu + (\beta_3 + \beta_1)(1 - u_1) & 0 & 0 \\ \beta_1(1 - u_1) & -[\mu + \beta_2(1 - u_2)] & \gamma \\ \beta_3(1 - u_1) & \beta_2(1 - u_2) & -(\mu + \gamma + \nu + \delta) \end{pmatrix},$$

and

$$B = \begin{pmatrix} I(1 - u_1) \\ 0 \\ 0 \end{pmatrix}.$$

Then,

$$\| \psi(X_1) - \psi(X_2) \| = \| (AX_1 + B) - (AX_2 + B) \|,$$

$$\| \psi(X_1) - \psi(X_2) \| = \| AX_1 - AX_2 \|,$$

$$\| \psi(X_1) - \psi(X_2) \| \leq \| A \| . \| (X_1 - X_2) \|.$$

Therefore, the function ψ is uniformly Lipschitz continuous. Hence, from the definition of the controls $u_1(t), u_2(t)$ and the limitations $E(t) \geq 0, D(t) \geq 0$ *and* $C(t) \geq 0$, it can be concluded that the solution of the system 11 exists (Birkhoff & Rota, 1989).

Existence of an optimal control pair

Lemma 1. *There exist optimal solutions* $(u_1^*, u_2^*) \in U$ *such that* $J(u_1^*, u_2^*) = \min_{u_1, u_2 \in U} J(u_1, u_2)$ *for the optimal control problem indicated in system 11.*

Proof: By using Fleming and Rishel result (Fleming & Rishel, 2012) and performing the following steps, it is possible to obtain the existence of optimal control.

- According to theorems 3 and 4, the set of controls and associated state variables are non-empty.
- $J(u_1, u_2) = \int_0^T (D + C + Au_1^2 + Bu_2^2)dt$ is convex in u_1 and u_2.
- By definition, the control space *U* is convex and closed.
- The integrand in the objective functional, $(D + C + Au_1^2 + Bu_2^2)$ is obviously convex in $U \times U$.
- There exist constants a, b, c *such that* $(D + C + Au_1^2 + Bu_2^2) \geq a + b|u_1|^\alpha + c|u_2|^\alpha$, where $\alpha > 1$.

Characterization of an optimal control pair

The necessary conditions for the optimal control pair arise from Pontryagin's maximum principle (Chambers *et al*., 1965).

Theorem 5.

Given an optimal control (u_1^*, u_2^*) *and solutions* E^*, D^* and C^* *of the associated state system 11, there exist adjoint variables* λ_1, λ_2 and λ_3 *satisfying:*

$$\lambda_1' = \lambda_1\mu + \beta_3(1 - u_1^*)(\lambda_1 - \lambda_3) + \beta_1(1 - u_1^*)(\lambda_1 - \lambda_2),$$

$$\lambda_2' = -1 + \lambda_2\mu + \beta_2(1 - u_2^*)(\lambda_2 - \lambda_3), \quad ...(13)$$

$$\lambda_3' = -1 + \lambda_3(\mu + \nu + \delta) + \gamma(\lambda_3 - \lambda_2),$$

With transversality conditions $\lambda_1(T) = \lambda_2(T) = \lambda_3(T) = 0$ *and the optimal control pair*

$$u_1^* = min\left(1, max\left(0, \frac{1}{2A}[I\lambda_1 + E\beta_1(\lambda_2 - \lambda_1) + E\beta_3(\lambda_3 - \lambda_1)]\right)\right),$$

$$u_2^* = min\left(1, max\left(0, \frac{D}{2B}[\beta_2(\lambda_3 - \lambda_2)]\right)\right) \quad ...(14)$$

Proof: the Hamiltonian *H* at time *t* is defined by:

$$H = D + C + Au_1^2 + Bu_2^2 + \lambda_1 f_1(E^*, D^*, C^*) + \lambda_2 f_2(E^*, D^*, C^*) + \lambda_3 f_3(E^*, D^*, C^*).$$

Here,

$$f_1(E, D, C) = I(1 - u_1) - \big(\mu + (\beta_3 + \beta_1)(1 - u_1)\big)E,$$
$$f_2(E, D, C) = \beta_1(1 - u_1)E - \big(\mu + \beta_2(1 - u_2)\big)D + \gamma C,$$
$$f_3(E, D, C) = \beta_3(1 - u_1)E + \beta_2(1 - u_2)D - (\mu + \gamma + \upsilon + \delta)C.$$

The optimality condition yields the optimal control:

$$\frac{\partial H}{\partial u_1} = 0 \Rightarrow 2Au_1 - I\lambda_1 + \lambda_1[(\beta_1 + \beta_3)E] + \lambda_2[-\beta_1 E] + \lambda_3[-\beta_3 E] = 0,$$

$$\frac{\partial H}{\partial u_1} = 0 \Rightarrow u_1^* = \frac{1}{2A}[I\lambda_1 + E\beta_1(\lambda_2 - \lambda_1) + E\beta_3(\lambda_3 - \lambda_1)].$$

$$\frac{\partial H}{\partial u_2} = 0 \Rightarrow 2Bu_2 + \lambda_2\beta_2 D - \lambda_3\beta_2 D,$$

$$\frac{\partial H}{\partial u_2} = 0 \Rightarrow u_2^* = \frac{D}{2B}[\beta_2(\lambda_3 - \lambda_2)].$$

We can obtain the adjoint variables λ_1, λ_2 and λ_3 by the following system:

$$\lambda_1' = -\frac{dH}{dE} = \beta_1(1 - u_1^*)(\lambda_1 - \lambda_2) + \beta_3(1 - u_1^*)(\lambda_1 - \lambda_3) + \mu\lambda_1,$$

$$\lambda_2' = -\frac{dH}{dD} = -1 + \beta_2(1 - u_2^*)(\lambda_2 - \lambda_3) + \mu\lambda_2,$$

$$\lambda_3{}' = -\frac{dH}{dC} = -1 + (\lambda_3 - \lambda_2)\gamma + \lambda_3(\mu + \nu + \delta). \quad ...(15)$$

$\rightarrow \lambda_1(T) = \lambda_2(T) = \lambda_3(T) = 0.$

Numerical simulation

Using a fourth-order Runge-Kutta scheme, we numerically solved the resulting optimality systems 7 and 11. This method involves a two-step process. It begins by forward solving the state equations using an initial guess for the control parameters u_1 and u_2. As the forward solution progresses, the controls are continuously updated based on control equations 9 or 14. In parallel, the method solves adjoint equations backwards initialized with transversality conditions until results converge; this process is continued iteratively. This process is called Forward Backward Sweep Method.

There are many types of tests available to obtain the convergence behavior of the numerical solutions (Bellonietal, 1993; Lenhart & Workman, 2007). We considered the evolution of the size between two consecutive solution with respect to the number of iterations. Suppose that $X = (E, D, C)$ and $U = (u_1, u_2)$ are the state and control vectors. X_{k+1}, U_{k+1} denote the vectors of estimated values of the current iteration and X_k, U_k are those of the previous iteration. Then we define,

$$\|X_{k+1} - X_k\| = \sum_{i=1}^{N+1} |X_{k+1}(i) - X_k(i)|$$

and

$$\|U_{k+1} - U_k\| = \sum_{i=1}^{N+1} |U_{k+1}(i) - U_k(i)|$$

In order to define the stopping criteria for the optimization algorithm, define

$$test_X = \delta\|X_{k+1}\| - \|X_{k+1} - X_k\| \text{ and } test_U = \delta\|U_{k+1}\| - \|U_{k+1} - U_k\|$$

for some $\delta > 0$. Then we stop the algorithm if, $\min(test_X, test_U)$ is sufficiently small. The utilized optimization algorithm with the forward-backward sweep method is presented below.

Algorithm 1 Optimization algorithm with forward backward sweep method

Input: Initial state X_0, initial control U_0, tolerance (tol), set parameters.
Output: Optimal control U^*, optimal state X^*
Set $k = 0$
Test = *min* $(test_X, test_U)$ (initially set as a constant value.)
while Test $\geq$ *tol*
1. Solve the state system (given U_k)
2. Solve the adjoint system
3. Compute the cost functional
4. Update U_{k+1} using 14 or 9
5. Compute *Test* = *min* $(test_X, test_U)$
6. Set $k = k+1$

end
$U^* = U_k$
$X^* = X_k$

The appropriate parameter values are selected for the numerical simulation, and the year 2007 is used as the starting point for the simulations.

The weight constants are chosen in the following way because of the difference in scales between the control and state functions: For the *EDC* model with variable incidence of pre-diabetes, A = 3,550,000 and for the *EDC* model with two controls, A = 4,550,000 and B = 1,550,000. Also, initial states are chosen as E(0) = 1,710,456, D(0) = 148,428 and C(0) = 103,899 which are the relevant values for Sri Lanka in the year 2007.

Table 2: Parameter values used in numerical simulation

Parameter	Value year^{-1}	Description
μ	0.0059	Natural death rate
v	0.005	Severely disabling rate of diabetes with complications
γ	0.05	Curing rate of complications
δ	0.059	The death rate of people with diabetes complications
β_1	0.03	Diabetes developing probability
β_2	0.0067	Complication developing probability of a diabetic person
β_3	0.0005	The probability of prediabetes getting complications
I	565,440	Incidence of pre-diabetes

RESULTS AND DISCUSSION

EDC model with variable incidence of pre-diabetes (I)

Control strategies and the compartment sizes of the proposed model were estimated using the numerical solutions of the optimal control problem. The results of the current model indicate that the incidence rate *I* may not behave as a constant for a long time period. Figures 4, 5, and 6 illustrate the variation in the population sizes of individuals with diabetes (with and without complications) and those with pre-diabetes, under both constant incidence rate and incidence rate varying according to the logistic growth of the population. Figure 7 presents the variation in the control for both scenarios. Figure 8 shows the behaviour of the objective functional when the incidence rate is constant, while Figure 9 presents it when the incidence rate varies according to the logistic growth of the population.

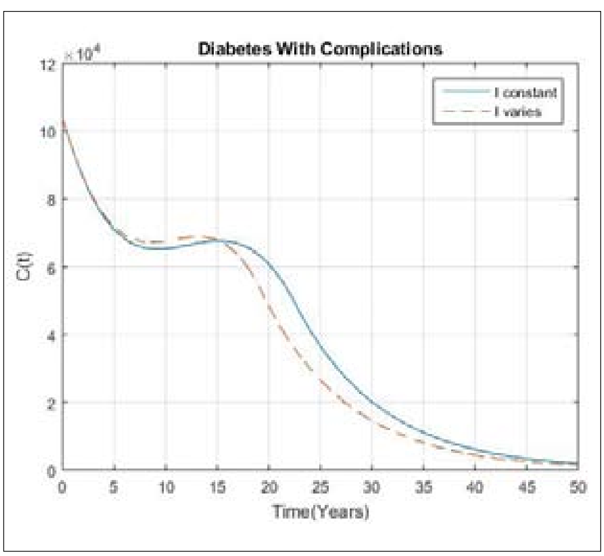

Figure 4: The evolution of the number of diabetes incidences with complications, with constant *I* and variable incidence rate (*I*)

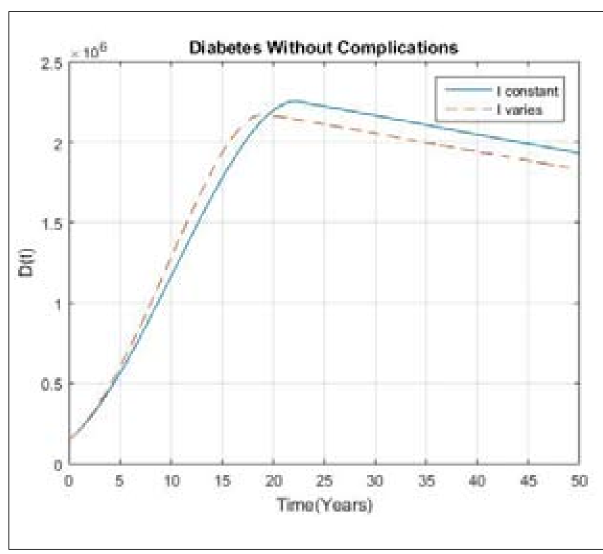

Figure 5: The evolution of the number of diabetes incidences, without complications with constant and variable incidence rate (*I*).

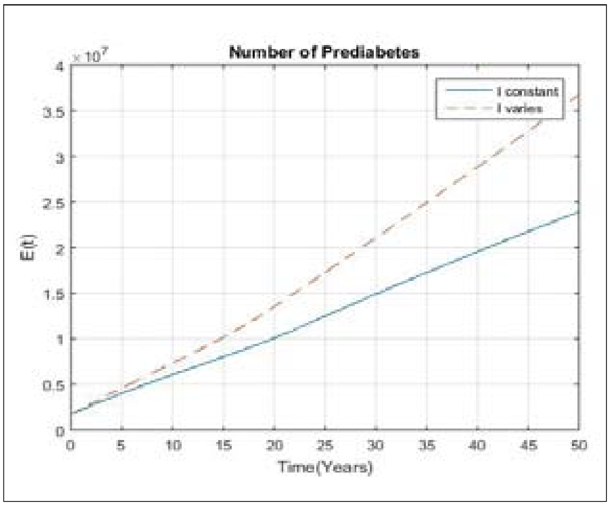

Figure 6: The evolution of the number of pre-diabetes incidences with constant and variable incidence rate (*I*).

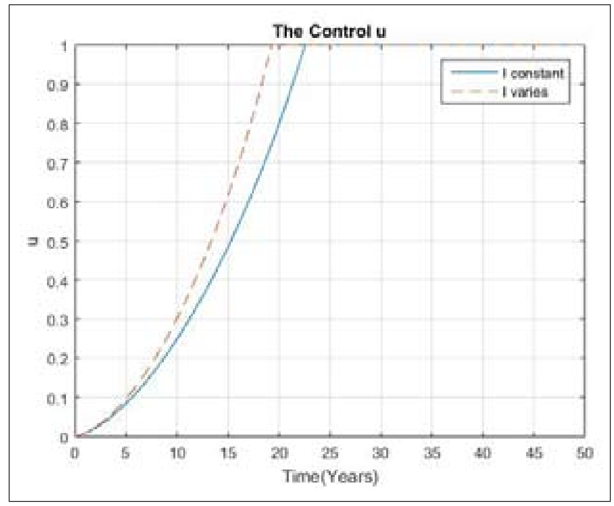

Figure 7: The behaviour of the control with constant and variable incidence rate (*I*).

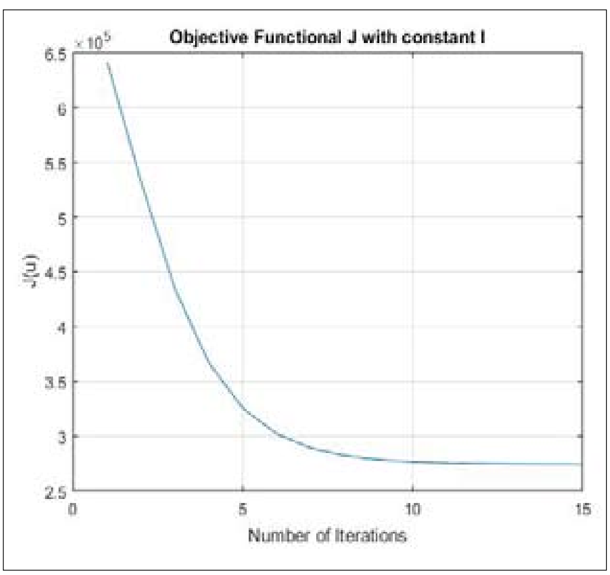

Figure 8: Behaviour of the objective functional against the number of iterations, when the incident rate is constant.

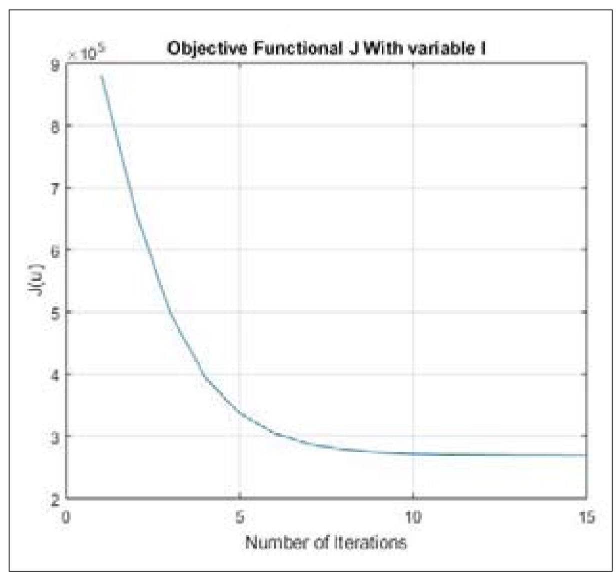

Figure 9: Behaviour of the objective functional against the number of iterations, when the incident rate varies.

The observation of the presented model reveals that with a constant incident rate, the number of incidences of pre-diabetes, diabetes without complications, and diabetes with complications will reach 23.91 million, 19.33 million and 1839 in 50 years, respectively. Under the same parameter values, but with variable incident rate, the population of people with pre-diabetes, diabetes without complications, and diabetes with complications will reach 36.73 million, 18.32 million, and 1338 in 50 years, respectively. Moreover, with a variable incidence of pre-diabetes (*I*), the control u reaches its maximum value within 19 years, while it takes 23 years for a constant incidence of pre-diabetes (*I*).

EDC Model with two controls

In this section, we present the results of our second model, which demonstrates how pre-diabetes and diabetes (with and without complications) vary under the influence of two control variables. We also examine the behaviour of the objective functional and the control strategies u_1 and u_2.

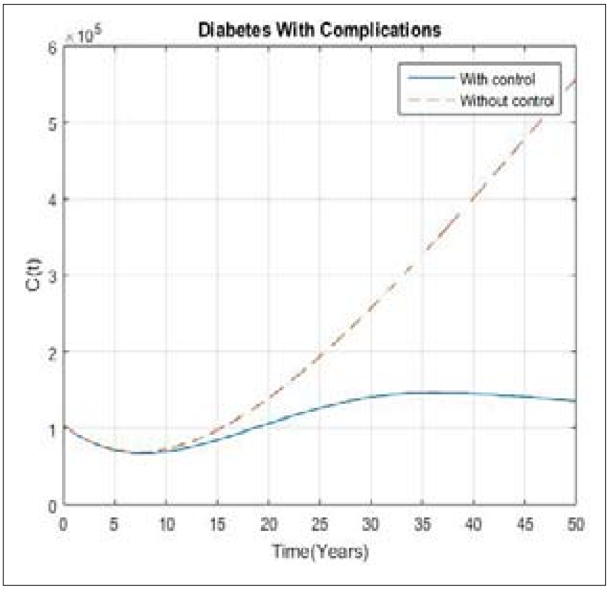

Figure 10: The evolution of the number of incidences of diabetes with complications, with and without controls.

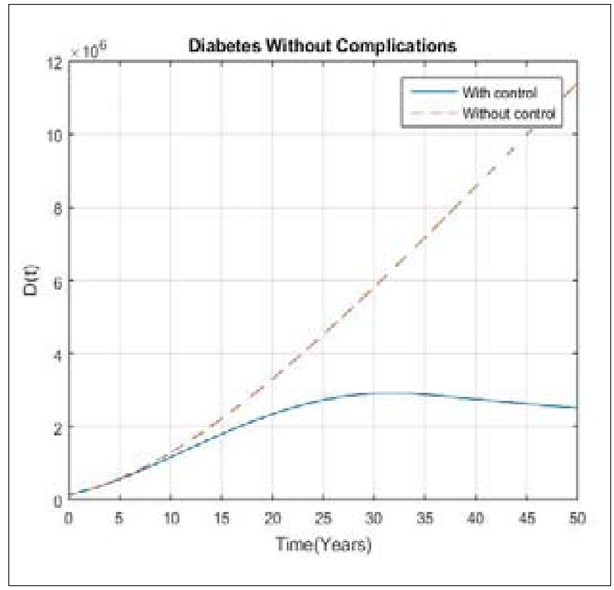

Figure 11: The evolution of the number of incidences of diabetes without complications, with and without controls.

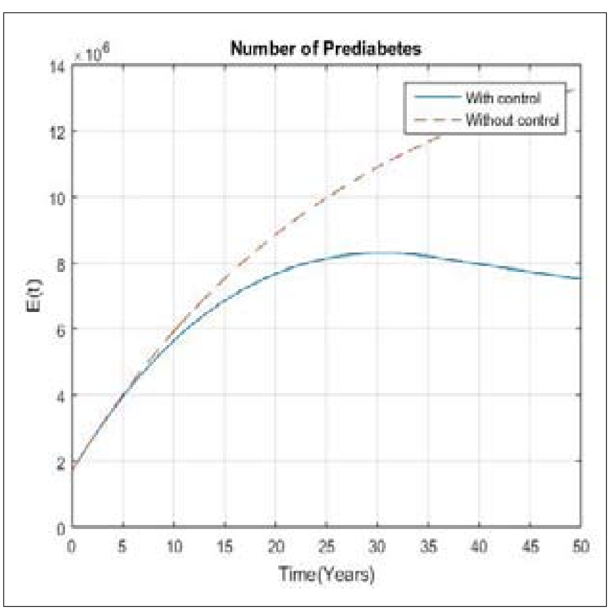

Figure 12: The evolution of the number of incidences of pre-diabetes, with and without controls.

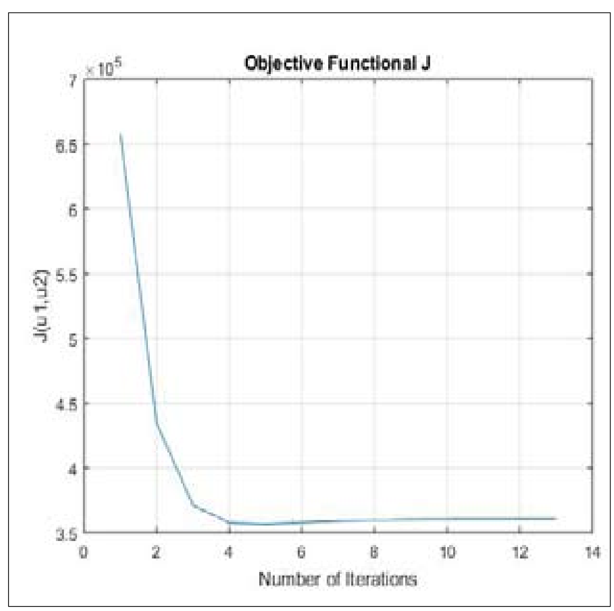

Figure 13: The behaviour of the objective functional $J(u_1, u_2)$.

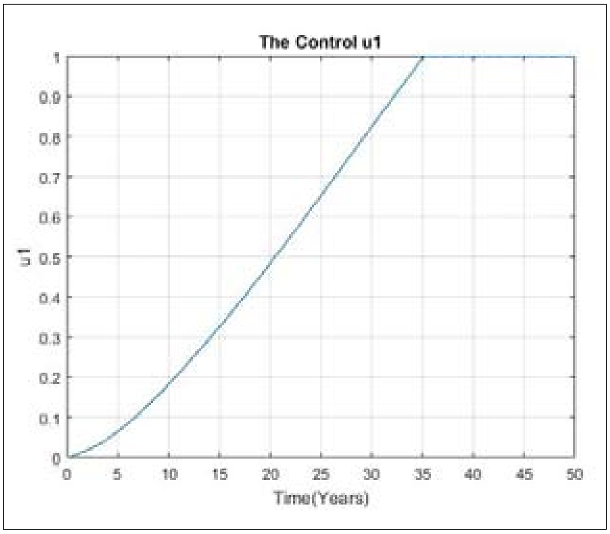

Figure 14: The behaviour of the control u_1.

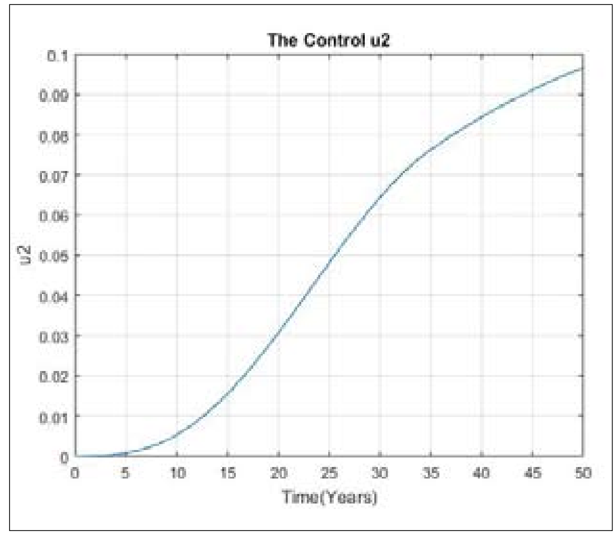

Figure 15: The behaviour of the control u_2.

In this model, we observed that the number of incidences of pre-diabetes, diabetes without complications, and diabetes with complications will reach 13.29 million, 11.4 million, and 0.5572 million, respectively, in 50 years without optimal control. Under the same parameter values, but with optimal control, the population of patients with pre-diabetes, diabetes without complications, and diabetes with complications will reach 7.5 million, 2.508 million, and 0.1356 million in 50 years, respectively. According to Figures 14 and 15, the control u_1 should receive more attention than the control u_2 during the considered time period. Further, the control u_1 should be conducted at full capacity after 35 years of period.

Error Analysis of the Solution

In this section, an error analysis of the solution is conducted by evaluating the errors and convergence rates of both the state and control variables at different step sizes to check the convergence of the proposed simulation algorithm. The obtained results are shown in Table 3, Table 4, and Figure 16. The analysis shows that as the step size decreases, the errors for both the state and control variables significantly decrease, indicating improved accuracy of the algorithm. The tables also show the logarithmic ratios of these errors, which further demonstrate the increasing order of convergence. This consistent improvement in accuracy with smaller step sizes highlights the effectiveness and reliability of the solution method employed.

Table 3: Error and order of convergence of state variables (h = 0.4)

Step size	$\lVert X_h \rVert$	$\frac{\lVert X_h - X_{h/2} \rVert}{\lVert X_h \rVert}$	$\frac{\lVert X_h - X_{h/2} \rVert}{\lVert X_{h/2} - X_{h/4} \rVert}$	$\log_2\left(\frac{\lVert X_h - X_{h/2} \rVert}{\lVert X_{h/2} - X_{h/4} \rVert}\right)$
h	0.3836×10^{9}	0.115888×10^{-4}	4.3947	2.1344
$h/2$	0.7653×10^{9}	0.013085×10^{-4}	3.2190	1.6740
$h/4$	1.5285×10^{9}	0.002052×10^{-4}	3.0245	1.5959
$h/8$	3.0550×10^{9}	0.000342×10^{-4}	6.5338	2.6891
$h/16$	6.1080×10^{9}	0.000026×10^{-4}		
$h/32$	0.1221×10^{9}			

Table 4: Error and order of convergence of control variables

Step size	$\|U_h\|$	$\frac{\|U_h - U_{h/2}\|}{\|U_h\|}$	$\frac{\|U_h - U_{h/2}\|}{\|U_h\|}$	$\log_2\left(\frac{\|U_h - U_{h/2}\|}{\|U_{h/2} - U_{h/4}\|}\right)$
h	40.7886	0.7328×10^{-5}	5.1170	2.3549
$h/2$	81.3029	0.0708×10^{-5}	4.1384	1.9424
$h/4$	162.3316	0.0123×10^{-5}	2.5669	1.3578
$h/8$	324.3892	0.0025×10^{-5}	7.4125	2.7519
$h/16$	648.5043	0.0001×10^{-5}		
$h/32$	1296.7344			

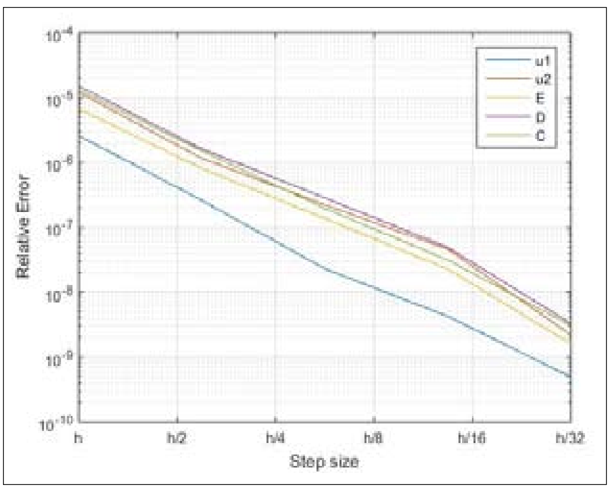

Figure 16: Variation of Relative Errors of State Variables and Controls against Step Size.

CONCLUSION

The incidence of pre-diabetes (E), diabetes without complications (D) and diabetes with complications (C) is a huge burden for the healthcare sectors in the world. This paper proposes two mathematical models considering the above-mentioned subclasses (*EDC*) and two diabetes control strategies. In the first model, we considered two cases, *EDC* model with a constant incidence rate and *EDC* model with variable incidence rate. In the case of variable incidence rates, it is assumed that the incidence rate is proportional to the time-dependent total population size. In the second model, we considered *EDC* model with two control strategies, which are awareness programmes by raising the consciousness of the importance of following a diet plan and maintaining good health care, and regular testing and awareness programmes for diabetes without complications. We observed that under control strategies, the population sizes of patients with pre-diabetes, diabetes without complications, and diabetes with complications decreased by 44%, 78%, and 76% respectively, after the end of 50 years. Therefore, the numerical simulation of the obtained results showed the effectiveness of the proposed control strategies. Since diabetes is a worldwide problem with different rates of incidence, prevalence, mortality, and morbidity, the current mathematical models can be further improved for various contexts based on the values of the parameters and other appropriate control strategies.

REFERENCES

Akhtar, S., Ali, A., Asghar, M., Hussain, I., & Sarwar, A. (2023). Prevalence of type 2 diabetes and pre-diabetes in Sri Lanka: A systematic review and meta-analysis. *BMJ Open*, *13*(8), 1–8. https://doi.org/10.1136/bmjopen-2022-068445

Belloni, M., Buttazzo, G., & Freddi, L. (1993). Completion by Gamma-convergence for optimal control problems. *Annales de La Faculté Des Sciences de Toulouse: Mathématiques*, *2*(2), 149–162.

Birkhoff, G., & Rota, G. C. (1989). *Ordinary Differential Equations*. Waltham: Blaisdell Publishing Co.

Census of Population and Housing 2024 Enumeration Stage. (2025). Retrieved July 20, 2025, from https://www.statistics.gov.lk//Resource/en/Population/CPH_2024/CPH2024_Preliminary_Report.pdf

Chambers, M. L., Pontryagin, L. S., Boltyanskii, V. G., Gamkrelidze, R. V., Mishchenko, E. F., & Brown, D. E. (1965). The mathematical theory of optimal processes. *OR*, *16*(4), 493. https://doi.org/10.2307/3006724

Derouich, M., Boutayeb, A., Boutayeb, W., & Lamlili, M. (2014). Optimal control approach to the dynamics of a population of diabetics. *Applied Mathematical Sciences*, *53–56*. https://doi.org/10.12988/ams.2014.43155

Fleming, W. H., & Rishel, R. W. (2012). *Deterministic and stochastic optimal control* (Vol. 1). Springer Science and Business Media.

International Federation of Diabetes. (2025). *What Is Diabetes | International Federation of Diabetes*. Retrieved March 7, 2022, from https://idf.org/about-diabetes/what-is-diabetes/

Katulanda, P., Sheriff, M. H. R., & Matthews, D. R. (2009). The diabetes epidemic in Sri Lanka–a growing problem. *Ceylon Medical Journal*, *51*(1).

Kouidere, A., Khajji, B., Balatif, O., & Rachik, M. (2021). A multi-age mathematical modeling of the dynamics of population diabetics with effect of lifestyle using optimal control. *Journal of Applied Mathematics and Computing*, *67*(1), 375–403.

Kouidere, A., Labzai, A., Ferjouchia, H., Balatif, O., & Rachik, M. (2020). A new mathematical modeling with optimal control strategy for the dynamics of population of diabetics and its complications with effect of behavioral factors. *Journal of Applied Mathematics*, *2020*(1), 1943410.

Lenhart, S., & Workman, J. T. (2007). Optimal control applied to biological models. In *Optimal control applied to biological models*. https://doi.org/10.1201/9781420011418

Navaseelan, U., & Judenimal, K. (2017). Diabetes mellitus complications among Sri Lankan adults admitted to two government hospitals: a cross sectional study. *The Malaysian Journal of Nursing (MJN)*, *9*(2), 3–10.

Prasan Rannan-Eliya, R., Wijemunige, N., Perera, P., Kapuge, Y., Gunawardana, N., Sigera, C., Jayatissa, R., Herath, H. M. M., Gamage, A., Weerawardena, N., Sivagnanam, I., Dalpatadu, S., Samarage, S., Samarakoon, U., Samaranayake, N., Pullenayegam, C., & Perera, B., (2023). Prevalence of diabetes and pre-diabetes in Sri Lanka: a new global hotspot - estimates from the Sri Lanka Health and Ageing Survey 2018/2019. *BMJ Open BMJ Open Diabetes Research and Care*, *11*, 3160. https://doi.org/10.1136/bmjdrc-2022-003160

Sri Lanka - Population, Migration, Density | Britannica. (2025). Retrieved July 18, 2025, from https://www.britannica.com/place/Sri-Lanka/Demographic-trends

Stewart, J. (2012). *Single Variable Calculus Instructor Solutions Manual, Early Transcendentals* (7th ed.). Cengage Learning.

WHO, 2025. *World Health Organization*. Retrieved March 7, 2022, from https://www.who.int/news-room/fact-sheets/detail/diabetes

Yusuf, T. T. (2015). Optimal control of incidence of medical complications in a diabetic patients' population. *Futa Journal of Research in Sciences*, *11*(1), 180–189.

J.Natn.Sci.Foundation Sri Lanka 2025 53 (3): 233 - 244
DOI: http://dx.doi.org/10.4038/jnsfsr.v53i3.12431

RESEARCH ARTICLE

Food Science and Technology

Development of pasta using composite flour of sweet potato (*Ipomoea batatas*), soy (*Glycine max*) & rice (*Oryza sativa*) flours

JMJM Jayawardhana[1], MJM Fari[1*] and R Liyanage[2]
[1] *Department of Biosystems Technology, Faculty of Technology, South Eastern University of Sri Lanka, Oluvil, Sri Lanka.*
[2] *Department of Biosystems Technology, Faculty of Technology, University of Sri Jayewardenepura, Homagama, Sri Lanka.*

Submitted: 09 November 2024; Revised: 11 July 2025; Accepted: 29 July 2025

Abstract: Pasta made from wheat flour is a convenience food globally. This study investigates the use of composite flour to reduce wheat flour consumption in Sri Lanka and develops a blend of locally available ingredients, *viz.*, sweet potato (*Ipomoea batatas*) accession 'Carrot Bathala', soy (*Glycine max*), and rice (*Oryza sativa*), using a Taguchi orthogonal experimental design. Four samples (T_2, T_3, T_4, and T_8) were selected for final evaluation through preliminary sensory evaluation. The ratios of the three ingredients for samples T_2, T_3, T_4, and T_8 were 50:30:20, 41.6:33.3:25, 60:20:20 and 63.6:27.2:9, respectively. A pasta made from 100% wheat flour served as a control. The sensory evaluation was performed by 30 untrained panellists utilizing a 9-point hedonic scale and the results were analysed using a one-way Friedman test with a confidence interval of 95%. All treatments scored significantly higher in sensory properties than the control, with T_2 achieving the highest scores for appearance, taste, hardness, and overall acceptability. From nutritional perspective, T_2 contained significantly more fat (2.19%), fibre (2.54%), energy (510.3 kcal/100 g), ash (3.35%), and protein (14.57%) compared to the control. However, moisture (10.90%), carbohydrate (74.31%), and acid-insoluble ash (0.05%) were significantly higher in the control. T_2 had the lowest cooking time and water absorption (91.35%) but higher cooking loss (11.25%). The highest values of hardness, chewiness, and gumminess can be observed in pasta made from composite flour. The composite flour pasta met SLS420:2019 standards, suggesting its potential as a gluten-free alternative that could be commercialized in Sri Lanka.

Keywords: Composite flour, pasta, rice, soy, sweet potato.

INTRODUCTION

'Pasta' is an Italian word meaning 'dough' and the production and consumption of pasta have historically been predominant in Italy. Because it is more convenient, palatable, and has a longer shelf life than other bakery products like bread, pasta is consumed widely over the world. Semolina made out of wheat is the main ingredient in making pasta (Nilusha *et al.*, 2019). However, the preparation of pasta using composite flour with or without adding wheat flour has high potential in developing countries like Sri Lanka due to the non-availability of the wheat crops.

Rice is a staple food for the Sri Lankan community, providing a typical Sri Lankan with 45 percent of his daily calorie intake and 40 percent of his total protein needs. In addition, rice is rich in carbohydrates and fibres, has a low calorie, fat and cholesterol content and is also a gluten-free foodstuff (More *et al.*, 2013). The quality of products made from rice is strongly influenced by the content of amylose and amylopectin (Fari *et al.*, 2011).

Rice is the principal cereal grown for direct human consumption as a single grain. It is also consumed in the form of noodles, rice cakes, breakfast cereals, fermented sweet rice and as a snack food prepared by extrusion. The rice is also used to make beer, wine and mulled wine

* Corresponding author (mjmfari@seu.ac.lk; https://orcid.org/0009-0003-7529-0858)

(Bor, 1999). Rice flour produced by grinding whole rice grains or broken rice has resulted in a significant increase in the variety of products based on rice such as gluten-free bread, rice cakes, rice noodles, and baby food (Ronie & Hasmadi, 2022).

Soybean (*Glycine max*) belongs to the legume family. Dry soybean contains 40% protein, 20% oil, 35% both soluble (sucrose, raffinose, stachyose, etc.) and insoluble (dietary fibre) carbohydrates, and 5% ash. The moisture content of fresh soybeans is roughly 14%. Soy protein products are easily digestible by humans. Human digestion of soy protein ranges from 92% to 100%. The structure and amino acid composition of protein in soybean significantly impact the performance of soybean in product development, such as proper binding of water and fat emulsification and foaming (Jooyandeh, 2011). Traditionally, soybean was used mainly as fermented (*e.g.*, sauce, miso, natto) and non-fermented (*e.g.*, oil, milk, tofu, flour) food products. With the discovery of its structural and functional characteristics, soybeans are now used as a raw material in the form of whole beans or partially or fully defatted cakes or meal for the production of various soy-based food products. Soybean flour can also be made from partially or fully de-fatted beans (cake or meal) and used in the production of bakery products, soybean protein isolates and concentrates, extruded and processed foods, etc. (Nawab, 2010).

The sweet potato (*Ipomoea batatas*) is a tuberous-rooted perennial plant belonging to the Convolvulaceae family (Senanayake *et al*., 2013). Sweet potatoes are the fifth and seventh most significant food crops produced in the world and in developing nations, respectively (Parle & Monika, 2015). Compared with other root tuber crops, the sweet potato has the following positive attributes: wide production geography, adaptability to marginal conditions, short production cycle, high nutritional value, and sensory versatility in terms of flesh colours, taste, and texture. Besides, sweet potatoes are declared as first rank (superfood) in nutrition among vegetables due to their high nutritional value and numerous health benefits including anti-cancer, anti-diabetic, etc. (Islam, 2024). Furthermore, sweet potatoes contain magnesium, a crucial mineral, which promotes relaxation, calmness, and nerve health (Parle & Monika, 2015). Sweet potatoes contains β-anthocyanins, phenolics, dietary fibre, ascorbic acid, folic acid, and minerals (Bovell-Benjamin, 2007). Orange flesh sweet potato is especially high in β-carotene (*i.e.*, precursor to vitamin A) which will help to promote the consumption of sweet potatoes among children and pregnant women in Sri Lanka. Furthermore, it contains several antioxidants which may reduce the risks of cancers, and is useful for balancing blood pressure and improving the digestion of consumers (Chintha, 2020). Sweet potatoes are broadly grown as a staple food in many developing countries. In Sri Lanka, sweet potato is a traditional crop grown mainly in the wet and intermediate zones and about 35,000 tonnes are produced annually (Department of Census and Statistics, 2019). Sweet potatoes are traditionally consumed after boiling or cooking and it is processed in various ways for different uses including cleaning and sorting, cutting or slicing, cooking or boiling, mashing or pureeing, drying, freezing, canning or preserving, roasting or frying, baking, fermentation, and industrial processing (Islam, 2024). The sweet potato flour can be produced after the tubers have been cleaned, peeled, cut, dried and ground into a fine powder which can be stored for a longer period and used in various food products including bakery products, cakes, biscuits, breakfast foods, noodles, pasta, sauces, and fermented drinks (Dereje *et al.,* 2020). Sweet potato starch is used in traditional noodles, vermicelli, as a thickener or as a sugar syrup, which is used in many processed food products. Sweet potato starch and sugar are also used to produce fuel alcohol, monosodium glutamate, microbial enzymes, citric acid, lactic acid and other chemicals (Truong *et al*., 2018).

Sweet potato has been produced and consumed by Sri Lankan for ages now, and has a wide export potential (EDB, 2021). Today, most people are in the habit of consuming fast food products because of their busy lifestyles. Hence, sweet potato consumption is declining gradually compared with past years. Therefore, there is a better opportunity to develop a convenient food by using sweet potatoes, to promote the sweet potato among people, especially children. Pasta products have not been developed so far in Sri Lanka using these ingredients, according to the available literature.

In Sri Lanka, wheat flour is one of the most consumable ingredients for making different food especially, bread, roti, noodles, etc. However, due to its high price, consumers are unable to purchase them. Therefore, subsidiary foods must be developed as replacements for products made out of wheat flour. Pasta from composite flour can be taken as a subsidiary for the main meal. The objective of this study was to develop pasta with a composite flour mixture of high nutritional value made from locally available flour types like rice, soy and sweet potato.

MATERIALS AND METHODS

Material collection

Mature tubers of orange flesh sweet potato commonly known as 'Carrot Bathala' were collected from the Kubaloluwa farm in Gampola, Sri Lanka. The other ingredients, soybean and raw white rice were collected from the supermarket. Preparation of raw materials and identification of their physicochemical properties (physical properties and proximate analysis) were done in the Biosystems Technology laboratory, Faculty of Technology, South Eastern University of Sri Lanka. The pasta preparation and sensory evaluation studies were done in the Biosystems Technology Laboratory, Faculty of Technology, University of Sri Jayewardenepura, Sri Lanka.

Preparation of sweet potato

The sweet potato tubers were rinsed with potable water, peeled by hand, and trimmed using a knife to remove any undesirable portions. Then, the tubers were cut into small pieces using a knife (Senanayake *et al*., 2014). Thereafter the pieces were blanched for 5 min using a steamer (Julianti *et al*., 2019). After that, the sweet potato pieces were dried in a forced air drier (Model No: BOV-V230F, China) at 65 °C until the moisture content was reduced up to 12%.

Preparation of soy

Soy flour preparation was done according to the method of Bolarinwa & Oyesiji (2021). First, the soybeans were cleaned properly to remove impurities such as stones and then washed with portable water. Thereafter, the soybeans were dried under sunlight until a moisture content up to 12% was reached. Then, the soybeans were dehulled.

Preparation of rice

First, raw white rice was cleaned thoroughly to remove unwanted particles such as stones and sticks. Then the rice was washed with portable water. Then, the rice was dried under sunlight until a moisture content up to 12% was reached.

Preparation of flour

Dried sweet potato slices, dehulled soybeans, and dried rice were ground with the grain grinder (Model No: GRT-1500B, China) and sieved using a 180 µm sieve to obtain uniform-size flour. Finally, the flour was placed in a clean airtight container.

Formulation of composite flour

The sweet potato flour was kept as the main ingredient and rice flour and soy flour were incorporated for the preparation of composite flour. Composite flour treatments were developed according to the Taguchi experimental design (Mayasti *et al*., 2019). The sweet potato, soy, and rice were composite in the ratio of $\mathbf{T_1}$ 62.5:25:12.5, $\mathbf{T_2}$ 50:30:20, $\mathbf{T_3}$ 41.6:33.3:25, $\mathbf{T_4}$ 60:20:20, $\mathbf{T_5}$ 50:25:25, $\mathbf{T_6}$ 54.5:36.6:9, $\mathbf{T_7}$ 58.3:16.6:25, $\mathbf{T_8}$ 63.6:27.2:9, and $\mathbf{T_9}$ 53.8:30.7:15.3.

Pasta preparation

Pasta for all nine treatments was made using the electric pasta-making machine (Model No: Hamilton Beach 86650, China). Then pasta was dried in the forced air drier (Model No: BOV-V230F, China) at 50 ºC for 12 h. Finally, the samples were sealed and packaged separately using air-tight polypropylene pouches (300 gauge) and stored in a tightly sealed storage cupboard for further analysis. Samples were prepared while maintaining strict hygiene of equipment, utensils, and personnel to prevent any possible microbial contamination.

Preliminary assessment

A preliminary sensory evaluation was done for all the treatments to choose the most preferable treatments. Four samples were selected based on the preliminary sensory evaluation (T_2, T_3, T_4, T_8). A control pasta sample was prepared using wheat flour and used with the selected treatment for further studies.

Proximate analysis

Proximate analysis for moisture, total fat, ash, acid insoluble ash, crude protein, crude fibre, carbohydrates, and calories were calculated and expressed on a dry matter basis for the fresh sweet potato and pasta samples, according to the AOAC (2005) and SLS 420 (2019) standard methods. All the tests were performed in three replicates of each treatment.

Determination of moisture content (%)

The moisture content of fresh sweet potato tubers and pasta was determined by using the oven drying method according to SLS 420 (2019). Five grams of the prepared sample were measured into the previously weighed and dried dish. Then the dish was placed in a drying oven (Model No: 30-1060) at 105 ±2 ºC for 5 h. After 5 h the dish was cooled in a desiccator and the weight was measured. Again, the sample was put in the drying oven at 105 ±2 °C for 30 min. Then again sample was cooled and weighed. The process was continued until the weight remained constant. Finally, moisture content was measured using the following equation.

$$\text{Moisture content (\%)} = \frac{(m_1 - m_2)}{(m_1 - m_0)} \times 100 \quad ...(01)$$

m_0= weight of empty dish (g)
m_1 = weight of the dish + sample before drying (g)
m_2 = weight of the dish + sample after drying (g)

Determination of total ash content (%)

The total ash content was determined by using a muffle furnace (Model No: MF1400-30) according to the method prescribed in SLS 420 (2019). Five grams of the prepared sample were measured into the previously weighed and dried crucible. Then the sample was placed in a muffle furnace. The temperature was set to 600 ±2 °C for 5 h, until grey ash was obtained. Thereafter the sample was cooled inside the desiccator and its weight measured. Again, the sample was placed in a muffle furnace for 30 min. The sample was then cooled and weighed again. The process was continued until constant weight was obtained. Finally, the total ash content was measured using the following equation.

$$\text{Total ash content(\%)} = \frac{(m_3 - m_0)}{(m_2 - m_0)} \times 100 \quad ...(02)$$

m_0= weight of the empty crucible (g)

m_2 = weight of the crucible with dried sample (g)

m_3 = weight of the crucible with ash (g)

Acid insoluble ash (%)

Acid-insoluble ash determination was done according to SLS 420 (2019). Dilute hydrochloric acid (25 mL of a solution of 12.5 mL conc. HCl topped up to 1000 mL with distilled water) was added into the ash-contained dish (beaker). Previously tested ash samples were used for this test. Then the beaker was covered with a watch glass and placed in the water bath at 95 ±2 °C for 10 min. Thereafter dish was allowed to cool. The content was filtered through the Whatman ashless filter paper No. 42 and the filter paper was thoroughly washed with water until the washings are free from acid. After that filter paper with residue was placed in the drying oven (Model: 30-1060) and the temperature was set to 105 ±2 °C for 3 h. After that the dried sample was placed in a muffle furnace (Model: MF1400-30) at 600 ± 2 °C for 1 h. Thereafter the sample was cooled inside the desiccator and the weight was measured. Again, the sample was placed in the muffle furnace for 30 min, and once more cooled and weighed. The process was continued until constant weight was obtained. Finally, the total acid insoluble ash content was measured using the following equation.

$$\text{Acid insoluble ash content (\%)} = \frac{(m_4 - m_0)}{(m_2 - m_0)} \times 100 \quad ...(03)$$

Where,
m_0 = weight of empty dish (g)
m_2 = weight of dish with the dried sample taken for the determination of total ash
m_4 = weight of dish with acid insoluble ash

Crude protein (%)

Triplicate samples of 2 g were placed into a Kjeldahl flask with the catalyst mixture. Distilled water (10 mL) and concentrated sulphuric acid (20 mL) were sequentially added. The mixture was digested at 400 °C for 4 h until it became colourless. The digested solution was allowed to cool, decanted into a volumetric flask, and distilled water was added. An aliquot of 10 mL was pipetted into a Kjeldahl distillation flask and 90 mL of distilled water were added to make up the volume up to 100 mL. Afterward, 20 mL of 40% sodium hydroxide were also added to the mixture, which was distilled into a solution containing 10 mL of 4% boric acid. Three drops of mixed indicators were added to the distillate solution. The distillate, which was light blue in colour, was titrated against 0.1 N hydrochloric acid until the colour changed to pale pink. A blank was also prepared by the same procedure to ensure the accuracy (SLS 420, 2019).

$$\text{Crude protein (\%)} = \frac{V \times N \times M}{Ws \times 10} \times 6.25 \quad ...(04)$$

Where,
N = Concentration of acid
V = Volume of acid
M = Molecular Weight of nitrogen (14.007)
Ws = Sample weight
6.25 = Conversion Factor

Fat content (%)

The fat content was determined using Auto-Soxhlet Fat Extractor (Model: FAT-06A) according to the AOAC

2003.05 (AOAC, 2005). For this, an accurate weight (5 g) of the dried sample was taken and put in an extraction thimble and extracted using petroleum ether in Auto-Soxhlet Fat Extractor (Model: FAT-06A) for 6 h. The solvent was evaporated after extraction and the residue dried and weighed in order to determine the percentage composition of crude fat with reference to the initial weight of sample.

Total carbohydrate content (%)

Total carbohydrates were calculated as the difference between 100 and the sum of the moisture, crude protein, fat (lipid), and ash content (Grizotto & Aguirre, 2011).

$$\text{Carbohydrate content}(\%) = [100 - (\text{moisture} + \text{protein} + \text{lipid} + \text{ash})] \quad ...(05)$$

Crude fibre content (%)

The crude fibre content was determined according to AOAC 978.10 method. Approximately 5 g of dried sample was taken and boiled with 200 mL of 0.2 N sulfuric acid for 30 min. The boiled sample was filtered to drain the acid solution, and residue was washed with hot water to remove the acid residue completely. Further, the residue was boiled with 200 mL of 0.2 N sodium hydroxide. Then, the sample was filtered to drain the sodium hydroxide and washed with hot water to remove sodium hydroxide residue completely. The filtrate was collected into a crucible and placed it in an oven (TLPPL 131, India) at 105 °C for 2 h. After that the crucible was placed in a desiccator for 20 min and weighed. Then after, it was placed inside the muffle furnace (MF 1400 –30, India) at 550 °C for 2 h. Finally, the sample was placed in a desiccator for 20 min and the ash was weighed (AOAC, 2005).

$$\text{Fibre} = \frac{\text{weight of the crucible with fibre} - \text{weight of the crucible with ash}}{\text{weight of the original sample}} \times 100 \quad ...(06)$$

Calorie content (kcal/100 g)

Calorie content was determined using a Bomb Calorimeter (IKA C 6000) according to the method of Hopper *et al*., (2023).

Cooking characteristics

Cooking time (min)

The optimum cooking time was determined according to the method elaborated by Giménez *et al*. (2013). First, 25 g of dried pasta was boiled in 250 mL of distilled water. A small portion (3 to 4 strands) of the pasta was removed from the boiling water at 30-second intervals and squeezed between two glass slides. The cooking time of pasta was considered as the time when the white centre core disappeared.

Water absorption capacity (WAC) (%)

The water absorption capacity was determined according to the method of Giménez *et al.* (2013) with slight modifications. Initially, 25 g dried pasta samples were weighed and cooked in 250 mL boiling water for the determined cooking time. Then the cooked samples were drained for 5 min and the cooked pasta was immediately weighed. Water absorption capacity was expressed as the weight difference before and after cooking pasta. The calculation was done using the following equation.

$$\text{WAC}(\%) = \frac{\text{CPW} - \text{DPW}}{\text{DPW}} \times 100 \quad ...(07)$$

Where,

CPW = cooked pasta weight
DPW = dried pasta weight

Solid in gruel (%)

Solid in gruel determination was done according to SLS 420 (2019). Initially, 25 g dried pasta samples were weighed and cooked in 250 mL boiling water until the cooking time was reached. Then the water was collected by draining cooked pasta and the volume of drained water was noted (V). Then 20 mL of the drained water was transferred to an evaporating dish and dried in a drying oven (Model: 30-1060) at 105 ±2 °C for 2 h. Then the dish was cooled in a desiccator and the weight was measured. Again, the sample was kept in the drying oven at 105 ±2 °C for 30 min, then cooled and weighed as before. The process was repeated until a constant weight was obtained. Finally, the solid in the gruel was measured using the following equation.

$$\text{Total solid in gruel} = \frac{(m_1 - m_0)}{5} \times V \quad ...(08)$$

Where,
m_0 = Empty dish weight,
m_1 = Dish with total solids present in 20 mL of gruel
V = Volume in mL

Textural properties

Hardness, adhesiveness, resilience, stringiness, cohesiveness, springiness, gumminess and chewiness were determined using the CT3 Texture analyzer (Model No: MO8-372-GO318). Each sample were tested three times using a TA-PFS-C probe.

Sensory evaluation

The Organoleptic properties (appearance, taste, hardness, stickiness, and overall acceptability) of cooked pasta were evaluation by an untrained panel of thirty people: seventeen women and thirteen men, ages 20 to 55, frequent consumers of pasta and flour-based food, and with some experience of sensory evaluation. All panellists who performed the sensory evaluation ate breakfast 4 h prior. Panellists rinsed their mouths with bottled water between each sample testing. A nine-point hedonic scale, where 1 denotes a strong dislike and 9 denotes a strong liking, was used to assess each of the five attributes. The sensory evaluation was performed in an dedicated areas of Food Technology laboratory with adequate lighting and natural ventilation (Attanzio *et al*., 2019; Olivera & Salvadori, 2011).

Statistical analysis

All the descriptive analysis (table, graph) was done using Microsoft Excel 2013. Also, all the inferential analyses were done using the SPSS software version 26. One-way ANOVA and Tukey's Post Hoc test at the 0.05 significance level were used for analyzing the proximate and physico-chemical tests. In addition, the one-way Friedman test at a 0.05 significance level was used for analyzing sensory data.

RESULTS AND DISCUSSION

Proximate composition of sweet potato

There were no literature reports on the nutrient content of the sweet potato cultivar Carrot Bathala as it has not been officially released by the Horticultural Crop Research and Development Institute (HORDI) in Sri Lanka. The proximate composition of the Carrot Bathala variety on a dry basis is given in Table 1.

Table 1: Proximate composition of Carrot Bathala

Nutrient	Content
Moisture content (sweet potato tuber)	75.9 %
Moisture content- flour (dry basis)	7.58%
Total Ash content (dry basis)	2.64 %
The acid-insoluble ash (dry basis)	0.01 %
Total fat content (dry basis)	0.33 %
Crude protein (dry basis)	4.2 %
Carbohydrate (dry basis)	85.25 %
Crude fibre (dry basis)	7.96 %
Energy (dry basis)	465.9 kcal/100 g

Proximate composition of pasta samples

Moisture content

According to SLS 420 (2019) the maximum acceptable moisture content is 12%, and the moisture content of all treatments were less than 12%. There were no significant differences between treatments (i.e., pasta made from composite flour). However, the moisture content of wheat pasta (control) had significantly ($p < 0.05$) high moisture content (10.9%). Considering the results of moisture content, the moisture content gradually decreased with the increase of soy flour (Table 2). The studies by Farzana & Mohajan (2015), Aremu *et al.,* (2006) and Bolarinwa & Oyesiji (2021) also confirmed that the moisture content of pasta decreases with the increase of soy flour. Compared to wheat flour, soy flour has a higher percentage of the total dry matter and better emulsifying characteristics (Banureka & Mahendran, 2011). Aremu *et al*. (2006) reported that soybean flour may form a complex with water, resulting in a reduced free water availability for analysis.

Protein content

SLS 420 (2019) states that pasta must have a minimum crude protein content of 9%. All the treatments had protein contents greater than 9% and the results were significantly different among the treatments. The highest value for protein was reported at 18.65% in treatment T_3 (SWP 41.6, Soy 33.3, Rice 25) and the lowest value reported in the control sample (11.55%) (Table 2). Farzana & Mohajan (2015) reported that soybean is a high protein legume and an excellent substitute for cereal proteins with lysine restriction, and therefore the incorporation of soy flour increases the significant protein content of the biscuits. The use of soy flour as an economical protein supplement in biscuits, bread, pasta and other cereal products is therefore justified.

Table 2: Proximate composition of pasta samples

Treatment	Flour formulation (%)	Moisture content (%)	Crude protein (%)	Fat (%)	Crude fibre (%)	Carbohydrate (%)	Ash (%)	Acid insoluble ash (%)	Energy (kcal/100 g)
Control	100 wheat	10.90 ± 0.08[a]	11.55 ± 0.07[e]	1.32 ± 0.29[b]	0.42 ± 0.20[b]	74.31 ± 0.33[a]	1.91 ± 0.05[c]	0.05 ± 0.02[a]	468.53 ± 1.51[c]
T_2	SWP -50 Soy - 30 Rice -20	8.12 ± 0.06[b]	14.57 ± 0.05[c]	2.19 ± 0.37[a]	2.54 ± 0.17[a]	71.75 ± 0.42[b]	3.35 ± 0.03[ab]	0.01 ± 0[b]	510.30 ± 2.55[a]
T_3	SWP- 41.6 Soy -33.3 Rice -25	8.03 ± 0.05[b]	18.65 ± 0.14[a]	2.31 ± 0.27[a]	2.39 ± 0.30[a]	67.62 ± 0.28[c]	3.38 ± 0.03[a]	0.02 ± 0.01[ab]	491.30 ± 1.10[b]
T_4	SWP-60 Soy-20 Rice- 20	8.1 ± 0.04[b]	12.67 ± 0.13[d]	1.96 ± 0.02[ab]	2.32 ± 0.05[a]	74.0 ± 0.13[a]	3.26 ± 0.02[b]	0.01 ± 0.01[b]	490.13 ± 2.94[b]
T_8	SWP– 63.6 Soy-27.2 Rice-9	8.10 ± 0.03[b]	15.59 ± 0.12[b]	1.99 ± 0.01[a]	2.69 ± 0.04[a]	71.11 ± 0.04[b]	3.31 ± 0.06[ab]	0.01 ± 0.01[b]	469.6 ± 2.49[c]

Mean ± standard deviation [a,b,c,d,e] superscript significantly different at p = 0.05 column wise

Fat content

There is a significant difference in fat values between the control and the other treatments except T_4 (SWP 60, soy 20, rice 20). However, there is no significant difference between the treatments for composite flour pasta. Considering the results for fat content, higher values were confirmed for the composite flour mixtures containing more soy flour. Oluwamukomi *et al*. (2011) state that the addition of 10% soy flour showed a significant increase in fat content of the product concerned. Soybean is one of the protein-rich oil seeds, high in polyunsaturated fats, and containing two essential fatty acids, namely, linoleic acid and α-linolenic acid. Soy flour has a significantly higher fat content than wheat flour (Banureka & Mahendran, 2011).

Fibre content

The results of this study showed a significant difference between controls and other treatments and there was no significant difference between the treatments. The highest and lowest values were recorded in T_8 and control, respectively by 2.69 and 0.42 percent respectively. Progressive increase of fibre content was observed by increasing the proportion of sweet potato flour in the composite flour mixture. The findings of this study were consistent with the findings of Baah *et al*., (2022). Sweet potato is a low glycaemic food and a high source of dietary fibre (17%) reported by Krishnan *et al*. (2012).

Carbohydrate content

In line with the outcomes of this study, there was no significant difference between the control and the treatment T_4. The treatments T_2 and T_8 are nearly the same. However, there is a significant difference between treatment T_3 and other treatments. The lowest carbohydrate and the highest protein values were in T_3, while the highest carbohydrate content was shown in the control, together with the lowest protein content (Table 2). Increases in soy flour has resulted in the reduction of the carbohydrate content of the composite flour blends, aligning with the finding of Bolarinwa & Oyesiji (2021). Omeire *et al.* (2014) also reported a decrease in the carbohydrate content of noodles from a mixture of wheat, achi, and soya flour, with a rise in the percentage of soya flour in the mixture.

Ash content

SLS 420 (2019) states that the maximum amount of ash in wheat flour is 1%, however, if pasta is made with composite flours and mineral-fortified products, the total amount of ash on a dry basis cannot be more than 4%. In this case, wheat pasta (control) was not within the limit, and the ash content of composite flour products, did not exceed the standard limit (Table 2). The ash content of all the treatments was significantly higher than that of the control treatment. There was also a significant difference between T_3 (SWP 41.6, Soy 33.3, Rice 25) and T_4 (SWP 60, Soy 20, Rice 20) but no significant difference between the other treatments (T_2 and T_8). The ash content of all samples of sweet potato flour was significantly high than that of wheat flour, due to the high mineral content of the root and tubers (Yadav *et al*., 2014).

Acid-insoluble ash

The acid-insoluble ash content of the treatments was below the limit as per SLS 420 (2019). However, there is a significant difference between the control treatment and other treatments except for T_3 (Table 2). Other treatments showed no significant differences among them. It was reported that the acid-insoluble ash content is likely to be higher because of the possibility of chipping and percolating of the fine stone particles into the atta (whole wheat) during the grinding process (Inamdar *et al*., 2015).

Cooking behaviours of cooked pasta

Table 3: Cooking characteristics of pasta samples

Treatment	Flour Formulation (%)	Cooking time (Min)	Water absorption capacity (%)	Solid in gruel (%)
Control	100 wheat	13.1 ± 0.2^a	113.87 ± 3.70^a	8.50 ± 0.19^b
$\mathbf{T_2}$	SWP -50 Soy - 30 Rice -20	7.1 ± 0.2^b	91.35 ± 2.89^b	11.25 ± 0.18^a
$\mathbf{T_3}$	SWP- 41.6 Soy -33.3 Rice -25	7.0 ± 0^b	93.10 ± 1.67^b	11.12 ± 0.04^a
$\mathbf{T_4}$	SWP-60 Soy-20 Rice- 20	7.0 ± 0^b	92.62 ± 2.75^b	11.10 ± 0.06^a
$\mathbf{T_8}$	SWP– 63.6 Soy-27.2 Rice-9	7.1 ± 0.2^b	94.20 ± 3.02^b	11.20 ± 0.11^a

Mean ± standard deviation ^{a,b} superscript significantly different at $p = 0.05$ column wise

Cooking time

The cooking time of the control sample was significantly ($p < 0.05$) longer (13 min) than that of the composite flour pasta (7 min) as detailed in Table 3, possibly because the dietary fibre constituent in orange-fleshed sweet potato flour tends to disrupt the physical structure of the pasta, reducing the cooking time and limiting its ability to expand compared to commercial pasta (Wang *et al.,* 2019).

Water absorption capacity

Significantly higher water absorption capacity ($p < 0.05$) was indicated in control sample (113) than in composite flour pasta (Table 3). Petitot *et al.* (2010) reported durum wheat proteins are mainly composed of glutenin and gliadins that form intra and intermolecular disulphide bonds during processing. This leads to the development of a three-dimensional gluten network responsible for the unique textural properties of pasta.

Solid in gruel content

Based on the results, the solid in gruel content increased significantly ($p < 0.05$) in composite pasta treatments than in the control sample. According to the finding of Rayas-Duarte *et al.* (1996) the non-gluten components diluted the strength of the gluten and lead to a weakened structure of spaghetti. Hence, the leaching of more solid substances from the spaghetti into boiling water increased the solid gruel content. Furthermore, pasta samples composited with orange flesh sweet potato flour may have a higher cooking loss due to the fibre content of the orange flesh sweet potato flour (Baah *et al*., 2022; Foschia *et al.*, 2015).

Textural characters of pasta

Table 4: Textural characters of cooked pasta

Treatment	Flour formulation (%)	Hardness (g)	Adhesiveness (mJ)	Resilience	Cohesiveness	Springiness (mm)	Gumminess (g)	Chewiness (mJ)
Control	100 wheat	114.16 ± 23.62^{b}	0 ± 0^{a}	0.49 ± 0.04^{ab}	1.06 ± 0.19^{a}	2.35 ± 0.25^{a}	117.00 ± 26.28^{b}	2.73 ± 0.83^{b}
T_2	SWP -50 Soy - 30 Rice -20	327.5 ± 50.18^{a}	0 ± 0^{a}	0.41 ±0.03^{b}	0.94 ± 0.10^{a}	2.27 ± 0.14^{a}	243.30 ± 15.04^{a}	6.96 ± 2.05^{ab}
T_3	SWP- 41.6 Soy -33.3 Rice -25	328.33 ± 62.26^{a}	0.17 ± 0.29^{a}	0.58 ± 0.02^{a}	0.92 ± 0.22^{a}	2.67 ± 0.54^{a}	311.00 ± 73.08^{a}	12.10 ± 7.21^{a}
T_4	SWP-60 Soy-20 Rice- 20	256.66 ± 12.33^{a}	0 ± 0^{a}	0.46 ± 0.05^{ab}	0.96 ± 0.12^{a}	2.47 ± 0.66^{a}	226.66 ± 42.19^{a}	4.46 ± 1.22^{ab}
T_8	SWP– 63.6 Soy-27.2 Rice-9	245.83 ± 62.06^{a}	0 ± 0^{a}	0.40 ± 0.08^{b}	0.95 ± 0.02^{a}	2.40 ± 0.45^{a}	205.66 ± 13.20^{ab}	4.20 ± 0.20^{ab}

Mean ± standard deviation ^{a,b} superscript significantly different at $p = 0.05$ in column wise

Textural characteristics of the composite flour pasta and control sample are given in Table 4. Based on the results, there is no significant difference in adhesiveness, cohesiveness, or springiness between the treatment and control. However, the hardness of cooked pasta significantly differed from the control treatment. The highest value of hardness was found in the T3 sample (328.33 g). According to the study of Jiao *et al.* (2020), the hardness of rice flour was influenced by its amylose content and retrogradation rate . Furthermore, Kraithong & Rawdkuen (2021) explored how high amylose and protein contents promote higher values of hardness, cohesiveness, springiness, and chewiness. Except for treatment T_8 the gumminess of cooked pasta significantly differed from the control treatment. The results showed that gumminess and chewiness of composite pasta decreased with increasing sweet potato flour content. Santiago *et al*. (2016) revealed that the hardness, gumminess and chewiness of the purple sweet potato flour pasta was significantly lower than that of the control (wheat pasta). Also, a higher value of chewiness was recorded in the T3 sample with value of 12.1 mJ. The studies by Xiao *et al*. (2022) and Fari *et al*. (2011) reported that the amount of grain amylose content is an important factor in determining the quality of rice noodles, and higher hardness and chewiness of cooked rice noodles was generally associated with higher amylose content in the rice grain.

Sensory evaluation

Table 5: Sensory evaluation of pasta samples

Treatment	Formulation	Appearance	Taste	Hardness	Stickiness	Overall acceptability
Control	100 wheat	6.46 ± 1.67^{ab}	5.40 ± 1.83^{b}	6.03 ± 1.80^{ab}	5.57 ± 2.04^{b}	5.67 ± 1.80^{b}
T_2	SWP -50 Soy - 30 Rice -20	7.13 ± 1.07^{a}	7.36 ± 1.18^{a}	7.07 ± 0.98^{a}	6.83 ± 1.08^{a}	7.47 ± 1.10^{a}
T_3	SWP- 41.6 Soy -33.3 Rice -25	5.53± 1.79^{b}	6.20 ± 1.73^{b}	6.10 ± 1.39^{b}	5.93 ± 1.31^{b}	6.23 ± 1.54^{b}
T_4	SWP-60 Soy-20 Rice- 20	7.13 ± 1.19^{a}	6.43 ± 1.92^{b}	6.47 ± 1.45^{ab}	6.30 ± 1.66^{ab}	6.57 ± 1.40^{b}
T_8	SWP– 63.6 Soy-27.2 Rice-9	6.60 ±1.30^{a}	6.10 ± 1.42^{b}	6.20 ± 1.47^{ab}	6.27 ±1 .11^{ab}	5.93 ± 1.36^{b}

Mean ± standard deviation ^{a,b} superscript significantly different at p = 0.05 column wise

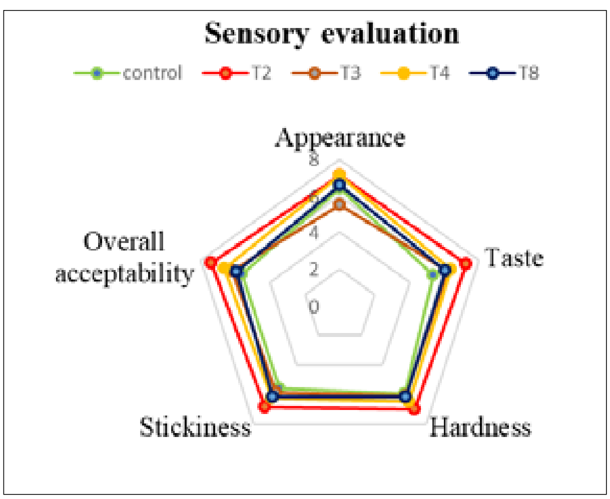

Figure 1: Spider diagram for sensory evaluation of pasta samples

The sensory results showed that the treatment T_2 and T_4 had the greatest appearance gains (Figure 1). Additionally, T_3 had the lowest appearance. According to the taste results, treatment T_2 was preferred by the majority of panellists, while control showed the least amount of preference. Most panellists were interested in treatment T_2 when comparing the results of hardness and had the most appropriate hardness of pasta according to the participant's preferences. For the stickiness, most participants preferred treatment T_2 with least preference for the control. Considering all the attributes, the highest value for overall acceptability was obtained for Treatment T_2. The least acceptability was obtained in the control sample. Overall, most of the panellists preferred the Treatment T_2 composite flour blend (sweet potato 50, soy 30, rice 20) with the control (wheat only) gaining least preference (Table 5).

CONCLUSION

A process flow and quality assessment of pasta made from a composite flour of sweet potato, soy, and rice were developed. The formulation T_2 (sweet potato 50%, soy 30%, and rice 20%) has been shown to have better results in all sensory characteristics, nutritional composition and acceptable textural properties. However, the control sample obtained the best results in terms of cooking behaviour. Low cooking behaviour was observed in all composite flour pasta treatments compared to wheat pasta with the cooking time of 7 min, water absorption between 91 – 94%, and solid in gruel (cooking loss) with 11%. The highest levels of hardness, chewiness, and gumminess are observed in pasta made from composite flour. In addition, pasta made from composite flour fulfils the requirement of the SLS 420 (2019) pasta product specification except for solid in gruel. In addition, the pasta made from composite flour had a higher nutritional value and better sensory characteristics. Therefore, the T_2 (sweet potato - 50, soy - 30, rice - 20) formulation was selected as the best treatment.

REFERENCES

AOAC (2005). Official Method 2003.05. *Official Methods of Analysis*. 18th ed. Gaithersburg, MD: Association of Official Analytical Chemists.

AOAC (2005). Official Method 978.10. *Official Methods of Analysis*. 18th ed. Gaithersburg, MD: Association of Official Analytical Chemists.

Aremu, M.O., Olonisakin, A., Bako, D.A., & Madu. P.C., (2006). Compositional Studies and Physicochemical Characteristics of Cashew Nut (*Anarcadium occidentale*) Flour." *Pakistan Journal of Nutrition 5*(4), 328–333.

Attanzio, A., Diana, P., Barraja, P., Carbone, A., Spanò, V., Parrino, B., Cascioferro, S. M., Allegra, M., Cirrincione, G., Tesoriere, L., & Montalbano, A. (2019). Quality, Functional & Sensory Evaluation of Pasta Fortified with Extracts from Opuntia Ficus-Indica Cladodes. *Journal of the Science of Food and Agriculture 99*(9), 4242–4247.

Baah, F. D, Oduro, I., & Ellis, W.O. (2005). Evaluation of the Suitability of Cassava and Sweet potato Flours for Pasta Production. *Journal of Science and Technology (Ghana) 25*(1).

Bolarinwa, O, I. & Oyesiji, O.O. (2021). Gluten Free Rice-Soy Pasta: Proximate Composition, Textural Properties & Sensory Attributes. *Heliyon 7*(1), e06052. https://doi.org/10.1016/j.heliyon.2021.e06052.

Bor, S.L. (1999) Rice Products (In Asian Foods: Science and Technology (1st ed.). (Eds. Ang, C.Y.W., Liu, K., & Huang, Y.-W.). CRC Press. https://doi.org/10.1201/9781482278798

Bovell-Benjamin, A. C. (2007). Sweet Potato: A Review of Its Past, Present, & Future Role in Human Nutrition. *Advances in Food & Nutrition Research 52*(06), 1–59.

EDB of Sri Lanka (2021, December, 09).Super food from Sri Lanka [Blog post]. Retrieved from https://www.srilankabusiness.com/blog/superfood-from-sri-lanka.html

Dereje, B., Girma, A., Mamo, D., & Chalchisa, T. (2020). Functional properties of sweet potato flour and its role in product development: a review. *International Journal of Food Properties*, *23*(1), 1639–1662. https://doi.org/10.1080/10942912.2020.1818776

Fari, M.J.M., Rajapaksa, D., & Ranaweera, K.K.D.S. (2011). Quality Characteristics of Noodles Made from Selected Varieties of Sri Lankan Rice with Different Physicochemical Characteristics. *Journal of the National Science Foundation of Sri Lanka 39*(1), 53–60.

Farzana, T., & Suman M. (2015). Effect of Incorporation of Soy Flour to Wheat Flour on Nutritional & Sensory Quality of Biscuits Fortified with Mushroom. *Food Science & Nutrition 3*(5), 363–369.

Foschia, M., Peressini, D., Sensidoni, A., Brennan, M.A., & Brennan, C.S. (2015). How Combinations of Dietary Fibres Can Affect Physicochemical Characteristics of Pasta. *Starch/Staerke 66*(11–12), 41–46. http://dx.doi.org/10.1016/j.lwt.2014.11.010.

Giménez, M. A. González, R.J., Wagner, J., Torres, R., Lobo, M.O., & Samman, N.C. (2013). Effect of Extrusion Conditions on Physicochemical & Sensorial Properties of Corn-Broad Beans (*Vicia Faba*) Spaghetti Type Pasta. *Food Chemistry 136*(2), 538–545.

Grizotto, R.K., & Aguirre, J.M. (2011). Study of the Flash Drying of the Residue from Soymilk Processing - Okara. *Food Science and Technology (Campinas) 31*(3), 645–653.

Hopper, Z., Desbrow, B., Roberts, S., & Irwin, C. (2023). Preparation procedures of food and beverage samples for oxygen bomb calorimetry: A scoping review and reporting checklist. *Journal of Food and Drug Analysis 31*(2), 232-243.

Inamdar, A. A., Suresh, D. S., & Prabhasankar, P. (2015). Chapati Making Quality of Whole Wheat Flour (Atta) Obtained by Various Processing Techniques. *Journal of Food Processing & Preservation 39*(6), 3032–3039.

Islam, S. (2024). Sweet potatoes [*Ipomoea batatas* (L.) lam]: the super food of the Next Century? An intensive review on their potential as a sustainable and versatile food source for future generations. *CyTA - Journal of Food*, *22*(1). https://doi.org/10.1080/19476337.2024.2397553

Jiao, A., Yang, Y., Li, Y., Chen, Y., Xu, X., & Jin, Z. (2020). Structural Properties of Rice Flour as Affected by the Addition of Pea Starch & Its Effects on Textural Properties of Extruded Rice Noodles. *.International Journal of Food Properties 23*(1), 809–819. https://doi.org/10.1080/10942912.2020.1761830.

Jooyandeh, H. (2011). Soy Products as Healthy & Functional Foods. *Middle-East Journal of Scientific Research 7*(1), 71–80.

Kraithong, S., & Rawdkuen, S. (2021). Quality Attributes and Cooking Properties of Commercial Thai Rice Noodles. *PeerJ* 9.

Krishnan, J. G., Menon, R., Padmaja, G., Sajeev, M.S., & Moorthy, S.N. (2012). Evaluation of Nutritional and Physico-Mechanical Characteristics of Dietary Fiber-Enriched Sweet Potato Pasta. *European Food Research and Technology 234*(3), 467–476.

Baah, R.O., Duodu, K.G., & Emmambux, M.N. (2022). Cooking Quality, Nutritional and Antioxidant Properties of Gluten-Free Maize – Orange-Fleshed Sweet Potato Pasta Produced by Extrusion. *Lwt 6*(1), 383–401.

Mayasti, N.K.I., Ushada, M., & Ainuri, M. (2019). Optimization of Gluten Free Spaghetti Products from Local Food with the Taguchi Method Approach. *IOP Conference Series: Earth and Environmental Science 251*(1), 1-10.

More, K D, Ghodke, S.V., & Chavan. D.H. (2013). Preparation of Gluten Free Rice Flour Biscuits. *Food Sci. Res. J*

4(2),111–115. http://www.researchjournal.co.in/upload/assignments/4_111-115.pdf.

Nawab, A. (2010). Soybean Processing and Utilization. In The Soybean Botany, Production and Uses (Ed Guriqbal Singh) CAB Interantional.

Nilusha, R. A.T., Jayasinghe, J. M.J.K., Perera, O. D.A.N., & Perera, P.I.P. (2019). Development of Pasta Products with Nonconventional Ingredients and Their Effect on Selected Quality Characteristics: A Brief Overview. *International Journal of Food Science* 2019.

Olivera, D.F., & Salvadori, V.O. (2011). Instrumental and sensory evaluation of cooked pasta during frozen storage. *International Journal of Food Science and Technology*, *46*, 1445–1454

Oluwamukomi, M. O., Oluwalana, I. B. & Akinbowale, O. F. (2011). Physicochemical and Sensory Properties of Wheat-Cassava Composite Biscuit Enriched with Soy Flour. *African Journal of Food Science 5*(2), 50–56.

Omeire, G.C., Umeji, O.F. & Obasi, N.E. (2014). Acceptability of Noodles Produced from Blends of Wheat, Acha and Soybean Composite Flours. *Nigerian Food Journal 32*(1), 31–37. http://dx.doi.org/10.1016/S0189-7241(15)30093-X.

Parle, M. & Monika. (2015). Sweet Potato As a Super-Food. *International Journal of Research in Ayurveda and Pharmacy 6*(4), 557–562.

Petitot, M., Boyer, L., Minier, C., & Micard, V. (2010). Fortification of Pasta with Split Pea and Faba Bean Flours: Pasta Processing and Quality Evaluation. *Food Research International 43*(2), 634–641. http://dx.doi.org/10.1016/j.foodres.2009.07.020.

Rayas-Duarte, P., Mock, C.M., & Satterlee, L.D. (1996). Quality of Spaghetti Containing Buckwheat, Amaranth, and Lupin Flours. *Cereal Chemistry 73*(3), 381–387.

Ronie, M.E. & Hasmadi, M. (2022). Factors affecting the properties of rice flour: a review. *Food Research 6*(6), 1 - 12

Senanayake, S.A., Gunaratne, A., Ranaweera, K.K.D.S., & Bamunuarachchi, A. (2013). Physico - Chemical Properties of Five Cultivars of Sweet Potato (*Ipomea Batatas* Lam (L)) Root Tubers Grown in Sri Lanka. *Tropical Agriculture 90*(2), 87–96.

Senanayake, S.A., Ranaweera, K.K.D.S., Bamunuarachchi, A., & Gunaratne, A. (2014). Comparative Analysis of Trypsin Inhibitor Levels in Sweet Potato Cultivars in Sri Lanka. *Journal of the National Science Foundation of Sri Lanka 42*(1), 63–69.

SLS 420 (2019). Specification of Pasta Products 2nd ed. Colombo: Sri Lanka Standards Institution.

Truong, V.D., Avula, R.Y., Pecota, K.V. & Yencho, G.C. (2018). Sweet potato Production, Processing, and Nutritional Quality. In Handbook of Vegetables and Vegetable Processing (eds M. Siddiq and M.A. Uebersax). https://doi.org/10.1002/9781119098935.ch35

Xiao, Z., Liao, C., Hu, Y., Zhang, K. Chen, J., Cao, F., Fang, S. & Huang, M, (2022). Quality Characteristics of Noodles Processed from Rice Grains of the Ratoon Crop. *Agronomy 12*(11), 1-8.

Yadav, B. S., Yadav, R.B., Kumari, M. & Khatkar, B.S. (2014). Studies on Suitability of Wheat Flour Blends with Sweet Potato, Colocasia and Water Chestnut Flours for Noodle Making. *Lwt 57*(1), 352–358. http://dx.doi.org/10.1016/j.lwt.2013.12.042.

J.Natn.Sci.Foundation Sri Lanka 2025 53 (3): 245 - 258
DOI: http://dx.doi.org/10.4038/jnsfsr.v53i3.12649

RESEARCH ARTICLE

Biological Imaging

Visualizing changes in internal layers of Chinese chives leaf under short-term ozone exposure with biospeckle optical coherence tomography

LKT Srimal[1,5*], UM Rajagopalan[2], H Kadono[3] and T Yonekura[4]
[1] *Department of the Mechanical and Manufacturing Engineering, Faculty of Engineering, University of Ruhuna, Sri Lanka.*
[2] *Department of Mechanical Engineering, Shibaura Institute of Technology, 3-7-5 Toyosu, Koto City, Tokyo, 135-8548, Japan.*
[3] *Graduate School of Science and Engineering, Saitama University, 255 Shimo-okubo, Sakura-ku, Saitama-shi, Saitama, 338-8570, Japan.*
[4] *Center for Environmental Science in Saitama, Kazo, Saitama 347-0115, Japan.*
[5] *Department of Mechanical Engineering, Faculty of Engineering, South Eastern University of Sri Lanka, Oluvil, Sri Lanka.*

Submitted: 24 April 2025; Revised: 22 August 2025; Accepted: 27 August 2025

Abstract: Ozone (O_3) stress can cause physiological changes as well as changes in the growth patterns of plants. Conventional techniques for studying these changes in plants require destruction of the sample and a subsequent analysis, thus the plant's responses to external stress are inferred indirectly. In this paper, we show that a biospeckle optical coherence tomography (bOCT) biospeckle imaging can be used to monitor the response of Chinese chives leaves to O_3 stress. A Fourier-domain OCT operating at a wavelength of 836 nm with a depth of resolution of 6 µm was used. The bOCT biospeckle image was obtained by calculating the standard deviation of the OCT signal along the time axis at each point of the selected portion of the cross-sectional image from the successively acquired OCT images. In the bOCT biospeckle images, the internal layer structure could be clearly visualized, especially the mesophyll cells with high contrast in comparison to the structural OCT image. In addition, an analysis of the average autocorrelation functions of the biospeckle signals revealed that the correlation length decreased in the mesophyll layer during O_3 exposure, possibly indicating the increase in movements of internal structures within the leaf. Our results suggest that biospeckle imaging can be a suitable technique for fast and non-destructive monitoring of environmental stresses on plants, in contrast to conventional techniques that require a few days' to a few weeks' time, with destruction followed by subsequent analysis, thus paving the way for significant time saving.

Keywords: Biological activities, biospeckles, correlation length, biospeckle optical coherence tomography (bOCT), ozone, temporal characteristics.

INTRODUCTION

Surface (tropospheric) ozone (O_3) is a secondary air pollutant, generated by a series of reactions involving oxides of nitrogen (NOx) and volatile organic compounds (VOCs) in the presence of UV radiation from sunlight (Darrall, 1989; Ashmore, 2005; Ainsworth, 2008; Kumar *et al.*, 2021; Santiago *et al.*, 2022; Yoshikado, 2023). Its disastrous effect is spreading over an enormous land area of world, especially in industrialized countries such as China, India, and even in Japan (Kobayashi *et al.*, 1995; Kobayashi & Okada, 1995; Beig *et al.*, 2007; Wang *et al.*, 2007; Lee & Goto, 2022; Santiago *et al.*, 2022; Wang *et al.*, 2022; Wei *et al.*, 2022, Yoshikado, 2023). The O_3 contaminated environment causes a wide range of effects including visible leaf injury, and growth and yield reductions in both agricultural crops and forest trees (Kobayashi & Okada, 1995; Wang *et al.*, 2007; Jiménez-Montenegro *et al.*, 2021; Feng *et al.*, 2021; Holder & Hayes, 2022; Panebianco *et al.*, 2022). Conventional techniques such as microscopic observation, and chemical analysis are commonly performed to monitor the effect of O_3 on plants for their structural changes (Calatayud *et al.*, 2003). However, these conventional techniques cannot be performed non-destructively in real-time and *in vivo*. Moreover, it is important to observe the internal structure of a plant leaf when it is under an environmental stress.

* Corresponding author (srimal@mme.ruh.ac.lk; https://orcid.org/0000-0002-3285-3214)

Recently, a non-invasive interferometric technique, statistical interferometry, that is capable of measuring fast and accurate measurement of growth changes under environmental stresses such as O_3 has been demonstrated *in vivo* (Rathnayake *et al.*, 2008; Kobayashi & Kadono, 2010; Thilakarathne *et al.*, 2014a, 2014b; DeSilva *et al.*, 2017). However, this measurement is limited to a small area of a sample. Here we consider an optical technique called optical coherence tomography (OCT) that has the potential for making a volumetric measurement at high speed and at micrometer resolutions (Huang *et al.*, 1991; Fercher, 1996; Fujimoto, 2003; Regar *et al.*, 2007; Srimal, 2015; Ge *et al.*, 2021; Saleah *et al.*, 2021; Saleah *et al.*, 2022; Saleah *et al.*, 2023).

The OCT technique is based on interferometric detection of a low coherent light backscattered from a sample and can provide non-contact two or three dimensional *in vivo* tomographic images of internal tissue structure. Since depth resolution of OCT is limited by the coherence length of the light source, a relatively high resolution of the order of a few micrometers can be achieved (Fujimoto & Drexler, 2008; Lee *et al.*, 2018; Zheng *et al.*, 2021; Bouma *et al.*, 2022). OCT is being widely employed for the visualization of the internal structure of tissues (Wijesinghe *et al.*, 2016a; Ravichandran *et al.*, 2017). Many pathological processes, such as dysplasia and cancer, alter the layered structure of healthy tissue and these changes can be detected by OCT (Steiner *et al.*, 2003; Gladkova *et al.*, 2008; Fercher, 2010; Lee *et al.*, 2018; Rajagopalan *et al.*, 2020; Li *et al.*, 2021b). On the other hand, it is widely used in the field of ophthalmology (Wijesinghe *et al.*, 2016b; Everett *et al.*, 2021; Wei & Gu, 2021; Micieli *et al.*, 2021; Drexler *et al.*, 2001; Wojtkowski *et al.*, 2002; Pircher *et al.*, 2011; Srinivasan *et al.*, 2009). Due to its high resolution, OCT technique for imaging plants (Hettinger *et al.*, 2000; Reeves *et al.*, 2002; Boccara *et al.*, 2007; Srimal, 2015; de Wit *et al.*, 2020; Beiu *et al.*, 2022; Li *et al.*, 2022) has been getting attention. Non-invasive visual inspection of plant leaf *in vivo* may be useful for evaluating the physiological state of plants under the influence of environmental stresses such as O_3, acid mine drainage (Li *et al.*, 2021a), effect of nanoparticles (De Silva *et al.*, 2023a), effect of heavy metals (De Silva *et al.*, 2021), and the effect of micro particles of plastics (De Silva *et al.*, 2022, 2023b).

The potential of OCT in monitoring such biological activities in human and animal organelles has been demonstrated, in the visual cortex of animal brains (Maheswari *et al.*, 2002, 2003; Khateeb *et al.*, 2022) and rat somatosensory cortex (Chen *et al.*, 2009; Hope *et al.*, 2021) and retina (Moayed *et al.*, 2011; Kashani *et al.*, 2021). We propose to monitor physiological changes in plants under environmental stress (O_3) by OCT (Srimal *et al.*, 2013, 2015; Lichtenegger *et al.*, 2020)

In OCT images, speckles are considered as a noise and are usually temporally averaged (Szkulmowski *et al.*, 2012; Silva *et al.*, 2022). In this study, we focused on the temporal characteristics of speckles, as those could indicate the dynamic activities within the tissues, also called biospeckles (Asakura, 1996; Tang *et al.*, 2021a, 2021b; Aizu &). When coherent laser light illuminates a sample under investigation, the backscattered light randomly interferes, and a speckle pattern is generated at a certain observation plane. If the investigating sample and the scatterers inside the sample are not moving, then the speckle pattern is also stationary. However, when the sample or the scatterers are moving as in biological tissues, the speckle pattern changes randomly resulting in biospeckles. In plants, such dynamic processes could be attributed to factors such as cytoplasmic streaming, organelle movement, cell growth and division, and biochemical reactions (Mogre *et al.*, 2020; Mathur, 2020; Braga *et al.*, 2009). Thus, the biospeckles can reflect the activities of biological tissue (Kurenda *et al.*, 2012; Ansari & Nirala, 2013; Zdunek *et al.*, 2014; Rajagopalan *et al.*, 2020; Li *et al.*, 2021a).

Especially, in agriculture, the analysis of seeds (Braga *et al.*, 2003; Li *et al.*, 2021a), the identification of plant diseases (Ravichandran *et al.*, 2016), leaf quality assessment (Wijesinghe *et al.*, 2016a, 2017b), detection of germination rate (Wijesinghe *et al.*, 2017a), the analysis of fungi (Braga Jr *et al.*, 2005; Singh *et al.*, 2021), monitoring of maturation and diseases in fruits (Pajuelo *et al.*, 2003; Wijesinghe *et al.*, 2018), observation of root growth (Braga *et al.*, 2009; De Silva *et al.*, 2023a, 2023b), and evaluation of animal semen (Carvalho *et al.*, 2009) were performed. In medicine, we can find applications in the study of the brain, skin and blood flow (Fujii *et al.*, 1985; Li *et al.*, 2006). A few reports exist on the application of OCT speckles in the observation of biological tissues (Mariampillai *et al.*, 2008, 2010; Baum *et al.*, 2020).

In this study, we propose a Biospeckle Optical Coherence Tomography (bOCT) based on biospeckle to study the effect of environmental stresses on plants in a short period of time which is not possible with other conventional methods (Srimal *et al.*, 2014; Srimal, 2015). Here, we examined the immediate response of leaves of *Allium tuberosom* commonly known as Chinese chives to short-term exposure of O_3, by analyzing the bOCT biospeckle signals coming from various depths. Mesophyll cell layers, and the immediate responses are better visualized using the bOCT images rather traditional OCT images.

MATERIALS AND METHODS

Optical system

A schematic of our spectral domain OCT (SD-OCT) system is shown in Figure 1. The light source is a super-luminescent diode (SLD) centred at wavelength 836.1 nm and having a bandwidth of 55.2 nm. A 99:1 optical fiber coupler was used to split the light into the sample and reference arms of the fiber-optic interferometer. Light reflected from the sample was combined with the light reflected from the reference mirror M1. The axial and lateral resolutions of the OCT system were estimated to be 6 μm and 22 μm, respectively. Identical lenses, L3 and L4, were placed in the sample and reference arms to cancel dispersion mismatch between the two arms. Collimating the output beam from the optical fiber of the circulator using lens, L5, the spectral interference signal was obtained by using grating, lens L6, and line-scan camera. We used line scan CCD camera (L104k-2k, BASLER, Germany) with 2048 pixels.

(a)
(b)

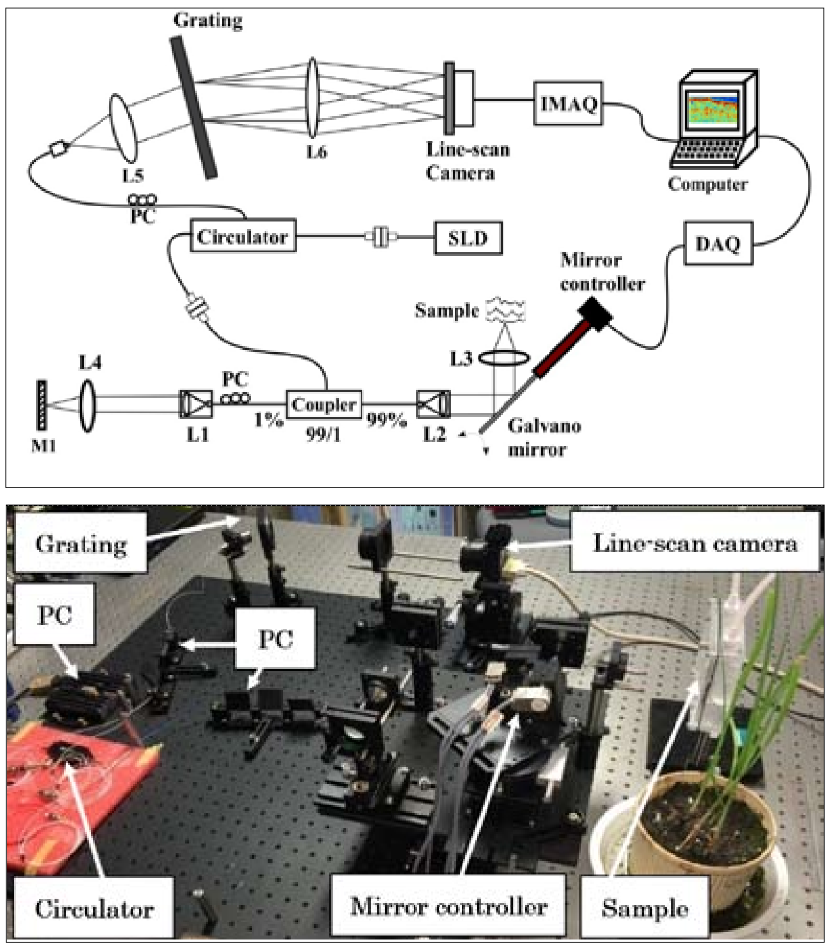

Figure 1: (a) A sketch, and (b) Photograph of, experimental setup of spectral domain optical coherence tomography system. SLD: super luminescent diode, L1~L6: lenses, M1: mirror, PC: polarization controller, DAQ: data acquisition device, IMAQ: image grabber.

A software application (using LabVIEW 2011, National Instruments, USA) was developed to realize the OCT system utilizing the biospeckle signals from a target area of the sample. Driving voltages for galvano mirrors were applied through a D/A converter of the data acquisition device (DAQ, PCIe-1429, National Instruments, USA) to laterally scan the beam across the sample surface. The imaging data from the line scan camera was acquired by an image grabber (IMAQ, PCIe-6351, National Instruments, USA).

Autocorrelation function of the biospeckle signal

While the scanning mechanism was being stopped at a lateral position of interest, the spectral interference signals were acquired with a sampling frequency of 25,000 lines/sec for1.2 seconds. The acquired spectral interference signal *I*(λ, *t*) from the camera at time, *t*, was first converted into the signal *I*(*k*, *t*) in wave number, *k*, space from wavelength, λ, space as given by,

$$I(k,t) = I(2\pi/\lambda, t). \quad ...(1)$$

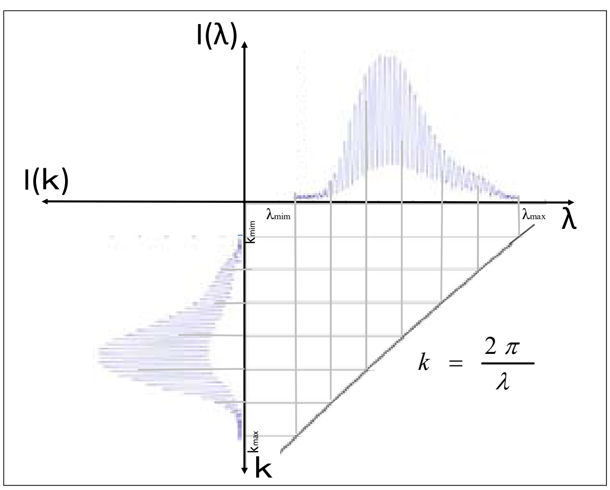

Figure 2: Transformation of signal in wavelength (λ) space to wave number (k) space (rescaling).

Next, the rescaled signal of $I(k,t)$ was Fourier transformed in order to obtain the depth resolved reflectivity profile *r(d,t)* of the sample along the sample beam as,

$$r(d,t) = \int_{-\infty}^{\infty} I(k,t)\, exp(-2\pi ikd)dk, \quad ...(2)$$

where d is the depth of the sample. Finally, a total of 25000×1.2 depth resolved reflectivity profiles were obtained. They were stored in the computer memory as a two-dimensional data array representing the variation along time, and we call this as time history OCT image. The rows and columns of the data array represent the depth positions, and their intensities in a sequence of regularly spaced time steps of 1/25,000 seconds, respectively.

The biological activity of the sample could be reflected in the temporal characteristics of intensity changes in the horizontal direction, that is, along the rows. Therefore, we utilized the autocorrelation function and its correlation length to evaluate the biological activities of the tissue.

By repeating the data acquisition 5 times, five-time history OCT images were acquired over 6 seconds. Power spectral densities $|R(d,f)|^2$ of time signals express by equation (2) were calculated at every depth position along the time axis. Here, *f* denotes temporal frequency. To get a higher signal to noise ratio (SNR), five power spectral densities corresponding to each depth position were averaged across the time history OCT images. Finally, averaged power spectral densities $\langle |R(d,f)|^2 \rangle$ were inverse Fourier transformed to get the autocorrelation functions $\Gamma(d,\tau)$ at a certain depth position, *d*, as given by,

$$\Gamma(d,\tau) = \int_{-\infty}^{\infty} \langle |R(d,f)|^2 \rangle\, exp(2\pi f\tau)\, df \quad ...(3)$$

We used the software, MATLAB (MATLAB2009a, MathWorks, USA) for calculations of the autocorrelation function. The temporal variations of biospeckles were quantified by calculating the correlation length (CL) which is half width half maximum of the autocorrelation function. This quantity was employed as a measure for the biological activities of layers at different depths of the Chinese chives leaf under O_3 stress. When the signal changes rapidly due to higher biological activity, the autocorrelation function is expected to become narrower and results in a decrease in CL.

Plant and ozone exposure system

Chinese chives were grown in a growth chamber (CMP 3244, Conviron, Controlled Environmental Ltd, Canada.) maintaining at a relative humidity of 55% - 65% during 6.00 A.M. to 6.00 P.M. for the day shift and 6.00 P.M. to 6.00 A.M. for the night shift. Photon flux densities of 260 - 350 µmol m^{-2} s^{-1} and 0 µmol $m^{-2}s^{-1}$ and an air temperature of 25°C and 18°C were set for day and night shifts, respectively. The plants were kept regularly watered. In the experiment, healthy young leaves of the plants, one to two weeks old, were employed and mounted in a leaf O_3 chamber. Three halogen lamps

(PHL-150, MEJIRO PRECISION, Japan) with the fiber optic light guides were used to illuminate the plant leaf at a photon flux density of 500 μmol m^{-2} s^{-1} during the experiments.

The O_3 exposure system (Figure 3) consists of an air pump, charcoal filters (CF), an O_3 generator (OES 10A, Dylec Inc., Japan), an O_3 monitor (Model 1150, Dylec Inc., Japan), and a main O_3 chamber (33.5 × 33.5 × 58 cm^3). A specially designed leaf O_3 chamber (10 × 10 × 2 cm^3), made up of PVC was connected to the main O_3 chamber to enable optical imaging of the leaf. Generated O_3 was fed into the main O_3 chamber with its concentration being precisely controlled by the O_3 monitor that constantly sent a feedback signal to the O_3 generator. In the experiments, the O_3 generation system approximately took 14 minutes to reach the target O_3 concentration of 240 ppb. The O_3 feedback system practically stabilized the concentration of O_3 within the leaf and main O_3 chambers at an accuracy of 0.5% during the experiment.

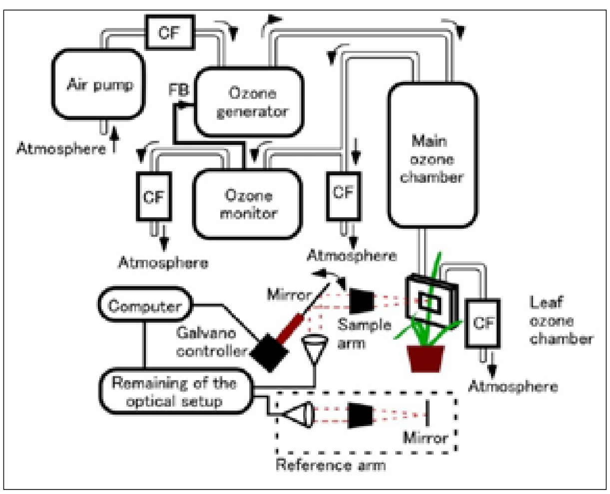

Figure 3: A schematic of the O_3 exposure system and a simplified sketch of SD-OCT system used in this study. CF: charcoal filter, FB: feed back signal. Arrows indicate the direction of air flow.

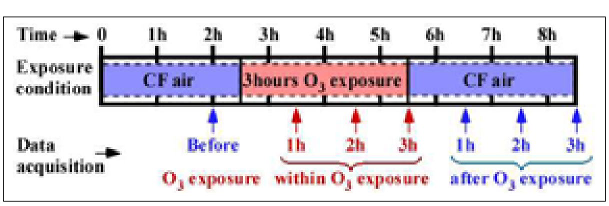

Figure 3: Timing protocol of O_3 exposure and data acquisition.

Timing protocol and data acquisition

Prior to the experiment, as an initial step, following mounting of the Chinese chives leaf in the leaf O_3 chamber, the leaf was acclimatized to the environmental condition by having a continuous flow of charcoal filtered air (10 liter/min.) into the leaf chamber for two hours. Next, after starting the O_3 generator half an hour was allocated for the O_3 concentration in the main O_3 chamber to reach 240 ppb. At the end of this half an hour period, on reaching the target O_3 concentration, connections of the O_3 air tubes were arranged in such a way that, air containing O_3 will reach leaf without passing through CF. O_3 exposure was carried out for 3 hours.

At the end of 3 hours of exposure, connection of O_3 tubes to the chamber were rearranged so as for the air to pass through CF before reaching the leaf chamber. Final CF air treatment was done to monitor the response of leaf after O_3 exposure. O_3 concentration of 240 ppb was chosen based on the criterion used in Japan, where serious warning for O_3 is issued (Lee & Goto, 2022; Rathnayake *et al.*, 2007). Both the temperature and the humidity were kept constant during a single session of the experiment with their variations being ± 2%.

bOCT biospeckle signal data corresponding to fixed lateral positions from the back surface of the leaf were acquired continuously at times including before O_3 exposure, during exposure at times of 1 hour, 2 hours, 3 hours, and after stopping O_3 exposure at 1 hour, 2 hours, and 3 hours. Before and after O_3 exposure, plant leaves were treated with CF air for 2.5 hours and 3 hours, respectively. The entire experimental duration was 8.5 hours.

Analyzing the biospeckle signals

To examine the bOCT biospeckles, OCT cross-sectional images were acquired successively over a certain period. Two different methods were used to analyze biospeckle signals coming from different spatial positions of the OCT cross-sectional image. In the first method, the magnitude of the fluctuation of the biospeckle signal, in other words, the standard deviation (SD) of the signal, was calculated along the time axis for each spatial position from the data array of OCT cross-sectional images. Then, a bOCT biospeckle image was constructed from the SDs of biospeckle signals.

In the second method, temporal characteristics of the biospeckle signals originating from different depths were analyzed. Averaged autocorrelation functions of bOCT biospeckle signals coming from layers at different depths of the leaf were calculated. From the correlation, half-width half maximum (HWHM) or the correlation length (CLs) was obtained. Longer CLs would indicate slower motion within the leaf and vice versa. Magnitude, SD, and temporal characteristics, CL, of the time varying biospeckle signal can reveal different information from that obtained by the conventional OCT, and they are proposed as measures to evaluate the changes in biological activities against O_3 stress on plants.

RESULTS AND DISCUSSION

Micro-structural cross-sectional observation with an optical microscope was done for a Chinese chives leaf (Figure 4). The epidermal cells layer indicated as *ue* (20 µm thick layer), and the oval shaped mesophyll cells marked as *mc* (around 90 µm in height), were clearly visible. Here, the epidermal layer is the outermost cell layer of the plant leaf, which regulates gas exchange, and protects the leaf against water loss. The mesophyll cell layer is the primary location for photosynthesis, governing most of the leaf's interior functions (Taiz & Zeiger, 2002).

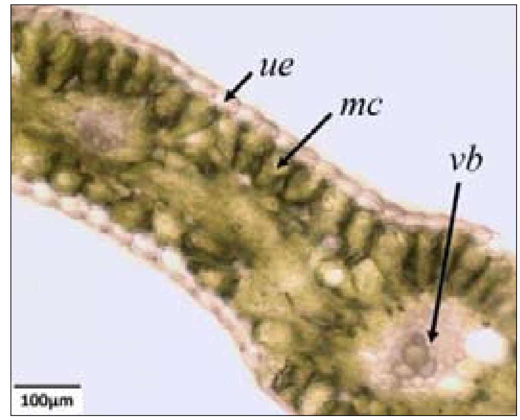

Figure 4: Optical microscopy (SZX7 Microscopy, U-TV0.5XC-3 Camera adaptor, OLYMPUS, Tokyo, Japan) analysis of the cross-section of a leaf of Chinese chives. ue-upper epidemis, mc-mesophyll cell, vb-vascular bundle.

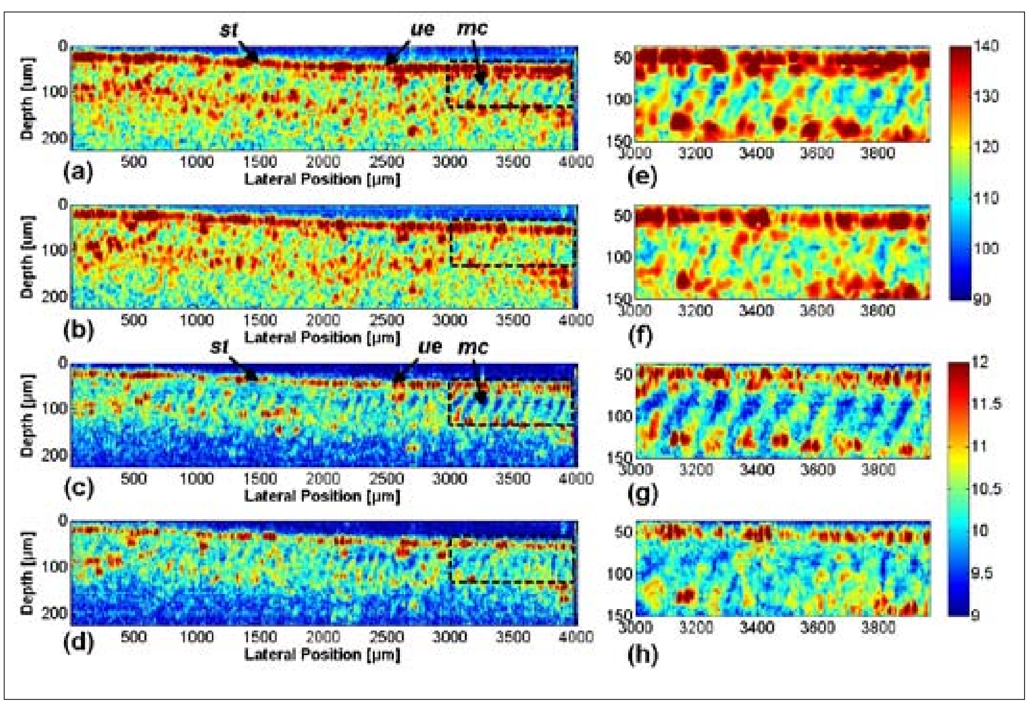

Figure 5: Conventional structural OCT cross-sectional images (a) before O_3 exposure, (b) 3 hours after starting O_3 exposure. Corresponding bOCT biospeckle images (c) before exposure, (d) 3 hours after starting O_3 exposure. Magnified views of the mesophyll cell layer encased in black dotted squares shown in (a), (b), (c), and (d) are shown, respectively in (e), (f), (g), and (h). ue: upper epidemis, mc: mesophyll cell.

Figures 5(a), and (b) show the conventional structural OCT image of Chinese chives leaf (abaxial surface) acquired before and 3 hours after starting O_3 exposure, respectively. Figures 5(c) and (d) represent the corresponding bOCT biospeckle SD images before, and 3 hours after starting O_3 exposure. The conventional OCT cross-sectional imaging can visualize the internal structure of biological tissues (Figure 5(a)). The epidermal cell layer can be clearly seen. However, the mesophyll cell layer was not clearly visible. In contrast, in the corresponding bOCT biospeckle image (Figure 5(c)), the layer structure becomes clearer, and it can be seen clearly in the magnified image shown in Figure 5(g) in comparison to the corresponding one in Figure 5(e) of the structural OCT image. Comparing with the microscopic image in Figure 3, the upper epidermal layer and the distinctive more oval shaped mesophyll cells can be clearly seen in the bOCT biospeckle image.

Comparing the effect of O_3 exposure duration, it was difficult to find a clear difference in conventional OCT images between Figures 5(a) and (b) or between (e), and (f). However, the variation due to O_3 exposure could be clearly seen in the bOCT biospeckle images between Figures 5(c) and (d), or (g) and (h). The oval shaped periodic structure that corresponds to mesophyll cells became unclear in biospeckle images with even 3 hours short term O_3 exposure. Earlier studies confirmed that cells belonging to mesophyll layer is the main target of O_3 injury (Turc *et al.*, 2023; Xu *et al.*, 2023; Vollenweider *et al.*, 2003). Next, biospeckle signals coming from different depth layers were analyzed for their temporal characteristics.

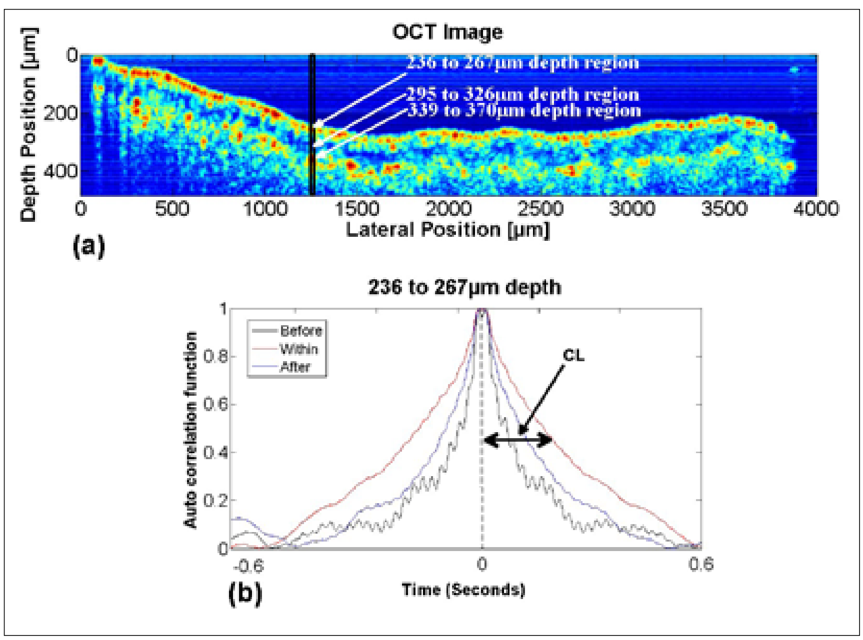

Figure 6: (a) OCT Image of the back surface of a leaf. (b) Averaged autocorrelation functions calculated for the epidermal layer over a region of 236 to 267μm across the depth.

It is clear from the origin of the biospeckles that in addition to its magnitude, SD, its temporal characteristics also reflect the dynamic properties of the cell organelles and scattering particles inside the plant leaf. To analyze the temporal characteristics of the signal, we examined the temporal autocorrelation function of the biospeckle signal.

In order to investigate the temporal autocorrelation function, the galvano mirrors used for scanning the beam laterally were fixed at a particular position of interest after the OCT images of the leaf were acquired (Figure 6(a)). Interference signals were acquired and the temporal autocorrelation functions corresponding to every depth position were calculated. The selected depth regions were the 236 to 267 µm depth region (epidermal layer), 295 to 326 µm depth region (mesophyll cell layer), and 339 to 370 µm depth region (layer below mesophyll cells). Autocorrelation functions within the same layer were averaged (along depth direction). The autocorrelation functions for different layers over different time periods of 1, 2, and 3 hours within the O_3 exposure duration were averaged and indicated as 'within'. In a similar way, autocorrelation functions for 1, 2, and 3 hours after exposure were averaged and indicated as 'after'.

Next, those autocorrelation functions were evaluated by defining the correlation length as half-width at half maximum, *i.e.*, CLs of biospeckle signals, and they were calculated for 'before', 'within', and 'after' O_3 exposure periods for each of the three different layers, namely, the *ue* layer, *mc* layer, and below *mc* layer.

The variation of CL under O_3 stress is shown in Figure 6(b) for the *ue* layer. It can be seen that CL increased with O_3 exposure, indicating that the rate of biological movements in this layer decreased with O_3 exposure in this layer. To focus on the relative change in biospeckle signal coming from three different layers of the leaf in response to O_3 exposure, CLs of biospeckle signals, those of 'within' and 'after' O_3 exposure were normalized using those obtained before O_3 exposure. These quantities are called as normalized correlation lengths (NCLs). NCLs from 16 measurements from the back surface of six different leaves (at least 2 measurements from one leaf) of Chinese chives, before, within, and after exposure to O_3 were averaged separately to obtain the averaged normalized correlation length (ANCL) as given by,

$$ANCL = \left\langle \frac{CL}{CL_b} \right\rangle, \qquad ...(4)$$

where, ‹...› denotes average over 16 measurements, and CL_b indicates the correlation length of the biospeckle signal before O_3 exposure. In the following discussion, the NCLs of biospeckle signals were used and shown for different layers in Figure 7. Under the short term of O_3 exposure, biological changes in different layers could be identified with ANCL.

ANCLs decreased in the *mc* layer and the below *mc* layer with O_3 exposure for the leaf. The reduction was significant (t-test, $P < 0.05$, Figure 7) in the case of the *mc* layer. However, for the *ue* layer ANCL appeared to be increased, but the increase was not statistically significant.

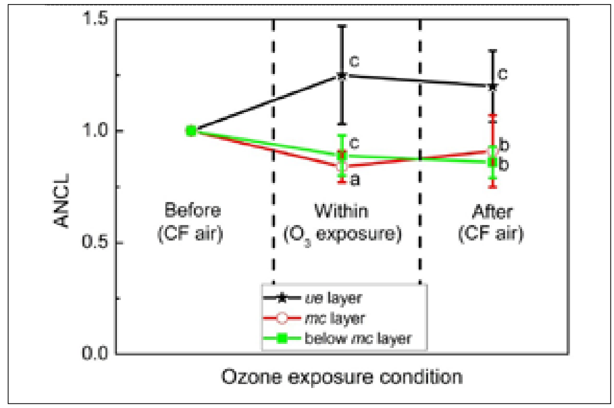

Figure 7: ANCLs of biospeckle signals coming from different layers (from the back surface) of Chinese chives leaves under O_3 exposures of 240 ppb. Each average value was plotted with standard error for 16 measurements. ue: upper epidemis, mc: mesophyll cell. The ANCL within O_3 exposure and after exposure were compared with that before exposure using statistical two samples t-test. (a, $P < 0.05$; b, $P < 0.07$; c, not significant).

Increase of CL, *i.e.*, slow fluctuation rate of the biospeckle signal, in the *ue* layer could be seen during and after the O_3 exposure. In contrast, the biospeckle fluctuation rate was increased during and even after O_3 exposure in the *mc* layer and the layer below mesophyll cells.

Earlier studies (Turc *et al.*, 2023; Xu *et al.*, 2023; Vollenweider *et al.* 2003; Faoro & Iriti 2009) too confirmed that palisade mesophyll cells are the main target of O_3 injury. Also, that the O_3 injury mainly occurs in the mesophyll cells whereas epidermal and stomatal cells and vascular cells resist until the last stage before total leaf necrosis. O_3 is taken up through the stomata and reacts with water and intercellular components to generate highly reactive oxygen species (ROS), that include peroxides and free radicals which are probably the real cause of the negative effect of O_3. Plants have a number of mechanisms that chemically and enzymatically remove these toxic compounds avoiding cellular damage (Kangasjärvi *et al.*, 1994, Sharma & Davis, 1997, Sandermann *et al.*, 1998, Dizengremel, 2001; Rajput *et al.*, 2021; Sachdev *et al.*, 2021). We expect that, once O_3 enters plant leaves, it activates these defense mechanisms. This may be a reason for the increase in biospeckle fluctuation rate in the *mc* layer and the layer below *mc*.

CONCLUSION

We showed that the bOCT biospeckle imaging technique can be successfully applied to monitor O_3 stress on plants. The internal cell structure of the leaf, especially the mesophyll cell layer and below, inside the Chinese chives leaf could be clearly visualized by the bOCT biospeckle imaging in contrast to the conventional OCT imaging. Further, with O_3 exposure, variation of magnitude of biospeckle signal fluctuation coming from mesophyll cell layer could be visualized with more of the oval shaped mesophyll cells becoming unclear in contrast to the conventional OCT image.

We showed that analysis of the temporal characteristics of biospeckle signal coming from different layers could identify changes in biological activity with O_3 exposure. This study demonstrates that the direct exposure to O_3 affects differently the bOCT biospeckle signals coming from different layers of Chinese chives, even though the period of exposure O_3 is short, only a few hours.

The bOCT based on biospeckle is found to be suitable for fast, non-destructive monitoring of environmental stresses on plants, which can potentially lead to significant time and cost saving, while conventional techniques require destruction and subsequent analysis.

Acknowledgement

This work was partly supported by the Grant-in-Aid for Science Research in JSPS (No. 24651023) of the Ministry of Education, Culture, Sports, Science and Technology in Japan.

REFERENCES

Ainsworth, E. A. (2008). Rice production in a changing climate: a meta-analysis of responses to elevated carbon dioxide and elevated ozone concentration. *Global Change Biology*, *14*(7), 1642-1650. https://doi.org/10.1111/j.1365-2486.2008.01594.x

Aizu, Y., & Asakura, T. (1996). Bio-speckles. *Trends in Optics*, 27-49. https://doi.org/10.1016/B978-012186030-1/50004-7

Ansari, M. Z., & Nirala, A. K. (2013). Biospeckle activity measurement of Indian fruits using the methods of cross-correlation and inertia moments. *Optik*, *124*(15), 2180-2186. https://doi.org/10.1016/j.ijleo.2012.06.081

Ashmore, M. R. (2005). Assessing the future global impacts of ozone on vegetation. *Plant, Cell and Environment*, *28*(8), 949-964. https://doi.org/10.1111/j.1365-3040.2005.01341.x

Baum, O. I., Zaitsev, V. Y., Yuzhakov, A. V., Sviridov, A. P., Novikova, M. L., Matveyev, A. L., Matveev, L. A., Sovetsky, A. A., & Sobol, E. N. (2020). Interplay of temperature, thermal-stresses and strains in laser-assisted modification of collagenous tissues: Speckle-contrast and OCT-based studies. *Journal of Biophotonics*, *13*(1), e201900199. https://doi.org/10.1002/jbio.201900199

Beig, G., Gunthe, S., & Jadhav, D. B. (2007). Simultaneous measurements of ozone and its precursors on a diurnal scale at a semi urban site in India. *Journal of Atmospheric Chemistry*, *57*, 239-253. https://doi.org/10.1007/s10874-007-9068-8

Beiu, R. M., Duma, V. F., Mnerie, C. A., Beiu, A. C., Dochia, M. A., Copolovici, L., Dobre, G., Bradu, A., & Podoleanu, A. (2022). *Optical coherence tomography versus microscopy for the study of Aloe vera leaves*. *Optics, Photonics and Digital Technologies for Imaging Applications*. SPIE.

Boccara, M., Schwartz, W., Guiot, E., Vidal, G., Paepe, R. D., Dubois, A., & Boccara, A. C. (2007). Early chloroplastic alterations analysed by optical coherence tomography during a harpin-induced hypersensitive response. *The Plant Journal*, *50*(2), 338-346. https://doi.org/10.1111/j.1365-313X.2007.03051.x

Bouma, B. E., de Boer, J. F., Huang, D., Jang, I. K., Yonetsu, T., Leggett, C. L., Leitgeb, R., Sampson, D. D., Suter, M., Vakoc, B. J., Villiger, M., & Wojtkowski, M. (2022). Optical coherence tomography. *Nature Reviews Methods Primers*, *2*(1), 79. https://doi.org/10.1038/s43586-022-00162-2

Braga Jr, R. A., Rabelo, G. F., Granato, L. R., Santos, E. F., Machado, J. C., Arizaga, R., ... & Trivi, M. (2005). Detection of fungi in beans by the laser biospeckle technique. *Biosystems Engineering*, *91*(4), 465-469. https://doi.org/10.1016/j.biosystemseng.2005.05.006

Braga, R. A., Dal Fabbro, I. M., Borem, F. M., Rabelo, G., Arizaga, R., Rabal, H. J., & Trivi, M. (2003). Assessment of seed viability by laser speckle techniques. *Biosystems Engineering*, *86*(3), 287-294. https://doi.org/10.1016/j.biosystemseng.2003.08.005

Braga, R. A., Dupuy, L., Pasqual, M., & Cardoso, R. R. (2009). Live biospeckle laser imaging of root tissues. *European Biophysics Journal*, *38*, 679-686. https://doi.org/10.1007/s00249-009-0426-0

Calatayud, A., Iglesias, D. J., Talón, M., & Barreno, E. (2003). Effects of 2-month ozone exposure in spinach leaves on photosynthesis, antioxidant systems and lipid peroxidation. *Plant Physiology and Biochemistry*, *41*(9), 839-845. https://doi.org/10.1016/S0981-9428(03)00123-2

Carvalho, P. H., Barreto, J. B., Braga Jr, R. A., & Rabelo, G. F. (2009). Motility parameters assessment of bovine frozen semen by biospeckle laser (BSL) system. *Biosystems Engineering*, *102*(1), 31-35. https://doi.org/10.1016/j.biosystemseng.2008.09.025

Chen, Y., Aguirre, A. D., Ruvinskaya, L., Devor, A., Boas, D. A., & Fujimoto, J. G. (2009). Optical coherence tomography (OCT) reveals depth-resolved dynamics during functional brain activation. *Journal of Neuroscience Methods*, *178*(1), 162-173. https://doi.org/10.1016/j.jneumeth.2008.11.026

Darrall, N. M. (1989). The effect of air pollutants on physiological processes in plants. *Plant, Cell and Environment*, *12*(1), 1-30. https://doi.org/10.1111/j.1365-3040.1989.tb01913.x

De Silva, Y. S. K., Rajagopalan, U. M., & Kadono, H. (2023a). Effect of alumina nanoparticles on lentil seed germination using biospeckle optical coherence tomography. *Applied Sciences*, *13*(16), 9203. https://doi.org/10.3390/app13169203

De Silva, Y. S. K., Rajagopalan, U. M., Kadono, H. & Li, D. (2023b). The synergy of microplastics with the heavy metal zinc has resulted in reducing the toxic effects of zinc on lentil (*Lens culinaris*) seed germination and seedling growth. *Heliyon*, *9*(11), e21464–e21464. https://doi.org/10.1016/j.heliyon.2023.e21464

De Silva, Y. S. K., Rajagopalan, U. M., Kadono, H., & Li, D. (2021). Positive and negative phenotyping of increasing Zn concentrations by biospeckle optical coherence tomography in speedy monitoring on lentil (*Lens culinaris*) seed germination and seedling growth. *Plant Stress*, *2*, 100041–100041. https://doi.org/10.1016/j.stress.2021.100041

De Silva, Y. S. K., Rajagopalan, U. M., Li, D., & Kadono, H. (2022). Optical screening method to observe the biological activities of lentil (*Lens culinaris*) seeds quantitatively under the exposure of polyethylene microplastics (PEMPs) using ultrahigh accurate biospeckle optical coherence tomography. In *Tissue Optics and Photonics II* (P. 19). SPIE. https://doi.org/10.1117/12.2620176

De Wit, J., Tonn, S., Van den Ackerveken, G., & Kalkman, J. (2020). Quantification of plant morphology and leaf thickness with optical coherence tomography. *Applied Optics*, *59*(33), 10304-10311. https://doi.org/10.1364/AO.408384

DeSilva, K. T. K. M., Rajagopalan, U. M., & Kadono, H. (2017). Highly sensitive optical interferometric technique reveals stress-dependent instantaneous nanometric growth fluctuations of Chinese chive leaf under heavy metal stress. *Ecotoxicology and Environmental Safety*, *137*, 86-93. https://doi.org/10.1016/j.ecoenv.2016.11.020

Dizengremel, P. (2001). Effects of ozone on the carbon metabolism of forest trees. *Plant Physiology and Biochemistry*, *39*(9), 729-742. https://doi.org/10.1016/S0981-9428(01)01291-8

Drexler, W., Morgner, U., Ghanta, R. K., Kärtner, F. X., Schuman, J. S., & Fujimoto, J. G. (2001). Ultrahigh-resolution ophthalmic optical coherence tomography. *Nature Medicine*, *7*(4), 502-507. https://doi.org/10.1038/86589

Everett, M., Magazzeni, S., Schmoll, T., & Kempe, M. (2021). Optical coherence tomography: From technology to applications in ophthalmology. *Translational Biophotonics*, *3*(1), e202000012. https://doi.org/10.1002/tbio.202000012

Faoro, F., & Iriti, M. (2009). Plant cell death and cellular alterations induced by ozone: key studies in Mediterranean conditions. *Environmental Pollution*, *157*(5), 1470-1477. https://doi.org/10.1016/j.envpol.2008.09.026

Feng, Z., Agathokleous, E., Yue, X., Oksanen, E., Paoletti, E., Sase, H., Gandin, A., Koike, T., Calatayud, V., Yuan, X., Liu, X., De Marco, A., Jolivet, Y., Kontunen-Soppela, S., Hoshika, Y., Saji, H., Li, P., Li, Z., Watanabe, M., & Kobayashi, K. (2021). Emerging challenges of ozone impacts on Asian plants: actions are needed to protect ecosystem health. *Ecosystem Health and Sustainability*, *7*(1), 1911602. https://doi.org/10.1080/20964129.2021.1911602

Fercher, A. F. (1996). Optical coherence tomography. *Journal of Biomedical Optics*, *1*(2), 157-173. https://doi.org/10.1117/12.231361

Fercher, A. F. (2010). Optical coherence tomography – development, principles, applications. *Zeitschrift für Medizinische Physik*, *20*(4), 251-276. https://doi.org/10.1016/j.zemedi.2009.11.002

Fujii, H., Asakura, T., Nohira, K., Shintomi, Y., & Ohura, T. (1985). Blood flow observed by time-varying laser speckle. *Optics Letters*, *10*(3), 104-106. https://doi.org/10.1364/OL.10.000104

Fujimoto, J. G. (2003). Optical coherence tomography for ultrahigh resolution in vivo imaging. *Nature Biotechnology*, *21*(11), 1361-1367. https://doi.org/10.1038/nbt892

Fujimoto, J. G. D. W., & Drexler, W. (2008). Introduction to optical coherence tomography. In *Optical coherence tomography: Technology and applications* (pp. 1-45). Springer. https://doi.org/10.1007/978-3-540-77550-8_1

Ge, X., Chen, S., Chen, S., & Liu, L. (2021). High resolution optical coherence tomography. *Journal of Lightwave Technology*, *39*(12), 3824-3835. https://doi.org/10.1109/JLT.2021.3061606

Gladkova, N., Maslennikova, A., Balalaeva, I., Feldchtein, F., Kiseleva, E., Karabut, M., & Iksanov, R. (2008). Application of optical coherence tomography in the diagnosis of mucositis in patients with head and neck cancer during a course of radio (chemo) therapy. *Medical Laser Application*, *23*(4), 186-195. https://doi.org/10.1016/j.mla.2008.07.008

Hettinger, J. W., Mattozzi, M. D. L. P., Myers, W. R., Williams, M. E., Reeves, A., Parsons, R. L., Haskell, R.C., Petersen, D.C., Wang, R., & Medford, J. I. (2000). Optical coherence microscopy. A technology for rapid, *in vivo*, non-destructive visualization of plants and plant cells. *Plant Physiology*, *123*(1), 3-16. https://doi.org/10.1104/pp.123.1.3

Holder, A. J., & Hayes, F. (2022). Substantial yield reduction in sweet potato due to tropospheric ozone, the dose-response function. *Environmental Pollution*, *304*, 119209. https://doi.org/10.1016/j.envpol.2022.119209

Hope, J., Goodwin, M., & Vanholsbeeck, F. (2021). Optical coherence tomography imaging of evoked neural activity in sciatic nerve of rat. *Journal of Physics D: Applied Physics*, 54(33), 334002. https://doi.org/10.1088/1361-6463/ac021b

Huang, D., Swanson, E. A., Lin, C. P., Schuman, J. S., Stinson, W. G., Chang, W., Hee, M.R., Flotte, T., Gregory, K., Puliafito, C.A., & Fujimoto, J. G. (1991). Optical coherence tomography. *Science*, *254*(5035), 1178-1181. https://doi.org/10.1126/science.1957169

Jiménez-Montenegro, L., Lopez-Fernandez, M., & Gimenez, E. (2021). Worldwide research on the ozone influence in plants. *Agronomy*, *11*(8), 1504. https://doi.org/10.3390/agronomy11081504

Kangasjärvi, J., Talvinen, J., Utriainen, M., & Karjalainen, R. (1994). Plant defence systems induced by ozone. *Plant, Cell and Environment*, *17*(7), 783-794. https://doi.org/10.1111/j.1365-3040.1994.tb00173.x

Kashani, A. H., Asanad, S., Chan, J. W., Singer, M. B., Zhang, J., Sharifi, M., Khansari, M. M., Abdolahi, F., Shi, Y., Biffi, A., Chui, H., & Ringman, J. M. (2021). Past, present and future role of retinal imaging in neurodegenerative disease. *Progress in Retinal and Eye Research*, *83*, 100938. https://doi.org/10.1016/j.preteyeres.2020.100938

Khateeb, K., Bloch, J., Zhou, J., Rahimi, M., Griggs, D. J., Kharazia, V. N., Le, M. N., Wang, R. K., & Yazdan-Shahmorad, A. (2022). A versatile toolbox for studying cortical physiology in primates. *Cell Reports Methods*, *2*(3). https://doi.org/10.1016/j.crmeth.2022.100183

Kobayashi, K., & Kadono, H. (2010). Expansion of the dynamic range of statistical interferometry and its application to extremely short- to long-term plant growth monitoring. *Applied Optics*, *49*(32), 6333-6339. https://doi.org/10.1364/AO.49.006333

Kobayashi, K., & Okada, M. (1995). Effects of ozone on the light use of rice (*Oryza sativa* L.) plants. *Agriculture, Ecosystems and Environment*, *53*(1), 1-12. https://doi.org/10.1016/0167-8809(94)00560-2

Kobayashi, K., Okada, M., & Nouchi, I. (1995). Effects of ozone on dry matter partitioning and yield of Japanese cultivars of rice (*Oryza sativa* L.). *Agriculture, Ecosystems and Environment*, *53*(2), 109-122. https://doi.org/10.1016/0167-8809(94)00564-U

Kumar, P., Kuttippurath, J., von der Gathen, P., Petropavlovskikh, I., Johnson, B., McClure-Begley, A., Cristofanelli, P., Bonasoni, P., Barlasina, M. E., & Sánchez, R. (2021). The increasing surface ozone and tropospheric ozone in Antarctica and their possible drivers. *Environmental Science and Technology*, *55*(13), 8542-8553. https://doi.org/10.1021/acs.est.0c08491

Kurenda, A., Adamiak, A., & Zdunek, A. (2012). Temperature effect on apple biospeckle activity evaluated with different indices. *Postharvest Biology and Technology*, *67*, 118-123. https://doi.org/10.1016/j.postharvbio.2011.12.017

Lee, J. H., & Goto, E. (2022). Ozone control as a novel method to improve health-promoting bioactive compounds in red leaf lettuce (*Lactuca sativa* L.). *Frontiers in Plant Science*, 13, 1045239. https://doi.org/10.3389/fpls.2022.1045239

Lee, J., Wijesinghe, R. E., Jeon, D., Kim, P., Choung, Y. H., Jang, J. H., Jeon, M., & Kim, J. (2018). Clinical utility of intraoperative tympanomastoidectomy assessment using a surgical microscope integrated with an optical coherence tomography. *Scientific Reports*, *8*(1), 17432. https://doi.org/10.1038/s41598-018-35563-5

Li, D., Rajagopalan, U. M., De Silva, Y. S. K., Liu, F., & Kadono, H. (2021a). Biospeckle optical coherence tomography (BOCT) in the speedy assessment of the responses of the seeds of *Raphanus sativus* L.(Kaiware Daikon) to acid mine drainage (AMD). *Applied Sciences*, *12*(1), 355. https://doi.org/10.3390/app12010355

Li, D., Rajagopalan, U. M., Kadono, H., & De Silva, Y. S. K. (2022). Speedy evaluation of simulated Acid Mine Drainage (AMD) on Rice by a non-invasive technique. *Plant Stress*, *6*, 100113. https://doi.org/10.1016/j.stress.2022.100113

Li, M., Rivera, S., Franklin, D., Nowak, E., Hallett, I., Kolenderska, S., Urbańska, M., Vanholsbeeck, F., & East, A. (2021). Use of optical coherence tomography and light microscopy for characterisation of mechanical properties and cellular level responses of 'Centurion' blueberries during weight loss. *Journal of Food Engineering*, *303*, 110596. https://doi.org/10.1016/j.jfoodeng.2021.110596

Li, P., Ni, S., Zhang, L., Zeng, S., & Luo, Q. (2006). Imaging cerebral blood flow through the intact rat skull with temporal laser speckle imaging. *Optics Letters*, *31*(12), 1824-1826. https://doi.org/10.1364/OL.31.001824

Lichtenegger, A., Gesperger, J., Niederleithner, M., Ginner, L., Woehrer, A., Drexler, W., Baumann, B., Leitgeb, R. A., & Salas, M. (2020). Ex vivo Alzheimer's disease brain tissue investigation: a multiscale approach using 1060 nm swept source optical coherence tomography for a direct correlation to histology. *Neurophotonics*, *7*(3), 035004. https://doi.org/10.1117/1.NPh.7.3.035004

Micieli, J., Lo, C., & Vuong, L. (2021). Recent advances and future directions on the use of optical coherence tomography in neuro-ophthalmology. *Taiwan Journal of Ophthalmology*, *11*(1), 3. https://doi.org/10.4103/tjo.tjo_76_20

Maheswari, R. U., Takaoka, H., Homma, R., Kadono, H., & Tanifuji, M. (2002). Implementation of optical coherence tomography (OCT) in visualization of functional structures of cat visual cortex. *Optics Communications*, *202*(1-3), 47-54. https://doi.org/10.1016/S0030-4018(02)01079-9

Maheswari, R. U., Takaoka, H., Kadono, H., Homma, R., & Tanifuji, M. (2003). Novel functional imaging technique from brain surface with optical coherence tomography enabling visualization of depth resolved functional structure *in vivo*. *Journal of Neuroscience Methods*, *124*(1), 83-92. https://doi.org/10.1016/S0165-0270(02)00370-9

Mariampillai, A., Leung, M. K., Jarvi, M., Standish, B. A., Lee, K., Wilson, B. C., Vitkin, A., & Yang, V. X. (2010). Optimized speckle variance OCT imaging of microvasculature. *Optics Letters*, *35*(8), 1257-1259. https://doi.org/10.1364/OL.35.001257

Mariampillai, A., Standish, B. A., Moriyama, E. H., Khurana, M., Munce, N. R., Leung, M. K., Jiang, J., Cable, A., Wilson, B.C., Vitkin, I.A., & Yang, V. X. (2008). Speckle variance detection of microvasculature using swept-source optical coherence tomography. *Optics Letters*, *33*(13), 1530-1532. https://doi.org/10.1364/OL.33.001530

Mathur, J. (2020). Morphology, behaviour and interactions of organelles. *Plant Science*, *301*, 110662. https://doi.org/10.1016/j.plantsci.2020.110662

Moayed, A. A., Hariri, S., Choh, V., & Bizheva, K. (2011). *In vivo* imaging of intrinsic optical signals in chicken retina with functional optical coherence tomography. *Optics Letters*, *36*(23), 4575-4577. https://doi.org/10.1364/OL.36.004575

Mogre, S. S., Brown, A. I., & Koslover, E. F. (2020). Getting around the cell: physical transport in the intracellular world. *Physical Biology*, 17(6), 061003. https://doi.org/10.1088/1478-3975/aba5e5

Pajuelo, M., Baldwin, G., Rabal, H., Cap, N., Arizaga, R., & Trivi, M. (2003). Bio-speckle assessment of bruising in fruits. *Optics and Lasers in Engineering*, *40*(1-2), 13-24. https://doi.org/10.1016/S0143-8166(02)00063-5

Pandiselvam, R., Mayookha, V. P., Kothakota, A., Ramesh, S. V., Thirumdas, R., & Juvvi, P. (2020). Biospeckle laser technique – A novel non-destructive approach for food quality and safety detection. *Trends in Food Science and Technology*, *97*, 1-13. https://doi.org/10.1016/j.tifs.2019.12.028

Panebianco, F., Rubiola, S., & Di Ciccio, P. A. (2022). The use of ozone as an eco-friendly strategy against microbial biofilm in dairy manufacturing plants: a review. *Microorganisms*, *10*(1), 162. https://doi.org/10.3390/microorganisms10010162

Pircher, M., Hitzenberger, C. K., & Schmidt-Erfurth, U. (2011). Polarization sensitive optical coherence tomography in the human eye. *Progress in Retinal and Eye Research*, *30*(6), 431-451. https://doi.org/10.1016/j.preteyeres.2011.06.003

Rajagopalan, U. M., Kabir, M., Lim, Y., & Kadono, H. (2020). Biospeckle optical coherence tomography in speedy visualizing effects of foliar application of plant growth hormone to Chinese chives leaves. *BMC Research Notes*, *13*, 1-6. https://doi.org/10.1186/s13104-020-05219-7

Rajput, V. D., Harish, Singh, R. K., Verma, K. K., Sharma, L., Quiroz-Figueroa, F. R., ... & Mandzhieva, S. (2021). Recent developments in enzymatic antioxidant defence mechanism in plants with special reference to abiotic stress. *Biology*, *10*(4), 267. https://doi.org/10.3390/biology10040267

Rathnayake, A. P., Kadono, H., Toyooka, S., & Miwa, M. (2007). Statistical interferometric investigation of nano-scale root growth: effects of short-term ozone exposure on ectomycorrhizal pine (*Pinus densiflora*) seedlings. *Journal of Forest Research*, *12*, 393-402. https://doi.org/10.1007/s10310-007-0040-x

Rathnayake, A. P., Kadono, H., Toyooka, S., & Miwa, M. (2008). A novel optical interference technique to measure minute root elongations of Japanese red pine (*Pinus densiflora* Seibold & Zucc.) seedlings infected with ectomycorrhizal fungi. *Environmental and Experimental Botany*, *64*(3), 314-321. https://doi.org/10.1016/j.envexpbot.2008.02.007

Ravichandran, N. K., Wijesinghe, R. E., Lee, S. Y., Choi, K. S., Jeon, M., Jung, H. Y., & Kim, J. (2017). Non-destructive analysis of the internal anatomical structures of mosquito specimens using optical coherence tomography. *Sensors*, *17*(8), 1897. https://doi.org/10.3390/s17081897

Ravichandran, N. K., Wijesinghe, R. E., Shirazi, M. F., Park, K., Lee, S. Y., Jung, H. Y., Jeon, M., & Kim, J. (2016). *In vivo* monitoring on growth and spread of gray leaf spot disease in *Capsicum annuum* leaf using spectral domain optical coherence tomography. *Journal of Spectroscopy*, *2016*(1), 1093734. https://doi.org/10.1155/2016/1093734

Reeves, A., Parsons, R. L., Hettinger, J. W., & Medford, J. I. (2002). *In vivo* three-dimensional imaging of plants with optical coherence microscopy. *Journal of Microscopy*, *208*(3), 177-189. https://doi.org/10.1046/j.1365-2818.2002.01086.x

Regar, E., van Leeuwen, A. M. G. J., & Serruys, P. W. (Eds.). (2007). *Optical coherence tomography in cardiovascular research*. CRC Press. https://doi.org/10.3109/9780203931561

Sachdev, S., Ansari, S. A., Ansari, M. I., Fujita, M., & Hasanuzzaman, M. (2021). Abiotic stress and reactive oxygen species: Generation, signaling, and defense mechanisms. *Antioxidants*, *10*(2), 277. https://doi.org/10.3390/antiox10020277

Saleah, S. A., Kim, S., Luna, J. A., Wijesinghe, R. E., Seong, D., Han, S., Kim, J., & Jeon, M. (2023). Optical coherence tomography as a non-invasive tool for plant material characterization in agriculture: A review. *Sensors*, *24*(1), 219. https://doi.org/10.3390/s24010219

Saleah, S. A., Lee, S. Y., Wijesinghe, R. E., Lee, J., Seong, D., Ravichandran, N. K., Jung, H. Y., Jeon M., & Kim, J. (2022). Optical signal intensity incorporated rice seed cultivar classification using optical coherence tomography. *Computers and Electronics in Agriculture*, *198*, 107014. https://doi.org/10.1016/j.compag.2022.107014

Saleah, S. A., Seong, D., Han, S., Wijesinghe, R. E., Ravichandran, N. K., Jeon, M., & Kim, J. (2021). Integrated quad-scanner strategy-based optical coherence tomography for the whole-directional volumetric imaging of a sample. *Sensors*, *21*(4), 1305. https://doi.org/10.3390/s21041305

Sandermann, H., Ernst, D., Heller, W., & Langebartels, C. (1998). Ozone: an abiotic elicitor of plant defence reactions. *Trends in Plant Science*, *3*(2), 47-50. https://doi.org/10.1016/S1360-1385(97)01162-X

Santiago, J. V., Inoue, K., & Tonokura, K. (2022). Modeling ground ozone concentration changes after variations in precursor emissions and assessing their benefits in the Kanto Region of Japan. *Atmosphere*, *13*(8), 1187. https://doi.org/10.3390/atmos13081187

Sharma, Y. K., & Davis, K. R. (1997). The effects of ozone on antioxidant responses in plants. *Free Radical Biology and Medicine*, *23*(3), 480-488. https://doi.org/10.1016/S0891-5849(97)00108-1

Silva, V. B., Andrade De Jesus, D., Klein, S., van Walsum, T., Cardoso, J., Brea, L. S., & Vaz, P. G. (2022). Signal-carrying speckle in optical coherence tomography: a methodological review on biomedical applications. *Journal of Biomedical Optics*, *27*(3), 030901-030901. https://doi.org/10.1117/1.JBO.27.3.030901

Singh, P., Chatterjee, A., Rajput, L. S., Rana, S., Kumar, S., Nataraj, V., Bhatia, V., & Prakash, S. (2021). Development of an intelligent laser biospeckle system for early detection and classification of soybean seeds infected with seed-borne fungal pathogen (*Colletotrichum truncatum*). *Biosystems*

Engineering, *212*, 442-457. https://doi.org/10.1016/j.biosystemseng.2021.11.002

Srimal, L. K. T. (2015a). *Development of functional optical coherence tomography (fOCT) for monitoring environmental effects on plants* (Doctoral dissertation, Saitama University, Saitama, Japan).

Srimal, L. K. T., Kadono, H., & Rajagopalan, U. M. (2013). Optical coherence tomography biospeckle imaging for fast monitoring varying surface responses of a plant leaf under ozone stress. *Proceedings of SPIE, the International Society for Optical Engineering*. https://doi.org/10.1117/12.2031062.

Srimal, L. K. T., Rajagopalan, U. M., & Kadono H. (2014). Optical Coherence Tomography (OCT) biospeckle signal analysis to investigate response of plant leaves to ozone. *Proceedings of the 23rd Congress of International Commission for Optics (ICO23), Santiago de Compostela, Spain.*

Srimal, L. K. T., Rajagopalan, U. M., & Kadono, H. (2015b). Functional optical coherence tomography (fOCT) biospeckle imaging to investigate response of plant leaves to ultra-short term exposure of Ozone. *Journal of Physics Conference Series*, *605*, 012013–012013. https://doi.org/10.1088/1742-6596/605/1/012013.

Srinivasan, V. J., Chen, Y., Duker, J. S., & Fujimoto, J. G. (2009). *In vivo* functional imaging of intrinsic scattering changes in the human retina with high-speed ultrahigh resolution OCT. *Optics Express*, *17*(5), 3861-3877. https://doi.org/10.1364/OE.17.003861

Steiner, R., Kunzi-Rapp, K., & Scharffetter-Kochanek, K. (2003). Optical coherence tomography: clinical applications in dermatology. *Medical Laser Application*, *18*(3), 249-259. https://doi.org/10.1078/1615-1615-00107

Szkulmowski, M., Gorczynska, I., Szlag, D., Sylwestrzak, M., Kowalczyk, A., & Wojtkowski, M. (2012). Efficient reduction of speckle noise in Optical Coherence Tomography. *Optics Express*, *20*(2), 1337-1359. https://doi.org/10.1364/OE.20.001337

Taiz, L., & Zeiger, E. (2002). *Plant Physiology*. Sunderland, MA. *Sinauer Associates, Inc., Publishers*, *3*, 484. https://pmc.ncbi.nlm.nih.gov/articles/PMC4242361/

Tang, X., Zhong, P., Gao, Y., & Hu, H. (2021a). Numerical model for evaluating the speckle activity and characteristics of bone tissue under the biospeckle laser system. *Journal of Innovative Optical Health Sciences*, *14*(06), 2150020. https://doi.org/10.1142/S1793545821500206

Tang, X., Zhong, P., Li, Z., Gao, Y., & Hu, H. (2021b). Evaluation of biological speckle activity: Using variational mode decomposition. *Optik*, *243*, 167475. https://doi.org/10.1016/j.ijleo.2021.167475

Thilakarathne, B. L. S., Rajagopalan, U. M., Kadono, H., & Yonekura, T. (2014). An optical interferometric technique for assessing ozone induced damage and recovery under cumulative exposures for a Japanese rice cultivar. *Springer Plus*, *3*, 1-12. https://doi.org/10.1186/2193-1801-3-89

Thilakarathne, B. L. S., Rajagopalan, U. M., Kadono, H., & Yonekura, T. (2014). High speed and high precision optical interferometric technique to investigate instantaneous growth related changes of plant leaves. *Plant Biotechnology*, *31*(3), 195-205. https://doi.org/10.5511/plantbiotechnology.14.0331a

Turc, B., Jolivet, Y., Cabané, M., Schaub, M., & Vollenweider, P. (2023). Ante- and post-mortem cellular injury dynamics in hybrid poplar foliage as a function of phytotoxic O_3 dose. *Plos one*, 18(3), e0282006. https://doi.org/10.1371/journal.pone.0282006

Vollenweider, P., Ottiger, M., & Günthardt-Goerg, M. S. (2003). Validation of leaf ozone symptoms in natural vegetation using microscopical methods. *Environmental Pollution*, *124*(1), 101-118. https://doi.org/10.1016/S0269-7491(02)00412-8

Wang, T., Xue, L., Feng, Z., Dai, J., Zhang, Y., & Tan, Y. (2022). Ground-level ozone pollution in China: a synthesis of recent findings on influencing factors and impacts. *Environmental Research Letters*, *17*(6), 063003. https://doi.org/10.1088/1748-9326/ac69fe

Wang, X., Manning, W., Feng, Z., & Zhu, Y. (2007). Ground-level ozone in China: distribution and effects on crop yields. *Environmental Pollution*, *147*(2), 394-400. https://doi.org/10.1016/j.envpol.2006.05.006

Wei, J., Li, Z., Li, K., Dickerson, R. R., Pinker, R. T., Wang, J., Liu, X., Sun, L., Xue, W., & Cribb, M. (2022). Full-coverage mapping and spatiotemporal variations of ground-level ozone (O_3) pollution from 2013 to 2020 across China. *Remote Sensing of Environment*, *270*, 112775. https://doi.org/10.1016/j.rse.2021.112775

Wei, X., & Gu, B. (Eds.). (2021). *Optical imaging in human disease and biological research*. Singapore: Springer. https://doi.org/10.1007/978-981-15-7627-0

Wijesinghe, R. E., Lee, S. Y., Kim, P., Jung, H. Y., Jeon, M., & Kim, J. (2016a). Optical inspection and morphological analysis of *Diospyros kaki* plant leaves for the detection of circular leaf spot disease. *Sensors*, *16*(8), 1282. https://doi.org/10.3390/s16081282

Wijesinghe, R. E., Lee, S. Y., Kim, P., Jung, H. Y., Jeon, M., & Kim, J. (2017a). Optical sensing method to analyze germination rate of *Capsicum annum* seeds treated with growth-promoting chemical compounds using optical coherence tomography. *Journal of Biomedical Optics*, *22*(9), 091502-091502. https://doi.org/10.1117/1.JBO.22.9.091502

Wijesinghe, R. E., Lee, S. Y., Ravichandran, N. K., Han, S., Jeong, H., Han, Y., Jung, H. Y., Kim, P., Jeon, M., & Kim, J. (2017b). Optical coherence tomography-integrated, wearable (backpack-type), compact diagnostic imaging modality for *in situ* leaf quality assessment. *Applied Optics*, *56*(9), D108-D114. https://doi.org/10.1364/AO.56.00D108

Wijesinghe, R. E., Lee, S. Y., Ravichandran, N. K., Shirazi, M. F., Kim, P., Jung, H. Y., Jeon, M., & Kim, J. (2018). Biophotonic approach for the characterization of initial bitter-rot progression on apple specimens using optical coherence tomography assessments. *Scientific Reports*, *8*(1), 15816. https://doi.org/10.1038/s41598-018-

33791-3

Wijesinghe, R. E., Park, K., Kim, P., Oh, J., Kim, S. W., Kim, K., Beop-Min Kim, Mansik Jeon, & Kim, J. (2016b). Optically deviated focusing method based high-speed SD-OCT for *in vivo* retinal clinical applications. *Optical Review*, *23*, 307-315. https://doi.org/10.1007/s10043-015-0154-x

Wojtkowski, M., Leitgeb, R., Kowalczyk, A., Bajraszewski, T., & Fercher, A. F. (2002). *In vivo* human retinal imaging by Fourier domain optical coherence tomography. *Journal of Biomedical Optics*, *7*(3), 457-463. https://doi.org/10.1117/1.1482379

Xu, Y., Feng, Z., Peng, J., & Uddling, J. (2023). Variations in leaf anatomical characteristics drive the decrease of mesophyll conductance in poplar under elevated ozone. *Global Change Biology*, *29*(10), 2804-2823. https://doi.org/10.1111/gcb.16621

Yoshikado, H. (2023). Correlation between air temperature and surface ozone in their extreme ranges in the greater Tokyo region. *Asian Journal of Atmospheric Environment*, *17*(1), 9. https://doi.org/10.1007/s44273-023-00010-z

Zdunek, A., Adamiak, A., Pieczywek, P. M., & Kurenda, A. (2014). The biospeckle method for the investigation of agricultural crops: A review. *Optics and Lasers in Engineering*, *52*, 276-285. https://doi.org/10.1016/j.optlaseng.2013.06.017

Zheng, S., Bai, Y., Xu, Z., Liu, P., & Ni, G. (2021). Optical coherence tomography for three-dimensional imaging in the biomedical field: a review. *Frontiers in Physics*, *9*, 744346. https://doi.org/10.3389/fphy.2021.744346

J.Natn.Sci.Foundation Sri Lanka 2025 53 (3): 259 - 272
DOI: http://dx.doi.org/10.4038/jnsfsr.v53i3.12624

RESEARCH ARTICLE

Earthquake Engineering

Effect of initial imperfections on the seismic performance of thin-walled steel hollow piers: A numerical approach

AGYM Kumara, ACD Pigera, NAI Ayodya, JASC Jayasinghe* and CS Bandara
Department of Civil Engineering, Faculty of Engineering, University of Peradeniya, Peradeniya, Sri Lanka.

Submitted: 30 March 2025; Revised: 10 August 2025; Accepted: 27 August 2025

Abstract: This research investigates the influence of initial imperfections on the seismic performance of steel hollow piers, which are crucial components of bridges and other critical structures. The study focuses on two main types of initial imperfections: residual stresses and global geometric imperfections, which are key parameters influencing the seismic performance of thin-walled steel hollow piers. The goal is to understand how these imperfections affect the pier's ductility, maximum energy dissipation capacity, and overall behaviour under uni-directional cyclic loads which simulates the seismic loading conditions. A numerical model was developed using the finite element method (FEM), incorporating various imperfection profiles and tested under different loading directions. Parametric studies were conducted to observe the effects of imperfections within permissible limits, as well as beyond those limits. The results revealed that the residual stresses had a negligible impact on seismic performance. However, global geometric imperfections significantly influenced the performance when the bend exceeded the allowable limit, and loaded in line with the imperfection, which is particularly critical. The study shows that global imperfections lead to a significant reduction in maximum strength, with reductions as high as 24% when loaded in line with the imperfection and between 1% and 11% when loaded perpendicularly, and these findings indicate that global imperfections play a dominant role in failure modes due to lateral cyclic loading.

Keywords: Cyclic loading, FE modelling, geometric imperfections, residual stresses, steel hollow piers.

INTRODUCTION

Steel hollow box piers, constructed from welded steel plates, are widely used as essential lateral and vertical force-resisting elements in structures such as bridges, towers, flyovers, wind turbines, buildings, offshore platforms, elevated storage tanks, and transmission towers due to their compact cross-section and advantages such as high earthquake resistance, strength-to-weight ratio, and torsional stiffness (Kearns *et al.*, 1976; Thevega *et al.*, 2021). However, with global population growth and rapid urbanization, structural damage due to seismic events has become increasingly critical. Earthquakes are among the most destructive natural disasters, causing significant economic losses and casualties. Dense urban populations and critical infrastructure in earthquake-prone areas heighten the risks to vital structures like bridges (Aoki *et al.*, 2005). In Japan, for instance, earthquakes between 1923 and 1983 damaged over 3,000 bridges, emphasizing the need for improved seismic design (Kearns *et al.*, 1976).

Traditional seismic design models primarily consider constant axial loads and uni-directional forces. However, real-world seismic movements are multi-dimensional and highly complex. Research indicates that multi-directional

* Corresponding author (supunj@eng.pdn.ac.lk; https://orcid.org/0000-0003-1054-9358)

cyclic lateral stresses impact thin-walled steel tubular columns more severely than single-directional forces. Global buckling under cyclic loading can significantly reduce the strength and ductility of columns, increasing their susceptibility to failure (Aoki *et al.*, 2005). The most common failure mode in steel columns of highway bridge piers under lateral cyclic loading is excessive lateral deformation caused by local buckling of steel plates (Thevega *et al.*, 2021). Both local and global buckling contribute to strength and ductility reduction, ultimately leading to failure.

Imperfections in fabrication of such structures are an unavoidable circumstance. These imperfections can be mainly categorized into three sections: residual stresses, local geometric imperfections, and global geometric imperfections (Sato *et al.*, 2017). This study focuses on the effects of global imperfections and residual stresses on seismic performance. Early geometric imperfections and residual stresses influence the initial stiffness and strength of thin-walled structures under monotonic loading (Mamaghani *et al.*, 1996; Banno *et al*., 2005). While previous studies, such as those by Jenothan *et al.* (2023), did not account for initial geometric imperfections and residual stresses due to a lack of quantification in tested columns, this study aims to bridge that research gap.

The main focus of this study is to evaluate the seismic performance of thin-walled steel hollow piers by analyzing the effects of initial imperfections, including residual stresses and global geometric imperfections. A finite element (FE) model of the steel pier was developed using ABAQUS software, with validation achieved through comparison with experimental data from Susantha *et al.* (2007). Parametric studies were conducted numerically to assess the influence of residual stresses and geometric imperfections. A selected residual stress distribution from the literature was applied to the model to examine its impact on seismic behaviour. Various curved shape profiles with increasing deflection values were introduced to evaluate global geometric imperfections, as referenced by Sato *et al.* (2017), both within and beyond permissible limits. The study also analyzed how different loading directions influenced the pier's strength and stability.

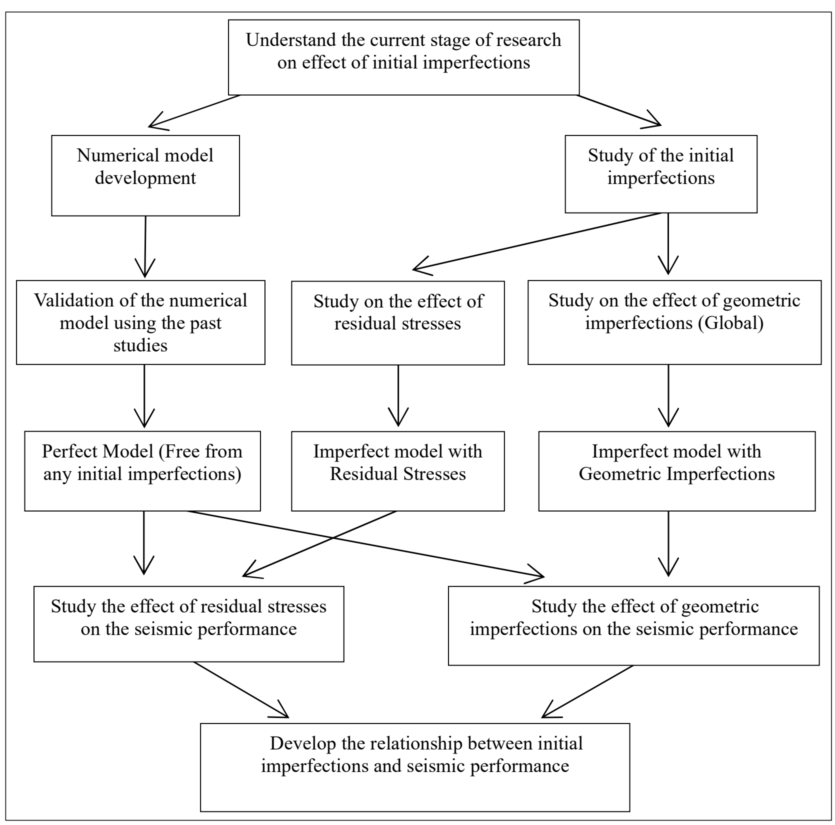

Figure 1: Flow chart of methodology

In addition to these factors, key design parameters such as axial load-to-yield load ratio (P/P_y), width-to-thickness ratio (R_f), and slenderness ratio (λ) were examined in relation to imperfections. The seismic performance was evaluated by analyzing normalized ductility (δ_{max}/δ_y) and maximum strength capacity (H_{max}/H_y), providing insights into how imperfections affect the pier's response during seismic events.

MATERIALS AND METHODS

Methodology

A research methodology was developed addressing all the research gaps, leading to a parametric study. Following validation of the numerical model, parametric studies were conducted as outlined in the overall methodology diagram shown in Figure 1, which presents a structured approach, beginning with an initial literature review of research on initial imperfections, followed by detailed parametric studies targeting two imperfection types: residual stress (RS) and global geometric imperfections (GI).

Material properties

This study utilizes ABAQUS, a commercial finite element software, to perform FE analysis, incorporating both material and geometric nonlinearities throughout the computation. Accurate material properties are the main factor in obtaining realistic results through numerical simulations. A number of material models for common materials such as steel, concrete and various composites are readily available in ABAQUS. Basic material properties such as yield stress, ultimate stress, Young's modulus, and Poisson's ratio, which determine the behaviour of steel, were introduced to the software. A combined hardening material model is employed, incorporating the Von Mises yield criterion alongside an associated plastic flow rule, effectively modeling the inelastic behaviour of materials under cyclic loading. Normal-strength steel, specifically SM490 (Susantha *et al.*, 2005) grade as per Japanese Industrial Standards, is used in this investigation. The detailed material properties, consistent with those used by Susantha *et al.* (2005), are provided in Table 1. A simplified bilinear material model shown in Figure 2 was used for the analysis for efficient computations without compromising the accuracy of the results.

Table 1: Material properties (Susantha *et al.*, 2005)

Parameters	Values
Yield stress (σ_y)	412 MPa
Young's modulus (E_s)	206000 MPa
Ultimate stress (σ_u)	650 MPa
Poisson's ratio (v)	0.276

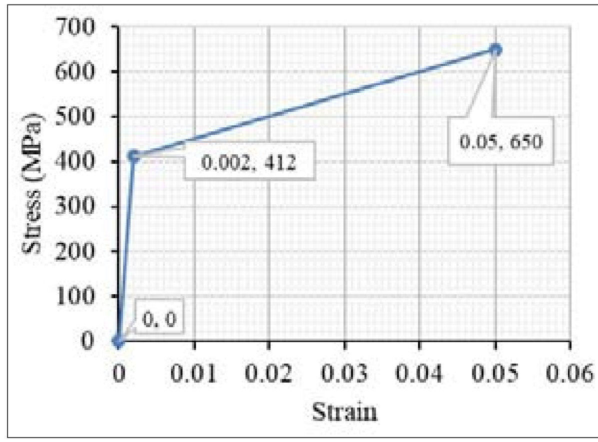

Figure 2: Bilinear stress-strain steel model

Geometric details of columns

Figure 3 displays the longitudinal dimensions of the modeled pier in a 3D view, highlighting cross-sectional and diaphragm dimensions. The same cross-sectional details were applied for validation and the residual stress study, while the parametric analysis for global imperfections included variations in cross-sectional dimensions and pier heights.

Loading procedure

The loading setup in this study starts with an initial axial force to represent the loads coming from the superstructure, denoted as P, followed by the application of unidirectional cyclic lateral loads. The axial force P is represented as a ratio, P/P_y, where P_y refers to the axial force at the yield stress of the steel, in a given cross-section, set to 0.2 in this analysis. A uni-directional cyclic load, which is varying according to the pattern shown in Figure 4 was applied at the top of the model to represent simplified earthquake condition while keeping the constant axial load applied, as shown in Figure 5.

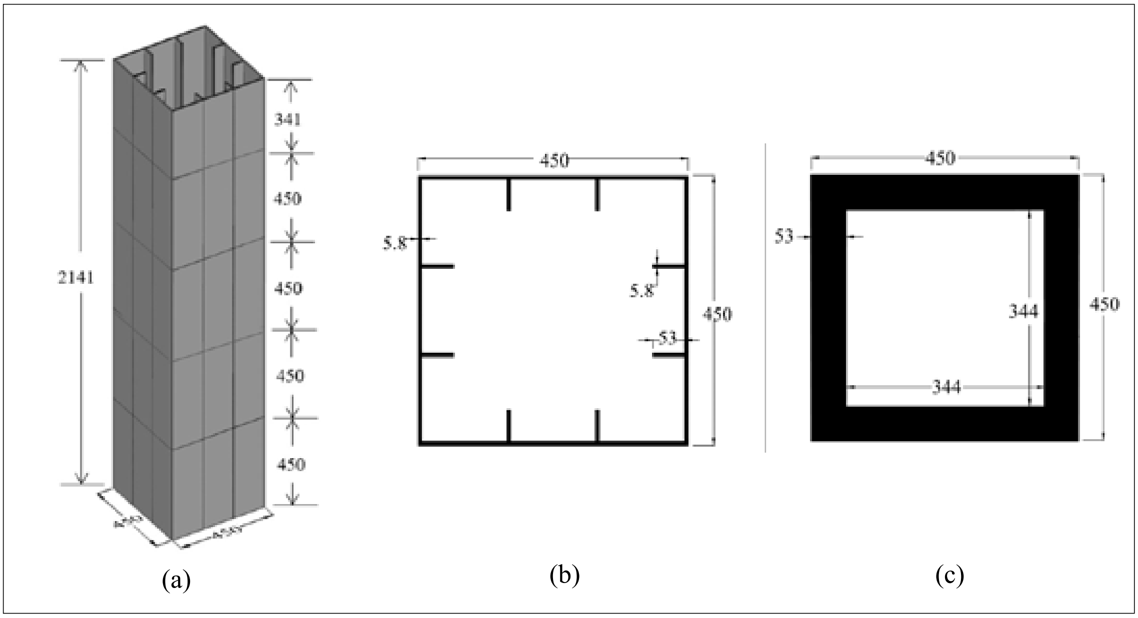

Figure 3: Dimensions of modelled pier: (a) longitudinal, (b) cross-section and (c) intermediate diaphragms (all dimensions are in millimetres)

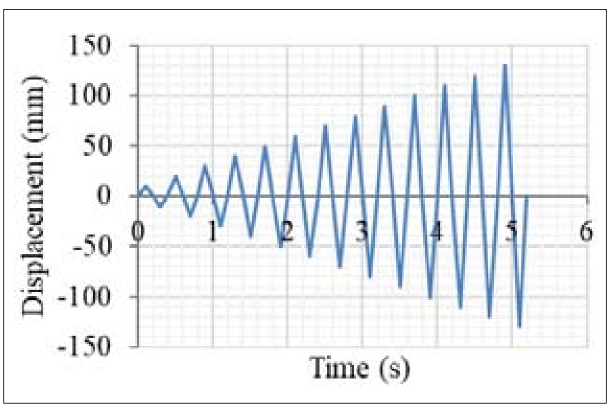

Figure 4: Cyclic loading pattern

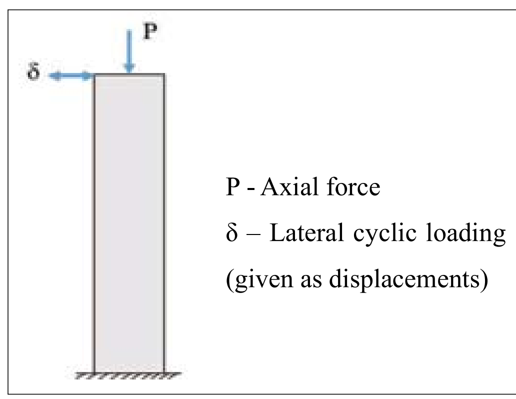

Figure 5: Loading arrangement

A 'perfect model,' which excludes any initial imperfections, was developed in order to compare the performances of the piers in which the initial imperfections were introduced. In this model, the box pier, longitudinal stiffeners, and diaphragms are represented using four-node shell elements with reduced integration (S4R) and five integration points through the thickness. A fixed boundary condition is applied at the base, and axial and lateral cyclic loads are introduced through a reference point linked to the top of the column via a rigid connection. Observations from the previous studies shows that the square box columns made of thin-walled steel indicate that local buckling typically occurs between the base and the bottom diaphragm near the column base. The entire pier is meshed with a 25 mm S4R element size as shown in Figure 6. Mesh convergence testing verified that this mesh density provides accurate results while keeping computational time manageable.

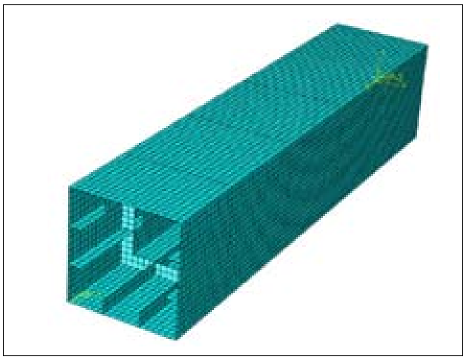

Figure 6: Numerical model of the steel pier

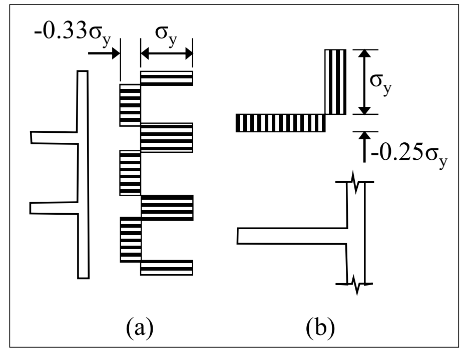

Figure 7: Assumed residual stress distributions: (a) panel and (b) stiffener (Susantha *et al.*, 2005)

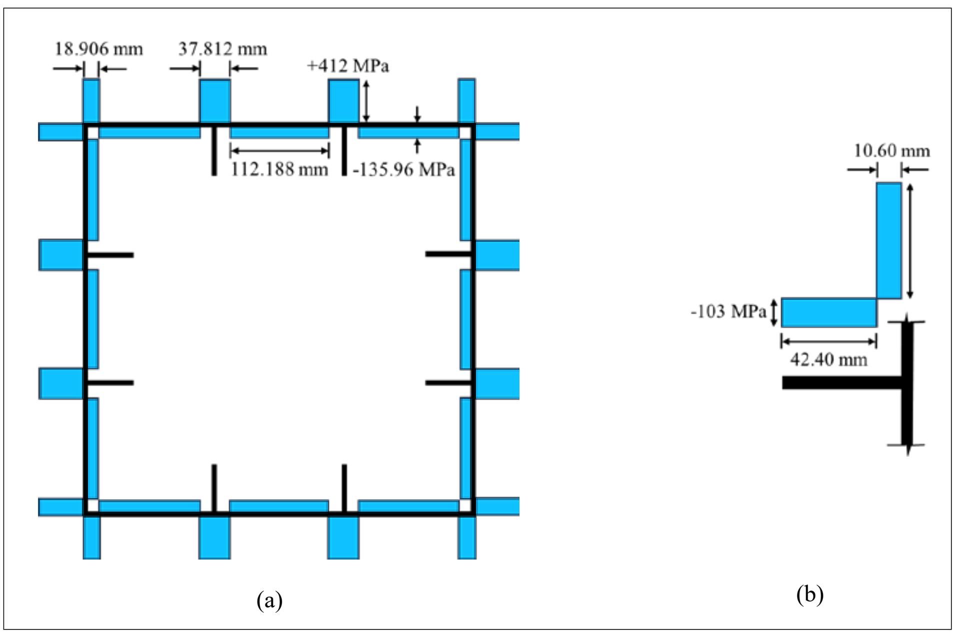

Figure 8: Calculated residual stress distribution values: (a) test pier and (b) stiffener

Numerical model with residual stress

This section evaluates the impact of residual stress on the seismic behaviour of steel piers. The investigation was based on the claim by Jenothan *et al.* (2023a) that neither initial geometric imperfections nor residual stresses from welding flange and web plates significantly influence cyclic behaviour beyond the first half-cycle. To verify this, a residual stress distribution proposed by Susantha *et al.* (2005) was selected and applied to the pier, as shown in Figure 7. A similar distribution was also recommended by Yao & Fujikubo (2016) for T-sections.

The proposed model for the residual stress distribution accurately represents its effects on the pier, providing the necessary details for precise stress modeling and calculation. The residual stress is applied in the axial direction following specified values, ensuring a realistic representation in the numerical model. Figure 8 illustrates the applied stress distribution, which is also incorporated into the steel plate, stiffeners, and diaphragms.

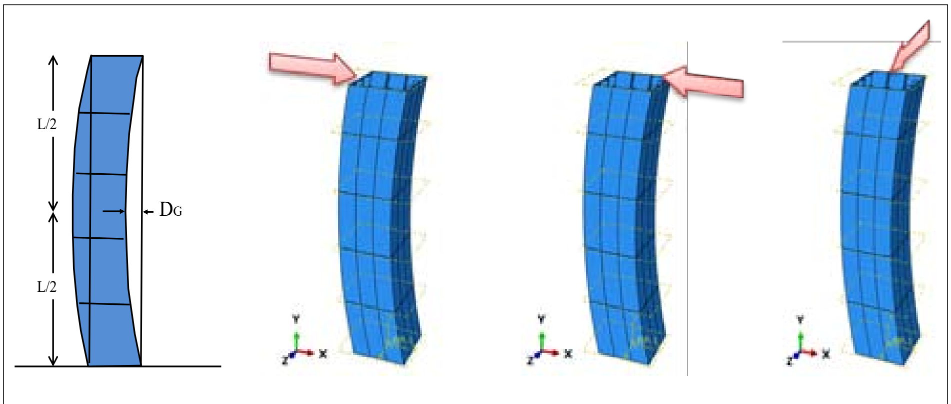

Figure 9: Global geometric imperfection modeling: (a) indication of the curved profile, (b) unidirectional cyclic loading applied in +X-direction and (c) unidirectional cyclic loading applied in -X-direction (d) unidirectional cyclic loading applied in Z-direction

Table 2: Profiles of global geometric imperfections (Permissible range: $D_G \leq L/1500$)

Profile	Initial central deflection (D_G)	Loading Direction
GI 1	$2141 \times \frac{3/3}{1500} = 1.427$ mm	
GI 2	$2141 \times \frac{2/3}{1500} = 0.951$ mm	X - Direction
GI 3	$2141 \times \frac{1/3}{1500} = 0.476$ mm	
GI 4	$2141 \times \frac{3/3}{1500} = 1.427$ mm	
GI 5	$2141 \times \frac{2/3}{1500} = 0.951$ mm	Z - Direction
GI 6	$2141 \times \frac{1/3}{1500} = 0.476$ mm	

Numerical model with global geometric imperfections

The global geometric imperfection taken into account is a bend in the steel pier, as suggested by Sato *et al.* (2017). Therefore, the numerical model must integrate this imperfection profile while maintaining the same arrangement of stiffeners and intermediate diaphragms, as illustrated in Figure 9. In the parametric study, a single curved shape profile with varying bend amplitudes was examined to analyze the way it is influenced by unidirectional cyclic loading, as mentioned in Table 2. The study identifies different cases of global geometric imperfections based on the direction of cyclic load application, as depicted in Figure 9 (b), (c) and (d). The exaggerated shapes illustrating these profiles are presented in Figure 9 (a) to provide a clear indication of the curved profile. To further investigate the effect of these bends, a parametric study was conducted using steel piers with the same cross-sectional arrangement.

Table 3: The selected values for the parametric study

Width to thickness ratio - R_f	Slenderness ratio - λ	Applied axial load to yield load ratio - P/Py
0.5	0.3	0.15
0.6	0.4	
0.7	0.5	0.20
0.8	0.6	

The selected values for the parametric study are provided in Tables 2 and 3. The bend shapes are selected within a range of 0 mm to 70 mm, both within and outside the permissible range specified by Sato *et al.* (2017), where the permissible deviation for global imperfections was ≤ L/1500. Global geometric imperfections are introduced by modeling the curved shape in ABAQUS software. The results obtained from these simulations are used to determine a fixed curvature for further studies on the sensitivity analysis. The sensitivity analysis was focused on the main design parameters of steel piers, such as width-to-thickness ratio, slenderness ratio, and axial load-to-yield load ratio, while keeping the stiffener properties and loading arrangement constant. Tables 4 and 5 contain the critical data necessary to model the test piers in this sensitivity analysis.

Table 4: Essential values for modeling (P/P_y=0.15)

No	P/P_y	R_f	λ	P(kN)	δ_y	H_y/(kN)
1	0.15	0.50	0.30	905.51	10.75	469.06
2	0.15	0.50	0.40	905.51	18.70	343.61
3	0.15	0.50	0.50	905.51	28.38	266.70
4	0.15	0.50	0.60	905.51	39.30	214.46
5	0.15	0.60	0.30	795.49	10.82	409.93
6	0.15	0.60	0.40	795.49	18.85	300.08
7	0.15	0.60	0.50	795.49	28.55	233.24
8	0.15	0.60	0.60	795.49	39.68	187.13
9	0.15	0.70	0.30	691.05	10.70	353.03
10	0.15	0.70	0.40	691.05	18.50	259.54
11	0.15	0.70	0.50	691.05	28.14	201.18
12	0.15	0.70	0.60	691.05	39.03	161.61
13	0.15	0.80	0.30	606.96	10.42	308.77
14	0.15	0.80	0.40	606.96	18.11	226.35
15	0.15	0.80	0.50	606.96	27.47	175.77
16	0.15	0.80	0.60	606.96	38.12	141.16

Table 5: Essential values for modeling (P/P_y=*0.20*)

No	P/P_y	R_f	λ	P(kN)	δ_y	H_y / (kN)
17	0.20	0.50	0.30	1207.34	10.17	443.78
18	0.20	0.50	0.40	1207.34	17.54	322.30
19	0.20	0.50	0.50	1207.34	26.32	247.32
20	0.20	0.50	0.60	1207.34	35.93	196.03
21	0.20	0.60	0.30	1060.65	10.24	387.84
22	0.20	0.60	0.40	1060.65	17.69	281.48
23	0.20	0.60	0.50	1060.65	26.48	216.31
24	0.20	0.60	0.60	1060.65	36.27	171.04
25	0.20	0.70	0.30	921.40	10.12	333.99
26	0.20	0.70	0.40	921.40	17.35	243.46
27	0.20	0.70	0.50	921.40	26.09	186.56
28	0.20	0.70	0.60	921.40	35.67	147.71
29	0.20	0.80	0.30	809.29	9.86	292.13
30	0.20	0.80	0.40	809.29	16.99	212.32
31	0.20	0.80	0.50	809.29	25.47	163.01
32	0.20	0.80	0.60	809.29	34.84	129.02

RESULTS AND DISCUSSION

Validation of the numerical model

The importance of mesh density in getting accurate results was checked through a mesh sensitivity analysis. Figure 10 shows how different mesh sizes, from 50 mm to 10 mm, affect base shear results. This confirms that refining the mesh is necessary for reliable analysis. Based on this, a 25 mm mesh size was selected for the study.

The loading pattern displayed in Figure 4 was applied to the steel hollow column for model validation, with reference to experimental data from Susantha *et al.* (2007). The envelop curve of the FEM numerical model, shown in Figure 11, demonstrates favourable agreement with the experimental curve.

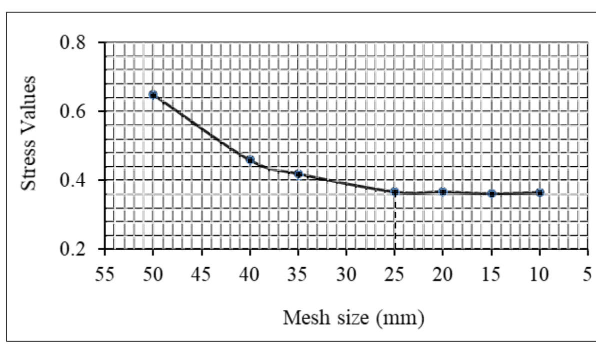

Figure 10: Variation of base stress with size of the mesh

Additionally, the numerical deformation shapes matched precisely with those from the experimental study. Figure 12 illustrates a comparison of the buckling shape at the fixed base observed by Susantha *et al.* (2007) with the buckling shape of the perfect model.

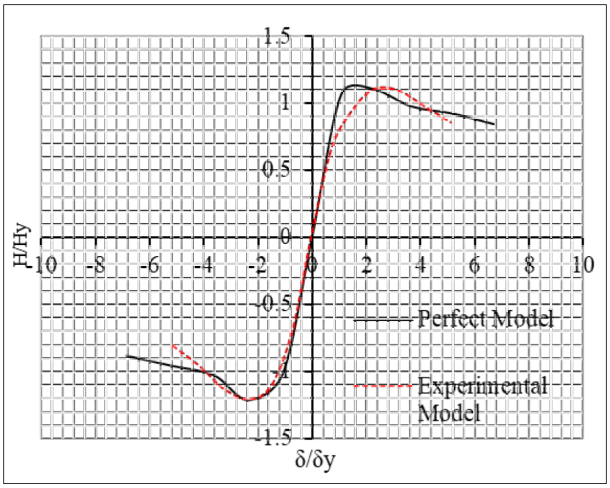

Figure 11: Envelope

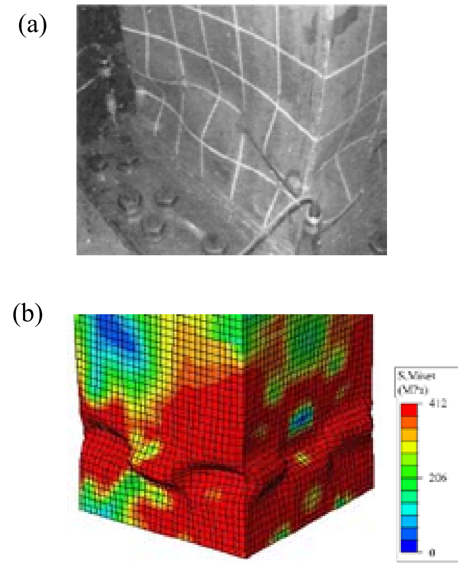

Figure 12: Buckling behaviour: (a) experimental model and (b) numerical model (Susantha *et al.*, 2007)

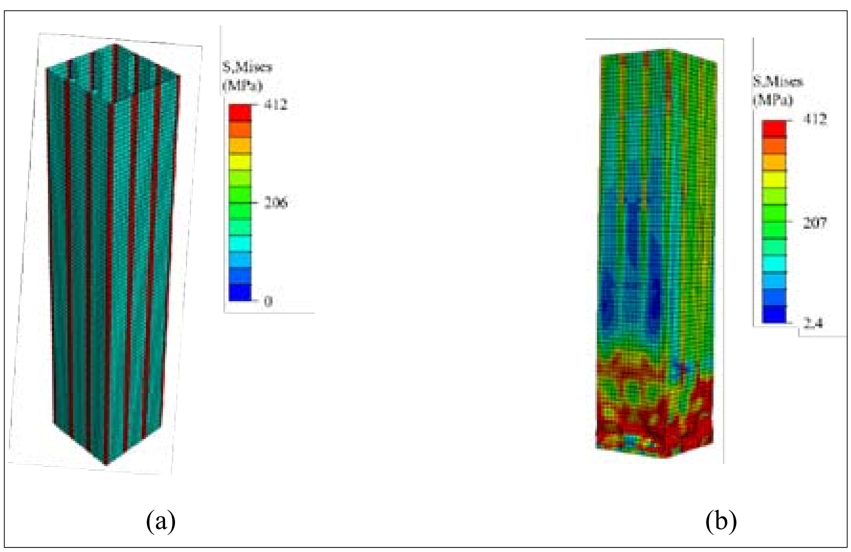

Figure 13: Model with residual stresses: (a) residual stress distribution of the pier and (b) deformed shape and von Mises stresses after failure

Results of residual stress study

In this study, residual stress distribution derived from Susantha *et al.* (2007) was incorporated into the test model, which allowed us to evaluate its impact on the seismic performance of steel hollow piers. A comparison with an idealized model under similar seismic conditions indicated that residual stress has a minimal impact on the seismic behaviour of steel piers. Figure 13(a) provides a visual representation of the stress distribution across the pier following the application of residual stresses, while Figure 13(b) illustrates the deformed shape and corresponding stress values after being subjected to lateral cyclic loading until failure.

Figure 14 presents a comparison between the perfect model (free from any initial imperfections) and the performance of the model with residual stresses, employing the envelop curve. Based on the results, the effect of residual stress on the seismic performance of steel hollow sections is negligible. The numerical analysis and comparison with experimental data indicate that the presence of residual stress does not significantly alter the structural behaviour under seismic loading.

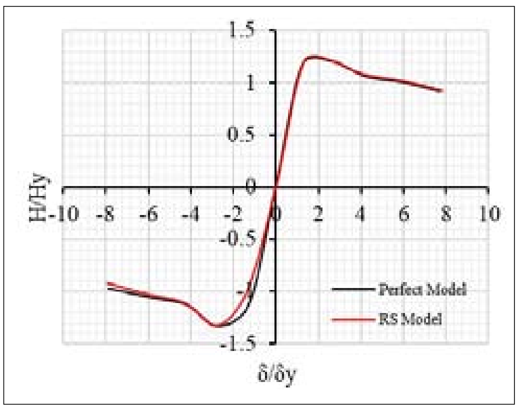

Figure 14: Comparison of the perfect model performance and RS model performance using envelop curve

Results of global geometric imperfections study

This section presents the results of the study on global geometric imperfections. First, the permissible range was checked using the test pier, as described by Sato *et al.* (2017). The results within this range are shown in Figure 15. Since there was no strength reduction within the permissible range, we examined cases beyond this limit (D_G > L/1500), as shown in Figure 16. A significant effect was observed when the bend profile was D_G = L/50. This condition was used for sensitivity analysis to evaluate its impact on R_f, H/H_y, and P/P_y, as presented in Table 3. The analysis was conducted for both X-direction and Z-direction loading conditions.

Tables 6 and 7 present the results for δ_{max}/δ_y of the sensitivity analysis conducted in this study.

Table 6, δ_{max}/δ_y variation with R_f values for P/P_y = 0.15 does not show a consistent trend in δ_{max}/δ_y changes with different R_f values. In most cases, the δ_{max}/δ_y decreases as the λ value increases, although there are instances where it increases significantly. The overall tendency is a decrease in δ_{max}/δ_y with rising λ values, but this variation occurs because δ_{max}/δ_y is influenced by multiple factors related to the cross-sectional parameters. Additionally, with the inclusion of global imperfections, the δ_{max}/δ_y shows variation when compared to the perfect model response. This indicates that δ_{max}/δ_y is indeed influenced by global imperfections. Further studies with possible experimental work should be conducted to identify a trend in variations of these parameters when the models are subjected to global imperfections.

Tables 6 and 7 present the results for δ_{max}/δ_y of the sensitivity analysis conducted in this study.

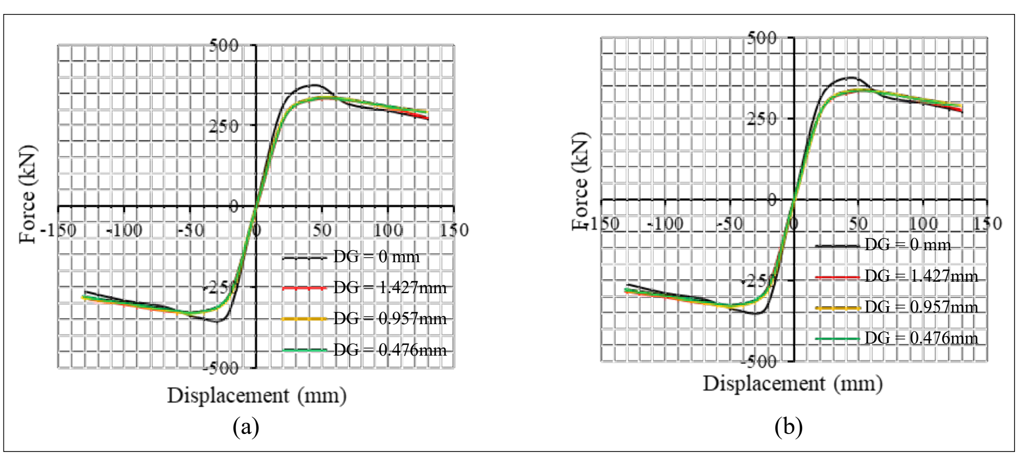

Figure 15: Results on permissible range: (a) X-direction loading and (b) Z-direction loading

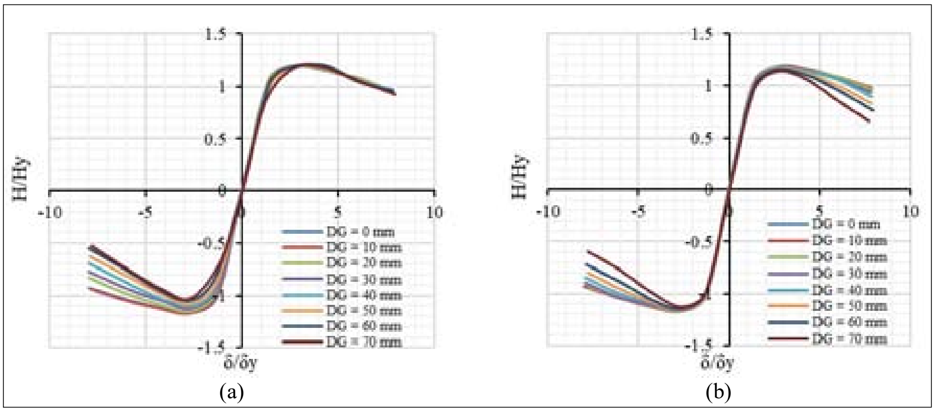

Figure 16: Comparison of results with different D_G values (a) X-direction loading, (b) Z-direction loading

Table 6: δ_{max}/δ_y variation with R_f values for $P/P_y = 0.15$

	X direction loading	Z direction loading
+ displacement	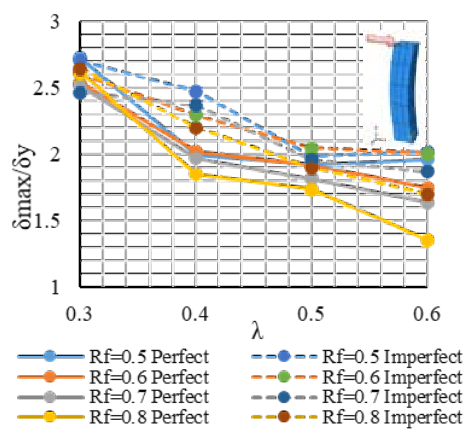	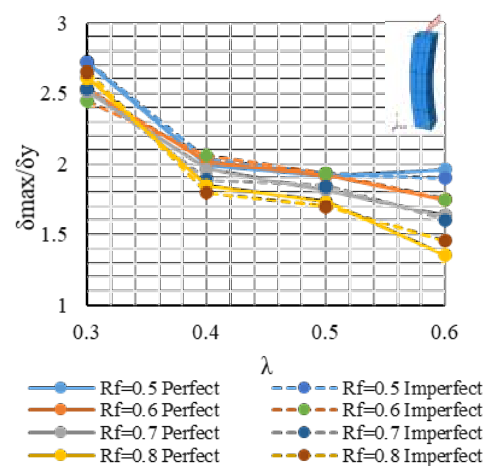
- displacement	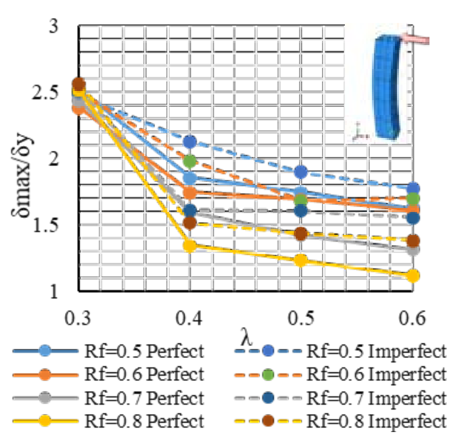	

Table 7: δ_{max}/δ_y variation with R_f values for $P/P_y = 0.20$

	X direction loading	Z direction loading
+ displacement	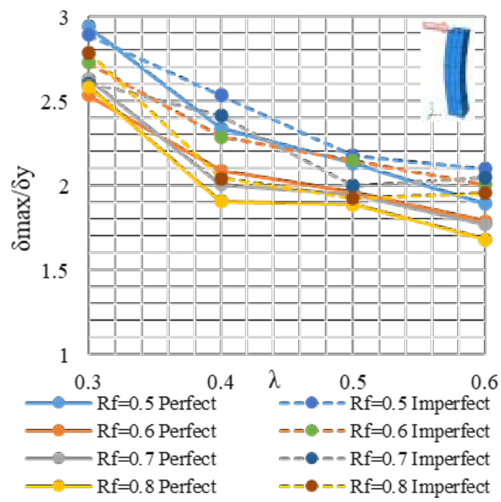	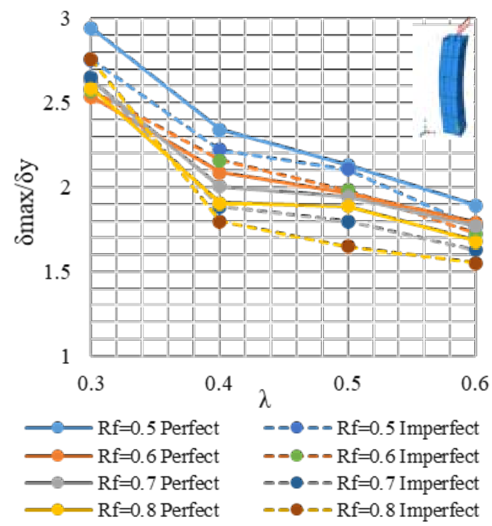
- displacement	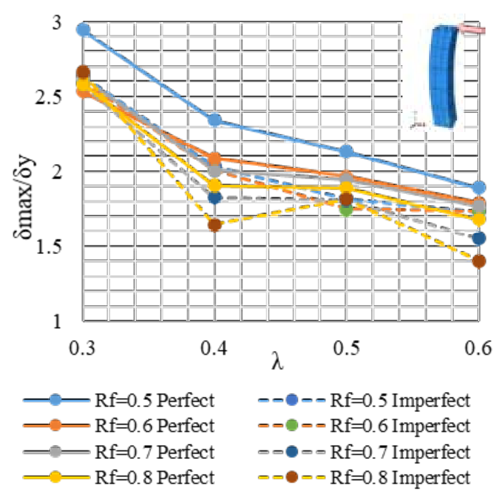	

For the case of P/P_y = 0.20, a clear trend could not be identified from the study either. However, similar to the P/P_y = 0.15 scenario, a reduction in δ_{max}/δ_y with increased λ values was observed, as shown in Table 7.

Tables 8 and 9 present the results for H_{max}/H_y of the sensitivity analysis conducted in this study.

From above percentage reduction values, it can be identified that the +X direction displacement heavily affects the maximum strength of the pier. For the case of R_f = 0.8 and λ = 0.6, there is a 24% reduction in +X direction displacement, but less than 11% in the -X direction. For the Z direction, both negative and positive displacements exhibit similar behaviour due to symmetry, with reductions ranging between 1% and 11%.

Table 8: Percentage reduction of H_{max}/H_y (P/P_y = 0.15)

R_f	λ	H_{max}/H_y +X Perfect	Imper-fect	% reduction	-X Perfect	Imper-fect	% reduction	Z Perfect	Imper-fect	% reduction
0.5	0.3	1.25	1.18	**5.49**	1.25	1.25	**-0.28**	1.25	1.23	**1.20**
	0.4	1.17	1.07	**8.91**	1.17	1.15	**1.77**	1.17	1.13	**4.02**
	0.5	1.14	1.01	**11.09**	1.14	1.12	**1.63**	1.14	1.09	**4.01**
	0.6	1.04	0.93	**10.19**	1.04	1.06	**-2.39**	1.04	0.97	**6.25**
0.6	0.3	1.22	1.13	**7.77**	1.22	1.19	**2.71**	1.22	1.19	**2.98**
	0.4	1.16	1.02	**11.71**	1.16	1.08	**6.53**	1.16	1.10	**4.88**
	0.5	1.12	0.97	**13.41**	1.12	1.08	**3.67**	1.12	1.08	**3.45**
	0.6	1.02	0.88	**13.70**	1.02	1.05	**-2.72**	1.02	0.95	**6.46**
0.7	0.3	1.20	1.10	**8.18**	1.20	1.14	**4.78**	1.20	1.17	**2.07**
	0.4	1.12	0.98	**12.22**	1.12	1.09	**3.15**	1.12	1.06	**5.00**
	0.5	1.09	0.93	**15.20**	1.09	1.05	**3.86**	1.09	1.04	**4.62**
	0.6	1.00	0.81	**18.92**	1.00	0.98	**1.94**	1.00	0.92	**8.38**
0.8	0.3	1.17	1.04	**10.86**	1.19	1.13	**5.39**	1.16	1.08	**7.27**
	0.4	1.10	0.90	**18.60**	1.11	1.07	**3.57**	1.10	1.01	**8.13**
	0.5	1.04	0.86	**17.06**	1.07	1.03	**4.01**	1.03	0.98	**4.85**
	0.6	0.98	0.79	**20.05**	0.97	0.92	**5.37**	1.00	0.90	**10.20**

Table 9: Percentage reduction of H_{max}/H_y (P/P_y = 0.20)

Rf	λ	H_{max}/H_y +X Perfect	Imper-fect	% reduction	-X Perfect	Imper-fect	% reduction	Z Perfect	Imper-fect	% reduction
0.5	0.3	1.28	1.19	**7.62**	1.28	1.28	**0.37**	1.28	1.25	**2.46**
	0.4	1.17	1.07	**8.71**	1.17	1.16	**1.05**	1.17	1.15	**2.12**
	0.5	1.13	1.02	**10.15**	1.13	1.13	**0.08**	1.13	1.10	**2.50**
	0.6	1.07	0.90	**15.34**	1.07	1.06	**0.28**	1.07	1.00	**6.34**
0.6	0.3	1.23	1.13	**7.97**	1.23	1.21	**1.37**	1.23	1.21	**1.55**
	0.4	1.16	1.01	**12.90**	1.16	1.11	**4.90**	1.16	1.11	**4.26**
	0.5	1.11	0.95	**14.64**	1.11	1.02	**8.30**	1.11	1.08	**2.74**
	0.6	1.05	0.84	**19.97**	1.05	1.00	**4.71**	1.05	0.97	**7.76**
0.7	0.3	1.20	1.10	**8.66**	1.20	1.12	**6.99**	1.20	1.18	**2.02**
	0.4	1.13	0.98	**13.10**	1.13	1.07	**5.12**	1.13	1.07	**4.80**
	0.5	1.08	0.88	**18.37**	1.08	1.01	**6.70**	1.08	1.05	**2.95**
	0.6	1.04	0.78	**24.97**	1.04	0.97	**6.64**	1.04	0.93	**10.46**
0.8	0.3	1.17	0.99	**15.95**	1.17	1.04	**11.09**	1.17	1.10	**6.24**
	0.4	1.09	0.95	**12.85**	1.09	0.99	**8.81**	1.09	1.01	**6.99**
	0.5	1.04	0.87	**15.73**	1.04	0.99	**4.60**	1.04	0.95	**8.14**
	0.6	1.00	0.76	**24.00**	1.00	0.94	**6.06**	1.00	0.89	**10.79**

CONCLUSION

This section summarizes the key findings on how residual stress and global geometric imperfections impact the seismic performance of steel hollow piers. The conclusions are drawn from parametric studies, highlighting the effects of global imperfections, especially residual stresses, on the overall behaviour of piers under seismic loading. These findings provide valuable insights into the role of global imperfections and lay the groundwork for future studies on the combined effects of multiple imperfections.

- The results indicate that residual stress minimally impacts the seismic performance of steel hollow piers. Comparisons with the perfect model reveal negligible differences in ductility and maximum strength, suggesting that residual stress does not significantly influence failure modes or overall seismic behaviour, and its effect is relatively minor in this context.

- Global geometric imperfections have a significant impact on the seismic performance of steel hollow piers when they exceed the permissible range (D_G > L/1500). The effect becomes more pronounced as P/P_y and λ values increase, indicating a strong correlation between these parameters and the reduction in ductility and strength (up to 24%) which emphasizes the significance of considering the effect of global imperfections in steel box piers in the design stages. Additionally, the direction of loading relative to the imperfection shape plays a critical role, with loading towards the bend causing a more significant reduction in performance compared to other directions.

- The direction of loading relative to the imperfection profile notably affects seismic behaviour. Loading in the +X direction results in a more pronounced reduction in performance compared to the -X direction. In the Z direction, although the behaviour is not perfectly symmetrical, the observed differences are minor.

REFERENCES

Alpsten, G.A., & Tall, L., 1970. *Residual stresses in heavy welded shapes* (pp. 93-105). American Welding Society.

Aoki, T., & Susantha, K.A.S. (2005). Seismic Performance of Rectangular-Shaped Steel Piers under Cyclic Loading. *Journal of Structural Engineering*, 131(2), pp.240–249. doi:https://doi.org/10.1061/(asce)0733-9445(2005)131:2(240)

Bambach, M.R., & Rasmussen, K.J.R., 2001, June. Residual stresses in unstiffened plate specimens. In *Third International Conference on Thin-Walled Structures, Cracow, Poland* (pp. 87-93).

Bjorhovde, R., Brozzetti, J., Alpsten, G.A., & Tall, L., 1972. Residual stresses in thick welded plates. *WELD J--MIAMI FLA--*, *51*(8), p.292.

British Standards Institution (2022). *BS EN 1993-1-5. Eurocode 3. Design of Steel Structures*.

Cao, X., Xu, Y., Kong, Z., Shen, H., & Zhong, W., 2017. Residual stress of 800MPa high strength steel welded T section: Experimental study. *Journal of Constructional Steel Research*, 131, pp.30–37. https://doi.org/10.1016/j.jcsr.2016.12.001.

Chen, B.-Q., & C. Guedes Soares (2021). Experimental and numerical investigation on welding simulation of long stiffened steel plate specimen. *Marine Structures*, 75, pp.102824–102824. https://doi.org/10.1016/j.marstruc.2020.102824.

Chen, S., Xie, X., & Hanqing Zhuge (2019). Hysteretic model for steel piers considering the local buckling of steel plates. Engineering Structures, 183, pp.303–318. https://doi.org/10.1016/j.engstruct.2018.12.101.

Clarin, M., 2003. Measurement of longitudinal residual stresses in a cold formed rectangular hollow section. *Structural Design of Cold Worked Austenitic Stainless Steel, Internal Rep*, pp.08-30.

Clarin, M., 2004. *High strength steel: local buckling and residual stresses* (Doctoral dissertation, Luleå tekniska universitet).

Dang, J., Yuan, H., Igarashi, A., & Aoki, T. (2017). Multiple-Spring Model for Square-Section Steel Bridge Columns under Bidirectional Seismic Load. *Journal of Structural Engineering*, 143(5), p.04017005. https://doi.org/10.1061/(asce)st.1943-541x.0001735.

Dwight, J.B., Chin, T.K., & Ractliffe, A.T., 1968. Local buckling of thin-walled columns, effect of locked-in welding stresses. *CIRIA, Res. Rep. No. 12, May 1968*.

Fujie, W., Taguchi, M., Kang, L., Ge, H., & Xu, B., 2020. Ductile crack initiation evaluation in stiffened steel bridge piers under cyclic loading. *Steel and Composite Structures*, *36*, pp.463-480.

Goto, Y., Jiang, K., & Obata, M. (2006). Stability and Ductility of Thin-Walled Circular Steel Columns under Cyclic Bidirectional Loading. *Journal of Structural Engineering-asce*, 132(10), pp.1621–1631. https://doi.org/10.1061/(asce)0733-9445(2006)132:10(1621).

Haffar, M.Z., Kövesdi, B., & Adany, S. (2021). Buckling of compressed plates with closed-section longitudinal stiffeners: Two new mathematical models for resistance prediction. *Structures*, 33, pp.3526–3539. https://doi.org/10.1016/j.istruc.2021.06.083.

Hassan, M.S., Salawdeh, S., & Goggins, J. (2018). Determination of geometrical imperfection models in finite element analysis of structural steel hollow sections under cyclic axial loading. *Journal of Constructional Steel Research*, 141, pp.189–203. https://doi.org/10.1016/j.jcsr.2017.11.012.

Hsu, H., & Juang, J.-L. (2000). Performance of thin-walled box columns strengthened with internal braces. *Thin-Walled*

Structures, 37(3), pp.241–258. https://doi.org/10.1016/s0263-8231(00)00020-3.

Ingvarsson, L., 1977. *Cold-forming residual stresses and box columns built up by two cold-formed channel sections welded together*. Department of Structural Mechanics and Engineering, Royal Institute of Technology.

Jenothan, M., Jayasinghe, J.A.S.C., & Bandara, C.S. (2023). Lateral behaviour and performance evaluation of steel piers under cyclic lateral loading. *Journal of Constructional Steel Research*, 201, p.107764. https: //doi.org/10.1016/j.jcsr.2022.107764

Jenothan, M., Jayasinghe, C., Bandara, C.S., & Dammika, A.J. (2024). Performance evaluation of steel hollow box piers under bidirectional lateral cyclic loading to enhance the existing seismic verification framework. *Journal of Constructional Steel Research*, 212, pp.108246–108246. https://doi.org/10.1016/j.jcsr.2023.108246

Jenothan, M., Jayasinghe, C., Bandara, C.S., & Dammika, A.J. (2023). Thin-Walled Hollow Steel Box Piers with Energy Dissipation Mechanism Under Bi-directional Cyclic Loading. *Lecture Notes in Civil Engineering*, pp.29–45. doi:https: //doi.org/10.1007/978-981-99-3471-3_3

Jiang, H., Hu, X., Wang, T., & Sun, Z., 2021, July. Experimental and numerical study on thin-walled hollow bridge piers. In *IOP Conference Series: Earth and Environmental Science* (Vol. 820, No. 1, p. 012004). IOP Publishing.

Kollár, D., Völgyi, I., & Joó, A.L. (2023). Assessment of residual stresses in welded T-joints using contour method. *Thin-Walled Structures*, 190, pp.110966–110966. https://doi.org/10.1016/j.tws.2023.110966.

Kövesdi, B., Haffar, M.Z., & Ádány, S. (2021). Buckling resistance of longitudinally stiffened plates: Eurocode-based design for column-like and interactive behavior of plates with closed-section stiffeners. *Thin-Walled Structures*, 159, p.107266. https://doi.org/10.1016/j.tws.2020.107266.

Lagerqvist, O., & Olsson, A., 2001. Residual stresses in welded l-girders made of stainless steel and structural steel. In *Nordic Steel Construction Conference: 18/06/2001-20/06/2001*. Helsinki University of Technology.

Mamaghani, I.H.P. (2008). Seismic Design and Ductility Evaluation of Thin-Walled Steel Bridge Piers of Box Sections. *Transportation Research Record: Journal of the Transportation Research Board*, 2050(1), pp.137–142. https://doi.org/10.3141/2050-14

Nishino, F., Ueda, Y., & Tall, L. (1967). "Experimental Investigation of the Buckling of Plates with Residual Stresses", ASTM Special Technical Publication, No. 419. pp. 12-30

Rossini, N.S., Dassisti, M., Benyounis, K.Y., & Olabi, A.G. (2012). Methods of measuring residual stresses in components. *Materials and Design*, 35, pp.572–588. https://doi.org/10.1016/j.matdes.2011.08.022

Sato, A., Mitsui, K., Aoyama, M., & Inden, A. K. (2017). Effect of initial imperfection on elasto-plastic behavior of square steel tubular columns under compressive axial force with monotonic antisymmetric bending moment. *Journal of Structural and Construction Engineering*, *82*(741), 1787-1797. https://doi.org/10.3130/aijs.82.1787

Shen, Z., & Zhang, Q. (1991). Interaction of Local and Overall Instability of Compressed Box Columns. *Journal of Structural Engineering-ASCE*, 117(11), pp.3337–3355. doi:https://doi.org/10.1061/(asce)0733-9445(1991)117:11(333)

Shi, G., Zhou, W., Bai, Y., & Lin, C. (2014). Local buckling of 460MPa high strength steel welded section stub columns under axial compression. *Journal of Constructional Steel Research*, 100, pp.60–70. https://doi.org/10.1016/j.jcsr.2014.04.027

Smith, D.J., & Bonner, N.W. (1996). "Measurement of Residual Stresses Using the Deep Hole Method", PVP-Vol. 327, Residual Stresses in Design Fabrication, Assessment and Repair, ASME, 1996.

Susantha, K.A.S., Aoki, T., & Jayasinghe, M.T.R. (2007). Finite Element Analysis of Steel Columns Subjected to Bi-directional Cyclic Loads. *Engineer: Journal of the Institution of Engineers, Sri Lanka*, 40(4), p.35. https://doi.org/10.4038/engineer.v40i4.7152

T. Thevega, K. Rajavijayan, Jayasinghe, C., & K.A.S. Susantha (2021). Strength and Ductility of Stiffened Steel Box Columns of Various Cross-Sectional Configurations under Lateral Cyclic Loadings. 54(2), pp.25–25. https://doi.org/10.4038/engineer.v54i2.7440

Usami, T., & Ge, H.B. (1998). Cyclic behaviour of thin-walled steel structures—numerical analysis. *Thin-Walled Structures*, 32(1-3), pp.41–80. https://doi.org/10.1016/s0263-8231(98)00027-5

Walker, D., 2001. Residual stress measurement techniques. *Advanced Materials & Processes*, *159*(8), pp.30–30.

Watanabe, E., Sugiura, K., & Oyawa, W.O., 2000. Effects of multi-directional displacement paths on the cyclic behaviour of rectangular hollow steel columns. *Doboku Gakkai Ronbunshu*, *2000*(647), pp.79–95. https://doi.org/10.2208/jscej.2000.647_79

Watanabe, E., Sugiura, K., Nagata, K., & Kitane, Y. (1998). Performances and damages to steel structures during the 1995 Hyogoken-Nanbu earthquake. *Engineering Structures*, 20(4-6), pp.282–290. https://doi.org/10.1016/s0141-0296(97)00029-1

Weisman, C., & Kearns, W.H. *eds.*, 1976. *Welding Handbook: Metals and their weldability* (Vol. 4). American Welding Society.

J.Natn.Sci.Foundation Sri Lanka 2025 53 (3): 273 - 282
DOI: http://dx.doi.org/10.4038/jnsfsr.v53i3.12365

RESEARCH ARTICLE

Deep Learning

Aerial crack detection in building structures using convolutional neural networks

CS Silva*, **DMKI Dissanayake, RSMPW Rathnayake and NTA Sathsara**
Instrumentation and Automation Technology, Faculty of Technology, University of Colombo, Pitipana, Homagama, Sri Lanka.

Submitted: 19 September 2024; Revised: 11 June 2025; Accepted: 02 August 2025

Abstract: Evaluating cracks is a crucial step in preserving concrete structures. Manual visual observation of the surface is the common method for inspecting concrete cracks, but it is inherently subjective and depends on the inspectors' expertise. Moreover, it is inefficient, costly, and often hazardous when building structures are hard to reach. In structural health monitoring, unmanned aerial vehicles (UVAs) outfitted with advanced sensing and imaging technologies offer the capacity to detect and assess defects, such as corrosion and cracking, in buildings and infrastructure, thereby facilitating proactive maintenance and early hazard identification. This study presents the design and implementation of a UAV system integrating both sonar and visual sensors, aimed at detecting and classifying building cracks through deep learning techniques. The combined use of heterogeneous sensors represents a novel approach that capitalizes on their respective strengths while mitigating individual drawbacks. The detection of crack presence and depth is accomplished using sonar sensors. Visual capture is then initiated triggering the cameras only after a crack is detected by the sonar to minimize processing overhead during image analysis. The images of the cracks acquired by the vision sensors are processed by a customized convolutional neural network model which shows 99% accuracy in detecting and identifying the cracks.

Keywords: Convolutional neural network, crack detection and identification, deep learning, sonar sensors, unmanned aerial vehicle, vision sensors.

INTRODUCTION

Finding structural flaws is crucial for several reasons. Building cracks typically point to underlying structural issues, including poor foundations, settlement, or structural stress. Finding cracks enables an evaluation of the building's structural soundness and establishes whether there is a danger of collapse or failure. Manual contact measurements were traditionally used to detect cracks in structures. However, they were time-consuming and showed inconsistent results. The introduction of new technology rendered the crack analysis, more reliable and efficient, and equally important, such technology can overcome other limitations of conventional visual inspection methods. The objective of this research is to demonstrate a fully integrated system that combines custom made UAV with convolutional neural networks (CNNs) for the detection and identification of cracks in buildings

Perception modalities for crack detection

Non-imagery sensors were primarily utilized in the literature to identify building cracks. A four-point bending test was suggested by Chakraborty *et al.* (2019) to assess the implanted sensors' sensitivity to spot cracking and its spread. Babu *et al.* (2022) have proposed crack detection using ultrasound sensors to automatically detect invisible cracks in concrete structures. GSM and GPS modules were used to track the locations of cracks in concrete structures (Babu *et al.*, 2022) . The sensors are embedded in cubes and cylinders of concrete that have been combined with cement, fine sand, coarse sand, and water. The cylinders and cubes are weighed after curing, and any identified cracks are shown on an LCD screen (Babu *et al.*, 2022).

* Corresponding author (chathurika@iat.cmb.ac.lk; https://orcid.org/0000-0002-3914-5392)

The majority of automated crack detection methods use surface images captured using vision sensors such as monocular RGB cameras, an array of RGB cameras, a line-scanning camera, or 2D projections of 3D scans (Yuan *et al*., 2023). The textural, intensity, contours, and shape information extracted through these sensory images is then examined to identify cracks on buildings. However, the challenge of detecting cracks in an outdoor environment is to ensure sufficient illumination on the surface such that the contrast between cracks and the surface can be visually distinguished. Moreover, the images could also suffer from illumination imbalance due to the sensor-light setup or external factors such as shadows cast from objects such as trees and lamp posts (Yuan *et al.*, 2023).

More recently there has been an increasing trend towards using image-based methods for crack detection and analysis. These techniques involve taking pictures of the intended component and using programming to locate and categorize cracks. The methods can be categorized into two types, namely, image processing and machine learning. Velumani *et al.* (2020) establish an image processing methodology for the automated identification and examination of cracks. To enhance image quality, the suggested model uses the gray intensity correction method, specifically the min max grey level differentiation (M2GLD). Crack detection also makes use of the Otsu image binarization process. The experimental findings show that the M2GLD approach and the Otsu test work well together to identify crack faults in digital photos. Hoang *et al.* (2018) have proposed developing an automated fracture detection tool for concrete wall surfaces using edge detection methods such as Roberts, Prewitt, Canny, and Sobel. Hoang e*t al.* (2022), forward an innovative method based on computer vision for detecting sealed cracks. This technique uses image processing and metaheuristic-optimized feature extraction to capture visual appearance and texture in pavement photographs. It uses the Salp Swarm algorithm and multiclass support vector machine for pattern recognition, achieving 91.33% accuracy in detecting cracks and 92.83% accuracy in sealing them. Munawar *et al.* (2021) present a review on crack detection methods based on image processing. This review provides a comprehensive analysis and comparison of these methods, highlighting the most promising automated approaches for crack detection. Similarly, Gupta and Dixit (2022) discuss the use of thresholding-based methods in crack detection. The concept of thresholding is to select the higher pixel value by the selected threshold value. These studies highlight the potential of using image-based techniques for crack detection but also emphasize the challenges posed by varying illumination conditions and the need for effective feature extraction and representation.

Moreover, integration of feature representation and classification in deep learning creates a powerful pipeline that requires minimal pre-processing of raw data, thus eliminating the need for manual feature extraction. As a result, the development of image-based deep neural network architectures has paved the way for the use of deep neural network (DNN) techniques in detecting cracks in images (Ali, *et al.*, 2021). Convolutional Neural Networks (CNNs) are a type of deep neural network that is developed primarily for processing structured grid-like data, such as images. Their design comprises numerous layers, each serving a specific purpose in extracting hierarchical representations from input data. Input layer, convolutional layer, activation function, pooling layer, fully connected layer, and output layer are some of layers exhibit in CNNs to analyse and learn from complicated visual data.

Yang *et al.* (2021) proposed to identify structural cracks. This experiment uses transfer learning on the ImageNet dataset, with a maximum of 50,020 training batches. Leaky ReLU and stochastic gradient descent are used as the activation function and optimizer. Tan *et al.* (2023) have developed an automatic crack detector using a state-of-the-art technique called deep learning mask regional network (R-CNN). The mask R-CNN algorithm segments objects in natural images, enabling efficient crack detection. According to Alzubaidi *et al.* (2021) the application of deep architectures inspired by the fields of artificial intelligence and computer vision has made a significant impact on the task of crack detection. They present a comprehensive literature review of deep learning-based crack detection studies and the contributions that they have made to the field. The studies are categorized according to the computer vision aspect and at deeper levels to facilitate exploring the studies that utilized similar approaches to address the crack detection problem. Ali *et al.* (2021) propose a convolutional neural network model for crack detection in concrete structures. According to the results, VGG-16 outperforms the other models. Słoński (2019) has compared the performance of four deep convolutional neural networks in the problem of image-based automated detection of concrete surface cracks as a binary classification problem, and it is solved by training a deep convolutional neural network on a small dataset. The classification accuracy of the best deep convolutional neural network on the testing set is about 94%. Fang *et al.* (2020) trained a deep convolution neural network (DCNN) by using an existing dataset and then retrained the architecture by using a self-created dataset of 184K images.

There are some pre-trained models such as VGG-16 (Simonyan & Zisserman, 2014), VGG-19 (Simonyan & Zisserman, 2014), and ResNet-50 (He *et al.*, 2016). The VGG-19 denotes its distinctive architectural design consisting of 19 layers (Simonyan & Zisserman, 2014). The VGG-19 model developed by the Visual Graphics Group (VGG) at the University of Oxford, represents a significant advancement in the domain of deep learning and computer vision. Unlike pre-defined architectures such as VGG and ResNet, a customized model offers the flexibility to adjust the number, type, and configuration of layers, including convolutional, pooling, and fully connected layers. This adaptability allows researchers and practitioners to design networks that precisely suit the requirements of diverse applications, enhancing performance and efficiency (Zeiler & Fergus, 2013).

Unmanned arial vehicle-based crack detection

An aerial vehicle is defined as any aircraft capable of maintaining airborne stability through the dynamic interaction of air against its lifting surfaces. This broad category of aviation encompasses airships, balloons, helicopters, and aeroplanes. Fixed-wing aerial vehicles, including UAV, primarily generate lift by propelling their wings forward. Ahmed *et al.* (2022) have conducted a comprehensive survey of recent developments in commercially available UAVs, providing insights into their structure, working methodology, flying features, and navigation control. The classification system for aerial vehicles is primarily divided into three categories: fixed-wing aircraft, rotary-wing aircraft, and hybrid UAVs. Each type has its unique set of advantages and disadvantages. Scott *et al.* (2022) provide a systematic review of predictive maintenance focused on a defence domain context, with a particular focus on the operations and sustainment of fixed-wing defence aircraft. Meanwhile, Muhammed and Virk (2023) offer a comprehensive review of studies related to rotary-wing UAVs. Sinnemann *et al.* (2022) discuss the enormous possibilities offered by the cooperation of UAVs and mobile robot manipulators (MRMs) in modern industry.

Hexacopter and quadcopter are another two classifications of UAVs. A hexacopter is equipped with six rotors, and offers superior stability, payload capacity, and flight agility compared to quadcopter variants (Shelare *et al.*, 2023). A quadcopter, also known as a quadrotor, is an aircraft equipped with four rotors on its rotor blades (Husnain *et al.*, 2023). To ensure the total torque exerted on the aircraft is zero, these rotors operate in pairs, with one pair rotating clockwise and the other counter-clockwise (Idrissi *et al.,* 2022).

In the literature, UAVs are mostly equipped with sensors for the purpose of detection of building cracks using computer vision and machine learning. N-Ho Kim *et al.* used a commercial UAV with high-resolution vision sensors for crack identification in ageing concrete bridges. The method generates a background model using point cloud data and deep learning algorithms. The UAV-based method is effective in detecting and quantifying cracks in various structures. These studies highlight the potential of UAVs and image-based computer vision in the field of crack detection (Phang *et al.*, 2021; Yang, 2023).

Previous studies in UAV-based crack detection have demonstrated the use of either visual sensors or range sensors in isolation. This research aims to synergize both sensor modalities—combining vision and range sensing—to enhance the detection and characterization of building cracks through aerial images.

MATERIALS AND METHODS

Design and development of the drone

The UAV used in this research, as shown in Figure 1, is a custom-made quad-quaptor with a flight controller consisting of TM32F411CEU6 (Black Pill) as the micro-controller. Sensors include MPU6050 for real-time angular velocity and linear acceleration measurements, BMP280 for altitude measurements based on barometric pressure, GY-271 for the measurements of the Earth's magnetic field, and a Neo6M GPS module for positioning. A FlySky FS-i6 Transmitter is used for manual control of the UAV which utilizes the i-BUS protocol to communicate between the transmitter and the flight controller. The four 850 kV brushless motors

Figure 1: Quad-quaptor developed in the research used for image acquisition

were used to generate the thrust required for flight. The drone is powered by a 3300 mAh LiPo (lithium polymer) 3S Battery. The Rev 1.3 camera features a 5-megapixel Omni-vision OV5647 sensor. It can capture still images up to 2592 x 1944 pixels, sufficient for most entry-level image capture needs. The Raspberry Pi 3B+ was integrated into the drone as the central processing unit for camera operations. The 8MP Raspberry Pi Camera and two HC-SR04 ultrasonic sensors were connected to the Raspberry Pi, to detect and identify the presence of the crack.

The HC-SR04 ultrasonic sensors, strategically positioned, continuously measured distances to nearby objects. These sensors emitted ultrasound bursts, which are reflected off the objects and returned. By analysing the time taken for the reflected ultrasound to reach the sensor, the distance was accurately determined. These distance values were crucial for real-time obstacle detection and navigation. The camera module captured visual information from the surroundings. It provided high-resolution images that aided in object recognition, scene analysis, and contextual awareness. To ensure efficient collaboration and real-time decision-making, both the distance measurements and captured images were shared with a database.

Design and development of the web application

The primary purpose of developing the web application is to enable real-time monitoring of building cracks from a ground station and share them with the relevant parties. The web application shown in Figure 2, developed using React, seamlessly integrates images captured by the Raspberry Pi and the corresponding average distances computed by the ultrasonic sensors, all of which are transmitted via Firebase. In addition, the GPS module supplies real-time location data. The web application effectively displays the received images and their corresponding distance measurements. This visual representation provides valuable insights into the drone's surroundings and the accuracy of the distance measurements, enabling effective monitoring and analysis.

The presence of the crack is indicated as positive or negative in the dashboard of the web application as shown in Figure 3.

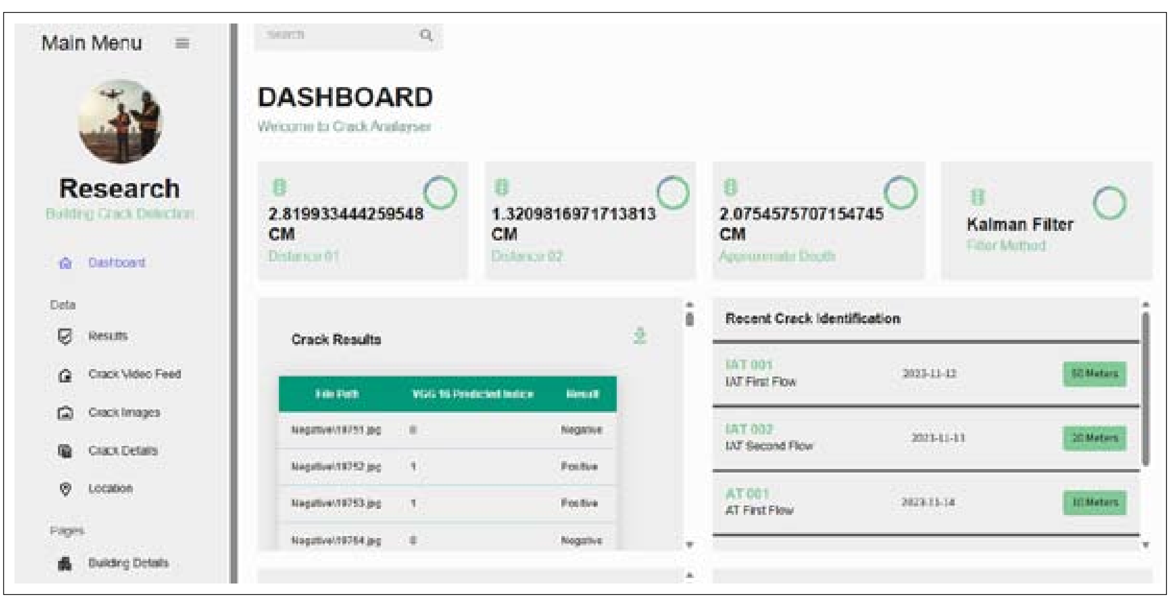

Figure 2: Interface of web application

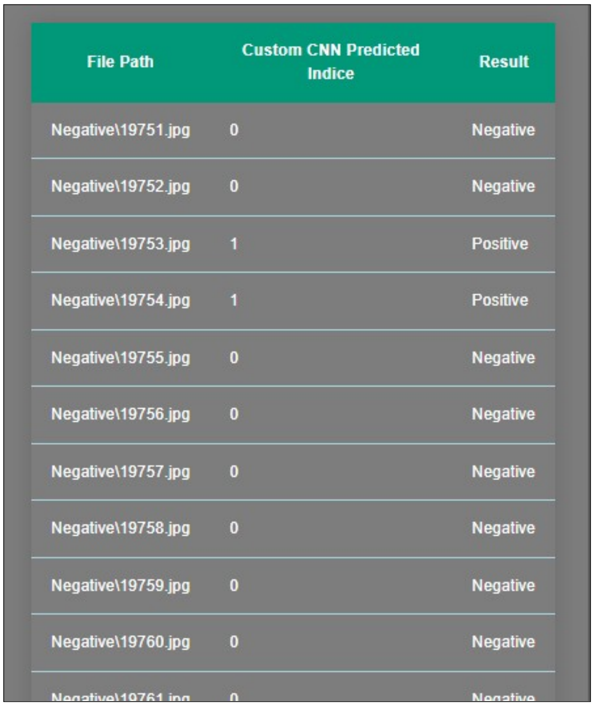

File Path	Custom CNN Predicted Indice	Result
Negative\19751.jpg	0	Negative
Negative\19752.jpg	0	Negative
Negative\19753.jpg	1	Positive
Negative\19754.jpg	1	Positive
Negative\19755.jpg	0	Negative
Negative\19756.jpg	0	Negative
Negative\19757.jpg	0	Negative
Negative\19758.jpg	0	Negative
Negative\19759.jpg	0	Negative
Negative\19760.jpg	0	Negative
Negative\19761.jpg	0	Negative

Figure 3: Results of CCNN model on web application

Construction of deep learning models

In this study, both sonar and vision sensors were employed collaboratively to facilitate a comprehensive assessment of structural cracks in buildings. Ultrasonic waves emitted by sonar sensors are designed to penetrate into cracks, resulting in an increased measured distance between the UAV and the building surface—an indication of the presence of a crack. Upon such detection, the vision sensor (camera) is activated to capture an image of the affected area. This dual-sensing approach minimizes unnecessary image capture in areas without structural damage, thereby significantly reducing computational load and enhancing system efficiency.

This experiment was carried out with a dataset consisting of images collected from different surfaces of buildings with the available background light. The total dataset comprises 2,500 cracked and 2,500 non-cracked images as shown in Figure 5. This dataset is partitioned into training, validation, and testing subsets to support the development and evaluation of the model. Specifically, 2,000 images from each class (cracked and non-cracked) are allocated for training purposes. For validation, 250 cracked and 250 non-cracked images are used, while the testing set also consists of 250 images. This balanced distribution across all subsets ensures fair and unbiased performance assessment during model training and evaluation. A customized convolutional neural network (CCNN) model was implemented, with its architectural design illustrated in Figure 4. The proposed model was developed by systematically fine-tuning various hyperparameters within the network architecture to optimize performance.

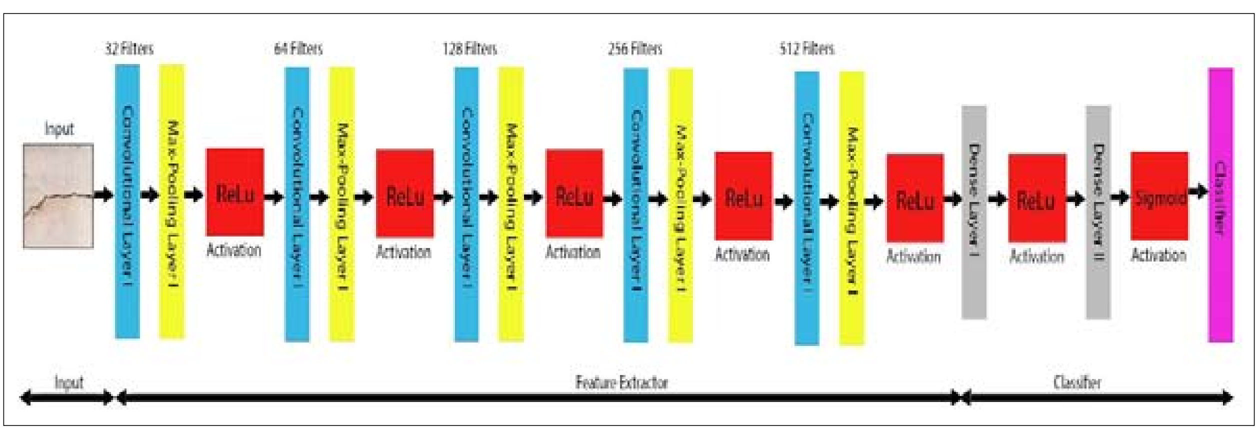

Figure 4: Architectural diagram of the proposed CCNN model

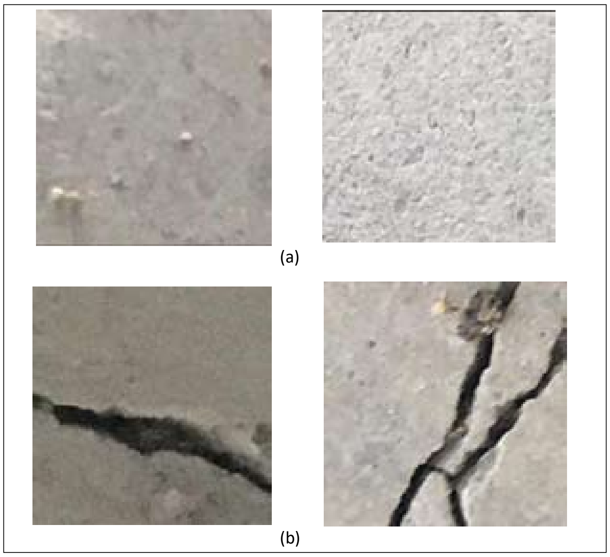

Figure 5: (a): Non-cracked images and (b) cracked images

Evaluation

Evaluation metrics such as precision, accuracy, F1-score, and confusion matrices have used in this research to assess the performance of the model.

Precision is an evaluation metric that measures the accuracy of positive predictions, indicating the model's ability to correctly identify true positives among all instances labelled as positive. Meanwhile, accuracy quantifies the overall correctness of the model's predictions across all classes or categories. The F1-score is a balanced measure of precision, and recall provides insight into the model's capability in handling imbalanced datasets.

Confusion matrices provide a comprehensive tabular representation of a model's predictions against actual values, delineating true positives, true negatives, false positives, and false negatives.

Model development and evaluation were conducted on a workstation with the following hardware and software configuration: RAM: 32 GB, CPU: Intel Core i7-11800H 2.30 GHz, and running a 64-bit Windows 11 operating system. The implementation was carried out using Anaconda JupyterLab 3.6.5 (Python 3.10), utilizing Keras 2.12 and TensorFlow 2.12 libraries.

RESULTS AND DISCUSSION

Drone performance results

This section showcases the evaluation of camera and image performance of the UAV developed for building crack detection. The drone's total payload, weighing 1405 g, includes a frame, flight controller with sensors, battery, enclosure, and propellers. This weight was carefully optimized to balance the drone's flight stability and power consumption.

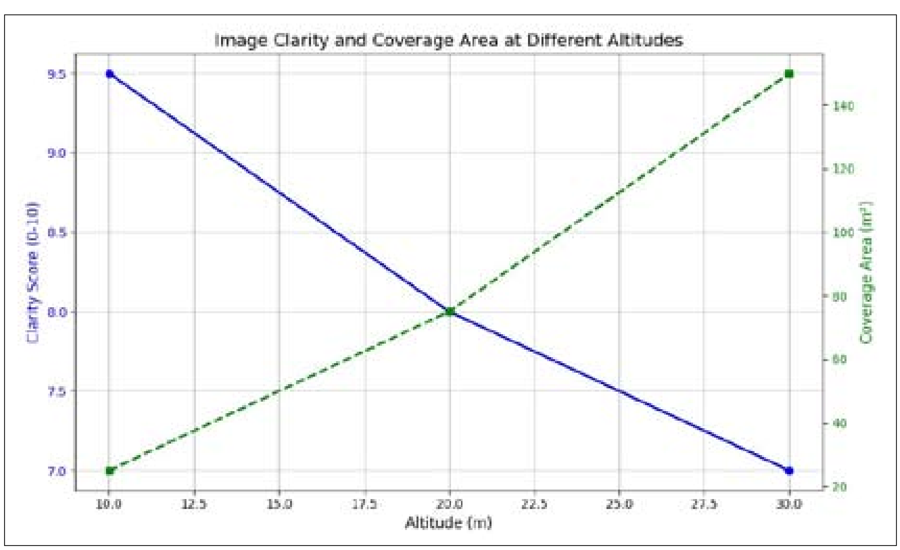

Figure 6: Image Clarity at Different Altitudes Data

Image clarity at different altitudes

The camera's image clarity and coverage area performance were evaluated at varying altitudes to determine the optimal flying height for crack detection. The image resolution remained constant at 2592 x 1944 pixels across all tested altitudes, but clarity and coverage area varied based on altitude.

Image clarity decreases as the altitude increases as shown in Table 1. At 10 meters, the camera provided the best clarity with a score of 9.5, which is ideal for detecting fine details of the cracks. At 20 meters, the clarity score drops to 8.0; at 30 meters, it decreases to 7.0. This may result in some loss of detail, potentially making it harder to detect smaller cracks. As expected, coverage area increases significantly with altitude: 25 m² at 10 meters, 75 m² at 20 meters, and 150 m² at 30 meters. Higher altitudes allow for covering larger areas in less time but at the reduction of image clarity. Image clarity and coverage area at different altitudes is shown at Figure 6.

Table 1: Image Clarity at Different Altitudes Data

Altitude (m)	Image Resolution (pixels)	Clarity Score (0-10)	Coverage Area (m²)
10	2592 x 1944	9.5	25
20	2592 x 1944	8.0	75
30	2592 x 1944	7.0	150

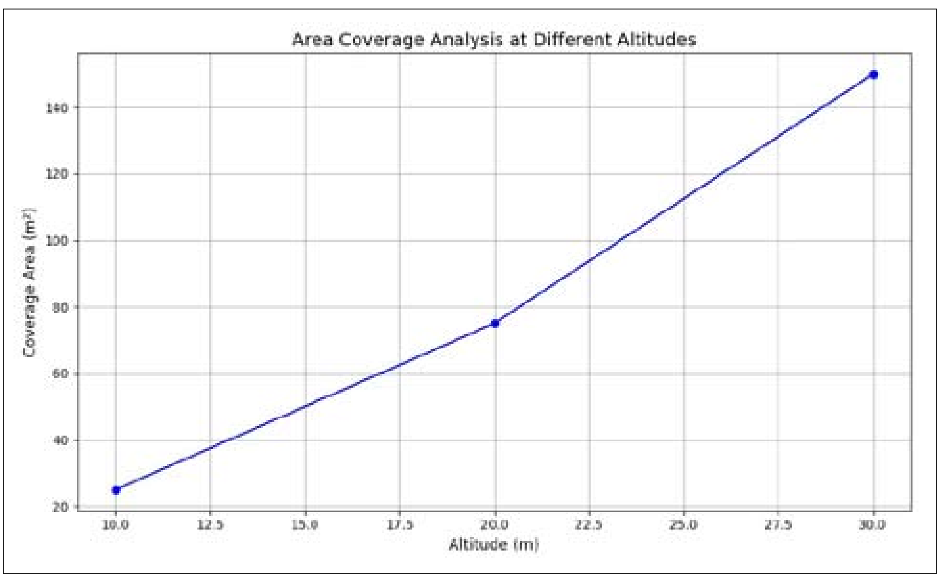

Figure 7: Line chart of area coverage at different altitudes

Area coverage analysis

The camera's field of view remained consistent across all altitudes, providing a 53° horizontal angle. However, the coverage area of each image increased with the altitude, as shown in the Table 2. Line chart representing the area coverage at different altitudes is shown in Figure7.

Table 2: Area coverage analysis data

Altitude (m)	Field of View (degrees)	Coverage Area (m²)
10	53	25
20	53	75
30	53	150

Results of deep learning models

CCNN achieves an accuracy of 99%, showcasing its effectiveness in overall classification performance. CCNN exhibits a precision of 98% and 98% indicating a low false-positive rate in their predictions. CCNN attains recall at 98%, highlighting its ability to effectively capture a significant portion of true positive instances. CCNN achieves an F1 score of 98%, emphasizing a harmonious balance between precision and recall.

The confusion matrices provide a detailed breakdown of the performance of customized CNN (Figure 8), consisting of two classes: the actual class (rows) and the predicted class (columns). True positives (TP) are 244; true negatives (TN), 246; false positives (FP), 4; and False Negatives (FN), 6. The model demonstrates exceptional performance with minimum false negatives, achieving a perfect balance between precision and recall.

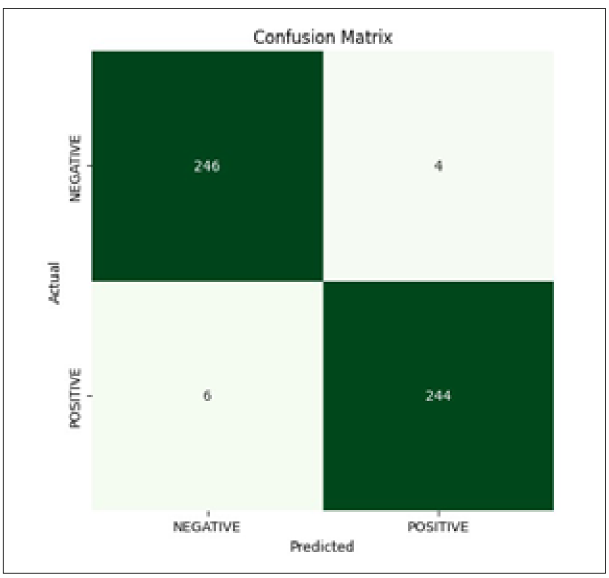

Figure 8: Confusion matrix of CCNN

The provided ROC curve and corresponding area under the curve (AUC) values offer a concise assessment of the classification performance for Customized CNN as shown in Figure 9. The ROC curve for customized CNN exhibits the highest performance, as reflected by the high AUC value of 0.99. This signifies that the model achieves an exceptional balance between true positive rate and false positive rate across various classification thresholds. The curve's proximity to the upper-left corner underscores the model's robust discriminative ability, indicating superior classification accuracy.

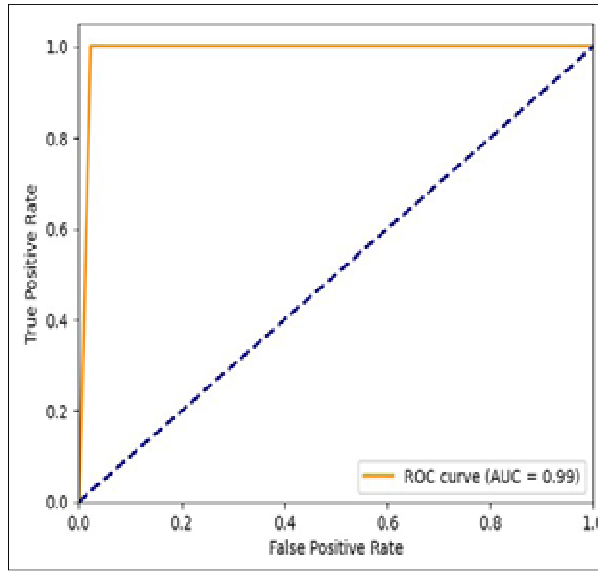

Figure 9: ROC curve of CCNN

CONCLUSION

In conclusion, this research embarks on an innovative exploration of an advanced approach to building crack detection. This research proposed an approach, leveraging both vision and non-visual sensors, to detect cracks through a comprehensive examination of the limitations in conventional image processing and the computational challenges of the deep learning model. The experiment, conducted with a UAV-mounted camera and sonar sensors, exemplifies the practical implementation of these methodologies. The customized deep CNN model underlines the significance of a tailored approach in achieving precision-driven building crack inspection. The resuts obtained from this research are compared with the state-of-art research (Ali *et al.*, 2021; Słoński, 2019; Fang *et al.*, 2020).The findings of this research contribute not only to the theoretical understanding of deep learning applications in infrastructure assessment but also provide practical insights for the deployment of UAVs for building crack detection.

To further improve this research, several enhancements can be considered. First, implementing a feature that automatically schedules maintenance tasks based on the detected cracks and their severity. Second, extending the system's capabilities to detect cracks in various types of structures beyond buildings, such as bridges and pavements, can broaden its applicability and utility. Further, it is expected to identify the features of the detected crack and classify them accordingly. The outlined deep learning techniques, experimental results, and model evaluations collectively contribute to the evolving landscape of accurate and efficient building crack detection.

REFERENCES

Ahmed, F., Mohanta, J., Keshari, A., & Yadav, P. (2022). Recent advances in unmanned aerial vehicles: A review. *Arabian Journal for Science and Engineering* 47, 7963–7984. https://doi.org/10.1007/s13369-022-06738-0

Ali, L., Alnajjar, F., Jassmi, H., Gocho, M., Khan, W., & Serhani, M. (2021). Performance evaluation of deep CNN-based crack detection and localization techniques for concrete structures. *Sensors* 21(5),1688. https://doi.org/10.3390/s21051688

Ali, R., Chuah, J. H., Talip, M. S., Mokhtar, N., & Shoaib, M. A. (2021). Structural crack detection using deep convolutional neural networks. *Automation in Construction*,133, 103989. https://doi.org/10.1016/j.autcon.2021.103989

Alzubaidi, L., Zhang, J., & Humaidi, A. (2021). Review of deep learning: concepts, CNN architectures, challenges, applications, future directions. *Journal of Big Data* , 8(1), 1-74. https://doi.org/10.1186/s40537-021-00444-8

Babu, J. C., Kumar, M. S., Sathishkumar, V. E., Rajendran, S., Kumar, S., Karthick, A., & Mahseena, A. M. (2022). IoT-based intelligent system for internal crack detection in building blocks. *Journal of Nanomaterial.*, 2022(1), 3947760. https://doi.org/10.1155/2022/3947760

Chakraborty, J., Katunin, A., Klikowicz, P., & Salamak, M. (2019). Early crack detection of reinforced concrete structure using embedded sensors. *Sensors,* 19(18), 3879. https://doi.org/10.3390/s19183879

Ding, G., Wu, Q., Zhang, L., Lin, Y., Tsiftsis, T., & Yao, Y. (2018). An amateur drone surveillance system based on the cognitive internet of things. *IEEE Communications Magazine, 56(1),* 29–35. https://doi.org/10.1109/MCOM.2017.1700452

Drone, R.(2023, November 24, 2023). Simple formula about quadcopter weight calculator and thrust calculator. https://www.rcdronegood.com/formula-quadcopter-weight-calculator-thrust/

Fang, F., Li L., Gu, Y., Zhu, H., & Lim, J.-H. (2020). A novel hybrid approach for crack detection. *Pattern Recognition.* https://doi.org/10.1016/j.patcog.2020.107474.

Gupta, P., & Dixit, M. (2022). Image-based crack detection approaches: A comprehensive survey. *Multimedia Tools and Applications, 81,* 40181–40229. https://doi.org/10.1007/s11042-022-13152-z

He, K., Zhang, X., Ren, S., & Sun, J. (2016). Deep residual learning for image recognition. *IEEE Conference on Computer Vision and Pattern Recognition (CVPR)*, 770–778.

Hoang, N., & Nguyen, Q. (2018). Metaheuristic optimized edge detection for recognition of concrete wall cracks: A comparative study on the performances of roberts, prewitt, canny, and sobel algorithms.*Advances in Civil Engineering,* 2018(1), 7163580. https://doi.org/10.1155/2018/7163580

Hoang, N., Huynh, T., Tran, X., & Tran, V. (2022). A novel approach for detection of pavement crack and sealed crack using image processing and salp swarm algorithm optimized machine learning. *Advances in Civil Engineering,* 2022(1), 9193511. https://doi.org/10.1155/2022/9193511

Husnain, A., Mokhtar, N., Mohamed Shah, N., & Dahari, M. I. (2023). A systematic literature review on autonomous path planning of unmanned aerial vehicles. *Drones,* 7(2), 118. https://doi.org/10.3390/drones7020118

Idrissi, M., Salami, M., & Annaz, F. (2022). A review of quadrotor unmanned aerial vehicles: Applications, architectural design and control algorithms. *Journal of Intelligent & Robotic System.,* 104. https://doi.org/10.1007/s10846-021-01527-7

Kim, B., Yuvaraj, N., Preethaa, K., & Pandian, R. (2021). Surface crack detection using deep learning with shallow CNN architecture for enhanced computation. *Neural Computing and Applications,33,* 9289–9305. https://doi.org/10.1007/s00521-021-056

Muhammed, M., & Virk, M. (2023). Ice accretion on rotary-wing unmanned aerial vehicles—A review study. *Aerospace,* 10(3), 261.. https://doi.org/10.3390/aerospace10030261

Munawar, H., Hammad, A., Haddad, A., Soares, C., & Waller, S. (2021). Image-based crack detection methods: A review. *Infrastructures*, 6(8), 115. https://doi.org/10.3390/infrastructures6080115

Phang, J., Lim, K., & Chiong, R. (2021). A review of three dimensional reconstruction techniques. *Multimedia Tools and Applications, 80,* 17879–17891. https://doi.org/10.1007/s11042-021-10605-9

Scott, M., Verhagen, W., Bieber, M., & Marzocca, P. (2022). A systematic literature review of predictive maintenance for defence fixed-wing aircraft sustainment and operations. *Sensors*, *22 (18),* 7070.https://doi.org/10.3390/s22187070

Shelare, S., Belkhode, P., Nikam, K., Yelamasetti, B., & Gajbhiye, T. (2023). A payload based detail study on design and simulation of hexacopter drone. *International Journal on Interactive Design and Manufacturing.*18,2675–2692. https://doi.org/10.1007/s12008-023-01269-w

Ahmed, F., Mohanta, J., Keshari, A., & Yadav, P. (2022). Recent advances in unmanned aerial vehicles: A review. *Arabian Journal for Science and Engineering* 47, 7963–7984. https://doi.org/10.1007/s13369-022-06738-0

Ali, L., Alnajjar, F., Jassmi, H., Gocho, M., Khan, W., & Serhani, M. (2021). Performance evaluation of deep CNN-based crack detection and localization techniques for concrete structures. *Sensors* 21(5),1688. https://doi.org/10.3390/s21051688

Ali, R., Chuah, J. H., Talip, M. S., Mokhtar, N., & Shoaib, M. A. (2021). Structural crack detection using deep convolutional neural networks. *Automation in Construction*,133, 103989. https://doi.org/10.1016/j.autcon.2021.103989

Alzubaidi, L., Zhang, J., & Humaidi, A. (2021). Review of

deep learning: concepts, CNN architectures, challenges, applications, future directions. *Journal of Big Data* , 8(1), 1-74. https://doi.org/10.1186/s40537-021-00444-8

Babu, J. C., Kumar, M. S., Sathishkumar, V. E., Rajendran, S., Kumar, S., Karthick, A., & Mahseena, A. M. (2022). IoT-based intelligent system for internal crack detection in building blocks. *Journal of Nanomaterial.*, 2022(1), 3947760. https://doi.org/10.1155/2022/3947760

Chakraborty, J., Katunin, A., Klikowicz, P., & Salamak, M. (2019). Early crack detection of reinforced concrete structure using embedded sensors. *Sensors,* 19(18), 3879. https://doi.org/10.3390/s19183879

Ding, G., Wu, Q., Zhang, L., Lin, Y., Tsiftsis, T., & Yao, Y. (2018). An amateur drone surveillance system based on the cognitive internet of things. *IEEE Communications Magazine, 56(1),* 29–35. https://doi.org/10.1109/MCOM.2017.1700452

Drone, R.(2023, November 24, 2023). Simple formula about quadcopter weight calculator and thrust calculator. https://www.rcdronegood.com/formula-quadcopter-weight-calculator-thrust/

Fang, F., Li L., Gu, Y., Zhu, H., & Lim, J.-H. (2020). A novel hybrid approach for crack detection. *Pattern Recognition.* https://doi.org/10.1016/j.patcog.2020.107474.

Gupta, P., & Dixit, M. (2022). Image-based crack detection approaches: A comprehensive survey. *Multimedia Tools and Applications, 81,* 40181–40229. https://doi.org/10.1007/s11042-022-13152-z

He, K., Zhang, X., Ren, S., & Sun, J. (2016). Deep residual learning for image recognition. *IEEE Conference on Computer Vision and Pattern Recognition (CVPR)*, 770–778.

Hoang, N., & Nguyen, Q. (2018). Metaheuristic optimized edge detection for recognition of concrete wall cracks: A comparative study on the performances of roberts, prewitt, canny, and sobel algorithms.*Advances in Civil Engineering,* 2018(1), 7163580. https://doi.org/10.1155/2018/7163580

Hoang, N., Huynh, T., Tran, X., & Tran, V. (2022). A novel approach for detection of pavement crack and sealed crack using image processing and salp swarm algorithm optimized machine learning. *Advances in Civil Engineering,* 2022(1), 9193511. https://doi.org/10.1155/2022/9193511

Husnain, A., Mokhtar, N., Mohamed Shah, N., & Dahari, M. I. (2023). A systematic literature review on autonomous path planning of unmanned aerial vehicles. *Drones,* 7(2), 118.. https://doi.org/10.3390/drones7020118

Idrissi, M., Salami, M., & Annaz, F. (2022). A review of quadrotor unmanned aerial vehicles: Applications, architectural design and control algorithms. *Journal of Intelligent & Robotic System.,* 104. https://doi.org/10.1007/s10846-021-01527-7

Kim, B., Yuvaraj, N., Preethaa, K., & Pandian, R. (2021). Surface crack detection using deep learning with shallow CNN architecture for enhanced computation. *Neural Computing and Applications,33,* 9289–9305. https://doi.org/10.1007/s00521-021-056

Muhammed, M., & Virk, M. (2023). Ice accretion on rotary-wing unmanned aerial vehicles—A review study. *Aerospace,* 10(3), 261.. https://doi.org/10.3390/aerospace10030261

Munawar, H., Hammad, A., Haddad, A., Soares, C., & Waller, S. (2021). Image-based crack detection methods: A review. *Infrastructures*, 6(8), 115. https://doi.org/10.3390/infrastructures6080115

Phang, J., Lim, K., & Chiong, R. (2021). A review of three dimensional reconstruction techniques. *Multimedia Tools and Applications, 80,* 17879–17891. https://doi.org/10.1007/s11042-021-10605-9

Scott, M., Verhagen, W., Bieber, M., & Marzocca, P. (2022). A systematic literature review of predictive maintenance for defence fixed-wing aircraft sustainment and operations. *Sensors*, *22 (18),* 7070.https://doi.org/10.3390/s22187070

Shelare, S., Belkhode, P., Nikam, K., Yelamasetti, B., & Gajbhiye, T. (2023). A payload based detail study on design and simulation of hexacopter drone. *International Journal on Interactive Design and Manufacturing.*18,2675–2692. https://doi.org/10.1007/s12008-023-01269-w

Simonyan, K., & Zisserman, A. (2014). Very deep convolutional networks for large-scale image recognition. *Computer Vision and Pattern Recognition.* https://arxiv.org/abs/1409.1556

Sinnemann, J., Boshoff, M., Dyrska, R., Leonow, S., Mönnigmann, M., & Kuhlenkötter, B. (2022). Systematic literature review of applications and usage potentials for the combination of unmanned aerial vehicles and mobile robot manipulators in production systems. *Production Engineering, 16, 579–596.* https://doi.org/10.1007/s11740-022-01109-y.

Słoński, M. (2019). A comparison of deep convolutional neural networks for image-based detection of concrete surface cracks. *Computer Assisted Methods in Engineering and Science, 26*, 105-112.https://doi.org/10.24423/cames.267

Tan, C., Uddin, N., & Mohammed, Y. M. (2023). Deep learning-based crack detection using mask R-CNN technique. *The international conference on structural health nonitoring of intelligent infrastructure.*

Velumani, P., Mukilan, K., Varun, G., Divakar, S., Doss, R., & Ganeshkumar, P. (2020). Analysis of cracks in structures and buildings. *Journal of Physics: Conference Series, 1706* https://doi.org/10.1088/1742-6596/1706/1/012116

Yang, C., Chen, J., Li, Z., & Huang, Y. (2021). Structural crack detection and recognition based on deep learning. *Applied Sciences,,* 11(6), *2868.* https://doi.org/10.3390/app11062868

Yang, T. (2023). 3D ToF LiDAR in mobile robotics: A review. http://arxiv.org/abs/2202.11025

Yuan, Q., Shi, Y., & Li, M. (2023). A review of computer vision-based crack detection methods in civil infrastructure: Progress and Challenges. *Remote Sensing,* 16(16), 2910. https://doi.org/10.3390/rs16162910.

Zeiler, M. D., & & Fergus, R. (2013). Visualizing and understanding convolutional networks. http://arxiv.org/*abs/1311.2901*.

Zhao, Y., Zhou, L., Wang, X., Wang, F., & Shi, G. (2023). Highway crack detection and classification using UAV remote sensing images based on crackNet and crack classification. *Applied Sciences , 13,* 7269. https://doi.org/10.3390/app13127269

J.Natn.Sci.Foundation Sri Lanka 2025 53 (3): 283 - 292
DOI: http://dx.doi.org/10.4038/jnsfsr.v53i3.12089

RESEARCH ARTICLE

Environmental Science

Performance evaluation of a lab-scale upflow anaerobic sludge blanket (UASB) reactor for landfill leachate treatment under ambient temperature conditions

HPDU Iroshani[1], PG Rathnasiri[2], Wasala MKRTW Bandara[3*], and PHGAD De Silva[4]
[1] *Sri Lanka Institute of Advanced Technical Education, Colombo, Sri Lanka.*
[2] *Department of Chemical and Process Engineering, Faculty of Engineering, University of Moratuwa, Moratuwa, Sri Lanka.*
[3] *Department of Civil and Environmental Engineering, Faculty of Engineering, University of Ruhuna, Sri Lanka.*
[4] *DAN Structures Pty Ltd, 7 Pilgrim Ct, Ringwood 3134 VIC. Australia*

Submitted: 12 March 2024; Revised: 10 August 2025; Accepted: 14 August 2025

This study presents a comprehensive performance evaluation of a lab-scale upflow anaerobic sludge blanket (UASB) reactor for treating landfill leachate under ambient temperature conditions (28 - 32°C), representative of tropical climates. The reactor was operated continuously for 94 days with real landfill leachate, investigating the system's treatment efficiency across varying hydraulic retention times (HRTs) from 6 to 10 h. Key performance indicators, including organic matter removal, biogas production, and heavy metal reduction, were systematically analyzed. The results demonstrated optimal treatment performance at 6 h HRT, achieving 64 ± 1% COD removal efficiency with a concomitant high methane yield of 86.1 ± 1.1% in the produced biogas. The reactor maintained stable operational conditions, with pH in the range 6.2 - 7.5 and oxidation-reduction potential consistently below -200 mV, confirming effective anaerobic digestion under ambient temperature conditions. Heavy metal removal efficiencies varied significantly, with maximum removal observed for lead (55 ± 1%) and chromium (47 ± 1%), while suspended solids removal reached 66% for total suspended solids (TSS) and and 29% for volatile suspended solids (VSS). The study provides critical insights into the applicability of UASB technology for landfill leachate treatment in tropical regions, highlighting both its strengths in organic load reduction and limitations in comprehensive contaminant removal under ambient temperature operation. The findings contribute to the development of sustainable, climate-appropriate leachate treatment solutions for regions with limited resources.

Keywords: Ambient temperature treatment, anaerobic digestion, landfill leachate, tropical climate, UASB reactor, wastewater treatment.

INTRODUCTION

Sanitary landfilling remains one of the most widely adopted methods for municipal solid waste (MSW) disposal due to its economic feasibility and environmental advantages when properly managed (Sewwandi *et al.*, 2011). However, a critical environmental concern associated with landfills is the generation of leachate, a highly contaminated wastewater that results from the percolation of rainwater through degrading solid waste. Leachate, characterized by high concentrations of organic matter, heavy metals, ammonium, and other pollutants, poses a significant threat to groundwater and adjacent surface water bodies. This risk is particularly pronounced in developing nations. For instance, studies in Sri Lanka have highlighted the substantial risk of contamination of soil and water bodies like rivers (Shayan *et al.*, 2020) by heavy metals from open dumpsites (Sewwandi *et al.*, 2011). As a developing country, Sri Lanka faces the persistent challenge of implementing a comprehensive solid waste management strategy that includes effective leachate treatment systems.

* Corresponding author (wasala@cee.ruh.ac.lk; https://orcid.org/0000-0001-8403-386X)

The physicochemical characteristics of leachate are highly variable and are typically assessed using parameters such as chemical oxygen demand (COD), biological oxygen demand (BOD), pH, total suspended solids (TSS), total kjeldahl nitrogen (TKN), and total phosphorus (TP). This variability is influenced by several factors, including landfill age, climatic and seasonal variations, and the composition of the deposited waste (Ifeanyichukwu, 2008). Notably, the age of a landfill can lead to significant variations in leachate composition, which in turn complicates the selection and design of treatment technologies (Baig *et al*., 1999).

The treatment of landfill leachate is notoriously difficult due to the presence of high concentrations of organic, inorganic, and inhibitory compounds, particularly ammonia. High ammonia levels can severely impede biological treatment processes. For example, Yuzer *et al.* (2012) demonstrated that increasing ammonia concentrations in an anaerobic digestion system caused COD and BOD removal efficiencies to plummet from 95% to as low as 15%.

Various biological treatment methods, including aerobic, anaerobic, and hybrid systems, have been investigated for leachate management. Anaerobic processes are often considered more effective for high-strength wastewater streams like leachate, owing to their lower operational costs and significantly lower sludge production, approximately 5–10% of that from aerobic systems (Karthikeyan & Kandasamy, 2009). To overcome the limitations of conventional anaerobic reactors, high-rate configurations have been developed. Among these, the up-flow anaerobic sludge blanket (UASB) reactor is a promising technology for treating high-strength wastewater. The UASB system utilizes a suspended blanket of granular sludge to efficiently entrap and degrade contaminants.

According to established design principles for high-rate anaerobic systems, UASB reactors are engineered to operate within specific performance envelopes. As detailed in seminal texts like Metcalf & Eddy's *Wastewater Engineering: Treatment and Reuse* (2004), typical design norms for treating high-strength industrial wastewaters under mesophilic conditions include organic loading rates (OLRs) ranging from 10 to 25 g-COD/L/d and expected COD removal efficiencies of 70–85%. Performance in tropical climates is often comparable, though it can be influenced by the unique characteristics of the waste stream, such as the high proportion of refractory organics found in mature leachate (Kurniawan *et al*., 2006). For instance, research on UASB treatment of landfill leachate in Brazil reported COD removals of 65-80% at OLRs between 8 and 16 g-COD/L/d (de Lemos Chernicharo, 2007), while studies in India on stabilized leachate showed efficiencies closer to 55-65% (Tatoulis *et al*., 2017). These benchmarks provide a critical framework for evaluating the feasibility and efficacy of new applications.

In tropical regions, ambient temperature is a crucial parameter affecting the efficiency of anaerobic treatment (Wasala *et al*., 2024). While optimal performance is often achieved under thermophilic conditions (45 °C - 60 °C), this would necessitate heating the wastewater, thereby incurring additional operational costs (Wasala *et al*., 2011). Sri Lanka's tropical climate provides an average ambient temperature between 20 °C and 35 °C, which aligns with the mesophilic range for anaerobic digestion. This presents an opportunity to develop cost-effective treatment systems that operate efficiently without external heating.

Building upon this premise, preliminary research at the University of Ruhuna, Sri Lanka, developed a lab-scale UASB reactor (Wasala *et al*., 2024) and demonstrated its potential for treating synthetic leachate under ambient temperatures, achieving an 80% COD removal efficiency (Fonseka *et al*., 2015). The present study is a direct continuation of this work, aiming to validate the applicability of the UASB reactor for treating real-world leachate. The leachate for this investigation is sourced from a 20-year-old municipal open dumpsite located near a natural water stream in Sri Lanka.

Given that treatment efficiencies are highly dependent on local climatic conditions and that there is a documented lack of appropriate on-site leachate treatment methods in Sri Lanka (Sewwandi *et al*., 2011), it is imperative to investigate solutions that are both cost-effective and suitable for the region. Therefore, the objective of this research is to optimize the operational parameters of a UASB reactor for the treatment of mature landfill leachate under the ambient tropical climatic conditions of Sri Lanka and to benchmark its performance against both established design norms and findings from similar research.

MATERIALS AND METHODS

Experimental setup and operational conditions

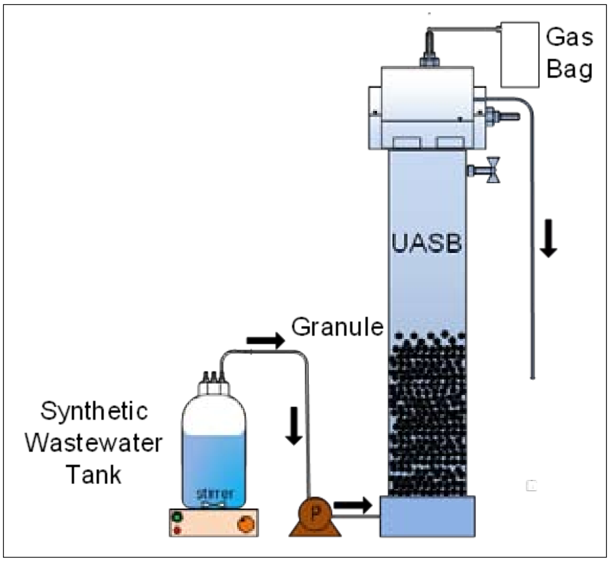

Figure 1: Schematic diagram of the UASB reactor

The experiment was conducted in a custom-fabricated, lab-scale up-flow anaerobic sludge blanket (UASB) reactor, constructed from perspex with a height of 60 cm, an internal diameter of 10 cm, and a working volume of 5 L (Figure 1). To ensure uniform influent distribution, the base of the reactor was fitted with a conical funnel leading to the inlet valve. Leachate was introduced from the bottom, while the top of the reactor was equipped with two separate valves for the collection of headspace biogas and the withdrawal of treated effluent. An additional sampling port on the reactor body allowed for the collection of mixed liquor samples during operation. To minimize the microbial lag phase, the reactor was inoculated with 1 L of anaerobic granular sludge, characterized by a total solids (TS) concentration of 29 g/L and a volatile solids (VS) concentration of 23 g/L. A variable displacement peristaltic pump (Biobase, Model BT 600M, China) continuously delivered the raw leachate influent. The pump's flow rate was maintained between 8.5 and 14 mL/min to achieve hydraulic retention times (HRT) ranging from 6 to 10 h. The experiment was operated continuously over a period of 94 days. Raw leachate was sourced from a local municipal landfill on a weekly basis and stored in a plastic feed reservoir connected to the pump inlet.

Analytical methods

A comprehensive suite of analytical methods was employed to monitor reactor performance and characterize the leachate. BOD was measured using the BOD Apparatus, and COD was quantified using the Hach method with a DR 1900-01 spectrophotometer. Key electrochemical parameters, including pH and oxidation-reduction potential (ORP), were continuously monitored using a PHC301 pH electrode and an MTC101 ORP probe, respectively, while temperature was measured with a standard laboratory thermometer. The concentrations of selected heavy metals (Pb, Hg, Cr, Cd, As, and Fe) were determined via inductively coupled plasma optical emission spectroscopy (ICP-OES).

Biogas composition (CH_4, CO_2, N_2, O_2, and H_2) in the reactor headspace was analyzed using a gas chromatograph (Gasboard 3200L, Hubei-Ruiyi Instrument Co. Ltd.) (Wasala *et al*., 2024). The daily biogas production volume was quantified by collecting the cumulative gas in a sealed bag and measuring its volume via the water displacement method. To ensure data robustness, the average gas production rate for each HRT was calculated from six replicate 24 h measurements. A consistent water column was used for all volumetric determinations to minimize measurement errors associated with gas dissolution.

Finally, total suspended solids (TSS) and volatile suspended solids (VSS) were determined gravimetrically in accordance with standard methods.

RESULTS AND DISCUSSION

Key operational parameters, including pH, temperature, and ORP, were monitored daily to assess the stability of the reactor environment. As illustrated in Figure 2, the pH of the influent leachate varied between 7.5 and 8.5, while the internal pH of the UASB reactor was consistently maintained within a stable range of 7.0 to 7.5.

This operational pH is significant, as it is directly influenced by the concentrations of ammonium ions and volatile fatty acids. The observed range is highly favorable for anaerobic processes, particularly for methanogenic Archaea, which exhibit optimal activity between pH 6.8 and 7.2 (Gerardi, 2003). The inherent buffering capacity of the system allowed the reactor to operate continuously within this ideal range without any external pH correction, supporting both acidogenic and methanogenic microbial populations.

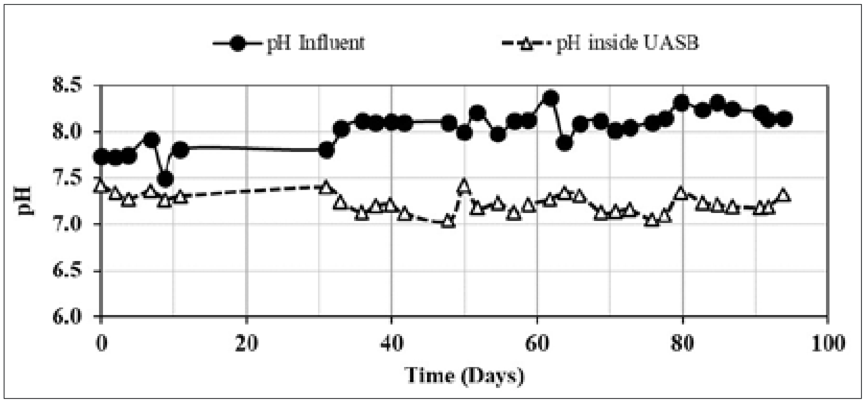

Figure 2: pH variation in influent (leachate) and inside the UASB

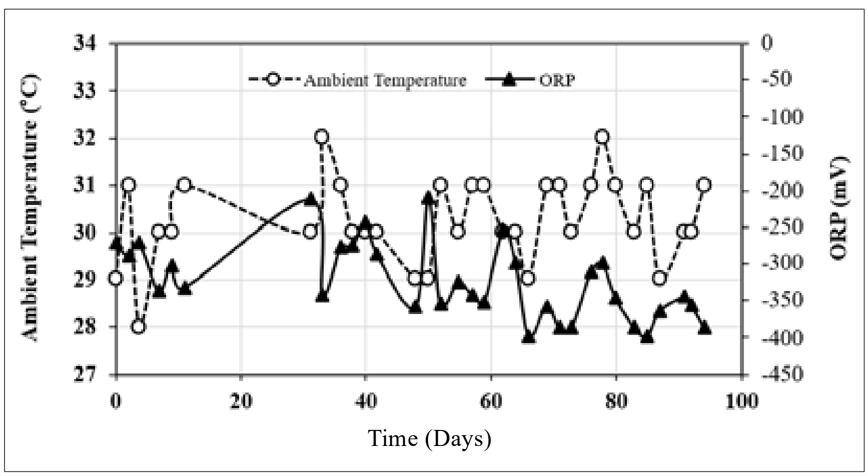

Figure 3: Ambient temperature and ORP variation inside the UASB reactor

Figure 3 presents the ambient temperature and ORP profiles recorded throughout the experiment. The reactor was operated under ambient conditions without thermal regulation, resulting in an internal temperature that fluctuated between 28 °C and 32 °C, with an average of 30 °C. Crucially, the ORP values remained consistently below -200 mV throughout the study, confirming that strictly anaerobic conditions were successfully established and maintained within the reactor.

BOD and COD removal efficiency

The reactor's performance was evaluated by systematically varying the OLR, controlled by adjusting the influent flow rate to alter the HRT. Throughout the study, the OLR was incrementally increased from 51.06 g-COD/L/d to 144.19 g-COD/L/d to identify the system's operational limits. The influent, sourced from a mature landfill, was characterized as a high-strength wastewater stream with average BOD_5 and COD concentrations of 7,918 mg/L and 23,625 mg/L, respectively. The resulting BOD_5/COD ratio was 0.34. This ratio can vary depending on the age of the landfill, and a value around 0.34 is typically observed in medium-aged leachates (5–10 years old), as reported by Bardi *et al.* (2017) and Ren *et al.* (2017).

As detailed in Figure 4, a clear performance peak was identified at an HRT of 6 h, corresponding to an OLR of 87.89 g-COD/L/d. Under these optimal conditions, the reactor achieved a maximum BOD_5 and COD removal efficiency of 69 ± 1% and 64 ± 1% respectively, and the most substantial absolute BOD_5 and COD reduction (a mean of BOD_5 is 3,942 mg/L and COD is 11,620 mg/L). This demonstrates the reactor's robust capacity for treating this challenging effluent under ambient tropical conditions. However, a critical operational threshold was observed: when the OLR was increased beyond this optimum, BOD_5 and COD removal efficiency decreased markedly. This trend aligns with previous findings where high loading rates lead to system instability, often termed shock loading (Satoh *et al*., 2017).

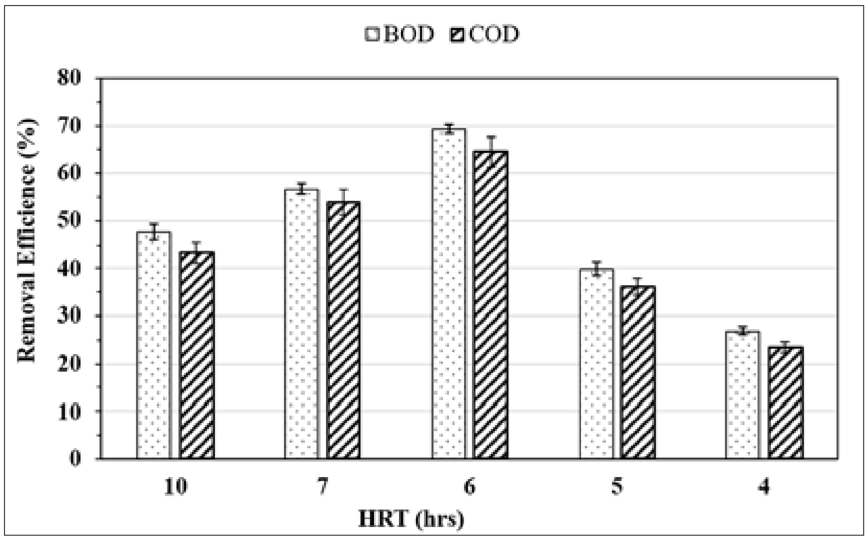

Figure 4: BOD5 and COD removal efficiencies variation with HRT

To evaluate the significance of these results, the reactor's performance was benchmarked against established design norms and similar research. Notably, the optimal OLR of 87.89 g-COD/L/d is substantially higher than the typical design range of 10–25 g-COD/L/d recommended by Metcalf and Eddy (2004) for high-strength anaerobic treatment. This exceptional loading capacity can be attributed to the well-acclimatized granular sludge, which demonstrated a remarkable ability to process the high substrate flux from the extremely concentrated leachate.

Furthermore, the 69% BOD_5 and 64% COD removal efficiency is highly competitive when compared to studies on similar stabilized or mature leachates in tropical regions. For example, Sponza and Ağdağ (2004) reported 62% COD removal from mature leachate, but at a much lower OLR of 12 g-COD/L/d. Similarly, Tatoulis *et al.* (2017) observed approximately 58% COD removal from stabilized leachate. The ability of our reactor to achieve a comparable efficiency at a significantly higher OLR highlights the robust metabolic activity of the microbial consortium established under Sri Lankan ambient conditions.

This comparative analysis confirms that while operating outside conventional OLR parameters, the UASB reactor provides effective treatment for highly concentrated, mature landfill leachate. The 64% COD removal achieved at ambient tropical temperatures, without supplementary heating, represents a viable and energy-efficient first-stage treatment, validating its potential for application in Sri Lanka and similar climatic regions. The sharp decline in performance beyond the 6-hour HRT, however, underscores the importance of maintaining the OLR below this critical threshold to prevent overloading and process failure, a finding corroborated by the biogas analysis.

Bio gas production

Biogas production and composition were systematically quantified for each HRT. As illustrated in Figure 5, the average biogas production rate varied with operational time, corroborating the COD removal profile. A maximum specific production rate of 23.35 ± 0.42 mL/h/L was achieved at the optimal HRT of 6 h, while the average rate across all conditions was 16.76 ± 0.85 mL/h/L. Decreasing the HRT below the 6 h optimum resulted in a corresponding decline in biogas generation.

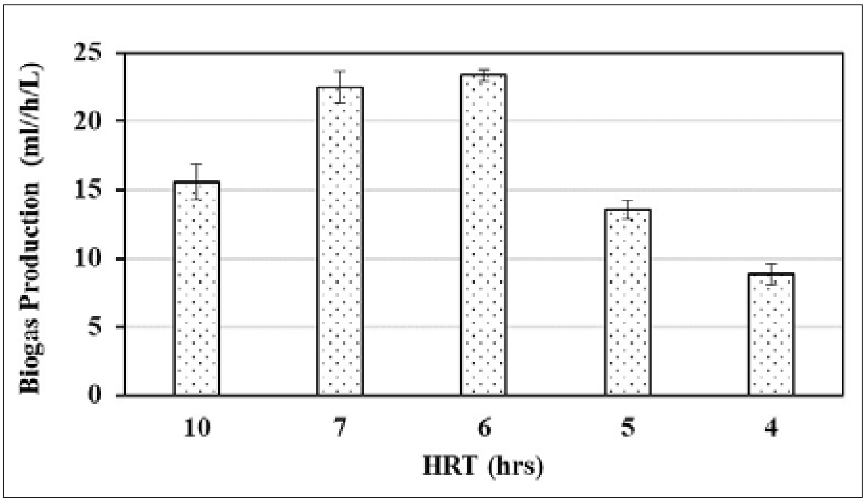

Figure 5: Bio Gas production rate variation with HRT

Table 1: Headspace biogas composition variation with HRT

HRT (hr.)	H_2 (ppm)	Gas concentration (%)		
		N_2	CH_4	CO_2
10	-	11.52 ± 2.77	82.99 ± 2.82	5.49 ± 0.65
7	-	10.31 ± 1.94	84.63 ± 1.26	5.06 ± 0.99
6	-	8.03 ± 1.24	86.11 ± 1.10	5.85 ± 0.89
5	137 ± 8	19.31 ± 0.42	68.32 ± 0.56	12.38 ± 0.39
4	252 ± 5	18.70 ± 0.84	73.16 ± 0.80	8.14 ± 0.14

The stability of the anaerobic process was further assessed by monitoring trace gas concentrations, as detailed in Table 1. The presence of H_2 in the headspace is a critical indicator of metabolic balance. As noted by Satoh *et al.* (2017), low H_2 partial pressure is essential for the syntrophic degradation of propionate and n-butyrate, and stress conditions such as short HRTs can lead to H_2 accumulation and subsequent process inhibition. In this study, operation at shorter HRTs (4 and 5 h) corresponded with an increase in H_2, N_2, and CO_2 concentrations, alongside a decrease in CH_4 percentage. The sudden increase in H_2 concentration to 252 ppm at the 4 h HRT suggests the system was approaching its metabolic equilibrium limit, indicating that further reductions in HRT would risk inducing an inhibitory state.

This observation is consistent with the findings of Pauss *et al.* (1990), who identified dissolved H_2 as a growth-limiting factor for acetogenic bacteria, which require its continuous removal by methanogens to maintain thermodynamic favorability. If the process is disrupted, competition for H_2 and acetate can intensify, particularly from sulphate-reducing bacteria, potentially leading to process failure. The low concentrations of N_2 detected (Table 1) are likely attributable to the release of dissolved nitrogen from the influent or the decomposition of nitrogenous compounds by non-methanogenic microorganisms.

Analysis of the biogas composition reveals that CH_4 was the predominant component across all tested HRTs. The CH_4 content varied with the HRT, reaching a maximum of 86.11 ± 1.10% at the 6 h HRT. This high methane yield indicates that the biogas produced under optimal conditions possesses a significant calorific value, reinforcing the selection of a 6 h HRT as the most effective operational parameter.

Removal of heavy metals

The role of heavy metals in anaerobic digestion is complex; while trace concentrations are essential for the activation of microbial enzymes and co-enzymes, higher concentrations can exert stimulatory, inhibitory, or toxic effects depending on the metal species and its bioavailability (Mudhoo & Kumar, 2013). Consequently, the reactor's capacity for heavy metal removal was evaluated specifically at the optimal HRT of 6 h.

Table 2: Heavy metal content variation with treatment

Heavy Metals	Influent (mg/L)	Initial granule (mg/L)	Effluent of UASB (mg/L)	Granule + Sludge (inside UASB (mg/L)
Pb	0.030 ± 0.002	0.011 ± 0.001	0.014 ± 0.002	0.676 ± 0.077
Hg	0.050 ± 0.002	0.000 ± 0.001	0.047 ± 0.002	0.144 ± 0.023
Cr	0.109 ± 0.002	0.032 ± 0.002	0.057 ± 0.003	2.116 ± 0.089
Cd	0.005 ± 0.001	0.002 ± 0.001	0.004 ± 0.001	0.041 ± 0.002
As	0.036 ± 0.002	0.002 ± 0.001	0.025 ± 0.002	0.467 ± 0.033
Fe	18.083 ± 0.072	0.732 ± 0.002	13.98 ± 0.06	169.80 ± 18.66

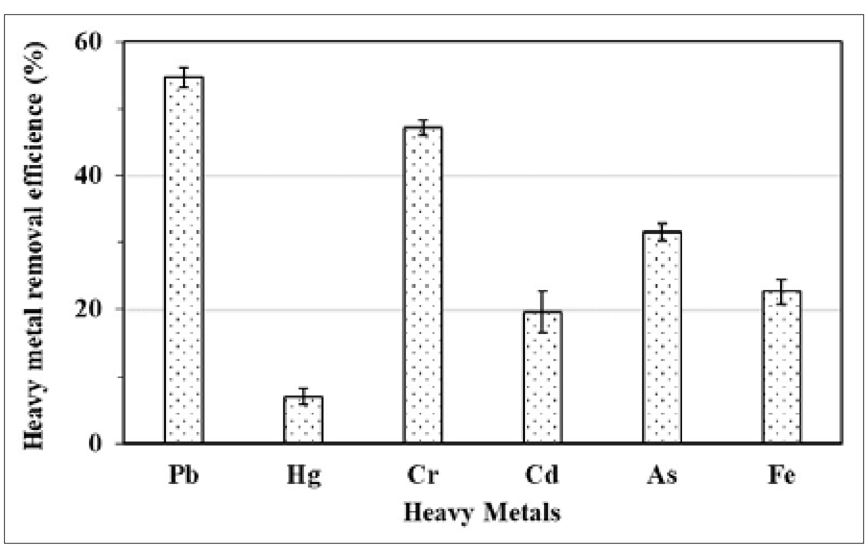

Figure 6: Heavy Metal removal efficiencies variation with HR

As detailed in Table 2, the influent leachate contained relatively low concentrations of most target metals, with the notable exception of Fe. However, low aqueous-phase concentrations in leachate do not necessarily imply an absence of metals in the waste. It is well-established that under the near-neutral pH conditions typical of anaerobic digesters, heavy metals tend to precipitate as insoluble sulphides, phosphates, and hydroxides (Berrueta & Castrillón, 1992; Kjeldsen *et al*., 2002). Evidence of this sequestration mechanism was confirmed by the post-treatment analysis of the reactor biomass, which showed a significant accumulation of heavy metals within the granular sludge (Table 2).

The overall removal efficiencies are presented in Figure 6. The system demonstrated the highest efficacy for Pb and Cr, with removal rates of 55 ± 1% and 47 ± 1%, respectively. In contrast, the UASB reactor was less effective for Cd, As, and Fe, while the removal of Hg was minimal at just 7 ± 1%.

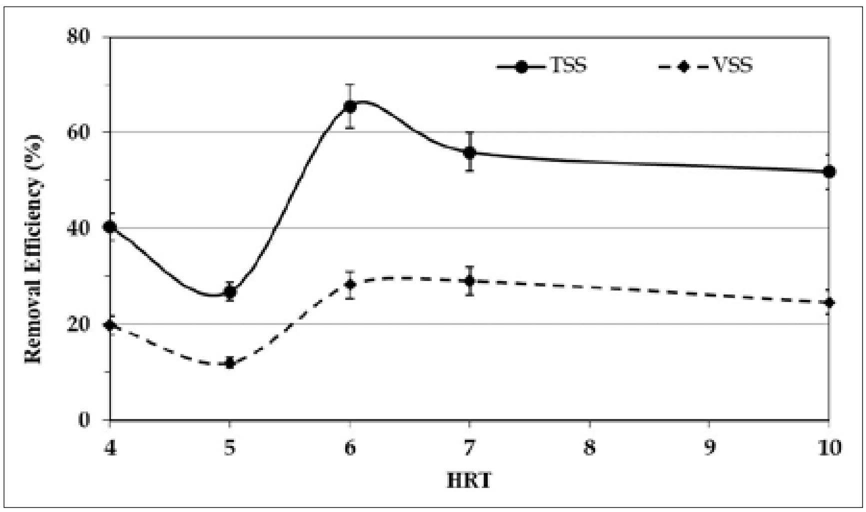

Figure 7: TSS and VSS removal efficiencies variation with HRT

Removal efficiencies of (TSS) and volatile suspended solids (VSS)

The influent leachate was characterized by high concentrations of TSS and VSS, with average values of 13,161 ± 1,864 mg/L and 4,495 ± 711 mg/L, respectively. The removal efficiencies for these solids across various HRTs are illustrated in Figure 7. A maximum TSS removal of 66% was achieved at the optimal HRT of 6 h, whereas the peak VSS removal of 29% was observed at an HRT of 7 h. Overall, the average removal efficiencies for TSS and VSS were 48% and 23%, respectively, indicating that the UASB reactor demonstrated modest efficacy for suspended solids removal from the liquid phase.

Table 3: TSS and VSS variation of granules initially and after the treatment

		TSS (mg/L)	VSS (mg/L)
Inoculated Granules		28832 ± 17	22737 ± 21
After treatment (In UASB reactor)	Granular	34654 ± 26	27381 ± 24
	Sludge	35602 ± 17	27667 ± 20

Conversely, a post-treatment analysis of the reactor biomass (Table 3) revealed a significant accumulation of both TSS and VSS within the granular sludge. This phenomenon can be attributed to a combination of the physical adsorption of suspended solids onto the granule surfaces and the concurrent generation of new biomass. The substantial increase in VSS is particularly significant; as reported by Risvi *et al.* (2015), an increase in VSS is a clear indicator of active biomass proliferation, given that over 90% of VSS typically comprises viable microbial cells, with the remainder being attributed to non-biodegradable volatile solids and cellular debris.

The evaluation of VSS/TSS ratio and OLR provided critical insights into the reactor's performance, revealing an average VSS/TSS ratio of 0.79 ± 0.05 that inversely correlated with increasing OLR, indicating robust microbial activity at optimal loading conditions (87.89 g-COD/L/d at 6 h HRT) but showing stress signs (ratio dropping to 0.73) at higher OLRs (144.19 g-COD/L/d). The system demonstrated remarkable resilience to common inhibitory factors, maintaining stable operation despite high ammonia levels (1,240 – 1,850 mg/L) through gradual biomass acclimatization and sufficient alkalinity buffering, while heavy metal effects were mitigated via sulphide precipitation and metal partitioning. Performance comparison showed the ambient-temperature UASB achieved competitive COD removal (64%) versus thermophilic systems, while avoiding energy-intensive heating. However, clear operational limits emerged at OLRs >90 g-COD/L/d, evidenced by 32% decreased methanogenic activity, VFA accumulation (1,450 mg/L propionate), and sludge washout. The VSS/TSS ratio proved to be a reliable bioindicator, with values >0.75 correlating with stable performance under these tropical ambient conditions, demonstrating the system's effectiveness within defined loading ranges while highlighting the need for OLR control to prevent overloading.

CONCLUSION

This study successfully demonstrated that a UASB reactor, operating under ambient tropical temperatures (28–32°C) without external heating, is a highly effective and robust technology for the first-stage treatment of high-strength, mature landfill leachate. The system achieved exceptional performance at an HRT of 6 h, corresponding to an OLR of 87.89 g-COD/L/d. At this peak, the reactor yielded a competitive 64% COD and 69% BOD_5 removal efficiency. This performance is particularly noteworthy as the operational OLR far exceeds the conventional design range of 10–25 g-COD/L/d, highlighting the remarkable capacity of the acclimatized granular sludge. This efficiency was directly corroborated by biogas analysis, which showed a maximum specific production rate of 23.35 mL/h/L and a peak methane content of 86.11%, underscoring the potential for valuable energy recovery. The reactor's stability was underpinned by its inherent buffering capacity, which maintained an ideal internal pH (7.0 – 7.5) for methanogenesis without chemical intervention, and its proven resilience to high ammonia concentrations. However, the research identified a clear operational boundary. Increasing the OLR beyond 90 g-COD/L/d (HRT < 6 h) led to a sharp decline in performance, marked by VFA accumulation, a 32% decrease in methanogenic activity, and a rise in H_2 gas concentration, a key indicator of metabolic stress and impending process failure. Furthermore, the VSS/TSS ratio proved to be a reliable bioindicator of system health, with a stable ratio above 0.75 correlating with optimal performance and a drop to 0.73 signaling overloading.

Regarding co-contaminant removal, the UASB reactor functions primarily as a sequestration system. It demonstrated moderate efficacy for heavy metals, with the highest removal observed for Pb (55 ± 1%) and Cr (47 ± 1%) through precipitation and accumulation within the sludge biomass. Conversely, removal was limited for Cd, As, and Fe, and minimal for Hg (7 ± 1%). Similarly, the system showed modest removal of suspended solids from the liquid phase.

In summary, the ambient-temperature UASB reactor is a viable solution for organic load reduction from mature landfill leachate in tropical regions. Its success hinges on maintaining the OLR below the critical threshold of 90 g-COD/L/d. While it effectively purifies the liquid effluent, the process concentrates heavy metals and solids into the sludge, necessitating proper management and disposal of this secondary waste stream.

REFERENCES

Baig, S., Coulomb, I., Courant, P., & Liechti, P. (1999). Treatment of landfill leachates: Lapeyrouse and Satrod case studies. *Ozone: Science & Engineering, 21*(1), 1–22. https://doi.org/10.1080/01919519908547239

Bardi, A., Yuan, Q., Siracusa, G., Chicca, I., Islam, M., Spennati, F., Tigini, V., Di Gregorio, S., Levin, D.B., Petroni, G. & Munz, G. (2017). Effect of cellulose as co-substrate on old landfill leachate treatment using white-rot fungi. *Journal of Bioresource Technology 241, 1067-1076.* https://doi.org/10.1016/j.biortech.2017.06.046

Berrueta, J., & Castrill, L. (1992). Anaerobic treatment of leachates in UASB reactors. *Journal of Chemical Technology & Biotechnology, 54*(1), 33–37. https://doi.org/10.1002/jctb.280540106

De Lemos Chernicharo, C. A. (2007). *Anaerobic Reactors* (Vol. 4). IWA Publishing.

Fonseka, H. A. M., Senewirathna, P. J., Bandara, W. M. K. R. T. W., & Ellawala, C. (2015). *Performance of a UASB reactor for leachate treatment under ambient temperature* [Unpublished undergraduate thesis]. University of Ruhuna.

Gerardi, M. H. (2003). *The microbiology of anaerobic digesters*. John Wiley & Sons. https://doi.org/10.1002/0471468967

Heyer, K.-U., & Stegmann, R. (1999). Leachate management. In T. H. Christensen, R. Cossu, & R. Stegmann (Eds.), *Landfilling of waste: Leachate* (pp. 1–23). E & FN Spon.

Ifeanyichukwu, M. J. (2008). *Water and environmental engineering* [Master's thesis, Lund University].

Karthikeyan, K., & Kandasamy, J. (2009). Upflow anaerobic sludge blanket (UASB) reactor in wastewater treatment. In S. Vigneswaran, M. Sundaravadivel, & S. Chaudhary (Eds.), *Water and wastewater treatment technologies* (Vol. II, pp. 180–198). Eolss Publishers.

Kjeldsen, P., Barlaz, M. A., Rooker, A. P., Baun, A., Ledin, A., & Christensen, T. H. (2002). Present and long-term composition of MSW landfill leachate: A review. *Critical Reviews in Environmental Science and Technology, 32*(4), 297–336. https://doi.org/10.1080/10643380290813462

Kurniawan, T. A., Lo, W. H., & Chan, G. Y. (2006). Physico-chemical treatments of landfill leachate. *Journal of Hazardous Materials, 129*(1-3), 80-90.

Metcalf and Eddy (2004) *Wastewater engineering: Treatment and reuse*. (4th Ed.), McGraw-Hill.

Mudhoo, A., Kumar, S. (2013) Effects of heavy metals as stress factors on anaerobic digestion processes and biogas production from biomass. *International Journal of Environmental Science and Technology, 10*, 1383–1398. https://doi.org/10.1007/s13762-012-0167-y

Pauss, A., Andre, G., Perrier, M., & Guiot, S. R. (1990). Liquid-to-gas mass transfer in anaerobic processes: Inevitable transfer limitations of methane and hydrogen in the biomethanation process. *Applied and Environmental Microbiology, 56*(6), 1636–1644. https://doi.org/10.1128/AEM.56.6.1636-1644.1990

Ren, Y., Ferraz, F., Lashkarizadeh,, M., & Yuan Q. (2017). Comparing young landfill leachate treatment efficiency and process stability using aerobic granular sludge and suspended growth activated sludge. *Journal of Water Process Engineering 17*, 161-167. https://doi.org/10.1016/j.jwpe.2017.04.006.

Rizvi, H., Ahmad, N., Abbas, F., & Yasar, A. (2015). Start-up of UASB reactors treating municipal wastewater and effect of temperature / sludge age and hydraulic retention time (HRT) on its performance. *Arabian Journal of Chemistry, 10* (Suppl. 2), S2223–S2231. https://doi.org/10.1016/j.arabjc.2013.12.016

Satoh, H., Bandara, W. M. K. R. T. W., Sasakawa, M., & Okabe, S. (2017). Enhancement of organic matter degradation and methane gas production of anaerobic granular sludge by degasification of dissolved hydrogen gas. *Bioresource Technology, 245*, 1135–1141. https://doi.org/10.1016/j.biortech.2017.08.144

Sewwandi, B. G. N., Wijesekara, S. S. R. M. D. H. R., Rajapaksha, A., Mowjood, M. I. M., & Vithanage, M. (2011, November 29–30). *Risk of soil and water pollution by heavy metals in landfill leachate*. [Paper presentation]. International Conference on Agricultural Engineering Novelty, Clean and Sustainable, Nakhon Pathom, Thailand.

Shayan, M. N. M., Tushara Chaminda, G. G., Ellawala, K. C., & Gunawardena, W. B. (2020). Evaluation of water quality of community managed water supply schemes (CMWSS) in Galle District. In M. Kumar, F. Munoz-Arriola, H. Furumai, & T. Chaminda (Eds.), *Resilience, response, and risk in water systems* (pp. 139–150). Springer. https://doi.org/10.1007/978-981-15-4668-6_8

Sponza, D. T., & Ağdağ, O. N. (2004). Treatment of landfill leachate in a UASB reactor: Effect of organic loading rate and hydraulic retention time. *Environmental Technology, 25*(6), 707-718.

Tatoulis, T., Akratos, S., Tekerlekopoulou, A. G., Vayenas, D. V., & Pavlou, S. (2017). Performance of a full-scale UASB reactor treating landfill leachate: The case of the Al-Safa an Al-Faisaliah landfill in Jeddah, KSA. *Waste and Biomass Valorization, 8*(3), 883-893.

Wasala M. K. R. T. W. Bandara, Satoh, H., Sasakawa, M., Nakahara, Y., Takahashi, M., & Okabe, S. (2011). Removal of residual dissolved methane gas in an upflow anaerobic sludge blanket reactor treating low-strength wastewater at low temperature with degassing membrane. *Water Research, 45*(11), 3533–3540. https://doi.org/10.1016/j.watres.2011.04.008

Wasala M. K. R. T. W. BAndara, Shayan, M. N. M., Thennakoon, R. M. W. C., Kumudumali, P. A. A., & Satoh, H. (2024). Introduction of plug-flow anaerobic sludge blanket (PASB) reactor for wastewater treatment. *Desalination and Water Treatment*, 319, 130-139. https://doi.org/10.5004/dwt.2024.30335

Yuzer, B., Akgul, D., & Mertoglu, B. (2012). Effect of high ammonia concentration on UASB reactor treating sanitary landfill leachate. *Fen Bilimleri Dergisi (FABAD), 24*(2), 59–67.

J.Natn.Sci.Foundation Sri Lanka 2025 53 (3): 293 - 306
DOI: http://dx.doi.org/10.4038/jnsfsr.v53i3.12590

RESEARCH ARTICLE

Agricultural Engineering

Effect of temperature on drying kinetics and quality attributes of coffee beans during hot air drying

AJ Fernando[*1,2] , KSP Amaratunga[3], DAN Dharmasena[3], and THKR De Silva[4]
[1] *Department of Agricultural Engineering and Soil Science, Faculty of Agriculture, Rajarata University of Sri Lanka, Anuradhapura, Sri Lanka.*
[2] *Postgraduate Institute of Agriculture, University of Peradeniya, Peradeniya, Sri Lanka.*
[3] *Department of Agricultural Engineering, Faculty of Agriculture, University of Peradeniya, Peradeniya, Sri Lanka.*
[4] *Department of Mathematics, Faculty of Science, University of Peradeniya, Peradeniya, Sri Lanka.*

Submitted: 09 March 2025; Revised: 29 July 2025; Accepted: 28 August 2025

Abstract: This study systematically investigates the thin-layer drying kinetics of coffee (*Coffea arabica*) cherries during hot air drying, with experiments conducted at four distinct temperatures: 40 °C, 60 °C, 80 °C, and 100 °C. A comprehensive analysis was performed using ten widely recognized mathematical models: Newton, Page, Modified Page, Henderson and Pabis, Logarithmic, Two-Term, Exponential Two-Term, Diffusion Approximation, Midilli, and Singh to model the experimental moisture ratio data and characterize drying behavior. The drying process was characterized by a predominant falling rate period, indicating that internal moisture diffusion governs the kinetics. Among the models evaluated, the Midilli model best fits the experimental data, achieving the highest R^2 (0.9952 at 40 °C, 0.9973 at 60 °C, 0.9994 at 80 °C, and 0.9995 at 100 °C) and the lowest *RMSE* values (0.0793% at 40 °C, 0.2092% at 60 °C, 0.0624% at 80 °C, and 0.0868% at 100 °C). Furthermore, the effective moisture diffusivity increased significantly with temperature, ranging from 1.154×10^{-7} m^{2}s^{-1} at 40 °C to 8.939×10^{-7} m^{2}s^{-1} at 100 °C. The corresponding activation energy for the drying process was calculated as 32.36 kJ mol^{-1}. The L^* value (lightness) decreased consistently as the temperature increased. The findings of this study advance the understanding of coffee cherry drying kinetics under hot air conditions and offer practical insights for optimizing drying parameters. This research contributes a robust framework for designing and controlling industrial drying processes, ultimately enhancing product quality and energy efficiency in coffee production. The implications of these results are significant for scaling up operations and reducing energy consumption in drying systems.

Keywords: Coffee, drying, midilli model, moisture diffusivity, thin layer drying.

INTRODUCTION

Coffee is one of the world's most cherished beverages, celebrated for its unique aroma and rich flavour. In 2024, the global coffee market was valued at USD 97.71 billion, with projections indicating growth to USD 102.98 billion by 2025 and reaching USD 156.85 billion by 2033, a compound annual growth rate of 5.4% from 2025 to 2033 (Straits Research, 2025). Various products fuel this expansive market, including roasted, instant, and ready-to-drink coffees. Recent analyses show robust global consumption, with European consumers accounting for a significant market share (International Coffee Organization [ICO], 2022). The beverage's popularity largely stems from its unique organoleptic properties, which are closely tied to postharvest processing techniques. Processes such as cherry harvesting, de-pulping, fermentation, drying, and storage initiate complex chemical transformations in green coffee beans, ultimately shaping the quality of the final brew (Huch & Franz, 2015; Sunarharum *et al.*, 2014).

Following harvest, coffee cherries undergo primary processing through one of three main methods: natural

[*] Corresponding author (jayaruwanifernando@gmail.com; https://orcid.org/0000-0003-2292-547X)

drying, wet processing, or semi-dry processing (Elhalis *et al.*, 2023). The choice of method and its duration depend on factors such as available resources, climatic conditions, and the intended quality of the final product. The natural drying method involves non-selective harvesting, either by hand or with machinery, followed by spreading the cherries on drying surfaces or the ground under direct sunlight for approximately 20 to 30 days. During this period, moisture content gradually reduces from 60-65% wet basis (wb) to around 12% (Silva *et al.*, 2000). Mechanical dryers can be used independently or in combination with solar drying to accelerate the drying process. However, precise control of the drying process is necessary, as excessive or inadequate drying can lead to chemical changes in the beans, ultimately influencing the quality of the final coffee product (Do Carmo *et al.*, 2020).

Drying is a crucial preservation method that reduces the moisture content of agricultural products, thereby lowering shipping costs and storage space requirements. In the case of coffee cherries, various drying techniques have been adopted to optimize efficiency and product quality. While traditional sun drying remains widely used, recent studies have explored alternative methods of drying. For instance, Deeto *et al.* (2018) demonstrated the effectiveness of solar drying for coffee cherries, and convective drying has been thoroughly investigated by Burmester and Eggers (2010), Nilnont *et al.* (2012), and Muhidong *et al.* (2013). Firdissa *et al.* (2022) reported that coffee beans processed using the semi-washed method and dried under natural sunlight and solar tunnel conditions achieved a specialty coffee Grade of Q1. Innovative approaches such as heat pump drying (Fernando *et al.*, 2021) and microwave drying (Ghosh & Venkatachalapathy, 2014) have emerged, offering promising alternatives to conventional techniques. These novel methods have the potential to enhance drying efficiency, improve product quality, and reduce energy consumption, making them valuable for modern coffee processing applications.

According to the American Society of Agricultural and Biological Engineers (ASABE) (2022), a thin layer is a uniformly thick layer of material exposed to air during drying, typically comprising no more than three layers of individual particles. This configuration facilitates the analysis of simultaneous heat and mass transfer processes during drying. Thin-layer drying has recently been studied by Salehi *et al.* (2024) for eggplant and Wang *et al.* (2024) for pelleted feed. While Phitakwinai *et al.* (2019) examined the thin-layer drying behavior of parchment coffee, the drying characteristics of coffee cherries under similar conditions remain unexplored. Consequently, this study aims to quantify the moisture transfer rate of coffee cherries across various temperature ranges using thin-layer drying data applicable to both drying and roasting processes. A best-fit mathematical model was utilized to develop a relationship for the drying coefficients of coffee cherries, and further analyses estimated the moisture diffusivity and activation energy of fresh coffee cherries. The findings from this research are expected to inform the design of a hot-air dryer for coffee cherries and provide recommendations for optimal drying conditions and process control.

MATERIALS AND METHODS

Coffee cherries

Freshly harvested *Coffea arabica* cherries were collected from plantations in Kandy, Sri Lanka (7.2906° N, 80.6337° E; approximately 500 m above sea level). The coffee cherries were visually examined to confirm uniform ripeness and manually cleaned to remove foreign material and defective fruits before conducting hot-air drying experiments.

Drying procedure

Drying experiments were carried out using a gravity convection laboratory oven (Fisher Scientific Econotemp Model 55G, USA). A thin layer (single layer) of coffee cherries was dried at four controlled temperatures: 40 °C, 60 °C, 80 °C, and 100 °C. The oven was preheated for one hour before each run to ensure thermal stability and steady-state conditions. While the oven provided precise temperature control, it lacked active airflow and humidity regulation. As a result, internal air velocity and relative humidity were not measured and may have fluctuated during the drying process. Nevertheless, gravity convection ovens are commonly used in thin-layer drying studies where temperature is the dominant parameter, and the setup provides sufficiently stable thermal conditions for modeling drying kinetics.

Moisture content was determined according to ISO Standard 11520-2 (International Standards Organization [ISO], 2001). Random samples of 10-15 g were collected, and each drying experiment was conducted in triplicate. The average moisture content was recorded for each sample and used in subsequent data analysis. The wet basis moisture content (MC_{wb}) of the coffee cherries was calculated using Equation 1.

$$MC_{wb} = \frac{Weight_{initial} - Weight_{final}}{Weight_{initial}} \times 100 \qquad ...(1)$$

where Wi is the initial mass of the sample and Wd is the oven-dry mass of the sample.

Mathematical modeling

Estimation of effective moisture diffusivity

Liquid and vapor diffusion predominantly govern the falling-rate drying stage in agricultural produce. This moisture transport is modeled using Fick's second law of diffusion (Equation 2), where the effective diffusivity quantifies the rate of moisture movement (Hui *et al.*, 2008).

$$\frac{\partial MC}{\partial t} = \nabla^2 \times D_{eff} \times MC \quad \text{(Crank, 1975)} \qquad ...(2)$$

Doymaz (2012) noted that the effective moisture diffusion coefficient (D_{eff}) reflects a material's drying capacity under various conditions. Equation 3 presents a simplified form of Fick's second law of diffusion, assuming an initially uniform moisture distribution and an infinite slab geometry.

$$\mathrm{MR} = \frac{\mathrm{MC(t)} - \mathrm{MC(eq)}}{\mathrm{MC_0} - \mathrm{MC(eq)}} = \frac{8}{\pi^2}\sum_{n=0}^{\infty}\frac{1}{(2n+1)^2} \times exp\left[-(2n+1)^2 \ \frac{\pi^2 D_{eff}\ t}{L^2}\right] \qquad ...(3)$$

where $\mathrm{MC(t)}$ is the dry basis moisture content during the drying process, $\mathrm{MC_0}$ is the dry basis moisture content of a product before starting the drying process, $\mathrm{MC(eq)}$ is the equilibrium dry basis moisture content, and L is the slab thickness (m) (ASABE, 2022).

Equation 4 has been applied to coffee cherries, considering sphere geometry.

$$\mathrm{MR} = \frac{\mathrm{MC(t)} - \mathrm{MC(eq)}}{\mathrm{MC_0} - \mathrm{MC(eq)}} = \frac{6}{\pi^2}\sum_{n=0}^{\infty}\frac{1}{n^2}\ exp\left[-n^2 \ \frac{\pi^2 D_{eff}\ t}{r_s^2}\right] \qquad ...(4)$$

where r_s is the sphere radius (m) (Hui *et al.*, 2008). The assumptions for applying Equation 4 for coffee cherries were as follows: the diffusion coefficient is not dependent on the moisture content of a product at a given temperature, during the drying process the coffee cherries are isothermal, there is a uniform initial moisture content distribution in the initial stage of the coffee cherries, the coffee cherries surface moisture content rapidly reaches equilibrium with the surrounding air properties, and the coffee cherry size and geometry is not changing during the drying. Furthermore, there is no mass reduction or gain inside the coffee cherry (adapted from: Kahveci & Cihan, 2008).

Table 1: Thin-layer drying models and their applications

Thin-layer drying models	**Applications**
Semi-theoretical models	
Models derived from Newton's law of cooling	
Lewis model / Newton/Simple/Exponential model $\mathrm{MR} = \frac{\mathrm{MC(t)} - \mathrm{MC(eq)}}{\mathrm{MC_0} - \mathrm{MC(eq)}} = \exp(-\mathrm{k_0 t})$ Lewis (1921)	Red chili (Hossain *et al.*, 2007), Soyabeans (Coradi *et al.*, 2022), Maize (Mondal *et al.*, 2022)
Page model $\mathrm{MR} = \frac{\mathrm{MC(t)} - \mathrm{MC(eq)}}{\mathrm{MC_0} - \mathrm{MC(eq)}} = \exp(-\mathrm{k_0 t^n})$ Page (1949)	Mint leaves (Ramirez-Gutierrez *et al.*, 2021), White mushrooms (Szadzińska & Mierzwa, 2021), Pomegranate (Adetoro *et al.*, 2020)
Modified Page model $\mathrm{MR} = \frac{\mathrm{MC(t)} - \mathrm{MC(eq)}}{\mathrm{MC_0} - \mathrm{MC(eq)}} = \exp[(-\mathrm{k_0 t})^n]$ White *et al.* (1980)	Pumpkin (Semai *et al.*, 2021), Red kidney beans (Jian & Jayas, 2018)

Thin-layer drying models	Applications
Models derived from Fick's second law of diffusion	
Henderson and Pabis model $$MR = \frac{MC(t) - MC(eq)}{MC_0 - MC(eq)} = a\exp(-k_0 t)$$ Henderson & Pabis, 1961	Paddy (Golpour *et al.*, 2021), Dill leaves (Dikmen *et al.*, 2019)
Logarithmic model $$MR = \frac{MC(t) - MC(eq)}{MC_0 - MC(eq)} = a \times \exp(-k_0 t) + C$$ Chandra & Singh, 1995	Sweet basil (Dikmen *et al.*, 2019), Yam (Kamal *et al.*, 2020)
Two-term model $$MR = \frac{MC(t) - MC(eq)}{MC_0 - MC(eq)} = a\exp(-k_0 t) + b\exp(-k_1 t)$$ Henderson, 1974	Rough rice (Foroughi-Dahr *et al.*, 2015), Parsley (Dikmen *et al.*, 2019)
Exponential two-term model $$MR = \frac{MC(t) - MC(eq)}{MC_0 - MC(eq)} = a\exp(-k_0 t) + (1-a)\exp(-k_0 a t)$$ Sharaf-Eldeen *et al.*, 1980	Starfruit slices (Dash *et al.*, 2013), Radish (Lee & Kim, 2009)
Approximation of diffusion $$MR = \frac{MC(t) - MC(eq)}{MC_0 - MC(eq)} = a\exp(-k_0 t) + (1-a)\exp(-k_0 b t)$$ Kaseem, 1998	Apricot (Zhang *et al.*, 2016), Yam slices (Sobukola *et al.*, 2008)
Midilli model $$MR = \frac{MC(t) - MC(eq)}{MC_0 - MC(eq)} = a\exp(-k_0 t^n) + bt$$ Midilli *et al.*, 2002	Pomegranate (Adetoro *et al.*, 2020), Mango (Mugodo & Workneh, 2021)
Empirical models	
Wang and Singh model $$MR = 1 + bt + at^2$$ Chen & Wu, 2001	Banana (Kadam & Dhingra, 2011; Omolola *et al.*, 2014;), Nata de coco (Fan *et al.*, 2011)

MR: moisture ratio, MC(t): moisture content at time t (dry basis), MC: initial moisture content (dry basis), MC(eq): equilibrium moisture content (dry basis), a, b, C, n: model constants, k_0, k_1: drying rate constants, t: time

Thin-layer drying models

The drying kinetics of most agricultural products predominantly occur during the falling-rate period and are typically predicted using theoretical, semi-theoretical, and empirical models. Table 1 lists ten widely used thin-layer drying models for determining the moisture ratio in various agricultural materials.

Activation energy

Arrhenius' equation describes the effect of drying temperature on the effective moisture diffusion coefficient (Equation 5) (Kashaninejad *et al.*, 2007; Perea-Flores *et al.*, 2012).

$$D_{eff} = D_0\, exp\left(-\frac{E_a}{RT}\right) \quad ...(5)$$

where D_0 is the diffusivity constant at infinite temperature, E_a is the activation energy (kJ mol^{-1}), R is the universal gas constant (8.314 J mol^{-1} K^{-1}), and T is the drying temperature in K.

Model parameter estimation and data analysis

Model fitting was conducted using a non-linear optimization method in Excel Solver, utilizing the generalized reduced gradient (GRG) non-linear algorithm. This method was employed to estimate the model parameters by minimizing the sum of squared errors between the experimental and predicted moisture ratio (MR) values. The obtained model parameters were specific to each drying condition, and different models were compared to select the best-fit equation that accurately describes the drying kinetics.

To evaluate the quality and validity of the fitted models, the coefficient of determination (R^2) and root mean square error (*RMSE*) were calculated. The R^2 quantifies the model's ability to predict future outcomes by assessing the agreement between measured and predicted values (Hossain *et al.*, 2007). R^2 values range from 0 to 1, with values closer to 1 indicating a stronger correlation between experimental data and model predictions (Neter *et al.*, 1990). The R^2 is indicated by Equation 6.

$$R^2 = 1 - \frac{Residual\ sums\ of\ square}{Corrected\ total\ sums\ of\ square} \qquad ...(6)$$

The differences between the model-predicted value and the observed value are measured by *RMSE* (Equation 7). Therefore, *RMSE* is a good measure of accuracy, providing a single measure of predictive power that incorporates the residuals. However, *RMSE* should approach zero (Changrue *et al.*, 2008), indicating that the results are less deviated from the mathematical model.

$$RMSE = \left\{\frac{1}{N}\sum_{i=1}^{N}\left(MR_{exp,i} - MR_{pre,i}\right)^2\right\}^{\frac{1}{2}} \qquad ...(7)$$

Colour difference (ΔE)

The colour values of the initial sample and final sample were measured to analyze the colour values (CIE - Commission Internationale de l'Eclairage L^*, a^*, and b^* values). The subscript '1' refers to the initial colour parameters of each sample at the beginning of the drying experiment. Subscript '2' refers to the colour at the time of measurement. Lightness-darkness (L^*), redness-greenness (a^*), and yellowness-blueness (b^*) are the corresponding colour coordinates.

Table 2: Colour scale

Colour change	Description
$\Delta E < 0.2$	No visible difference
$2 > \Delta E > 0.2$	Small difference
$3 > \Delta E > 2$	Colour difference visible with high quality screen
$6 > \Delta E > 3$	Colour difference visible with medium quality screen
$12 > \Delta E > 6$	High colour difference
$\Delta E > 12$	Different colours

Every colour measurement was performed in triplicate, and the average value was reported. The total colour difference (ΔE) was then determined using Equation 8, and the scale of ΔE is shown in Table 2 (Klement *et al.*, 2021).

$$\Delta E = \sqrt{(L_2^* - L_1^*)^2 + (a_2^* - a_1^*)^2 + (b_2^* - b_1^*)^2} \qquad ...(8)$$

where subscript 1 and 2 refer to initial and final values.

Hue angle (h*)

Hue angle is one of the primary properties of a colour, as defined technically in the CIECAM02 model, and it is determined by Equation 9 (Suchta *et al.*, 2020). Hue angle, ranging from 0 to 360 degrees in the redness-greenness (a^*) and yellowness-blueness (b^*) planes, is based on the concept of equal perceived difference.

$$h^* = tan^{-1}\frac{b^*}{a^*}\ (°) \qquad ...(9)$$

Colour saturation (C_{ab}^*)

The intensity of colour was measured by colour saturation (Schanda, 2007). Equation 10 was used to determine colour saturation.

$$C_{ab}^* = \sqrt{a^{*2} + b^{*2}} \qquad ...(10)$$

Saturation (S_{ab})

The saturation (Schanda, 2007) of a colour is determined by a combination of light intensities, calculated using Equation 11. The most saturated colour is achieved by using a single wavelength at high intensity, such as laser light.

$$S_{ab} = \frac{C_{ab}^*}{\sqrt{C_{ab}^{*2} + L^{*2}}} \times 100\ (\%) \qquad ...(11)$$

RESULTS AND DISCUSSION

Coffee cherries, initially containing approximately 70% moisture (wet basis), were dried until a constant moisture level was achieved. Figure 1 depicts the moisture content trajectories at drying temperatures of 40 °C, 60 °C, 80 °C, and 100 °C. The data demonstrate that moisture content declines continuously over time, with higher drying air temperatures markedly accelerating moisture removal and reducing total drying time. The drying curves did not exhibit a pre-heating phase or a constant rate period; the entire process occurred within the falling rate period. This observation indicates that moisture removal from the coffee cherries was predominantly governed by diffusion. These drying characteristics are consistent with those observed in other agricultural products, as reported for chili (Mihindukulasuriya & Jayasuriya, 2013; Fernando *et al.*, 2022), bay laurel leaves (Doymaz, 2014b), pomegranate (Adetoro *et al.*, 2020), apricot (Zhang *et al.*, 2016), and saffron petals (Sharayei *et al.*, 2018).

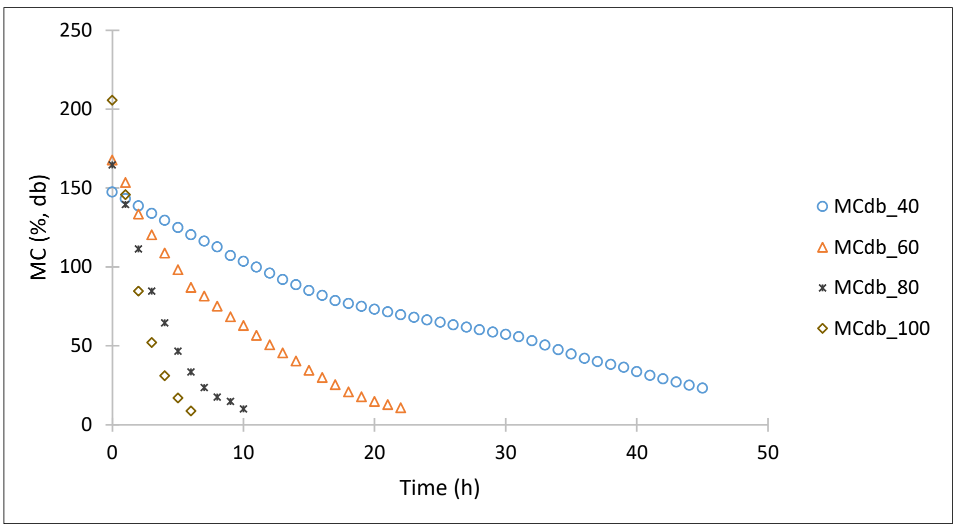

Figure 1: Moisture content variation of coffee cherries at different temperatures

The relationship between moisture content and drying time was evaluated by fitting the experimental data to various thin-layer drying models, as in Table 3. Further, Table 3 contains the constants for each model, along with the corresponding statistical analyses. All models exhibited high coefficients of determination (R^2 ranging from 0.9109 to 0.9998), confirming their suitability for characterizing the hot air drying behavior of coffee cherries.

Table 3: Model parameter values for the selected thin-layer drying models

Model	Model constants and coefficients	Drying Temperature			
		40°C	60°C	80°C	100°C
Newton (Lewis) $MR = \exp(-k_0 t)$	*k*	0.0361	0.1083	0.1622	0.4489
	R^2	0.9924	0.9955	0.9859	0.9960
	RMSE %	0.1410	0.1461	2.4305	0.1099
Page $MR = \exp(-k_0 t^n)$	*k*	0.0270	0.0885	0.0620	0.3657
	n	1.0862	1.0816	1.4848	1.2032
	R^2	0.9930	0.9957	0.9993	0.9995
	RMSE %	0.0877	0.5036	0.1753	0.0056

Model	Model constants and coefficients	Drying Temperature			
		40°C	60°C	80°C	100°C
Modified Page $MR = \exp[(-k_0 t)^n]$	*k*	0.0425	0.0736	0.0901	0.1498
	n	0.8500	1.4716	1.8011	2.9965
	R^2	0.9922	0.9955	0.9859	0.9960
	RMSE %	0.1310	0.0888	2.4041	0.1639
Henderson and Pabis $MR = a \exp(-k_0 t)$	*k*	0.0370	0.1100	0.1790	0.4608
	a	1.0224	1.0167	1.1183	1.0302
	R^2	0.9915	0.9949	0.9829	0.9958
	RMSE %	0.0863	0.2246	1.6413	0.1266
Logarithmic $MR = a \exp(-k_0 t) + C$	*k*	0.0291	0.0960	0.1564	0.4472
	a	1.1025	1.0392	1.1483	1.0369
	C	-0.1115	-0.0460	-0.0517	-0.0099
	R^2	0.9952	0.9976	0.9862	0.9960
	RMSE %	0.0891	0.2151	1.3225	0.3098
Two Term $MR = a \exp(-k_0 t) + b \exp(-k_1 t)$	k_0	0.0104	0.1100	0.1790	0.4608
	k_1	0.0256	0.1100	0.1790	0.4608
	a	-0.4070	0.3229	0.9676	0.9158
	b	1.3960	0.6939	0.1507	0.1144
	R^2	0.9951	0.9949	0.9829	0.9958
	RMSE %	0.0567	0.0183	1.0641	0.5094
Exponential Two Term $MR = a \exp(-k_0 t) + (1 - a) \exp(-k_0 a t)$	*k*	0.0444	3.9621	0.1622	0.4541
	a	1.5535	0.0265	0.9855	0.9090
	R^2	0.9934	0.9959	0.9859	0.9960
	RMSE %	0.0217	0.1103	2.4027	0.1404
Approximation of diffusion $MR = a \exp(-k_0 t) + (1 - a)\exp(-k_0 b t)$	*k*	0.0311	0.3426	0.1622	4.0247
	a	1.0539	-0.1210	0.1078	-0.2110
	b	-0.2205	0.3411	1.0000	0.1321
	R^2	0.9951	0.9956	0.9859	0.9998
	RMSE %	0.0247	0.3748	2.1030	0.1633
Midilli $MR = a \exp(-k_0 t^n) + bt$	*k*	0.0375	0.0951	0.0612	0.3675
	n	1.0060	1.0253	1.4989	1.2045
	a	-0.0015	0.9897	1.0021	1.0032
	b	0.9455	-0.0010	0.0003	0.0002
	R^2	0.9952	0.9973	0.9994	0.9995
	RMSE %	0.0793	0.2092	0.0624	0.0868
Wang and Singh $MR = 1 + bt + at^2$	*a*	-0.0285	-0.0729	-0.1096	-0.2205
	b	0.0002	0.0013	0.0029	0.0109
	R^2	0.9936	0.9883	0.9831	0.9109
	RMSE %	0.1070	1.2476	0.7832	4.5845

RMSE measures the average magnitude of the errors between the predicted and observed values. A lower *RMSE* indicates a closer fit to the data. At 40 °C and 60 °C, the Exponential Two-term model minimizes *RMSE*, meaning it has the lowest average error at these temperatures, even if its R^2 might not be the highest. At 80 °C and 100 °C, the Page model provides the lowest *RMSE* values, suggesting that although it may not explain the variability (R^2) as well as some other models, it offers the most accurate predictions regarding error magnitude.

Table 3 shows that the model that explains the most variability (high R^2) is not always the same as the one that minimizes error (low *RMSE*). This difference implies that the choice of model might depend on whether the priority is to understand the underlying process (explained variance) or to achieve precise predictions (minimal error). When choosing a model for practical applications, researchers might weigh whether they need one that best explains the data variability (using R^2) or one that offers the most precise predictions (using *RMSE*). Table 3 suggests that the optimal choice can shift with operating conditions, such as temperature, and that sometimes, a trade-off between explained variance and error minimization is necessary.

When evaluating the entire dataset, the Midilli model stands out with exceptionally high R^2 values at all temperatures: 0.9952 at 40 °C, 0.9973 at 60 °C, 0.9994 at 80 °C, and 0.9995 at 100 °C. These figures demonstrate that the model accounts for nearly all the variability in the drying data. Additionally, it maintains impressively low *RMSE* values, 0.0793% at 40 °C, 0.2092% at 60 °C, 0.0624% at 80 °C, and 0.0868% at 100 °C, indicating that its predictions closely match the observed values. The consistently high R^2 and low *RMSE* across all conditions confirm that the Midilli model explains the data's variability and makes highly accurate predictions.

Figure 2 presents the experimental moisture ratio profiles alongside the predictions from the Midilli model at various drying air temperatures over time. The close agreement between observed data and model predictions underscores the superior fit provided by the Midilli model in capturing the drying behavior of coffee cherries. This robust performance corroborates findings reported for other agricultural products, including mango (Mugodo & Workneh, 2021), pomegranate (Adetoro *et al.*, 2020), apricot (Zhang *et al.*, 2016), jackfruit (Saxena & Dash, 2015), bay laurel leaves (Doymaz, 2014b), turnip slices (Kaveh & Amiri Chayjan, 2017), peach (Doymaz, 2014a), apple slices (Zarein *et al.*, 2013), kiwifruit (Darıcı & Şen, 2015), chili (Mihindukulasuriya & Jayasuriya, 2013), and pepper (Darvishi *et al.*, 2014). These results highlight the model's effectiveness as a predictive tool for thin-layer drying kinetics. They reinforce its potential application in optimizing drying processes for coffee cherries and other agricultural materials.

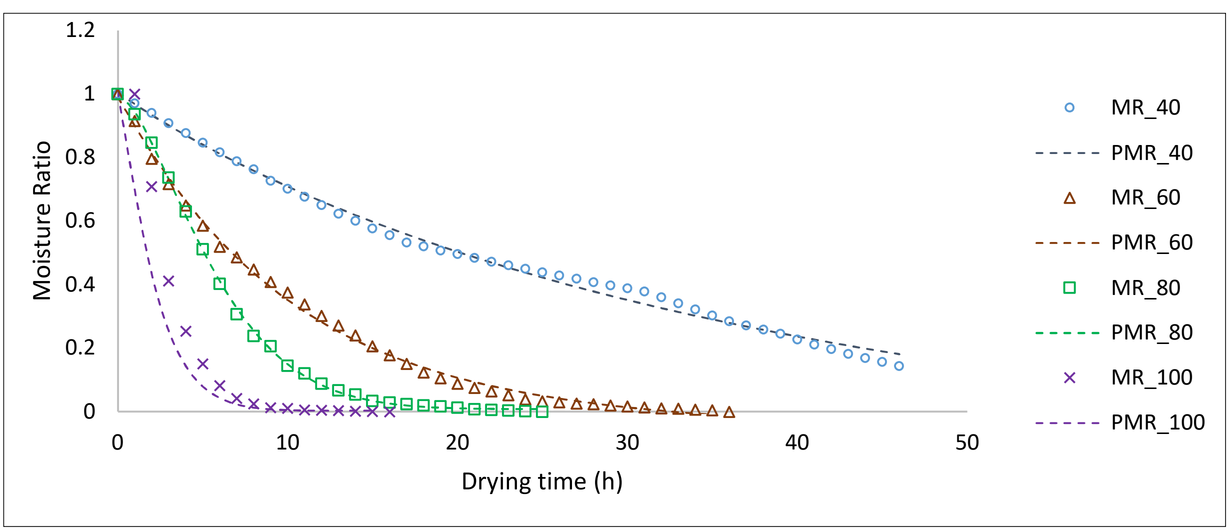

Figure 2: Experimental and predicted moisture ratios for coffee cherries applied to Midilli model

Table 4 presents the values of D_{eff} of coffee cherries at various temperatures. The effective moisture diffusivity was increased by increasing the drying air temperature from 40 °C to 100 °C.

Table 4: Effective diffusivity for coffee cherries at various temperatures

Temperature (°C)	Effective diffusivity (D_{eff}) (m^2s^{-1})
40	1.154×10^{-7}
60	3.276×10^{-7}
80	5.257×10^{-7}
100	8.939×10^{-7}

Diffusivity typically follows an Arrhenius relationship, meaning that as the temperature increases, the exponential increase in molecular movement leads to a higher effective diffusivity. In their study on the evolution and modeling of moisture diffusion in walnuts during combined hot air and microwave-vacuum drying, Man *et al.* (2024) found that the effective diffusivity (D_{eff}) increases with higher hot air temperatures. This increase is primarily due to the elevated temperature enhancing the kinetic energy of water molecules, thereby accelerating moisture diffusion (Lu *et al.*, 2020). Similarly, An *et al.* (2024) observed that when hot air temperature ranged from 30 to 45 °C, diffusivity varied between 2.190×10^{-9} and 3.022×10^{-9} m^2s^{-1} during the microwave hot air combined drying of peanut pods. Their findings indicate that a gradual increase in microwave power significantly impacts the moisture diffusion coefficient as the rising temperature augments the thermal energy within the water molecules of peanut pods, enhancing their mobility. Consequently, this increased energy transfer facilitates water molecules in overcoming their bonds, leading to more active moisture diffusion (Mohammadi *et al*., 2019).

Equation 5 was rearranged as in Equation 12 to determine the activation energy.

$$\ln(D_{eff}) = \ln(D_0) - \frac{E_a}{RT} \qquad ...(12)$$

Values of D_{eff} were calculated using Equation 8 for the coffee cherry drying experiments, plotted in Figure 3. The plot demonstrates a straight line in the experimental drying air temperature range. The activation energy was calculated to be 32.358 kJ mol^{-1} from the slope of the straight line, as predicted by the Arrhenius equation.

Table 5 compares the activation energy

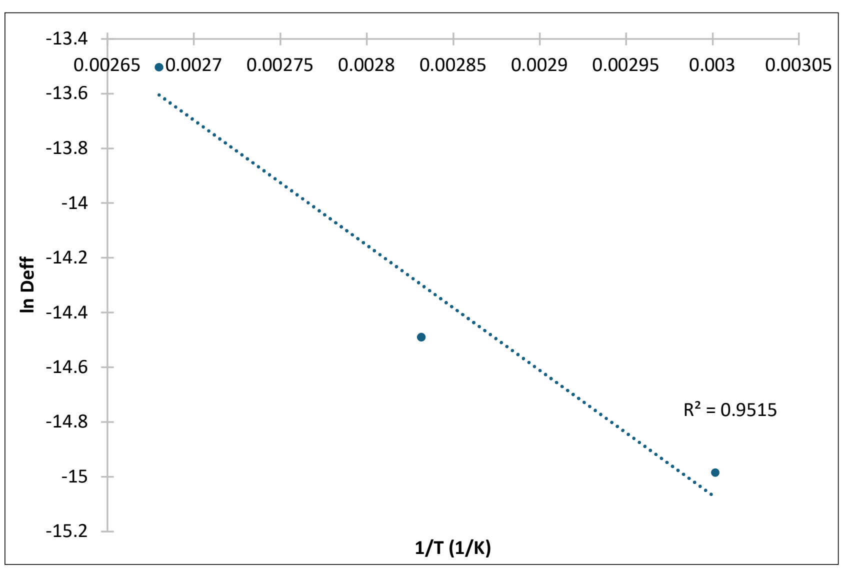

Figure 3: Logarithmic value of effective moisture diffusivity of coffee cherry as a function of the reciprocal of absolute drying air temperature

(E_a) of coffee cherries with that of other agricultural products. The observed variations in E_a among different products are attributed to inherent structural differences, particularly in the strength of water binding. Materials with strongly bound water require higher activation energy for moisture removal, indicating higher resistance to drying (Bezerra *et al.*, 2015).

Table 5: Activation energy for different products

Product	Activation energy (kJ mol^{-1})	Reference
Soybean	13.88	Niamnuy *et al*., 2012
Sweet sorghum stalk	24.10	Shen *et al*., 2011
Presoaked soybean	31.40	Irigoyen & Giner, 2014
Coffee cherries	32.36	Current research
Castor oil seeds	41.41	Perea-Flores *et al*., 2012
Passion fruit peel	29.57–34.73	Bezerra *et al*., 2015

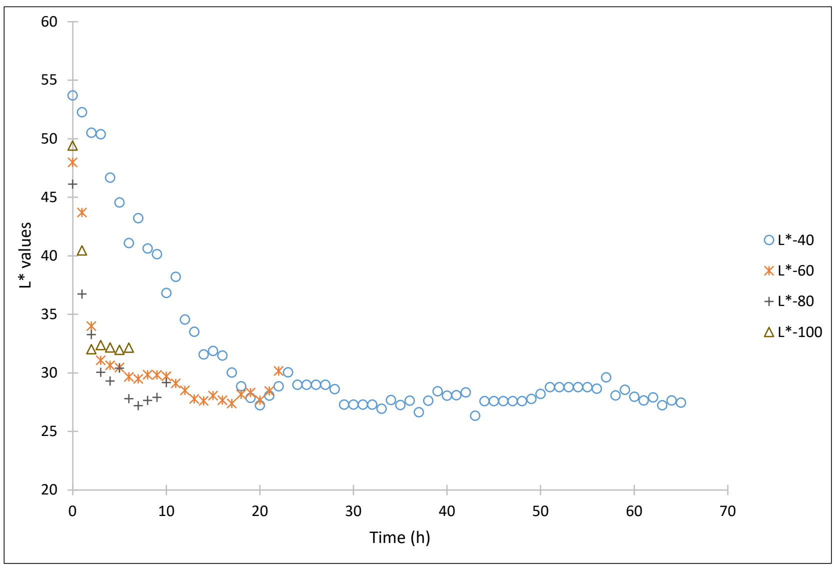

Figure 4: Lightness (L^*) values change during coffee drying at different temperatures

Table 6: Colour changes (ΔE) during coffee drying

Temperature (°C)	Colour coordinates	Before drying	After drying	Colour change (ΔE)
40	L^*	53.69 ± 1.6	27.94 ± 1.2	26.2
	a^*	-15.9 ± 0.3	5.48 ± 1.8	-19.7
	b^*	29.3 ± 2.4	5.73 ± 0.8	24.1
60	L^*	47.99 ± 2.0	27.27 ± 0.5	17.8
	a^*	-13.6 ± 5.2	5.49 ± 0.5	-18.9
	b^*	25.5 ± 1.1	5.79 ± 0.4	23.3
80	L^*	46.12 ± 2.5	27.4 ± 1.2	16.9
	a^*	1.07 ± 5.4	9.31 ± 1.6	-5.7
	b^*	23.99 ± 3.8	8.91 ± 1.4	16.6
100	L^*	49.41 ± 2.7	29.99 ± 0.5	17.3
	a^*	-10.6 ± 4.6	6.94 ± 0.5	-16.7
	b^*	22.66 ± 3.0	11.91 ± 0.2	14.2

The L^* value (lightness) drops at all drying temperatures. Drying removes water from the cherries, concentrating the natural pigments and increasing light absorption, which results in a darker appearance. Fresh coffee cherries exhibit negative a^* values, indicating a greenish colour. After drying, these values become positive, marking a shift toward red. The b^* value, which indicates yellowness, decreases markedly after drying.

Table 7: Colour properties of coffee during hot air drying

Temperature (°C)	Hue angle		Colour saturation		Saturation	
	Before drying	After drying	Before drying	After drying	Before drying	After drying
40	-1.07	0.81	33.34	7.93	52.75	0.27
60	-1.08	0.81	28.90	7.98	51.59	0.28
80	1.53	0.76	24.01	12.89	46.18	0.43
100	-1.13	1.04	25.02	13.78	45.17	0.42

Although the hue angle values are relatively small, the consistent shift from near-zero or slightly negative to positive values reinforces the observed change in a^* (from greenish to reddish). This shift indicates a subtle change in the overall tone of the cherries, consistent with pigment degradation and the formation of oxidation products. Both colour saturation and the measured saturation values drop steeply after drying. These reductions suggest that drying significantly diminishes the vividness and intensity of the cherries' colour, resulting in a more muted, less vibrant appearance.

The observed colour change is primarily due to the Maillard reaction and caramelization initiated by heat (Lee *et al.*, 2022). Extended exposure to high temperatures further degrades the colour, resulting in a more pronounced darkening of the material. The primary factors contributing to this deterioration include Maillard reactions, oxidation, and changes in the surface structure (Ray *et al.*, 2022).

CONCLUSION

The drying time for coffee cherries was reduced while the drying air temperature was increased from 40 °C to 100 °C. Therefore, the coffee cherry drying process primarily occurs during the falling rate period of the typical drying curve. The Midilli model provided the most accurate description of the drying kinetics, achieving the highest R^2 and the lowest *RMSE* values. The effective diffusivity values ranged from 1.154×10^{-7} to 8.939×10^{-7} m^2s^{-1} for the temperature range 40 °C to 100 °C for coffee cherries. This indicates an increase in effective moisture diffusivity at higher temperatures of the drying air. The activation energy of moisture diffusion was 32.36 kJ mol^{-1}. Drying leads to significant darkening of coffee cherries due to moisture loss, changes in pigment concentration, and non-enzymatic browning. These results provide data for controlling the drying conditions of coffee cherries.

Acknowledgement

The authors would like to acknowledge the support given by Mr. Tharindu Madushanka, Ms. Yashmi Jayaweera, Ms. Manuri Wimalaweera, and Chanaka Gunathunga during data collection.

REFERENCES

Do Carmo, K.B., do Carmo, J.C.B., Krause, M. R., & Peterle, G. (2020). Sensory and physiological quality of Arabic coffee under different fermentation times. *Bi*oscience Journal, 36(2). 429 - 438. https://doi.org/10.14393/BJ-v36n2a2020-43255

Doymaz, İ. (2012). Sun drying of seedless and seeded grapes. Journal of Food Science and Technology, 49, 214-220. https://doi: 10.1007/s13197-011-0272-9

Doymaz, I. (2014a). Suitability of thin-layer drying models for infrared drying of peach slices. Journal of Food Processing and Preservation, 38(6), 2232-2239. https://doi.org/10.1111/jfpp.12277

Doymaz, İ. (2014b). Thin-Layer Drying of Bay Laurel Leaves (Laurus nobilis L.). Journal of Food Processing and Preservation, 38(1), 449-456. https://doi.org/10.1111/j.1745-4549.2012.00793.x

Elhalis, H., Cox, J., & Zhao, J. (2023). Coffee fermentation: Expedition from traditional to controlled process and perspectives for industrialization. Applied Food Research, 3(1), 100253. https://doi.org/10.1016/j.afres.2022.100253

Fan, H., Wu, Y., Hu, X., Wu, J. & Liao, X. (2011). Characteristics of thin-layer drying and rehydration of nata de coco. International Journal of Food Science Technology, 46(7), 1438-1444. https://doi.org/10.1111/j.1365-2621.2011.02642.x

Fernando, A. J., & Amaratunga, S. (2022). Application of far-infrared radiation for sun-dried chili pepper (Capsicum annum L.): drying characteristics and color during roasting. Journal of the Science of Food and Agriculture, 102(9), 3781-3787. https://doi.org/10.1002/jsfa.11726

Fernando, A. J., Amaratunga, K. S. P., Madhushanka, H. T. N., & Jayaweera, H. R. Y. S. (2021). Drying performance of coffee in a batch-type heat pump dryer. Transactions of the ASABE, 64(4): 1237-1245. https://doi: 10.13031/trans.14268

Firdissa, E., Mohammed, A., Berecha, G., & Garedew, W. (2022). Coffee drying and processing method influence quality of arabica coffee varieties (Coffea arabica L.) at Gomma I and Limmu Kossa, Southwest Ethiopia. Journal of Food Quality, 2022(1), 9184374. https://doi.org/10.1155/2022/9184374

Foroughi-Dahr, M., Golmohammadi, M., Pourjamshidian, R., Rajabi-Hamaneh, M., & Hashemi, S.J. (2015). On the characteristics of thin-layer drying models for intermittent drying of rough rice. Chemical Engineering Communications, 202(8), 1024-1035. https://doi.org/10.1080/00986445.2014.900049

Ghosh, P., & Venkatachalapathy, N. (2014). Thin layer drying of hot-air assisted microwave drying of parchment coffee. International Journal of Latest Trends in Engineering and Technology, 4(4), 121-133.

Golpour, I., Guiné, R. P., Poncet, S., Golpour, H., Chayjan, A. R., & Parian, A. J. (2021). Evaluating the heat and mass transfer effective coefficients during the convective drying process of paddy (Oryza sativa L.). Journal of Food Process Engineering, 44(9)e13771. https://doi.org/10.1111/jfpe.13771

Henderson, S. M., & Pabis, S. (1961). Grain drying theory I: Temperature effect on drying coefficient. Agricultural and Food Sciences, Engineering, 6: 169–174. https://api.semanticscholar.org/CorpusID:208841650

Henderson, S. M. (1974). Progress in developing the thin layer drying equation. Transactions of the ASAE 17(6), 1167-1168. https://doi: 10.13031/2013.37052

Hossain, M. A., Woods, J. L., & Bala, B. K. (2007). Single-layer drying characteristics and colour kinetics of red chilli. International Journal of Food Science and Technology, 42(11):1367–75. doi:10.1111/j.1365-2621.2006.01414.x

Huch, M., & Franz, C. M. A. P. (2015). Coffee: fermentation and microbiota. In Advances in fermented foods and beverages (501-513). Woodhead Publishing. https://doi.org/10.1016/B978-1-78242-015-6.00021-9

Hui, Y. H., Clary, C., Farid, M. M., Fasina, O. O., Noomhorm, A., & Welti-Chanes, J. (2008). Food Drying. Science and Technology. DEStech Pub. Inc., PA, USA.

International Coffee Organization [ICO] (2022). World coffee consumption. https://www.ico.org/trade_statistics.asp

Irigoyen, R. T., & Giner, S. A. (2014). Drying-toasting kinetics of presoaked soybean in a fluidized bed. Experimental study and mathematical modeling with analytical solutions. Journal of Food Engineering, 128, 31-39. https://doi.org/10.1016/j.jfoodeng.2013.12.00

International Standards Organization [ISO] (2018). ISO 1446:2001 (R2018). Green coffee - Determination of water content - Basic reference method. Geneva, Switzerland: International Standard Organization.

Jian, F., & Jayas, D. S. (2018). Characterization of isotherms and thin-layer drying of red kidney beans, Part I: Choosing appropriate empirical and semi-theoretical models. Drying Technology, 36(14), 1696-1706. https://doi.org/10.1080/07373937.2017.1422514

Kadam, D. M., & Dhingra, D. (2011). Mass transfer kinetics of banana slices during osmo-convective drying. Journal of Food Process Engineering, 34(2), 511-532. https://doi.org/10.1111/j.1745-4530.2009.00373.x

Kahveci, K., & Cihan, A. (2008). Drying of Food Materials: Transport Phenomena. Nova Science Publishers Inc.

Kamal, M. M., Ali, M. R., Shishir, M. R. I., & Mondal, S. C. (2020). Thin-layer drying kinetics of yam slices, physicochemical, and functional attributes of yam flour. Journal of Food Process Engineering, 43(8), e13448. https://doi.org/10.1111/jfpe.13448

Kaseem, A. S. (1998). Comparative studies on thin layer drying models for wheat. In 13th International Congress on Agricultural Engineering, Vol. 6, February 2–6, Morocco.

Kashaninejad, M., Mortazavi, A., Safekordi, A., & Tabil, L. G. (2007). Thin-layer drying characteristics and modeling of pistachio nuts. Journal of Food Engineering, 78(1), 98-108. https://doi.org/10.1016/j.jfoodeng.2005.09.007

Kaveh, M., & Chayjan, A. R. (2017). Modeling thin-layer drying of turnip slices under a semi-industrial continuous band dryer. Journal of Food Processing and Preservation, 41(2), e12778. https://doi.org/10.1111/jfpp.12778

Klement, I., Vilkovský, P., Vilkovská, T., Orłowski, K. A., Barański, J., Chuchala, D., & Suchta, A. (2021). The influence of drying temperature on color change of hornbeam and maple wood used as surface and inner layers of wood composites. Applied Sciences, 11(22), 10673. https://doi.org/10.3390/app112210673

Lee, J. H., & Kim, H. J. (2009). Vacuum drying kinetics of Asian white radish (Raphanus sativus L.) slices. LWT-Food Science and Technology, 42(1), 180-186. https://doi.org/10.1016/j.lwt.2008.05.017

Lee, S. Y., Ferdinand, V., & Siow, L. F. (2022). Effect of drying methods on yield, physicochemical properties, and total polyphenol content of chamomile extract powder. Frontiers in Pharmacology 13, 1003209. https://doi.org/10.3389/fphar.2022.1003209

Lewis W. K. (1921). The rate of drying of solid materials. IandEC-Symposium of Drying, 3(5):42.

Lu, Y. J., Ren, G. Y., Duan, X., Zhang, L. D., Ling, Z. Z. (2020). Moisture migration properties and quality changes of fresh in-shell peanuts during hot air drying. Food Science, 41, 86–92. 10.7506/spkx1002-6630-20190311-134

Man, X., Li, L., Fan, X., Zhang, H., Lan, H., Tang, Y., & Zhang, Y. (2024). Evolution and Modelling of the Moisture Diffusion in Walnuts during the Combination of Hot Air and Microwave–Vacuum Drying. Agriculture, 14(2), 190. https://doi.org/10.3390/agriculture14020190

Midilli, A., Kucuk, H., & Yapar, Z. (2002). A new model for single-layer drying. Drying Technology, 20:1503–1513. https://doi.org/10.1081/DRT-120005864

Mihindukulasuriya, S.D.F., & Jayasuriya, H.P.W. (2013). Mathematical modeling of drying characteristics of chilli in hot air oven and fluidized bed dryers. Agricultural Engineering International: CIGR Journal 15(1):154–66.

Mohammadi, I., Tabatabaekoloor, R., & Motevali, A. (2019). Effect of air recirculation and heat pump on mass transfer and energy parameters in drying of kiwi fruit slices. Energy, 170, 149-158. https://doi.org/10.1016/j.energy.2018.12.099

Mondal, M. H. T., Akhtaruzzaman, M., & Sarker, M. S. H. (2022). Modeling of dehydration and color degradation kinetics of maize grain for mixed flow dryer. Journal of Agriculture and Food Research, 9, 100359. https://doi.org/10.1016/j.jafr.2022.100359

Mugodo, K., & Workneh, T. S. (2021). The kinetics of thin-layer drying and modelling for mango slices and the influence of differing hot-air drying methods on quality. Heliyon, p.e07182. https://doi.org/10.1016/j.heliyon.2021.e07182

Muhidong, J., Mursalim, & Rahman, A. (2013). The effect of airflow rate on single-layer drying characteristics of Arabica coffee. International Food Research Journal, 20(4): 1633-1637. https://api.semanticscholar.org/CorpusID:127661196

Neter, J., Wasserman, W., & Kutner, M. H. (1990). Applied linear statistical models. In: Regression Analysis of Variance and Experimental Designs. Richard D. Irwin Inc., USA.

Niamnuy, C., Nachaisin, M., Poomsa-ad, N., & Devahastin, S. (2012). Kinetic modelling of drying and conversion/degradation of isoflavones during infrared drying of soybean. Food Chemistry, 133(3), 946–952. https://doi:10.1016/j.foodchem.2012.02.010

Nilnont, W., Thepa, S., Janjai, S., Kasayapanand, N., Thamrongmas, C., & Bala, B. K. (2012). Finite element simulation of coffee (Coffea arabica) drying. Food and Bioproduct Processing, 90(2), 341–350. https://doi.org/10.1016/j.fbp.2011.06.007

Omolola, A. O., Jideani, A. I. O., & Kapila, P. F. (2014). Modeling microwave-drying kinetics and moisture diffusivity of Mabonde banana variety. International Journal of Agricultural and Biological Engineering, 7(6):107–13. https://doi:10.3965/j.ijabe.20140706.013

Page, G. E. (1949). Factors influencing the maximum rates of air drying shelled corn in thin layers. MS Thesis, Department of Mechanical Engineering, Purdue University, West Lafayette, IN.

Perea-Flores, M. J., Garibay-Febles, V., Chanona-Pérez, J. J., Calderón- Domínguez, G., Méndez-Méndez, J. V., Palacios-González, E., & Gutiérrez-López G. F. (2012). Mathematical modelling of castor oil seeds (Ricinus communis) drying kinetics in a fluidized bed at high temperatures. Industrial Crops and Products 38, 64–71. https://doi.org/10.1016/j.indcrop.2012.01.008

Phitakwinai, S., Thepa, S., & Nilnont, W. (2019). Thin-layer drying of parchment Arabica coffee by controlling temperature and relative humidity. Food Science & Nutrition, 7(9), 2921-2931. https://doi.org/10.1002/fsn3.1144

Ramirez-Gutierrez, D. M., Ileleji, K. E., & Deering, A. J. (2021). Evaluation of Novel Portable Passive and Cabinet Solar Dryers in Sun Drying of Mint Leaves under Indiana Weather Conditions. Transactions of the ASABE, 64(3), pp.1083-1094. https://doi: 10.13031/trans.14208

Ray, A., Mohanty, S., Jena, S., Sahoo, A., Acharya, L., Panda, P. C., et al. (2022). Drying methods affects physicochemical characteristics, essential oil yield, and volatile composition of turmeric (Curcuma longa L.). Journal of Applied Research on Medicinal and Aromatic Plants, 26, 100357. https://doi.org/10.1016/j.jarmap.2021.100357

Salehi, F., Goharpour, K., & Kamran, H. R. (2024). Effects of different pretreatment techniques on the color indexes, drying characteristics and rehydration ratio of eggplant slices. Results in Engineering, 21, 101690. https://doi.org/10.1016/j.rineng.2023.101690

Saxena, J., & Dash, K. K. (2015). Drying kinetics and moisture diffusivity study of ripe jackfruit. International Food Research Journal, 22(1):414–20.

Schanda, J. (Ed.). (2007). Colorimetry: Understanding the CIE system. John Wiley & Sons.

Semai, H., Bouhdjar, A., & Amari, A. (2021). An improved protocol for natural convective drying of pumpkin. Food and Feed Research, 48(1), 29-39. https://doi: https://doi.org/10.5937/ffr0-31341

Sharaf-Eldeen, Y. I., Blaisdell, J. L., & Hamdy, M. Y. (1980). A model for ear corn drying. Transactions of ASAE, 23:1261–1265, 1271. https://doi: 10.13031/2013.34757

Sharayei, P., Hedayatizadeh, M., Chaji, H., & Einafshar, S. (2018). Studying the thin-layer drying kinetics and qualitative characteristics of dehydrated saffron petals. Journal of Food Processing and Preservation, 42(9), p.e13677. https://doi: 10.1111/jfpp.13677

Shen, F., Peng, L., Zhang, Y., Wu, J., Zhang, X., Yang, G., Peng, H., Qi, H., & Deng, S. (2011). Thin-layer drying kinetics and quality changes of sweet sorghum stalk for ethanol production as affected by drying temperature. Industrial Crops and Products, 34(3), 1588–1594. https://doi.org/10.1016/j.indcrop.2011.05.027

Silva, C. F., Schwan, R. F., Dias, Ë. S., & Wheals, A. E. (2000). Microbial diversity during maturation and natural processing of coffee cherries of Coffea arabica in Brazil. International Journal of Food Microbiology, 60 (2–3), 251–260. https://doi.org/10.1016/S0168-1605(00)00315-9

Sobukola, O. P., Dairo, O. U., & Odunewu, A. V. (2008). Convective hot air drying of blanched yam slices. International Journal of Food Science and Technology, 43:1233–1238. https://doi.org/10.1111/j.1365-2621.2007.01597.x

Straits Research. (2025, February 12). Coffee market size, share & trends analysis report by product type (whole bean coffee, ground coffee, instant coffee, coffee pods, capsules), by distribution channels (on-trade, off-trade), by nature (conventional, organic), by grade (Arabica, Robusta, specialty, others), by application (hot drinks, ready-to-drink coffee, flavored beverages, food & beverage flavors, nutraceuticals, pharmaceuticals, cosmetics, others) and by region (North America, Europe, APAC, Middle East and Africa, LATAM) forecasts, 2025–2033 (Report Code: SRFB2811DR). https://straitsresearch.com/report/coffee-market

Suchta, A., Barański J., Orłowski, K., & Chuchała, D. (2020). The effect of drying intensity on the color changes of pine wood (Pinus Sylvestris L.). Trieskove a Beztrieskove Obrabanie Dreva 12, 79-84.

Sunarharum, W. B., Williams, D. J., & Smyth, H. E. (2014). Complexity of coffee flavor: A compositional and sensory perspective. Food Research International, 62, 315-325. https://doi.org/10.1016/j.foodres.2014.02.030

Szadzińska, J., & Mierzwa, D. (2021). The influence of hybrid drying (microwave-convective) on drying kinetics and quality of white mushrooms. Chemical Engineering and Processing-Process Intensification, 167,108532. https://doi.org/10.1016/j.cep.2021.108532

Wang, W., Chen, J., Jin, N., Wang, H., Wang, L., & Wu, J. (2024). Thin-Layer Drying Model, Drying Rate, and Effective Water Diffusion Coefficient of Pelleted Feed. International Journal of Chemical Engineering, 2024(1), 7092556. https://doi.org/10.1155/2024/7092556

White, G. M., Bridges, T. C., Loewer, O. J., & Ross, I. J. (1980). Seed coat damage in thin layer drying of soybeans. Transactions of the ASAE, 23(1), 224-0227. https://doi: 10.13031/2013.34559

Zarein, M., Samadi, S., & Barat, G. (2013). Kinetic drying and mathematical modeling of apple slices on dehydration process. Journal of Food Processing and Technology, 4(7):1–4. https://doi:10.4172/2157-7110.1000247

Zhang, Q. A., Song, Y., Wang, X., Zhao, W. Q., & Fan, X. H. (2016). Mathematical modeling of debittered apricot (Prunus armeniaca L.) kernels during thin-layer drying. CyTA-Journal of Food, 14(4), 509-517. https://doi.org/10.1080/19476337.2015.1136843

JOURNAL OF THE
NATIONAL SCIENCE FOUNDATION
OF SRI LANKA

GUIDANCE TO CONTRIBUTORS

GENERAL INFORMATION

Scope

The Journal of the National Science Foundation of Sri Lanka publishes the results of research in all aspects of Science and Technology. It is open for publication of Research Articles, Reviews, Research Communications and Correspondence.

Use of AI Tools in Manuscript Preparation

To ensure transparency and uphold scholarly standards, authors must disclose any use of Artificial Intelligence (AI) tools during the research and manuscript preparation process.
The use of AI tools (e.g., for language editing, summarization, data analysis, or figure generation) **must be declared in the manuscript, typically before the Acknowledgements**.
AI tools must not be credited as authors. Human authors remain fully responsible for the integrity, accuracy, and originality of the submitted work.
AI-generated content must be critically reviewed by the authors to ensure quality and ethical compliance, including data privacy and bias mitigation.
AI must not be used to fabricate or manipulate original research data, unless it is part of the approved research methodology and explicitly described.
Non-compliance with these guidelines may lead to rejection of the manuscript or post-publication corrective actions.

IT related and other non-empirical articles

The JNSF is a journal primarily devoted to natural sciences. It also considers for publication significant and novel contributions from formal sciences. Authors of emerging sub-disciplines of Computing and related areas such as Machine Learning, Artificial Intelligence and Data Sciences are requested to carefully adhere to the following guidelines when submitting manuscripts for this journal.

- Clear formulation of outcome-oriented **Research Objective/s** for targeted knowledge (sub)domain/s or (sub)discipline/s.
- Selection and comprehensive summarization of **appropriate Research Method/s** adopted to achieve the stated Research Objective/s.
- Reporting a sound **(Empirical) Evaluation** of the research finding/s thereby arguing reliability, validity, and generalizability of research claim/s.

Categories of manuscripts

Research Articles: Research Articles are papers that present complete descriptions of original research. Research Articles should include an Abstract, Keywords, Introduction, Methodology, Results and Discussion, Conclusion and Recommendations where relevant. References should be prepared according to the "Guidelines for the preparation of manuscripts". Maximum length of the article should be limited to 30 pages (Times New Roman, font size 12 , line space 1.5) with a word count less than 10,000 including references, figures and tables. Any articles above this limit will be returned. Please refer author guidelines for further details (https://jnsfsl.sljol.info/about/submissions#author-guidelines)

Reviews: Reviews are critical presentations on selected topics of Science or Technology. They should be well focused and organized and avoid general "textbook" style. As reviews are intended to be critical presentations on selected topics, the author (or the principal author in a multi-author review) need to have had substantial leadership in research supported by a publication track record in the areas covered by the review. A person/s wishing to submit a Review Article should obtain prior approval from the Editorial Board by submitting a concise summary of the intended article, along with a list of the author's publications in the related area (jnsf@nsf.gov.lk). Maximum length of the article should be limited to 40 pages (Times New Roman, font size 12 , line space 1.5) with a word count of 12,000 including references, figures and tables. Any articles beyond this limit will be returned.

Research Communications: Research Communications are intended to communicate important new findings in a specific area of limited scope that are worthy of rapid dissemination among the scientific community. Authors are required to provide a statement justifying the suitability of the submission for a Research Communication. The article should include an Abstract, Keywords, Introduction, Methodology, Results & Discussion, Conclusion and References. Maximum length of the article should be limited to 10 pages (Times New Roman, font size 12 , line space 1.5) with a word count of 2,500 including references, figures and tables. Any articles beyond this limit will be returned.

Correspondence: Correspondence will be accepted regarding one or more articles in the preceding four issues of the Journal, as well as Letters to the Editor. Articles covering important scientific events or any other news of interest to scientists, reviews of books of scientific nature, articles presenting views on issues related to science and scientific activity will also be considered. Publication will be made at the discretion of the Editor-in Chief. Maximum length of the article should be limited to 05 pages (Times New Roman, font size 12 , line space 1.5) with a word count of 1,500 including references, figures and tables. Any articles beyond this limit will be returned.

SUBMISSION OF MANUSCRIPT

Authors submitting articles to the JNSF should first create an account in the Sri Lanka Journals Online System (https://jnsfsl.sljol.info/). All manuscripts should be in MS Word format and must be submitted to the journal's online platform at https://jnsfsl.sljol.info/submit/start/. Submissions *via* emails are not encouraged. Please make sure that **no** author information is mentioned in the article submitted other than in the title page. Complete names and details of affiliations of all authors must be fed into the system during the online submission process. Authors are required to provide their personal, validated ORCID ID (by obtaining an ORCID ID from https:// orcid.org/) when submitting the manuscript. No change to the authors or order of authors will be accepted after the submission. All those who have made significant contributions should be listed as co-authors. The corresponding author should ensure that all contributing co-authors are included in the author list and have approved the final version of the paper and have agreed to its submission for publication.

All submissions should be in English. If the manuscript conforms to the guidelines specified, the date received will be the date that the manuscript was submitted to the online system.

Submissions are accepted for processing on the understanding that they will be reviewed and that they have not been submitted for publication elsewhere (including publication as a full paper or extended abstract as a part of Conference Proceedings).

Suggesting potential reviewers by authors
The authors are requested to suggest three names of referees when submitting their manuscript, in the Cover Letter space provided at the bottom of the page in the first stage of online submission. Referees should not be from the institution where the work was carried out and should not have been co-authors in previous publications. The address, institutional affiliation and e-mail of the suggested referees should be provided. Please note that the JNSF is not bound to select all or any of the suggested referees for sending the manuscript for reviewing

Authorship
All authors designated as authors should be eligible for authorship. Those who have made a substantial contribution to the concept or design of the work; or acquisition, analysis or interpretation of data are recognized as Authors.
The corresponding author should be prompt and ensure adherence to timelines when responding to requests, queries and recommendation of reviewers conveyed by or on behalf of the Editor-in Chief and Editorial Board.

Avoiding predatory references in manuscripts

Authors of the manuscripts should identify and not include predatory journal articles in the reference list.
If any paper that is cited is published in an Open Access journal, the authors are advised to ensure that the journal is listed in the DOAJ (Directory of Open Access Journals) or by the COPE (Committee on Publication Ethics). Please note that authors should check with DOAJ and COPE by themselves, and not assume that the statements given in the journal websites are accurate.
If the journal is included either in DOAJ or COPE, it can be presumed as legitimate. If not, authors need to review the journal website and published articles for characteristics of predatory journals. At the same time, authors can check whether the journal or relevant publisher is included in the directory of predatory journals and publishers.
If it is revealed that the manuscript is supported by articles published in predatory journals, it could be rejected by the JNSF at any stage of the publication process.

Supplementary materials
Any experimental data necessary to evaluate the claims made in the paper but not included in the paper should be provided as supplementary materials. Supplementary materials will be sent to the reviewers and published online with the manuscript if accepted. The supplementary materials should conform to Journal guidelines and should be uploaded as separate files. Authors should number Supplementary Tables and Figures as, for example, 'Supplementary Table S1'. Refer to each piece of supplementary material at the appropriate point(s) in the main article. Supplementary Materials may include description of the materials and methods, controls, or tabulated data presented in Tables or Figures, and programming codes.

Peer review
The manuscripts submitted to the JNSF will initially be screened by the Editorial Board and, if suitable, will be referred to at least two subject experts in the relevant field. The peer-review process of the JNSF is double-blind.
When revision of a manuscript has been requested, the revised manuscript should be submitted on or before the stated deadline. The authors' response to the comments of referees should be tabulated with the comment and response. The decision of the Editorial Board shall be final.
Accepted papers are subject to editing. The date of acceptance will be the date the Editorial Board accept the paper for publication.

Article processing fee
Article processing fee of US$ 250 will be levied for each manuscript in two stages, except when the corresponding author is affiliated with a Sri Lankan institution,
- An initial processing fee of US$ 20 will be levied for each manuscript at the peer-review stage.
- The remaining US$ 230 will be charged for accepted articles at the time of publication.

Payments can be made online via NSF Payment Portal (http://pg.nsf.gov.lk/)

Authors' declaration
The authors are required to accept the conditions indicated in the online author declaration statement.

Copyright
Articles in JNSF are published under the Creative Commons License CC-BY-ND. This license permits use, distribution and reproduction of articles for commercial and non-commercial purposes, provided that the original work is properly cited and is not changed in anyway. The copyright of the article is with the National Science Foundation of Sri Lanka. Therefore, authors are requested to check with institution's copyright and publication policy before submitting an article to the JNSF. Authors secure the right to reproduce any material that has already been published or copyrighted elsewhere. When an article is accepted for publication, the authors are required to submit the Transfer of Copyright document signed by all the authors.

Post-publication corrections
The Editorial Board reserves the right to take action on publishing an erratum or corrigendum. If serious errors are identified in a published article, the Journal may consider a retraction or publishing a correction.

STRUCTURE OF MANUSCRIPT

Manuscript
The manuscript should be free of errors and prepared in single column, using 1.5 line spaced text of Times New Roman 12 font leaving 1 inch margins. Pages should be numbered consecutively.

a. Style
The paper should be written clearly and concisely. The style of writing should conform to scholarly writing. Slang, jargon, unauthorized abbreviations, abbreviated phrasings should not be used. In general, the impersonal form should be used. Poor usage of language will result in rejection of the manuscript during initial screening.

b. Layout
Manuscripts other than review articles should be generally organized as follows: Title, Abstract, Keywords, Introduction, Methodology, Results and Discussion, Conclusions and Recommendations (where relevant), Acknowledgements and References. Pages should be arranged in the following order:

First page should include the title of the manuscript and **complete names and affiliations** of all authors. **Author information should not be mentioned in other places of the manuscript.** Any statement (including acknowledgment) which can reveal author identity should be removed. If a major part of the research has been published as an abstract in conference proceedings, it should be mentioned with citation in the space provided for "Comments for Editor". Authors must also indicate the **general and specific research area** of the manuscript in the title page.

***Title*:** Should accurately and concisely reflect the contents of the article.

***Running title*:** Should be a shortened title (limited to a maximum of 50 characters) that could be printed at the top of every other page of the Journal article.

***Abstract*:** Should be between 200 - 250 for research articles and 200 - 300 for reviews. It should not contain any references and should be able to stand on its own. It should outline objectives and methodology together with important results and conclusions.

***Keywords*:** Include a maximum of six keywords, which may include the names of organisms (common or scientific), methods or other important words or phrases specific to the study.

***Introduction*:** This should state the reasons for performing the work with a brief review of related research studies in the context of the work described in the paper. Objectives of the study should be clearly stated.

***Materials and Methods*:** This section should give the details of how you conducted your study. New methods may be described in detail with an indication of their limitations. Established methods can be mentioned with appropriate references. Sufficient details should be included to allow direct repetition of the work by others. Where human subjects are involved, they should be referred to by numbers or fictitious names. A paper reporting the results of investigations on human subjects or on animals must include a statement to the effect that the relevant national or other administrative and ethical guidelines have been adhered to, and a copy of the ethical clearance certificate should be submitted. Methods of statistical analyses used should be mentioned where relevant.

Results and Discussion
Results: the results should be concisely and logically presented. Repetition of the same results in figures, tables or text should be avoided.
Discussion: data essential for the conclusions emerging from the study should be discussed. Long, rambling discussions should be avoided. The discussion should deal with the interpretation of results. It should logically relate new findings to earlier ones. Unqualified statements and conclusions not completely supported by data should be avoided.
Molecular sequence data, such as gene or rDNA sequences, genome sequences, metagenomic sequences etc. must be deposited in a public molecular sequence repository, such as GenBank, that is part of the International Nucleotide Sequence Database Collaboration (INSDC). The accession numbers obtained must be cited in the text, Table or on Figures of phylogenetic trees of the manuscript.

***Conclusion*:** The conclusion should be brief, highlight the outcomes of the study and should be aligned with the objectives of the study. It should not contain references.

Competing Interest statement: The authors should include a statement on conflict of interest disclosing any financial or other substantive conflicts of interest that may influence the results or interpretation of the research in the space provided in the online article submission form. All sources of financial support for the project should also be disclosed.

***Acknowledgement*:** Should be brief and made for specific scientific, financial and technical assistance only. If a significant part of the research was performed in an institution other than the authors' affiliations should be acknowledged. All those who have made substantial contribution to the research but do not qualify to be authors should be acknowledged.

***References* :**
The JNSF uses APA (7th Edition) reference style
All research work of other authors, when used or referred to or cited, should be correctly acknowledged in the text and in the References.
All the references in the text should be in the list and vice versa

Citing references in the text:
- References to the literature must be indicated in the text and tables as per the Author-Year System, by the author's last name and year, in parenthesis (i.e. Able, 1997) or (Able & Thompson, 1998).
- Citation to work by more than two authors should be abbreviated with the use of et al. (i.e. Able *et al*., 1997).
- Multiple publications by the same first author in the same year should be coded by letters, (i.e. Thompson, 1991a, 1991b,1992,1993).
- Multiple citations of different authors should be made in chronological order and separated by a semicolon, (i.e. Zimmerman *et al*., 1986; Able *et al*., 1997).

Citing references in the List of references:
- The list of References should be arranged in alphabetical order based on the last name of the first author.
- In APA 7th ed., **up to 20 authors** should be included in a reference list entry. Write out the last name and first initial(s) for each contributor.

Example for 2–20 authors:

Wright, A., Komal, G., Siddharth, D., Boyd, G., Cayson, N., Beverley, K., Travers, K., Begum, A., Redmond, M., Mills, M., Cherry, D., Finley, B., Fox, M., Ferry, F., Almond, B., Howell, E., Gould, T., Berger, B., Bostock, T., & Fountain, A. (2020). Styling royalty. London Bridge Press.

- For references with more than 20 authors, after listing the 19th author replace any additional author names with an ellipsis (…) followed by the final listed author's last name and first initial(s).

Example for 21+ authors:

Kalnay, E., Kanamitsu, M., Kistler, R., Collins, W., Deaven, D., Gandin, L., Iredell, M., Saha, S., White, G., Woolen, J., Zhu, Y., Chelliah, M., Ebisuzaki, W., Higgins, W., Janowiak, J., Mo, K.C., Ropelewski, C., Wang, J., Leetmaa, A., … Joseph, D. (1996). The NCEP/NCAR 40-year reanalysis project. Bulletin of the American Meteorological Society, 77(3), 437-471. http://doi.org/fg6rf9

- All the initials of the author must be given after the last name and the year of publication should follow in parentheses.
- This should be followed by the full title of the referred publication.
- When journal articles are listed, the journal name should be given in full and in italics and followed by the volume number, issue number in parentheses and then the inclusive pages.
- Where there are several publications by the same author(s) and published in the same year they should be differentiated by adding a lower-case letter after the year.

Example

Clarke, P. N., & Fawcett, J. (2014a). Life as a mentor. *Nursing Science Quarterly*, 27(3), 213-215. https://doi.org/10.1177/0894318414534492

Clarke, P. N., & Fawcett, J. (2014b). Life as a nurse researcher. *Nursing Science Quarterly*, 27(1), 37-41. https://doi.org/10.1177/0894318413509708

- Digital object identifiers (DOIs) should be included for all references where available.

Details about this reference style can be obtained from below links
- https://apastyle.apa.org/style-grammar-guidelines/references
- https://apastyle.apa.org/style-grammar-guidelines/references/examples
- https://libguides.jcu.edu.au/apa

Abbreviations and Symbols: Unless common, these should be defined when first used, and not included in the abstract. The SI System of units should be used wherever possible. If measurements were made in units other than SI, the data should be reported in the same units followed by SI units in brackets, e.g. 5290 ft (1610 m).

Formulae and Equations: Equations should be typewritten and quadruple spaced. They should be started on the left margin and the number placed in parentheses to the right of the equation.

Nomenclature: Scientific names of plants and animals should be printed in italics. In the first citation, genus, species and authority must be given. e.g. *Borassus flabellifer* Linn. In latter citations, the generic name may be abbreviated, for example, *B. flabellifer* L.

Tables and figures: Tables and Figures should be clear and intelligible and kept to a minimum, and should not repeat data available elsewhere in the paper. Any reproduction of illustrations, tabulations, pictures etc. in the manuscript should be acknowledged.

Tables: Tables should be numbered consecutively with Arabic numerals and placed at the appropriate position in the manuscript. If a Table must be continued, a second sheet should be used and all the headings repeated. The number of columns or rows in each Table should be minimized. Each Table should have a title, which makes its general meaning clear, without reference to the text. All Table columns should have explanatory headings. Units of measurement, if any, should be indicated in parentheses in the heading of each column. Vertical lines should not be used and horizontal lines should be used only in the heading and at the bottom of the table. Footnotes to Tables should be placed directly below the Table and should be indicated by superscript lower case italic letters (^{a}, ^{b}, ^{c}, etc.).

Figures: All illustrations are considered as figures, and each graph, drawing or photograph should be numbered consecutively with Arabic numerals and placed at the appropriate position in the manuscript. Any lettering to appear on the illustrations should be of a suitable size for reproduction and uniform lettering should be used in all the Figures of the manuscript. Scanned figures or photographs should be of high quality (**300 dpi**), to fit the proportions of the printed page (12 × 17 cm). Each figure should carry a legend so that the general meaning of the figure can be understood without reference to the text. Where magnifications are used, they should be stated.

Units of measurement

Length: km, m, mm, µm, nm
Area: ha, km^2, m^2
Capacity: kL, L, mL, µL
Volume: km^3, m^3, cm^3
Mass: t, kg, g, mg, µg

Time: year(s), month(s), week(s), day(s), hour(s), minute(s), second(s)
Concentration: M, mM, N, %, g/L, mg/L, ppm
Temperature: °C, K
Gravity: x g

Molecular weight: mol wt
Others: Radio-isotopes: 32P
Radiation dose: Bq
Oxidation-reduction potential: rH
Hydrogen ion concentration: pH